Ph. D. Thesis

Nir S. Kampel

Forward and backward scattering experiments in ultra-cold Rubidium atoms

A Raman memory and Superradiance detuning asymmetry experiments

E	1	20/200
F P	2	20/100
T O Z	3	20/70
L P E D	4	20/50
P E C F D	5	20/40
E D F C Z P	6	20/30
F E L O P Z D	7	20/25
D E F P O T E C	8	20/20
L E F O D P C T	9	
F D P L T C E O	10	
P E Z O L C F T D	11	

Principal academic supervisor: Eugene S. Polzik

Additional academic supervisors: Jörg H. Müller

Thesis submitted :   17/12/2012

Abstract

In this thesis two different projects are described dealing with different aspects of light scattering. In the first we are examining the origin of backward scattering as manifest in Rayleigh superradiance. Here we have studied the onset dependence on the sign of the probe detuning. In the second project, we have studied coherent forward scattering in the form of a memory experiment. In such an experiment we convert the input light pulse to an atomic excitation, and at a later time convert back the atomic excitation into the retrieved light pulse.

In the first project, we investigate the source for the detuning sign difference in the onset of Rayleigh superradiance. We find a difference of up to a factor of three between red and blue detuning when using the $D1$ line in Rubidium 87. We model this by adding a detuning dependent loss term to a rate equation description of the superradiance. With a microscopic description of the loss term due to light assisted collisions followed by radiation trapping, we find a reasonable quantiative agreement between model and experiment.

In the second project we have realized off resonance Raman memory in an ultra-cold thermal sample in a magnetic trap, with total efficiency of 15%. In addition we have imaged the retrieved signal using a detection system that can distinguish between 30 independent modes, using balanced homodyne imaging.

The goal with the memory experiment, as presented in this thesis, is a first step towards multimode memory utilizing the high optical depth of the ultra-cold sample. Here we find that due to magnetic dephasing of the ground levels the coherence time is 7μs, and that as we increase the optical depth or the drive light power we get a reduction of the total efficiency contrary to our expectations of saturating the total efficiency.

Sammendrag

I denne tese beskrives to forskellige projekter der begge beskæftiger sig med forskellige aspekter af spredning af lys. I det første undersøges processen bag baglæns spredning, som forefindes i såkaldt Rayleigh superradians. I dette projekt har vi undersøgt ved hvilkt fortegn af detuningen af probe feltet denne superradians indtræffer. I det andet projekt er den kohærente fremadrettede spredning undersøgt. Dette er gjort ved et hukommelseseksperiment. I sådan et eksperiment konverteres en indsendt lys-puls til en eksitation af atomerne, og ved et senere tidspunkt bliver denne eksitation konverteret til en lys-pul igen der så opfanges.

I det første projekt undersøges mekanismen bag fortegns forskellen ved indtræfning af Rayleigh superradians. Der etableres en forskel på helt op til tre mellem den røde og blå detuning når $D1$ linien for Rubidium 87 benyttes. Vi modellerer dette ved at tilføje en detuning afhængig tabsproces i en rateligning der beskriver den observerede superradians, og estimerer tabsleddet som kollisioner assisteret ved lys efterfulgt af strålingsindfangning hvilket reducerer stofbølge kohærensen.

I det andet projekt har vi realiseret en ikke-resonant Raman hukommelse i en ultra-kold termisk prøve fanget i en magnetisk fælde, med en total effektivitet på 15%. Ud over dette har vi undersøgt det modtagne signal ved et detektionssystem der kan adskille imellem 30 forskellige kanaler, ved hjælp af såkaldt *Balanced Homodyne Imaging*.

Målet med hukommelseseksperimentet, som beskrevet i denne tese, er første

skridt mod realisering af hukommelse ved mange tilstande ved hjælp af den høje optiske dybde koefficient af den ultra-kolde prøve. Det er etableret at den magnetiske affasning af grundtilstandende fører til en kohærenstid på 7μs, og at ved at forstærke den optiske dybde koefficient eller intensiteten af drivnings-feltet, reduceres den totale effektivitet i modsætning til forventningerne om en mætning af den totale effektivitet.

To my loving family

Preface and Acknowledgements

I have joined Eugene Polzik research group in June 2008. Working in the BEC sub-group under the principle investigator Jörg Helge Müller. I am grateful to both of them for accepting me after coming from a different field of physics, allowing me learn and work in the wonderful field of quantum optics. Specifically I would like to thank Jörg whom I worked closely with for his endless patience and for the enjoyable discussions about physics from which I have learned so much. I'm grateful for the great supervision I got from Jörg, for his endless knowledge in physics, electronics, and programming. For allowing me to do mistakes and for always being willing to discuss problems, results, and the meaning of them.

When I arrived the lab was working towards showing correlation between the backward scattered photons and the atoms in the superradiant mode to the shot noise level. I joined this effort working with Franziska Kaminski (a Ph.D. student) and Rodolphe le Targat (a postdoc). I thank both for greeting me with open arms and for teaching me how the experiment works. Specifically, I would like to thank Rodolphe for his patience while teaching me how to operate and align the different components, and for his patience with the initial beginners mistakes.

At the end of 2009 Rodolphe has left the lab for another postdoc position at Hamburg university, and in early 2010 we were joined by a new postdoc, Axel Griesmaier. During this time we were working on imaging the Faraday rotation in a high dense, high optical depth ($OD = 680$) sample. Axel came and brought new spirit into the lab, and with his huge experience thought me a lot about how to work and how to maintain the experiment running. In September 2010 we have finished with the Faraday rotation imaging, and Franziska has started analyzing the data and left the lab.

At the same time, Mads Peter H. Steenstrup has joined as a new Ph.D. student and we have started working to better understand the source of the detuning asymmetry in Rayleigh superradiance. We finished taking the data for this project in the beginning of 2011, and sadly shortly after Axel left us. I would like to point out the nice working atmosphere Axel has brought with him and that I had lots of fun working with him. We then started working on off-resonant Raman memory, and as a first step we have decided to do the experiments in the magnetic trap and not to transfer the cloud to a dipole trap. We have started by measuring the Rabi oscillation by examining the time evolution of the light in a single shot, which have allowed us to test and improve the detection scheme. Then in September 2011 the work on the Rabi oscillation was stopped and we moved to the memory experiment and have finished taking data by April 2012.

We also had a bright bachelor student, Thomas Berlok, that have done his final Bachelor project in our lab. Here I was co-supervising him on a project called "Interaction of hot Bose-Einstein condensates with resonant light: An experimental study". In this project we studied how does resonant light influences a bi-modal cloud and can we increase the condensate fraction with the light pulse. I would like to thank Thomas for adding great (fun) atmosphere to the lab.

Here I want to thank Franziska Kaminski for the useful discussion and help throughout our long overlapping time period, including the late nights we shared in the lab.

I thank all Quantoppies for making quantop such a great place to work at. For the excellent coffee breaks with the "no physics" rule that every now and again was broken :-). For the late night dinners, for the early morning breakfast, for the early morning coffee and early morning smiles even when it is raining outside and you come in wet from head to tow.

I thank Jürgen Appel, for the very useful physics discussions and the huge help in all technical aspect I was deling with from electronics to optics. I thank Henrik Berelsen an electronic technical supporter at the Niels Bohr Institute, with whom I worked closely on designing several project. I have learned a lot from Henrik and enjoyed every minute working with him. I would also like to thank all the technical support team at the Niels Bohr Institute i worked with that consists from Henrik Bertelsen, Axel Boisen, Jimmy Cali Hansen, and Erik Grønbæk Jacobsen for their fast response and kind smiling help.

I thank my family and friends for the great mental support I got, and for the knowledge that there is always someone who watches my back.

Last but not least I would like to thank Lucy Lipkind, without whom I would not have reached this stage. Lucy is the first person that managed to teach me, in the second grad she managed not only to thought me how to read and write but also how to sit down, learn, and concentrate. Her help has allowed me, over time, to over come lots of the aspects of my dyslexia that still bothers me to this day.

Contents

Abbreviations and Acronyms

SR Superradiance

OD, d_0 resonant optical depth

DL Drive Light

SB Signal Beam

LO Local Oscillator

a_0 Bohr radius

AOM Acousto-Optic Modulator

RWA Rotating Wave Approximation

BEC Bose-Einstein condensate

TOF Time Of Flight

PBS Polarizing Beam Splitter

BW Band-Width

NNS Noise Normalized Signal

PID proportional integrate differential

DAC Digital to Analogue Converter

DDS Direct Digital Synthesizer

VCO Voltage Controlled Oscillator

NIR Near Infrared

STIRAP Stimulated Raman Adiabatic Passage

EIT electromagnetically induced transparency

CIRB controlled reversible inhomogeneous broadening

AFC atomic frequency comb

CV Continuous-variable

NBI Niels Bohr Institute (organisation)

QUANTOP Danish National Research Foundation Centre for Quantum Optics
     (organisation)

Introduction

The field of quantum information utilizes the following basic principles of quantum mechanics theory: the superposition principle and the collapse of the wave function after a measurement. An abstract description of the encoded information in a two level system a quantum bit (qubit), is achieved by a wave function $\psi = a\,|0\rangle + b\,|1\rangle$ with a and b are complex numbers that satisfy $|a|^2 + |b|^2 = 1$. This is different from classical information theory in which a bit is described by either $|0\rangle$ or $|1\rangle$, i.e. $a = 1$ & $b = 0$ or $a = 0$ & $b = 1$. One of the major conceptual differences between classical and quantum description is evident in the no cloning theorem [Wootters82] which states that one cannot clone (copy) a general state. Later there were two major achievements that have strongly influenced the development of the field, in quantum communication the BB84 protocol that allows a secure communication between two distinct parties [Bennett84, Gisin02], and Shor's algorithm to find the integer factorization of a large number [Shor94].

For different applications of quantum information different realization of the quantum bit have advantages. For example, using the photon polarization is very useful for implementing a communication between two distant locations while the internal degrees of freedoms of a trapped ion (or an atomic cloud) are better suited for quantum computation (or simulation). Combining the two enables utilizing the advantages from each realization, for example extending the distance over which entanglement is shared via entanglement swapping (the DLCZ protocol) [Duan01, Gisin02]. When combining entanglement swapping with a quantum memory one realizes a quantum repeater [Sangouard11].

In our group we are interested in studying the light-atom coupling with respect for quantum information, basically there are three different type of processes: beam-splitter (basis for memory scheme), parametric-gain[1] (basis for entanglement generation scheme), and quantum nondemolition (or Faraday) interaction (basis for entanglement, memory, and teleportation schemes) [Hammerer10]. In these three light-atom interactions the optical depth, i.e. the coupling strength for a given transition, is the relevant parameter and needs to be as large as possible [Hammerer10]. Therefore in our lab we have realized a system of ultra-cold atoms capable of reaching Bose-Einstein condensate with resonance optical depth as high as 3000 for a closed optical transition.

---

[1]Also called the two-mode squeezing.

1.1   Overview of lab projects

The work presented in this thesis has been performed in the BEC lab of the experimental quantum optics group at NBI. In our lab we have experimentally investigated the main three type of interactions in quantum information. We have projected the three Hamiltonians to the following experimental implementations:

1. *Parametric-gain interaction (or the two mode squeezer)* realized in a superradiance experiment. Here we started by studying the dynamics of the process [Hilliard08a], then we moved to measure the one-to-one correlation between the backward scattered photons and forward scattered atoms [Hilliard08b, Kaminski12b].

2. *Quantum nondemolition* as manifested in a Faraday rotation. Here we have developed a dual-port polarization-contrast imaging technique to measure the spatially dependence, and measure the angle as function of detuning at an optical depth of 680. Here we found an increase of the Faraday angle by a factor of 1.46 due to light assisted collisions [Kaminski12a, Kaminski12b].

3. *Beam-splitter-type interaction* is realized in an off-resonant Raman memory experiment. Here we utilize the high optical depth in our system[2] of about 200, to realize a memory that could be used as a quantum memory. The results of this experiment are presented in part II of this thesis.

In addition to the above projects we had two additional projects besides the quantum information applications. The first was motivated by a theoretical paper claiming that Rayleigh superradiance has a red/blue asymmetry [Deng10b], which has revived our interest in the onset of Rayleigh superradiance especially after the detuning asymmetry was shown experimentally [Deng10a]. Here we had a different mechanism in mind than the one suggested by Deng *et al.* that states, the detuning asymmetry originates from light assisted collisions followed by radiation trapping [Kampel12]. The results of this project are given in part I of this thesis.

The second side project was to investigate the effects of resonant light on a bimodal cloud. Wether it is possible to find a parameter regime in which we can increase the number of atoms in the condensate due to the resonant light. We found that this method is very good to remove the thermal part without influencing the condensed part. Since the light does not penetrate the BEC due to the high optical depth. This project was done as a bachelor project, that I was co-supervising. The results are summarized in [Berlok12].

I have joined the BEC lab during the superradiant one-to-one correlation measurements, and have contributed to all of the above projects except to the superradiance dynamics study. In this thesis we have decided to focus only on the superradiance detuning asymmetry and the memory experiments since the other experiments are well covered in the theses of Andrew Hilliard [Hilliard08b] and Franziska Kaminski [Kaminski12b].

---

[2]Note the optical depth is smaller from before due to unfavorable Clebsch-Gordan coefficients by a factor of six.

General production of the ultra-cold cloud

The bread and butter of all our different experiments is the production of the ultra-cold Rubidium 87 atoms. The preparation and characterization of the ultra-cold atomic clouds follows standard techniques. The specific implementation in our lab is described in details in the thesis of Andrew Hilliard [Hilliard08b] and in the thesis of Franziska Kaminski [Kaminski12b].

For completeness, the scientific features of the production and the key parameters of the atomic sample are summarized in the next few paragraphs. We produce a prolate cloud of ^{87}Rb in the atomic trappable state $\left|F_0 = 1, m_f = -1\right\rangle$ where F_0 is the ground state hyperfine quantum number and m_f is the Zeeman sublevel. The cloud is cooled down by evaporative cooling inside a magnetic trap, to either a Bose-Einstein condensate (BEC) or a thermal cloud depending on the end position of the rf-knife. At the end we produce a cold cloud with trap frequencies of $\omega_{\perp} = 2\pi \times 115.4\text{Hz}$, $\omega_{long} = 2\pi \times 11.75\text{Hz}$.

In Fig. 2.1 we show a schematic of the actual atomic setup with the vacuum system, where atoms are cooled and trapped in two different vacuum chambers. In the "loading chamber", we do the initial trapping in a 2D-MOT (or loading MOT) after releasing the Rubidium atoms from a dispenser. Then we push the atoms into the "science chamber" where the atoms are trapped in a 3D-MOT (or science MOT). The two chambers are separated by a differential pumping stage, which allows to maintain two orders of magnitude of pressure ratio between the chambers. The loading chamber has the higher background pressure, for the initial capture of the hot atoms. The science chamber needs (and has) a lower background pressure to reduce collisions with background particles [Stam07, Lin09]. This is important as we have 40 to 50 seconds of evaporation, and for some experiments we want to have a long life time. In our case this was done extremely well as we find that the BEC life time is of several minutes with about 50% of the atoms left after three minutes when the rf-knife removes the warm atoms.

The experimental sequence: First we load the atoms for 20 to 30 seconds, then compress and cool the atoms using optical molasses to about 10μK. Subsequently we turn off all the lasers and capture the atoms in a quadrupole trap. In the quadrupole trap we first do an evaporation step from 50MHz till 20MHz. Typically here we have a transfer efficiency of about 18% from the initial atom number (measured by fluorescence after recapturing in the 3D-MOT).

At this stage we adiabatically turn on the Ioffe coil, such that we produce a
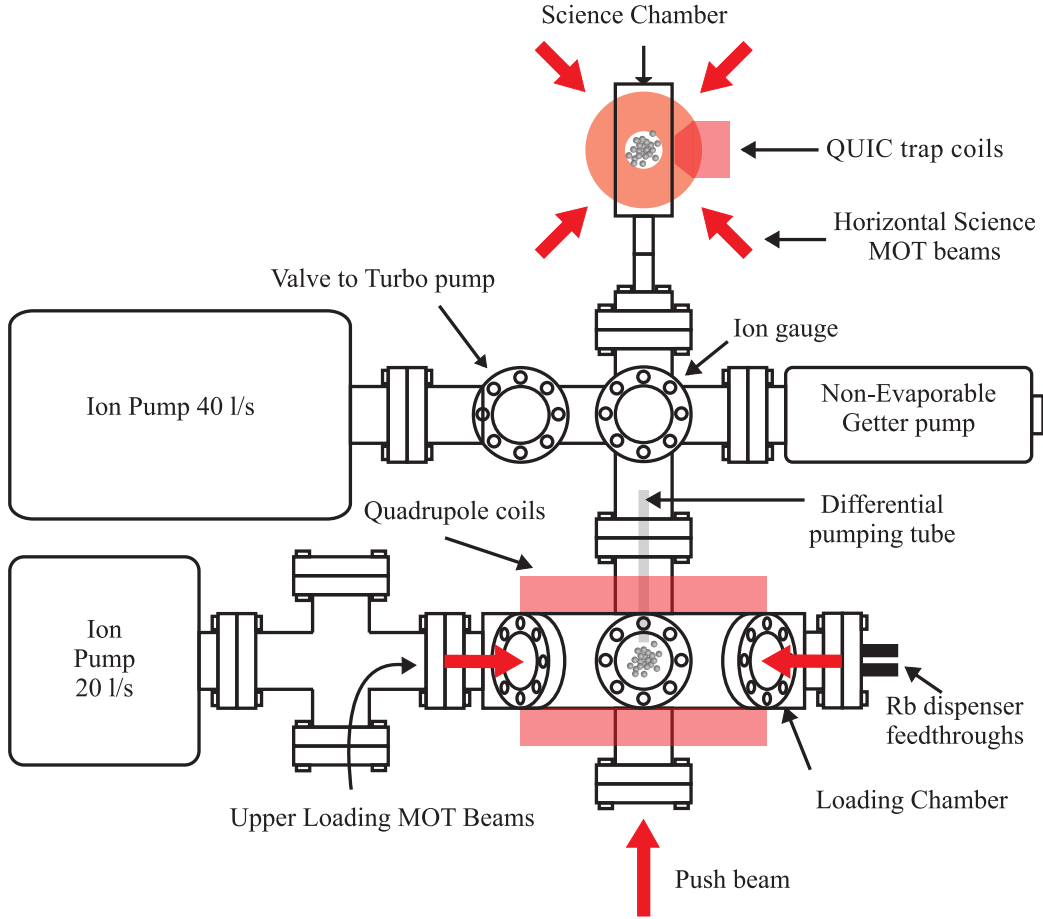
Figure 2.1: The atomic experimental setup including the vacuum system.

Ioffe-Pritchard trap configuration (or QUIC trap). After the atoms have been transferred (and moved 8mm in our case), we continue with the evaporation in a stiff trap until the evaporation efficiency is limited by 3-body losses. To reduce this we "relax" the trap[1], and do the last steps of the evaporation.

When cooling below the critical temperature we achieve a BEC containing about 10^6 atoms with Thomas-Fermi radii of $r_\perp = 6\mu$m and $r_{long} = 60\mu$m.

For the superradiance and memory experiments the cloud is probed/pumped along its long axis, i.e. right to left in Fig. 2.1. The physical optical access along this axis is through a 4mm hole in the Ioffe coil holder. The length of the cylindrical core (~ 100mm) restricts the focuss of the beam to $w_0 \geq 20\mu$s at the location of the cloud.

After the cloud interacted with the probe/pump light we investigate the cloud using absorbtion imaging after time of flight[2] (TOF). Before we image, the atoms are pumped into the state $|F = 2, m_f = -2\rangle$, then we probe the cloud for 50μs using the cycling transitions to the excited state $|F' = 3, m_f = -3\rangle$. For inferring the optical depth we also take a background and a bias images. From the optical depth image we deduce the cloud's parameters by fitting it to either a gaussian or a Thomas-Fermi profile. For more details see [Hilliard08b] and (or) [Kaminski12b].

---

[1]We do this by reducing the fields gradients, which lowers the trap frequencies. Thus we get lower densities and less 3-body losses [Stam07].

[2]The time of flight is limited to $15 - 45$ms. The lower limit is due to the camera focus range and the upper limit is due to the cell wall.

Part I

Superradiance - Detuning symmetry

Introduction to superradiance

Superradiance is the collective enhancement of spontaneous emission of independent atoms (or molecules) as first described by Dicke in 1954 [Dicke54]. Considering a collection of two level systems in which all atoms are initially in the excited state, a single spontaneous emission event triggers a collectively enhanced emission pulse heading along the direction of the high optical depth. The characteristic time scale for the collective emission is faster by the number of participating atoms compared to the spontaneous lifetime of an isolated atom.

After the development of the dye laser during the 1960s till the early 1980s superradiance (SR) was extensively studied as it was relatively easy to excite the atoms and achieve the population inversion criterion [Gross82]. Interest has restarted in the late 1990s with the achievement of ultra-cold atomic samples (BEC) [Inouye99, Schneble03], which allowed realizing SR without population inversion between electronically excited levels. In this configuration there are two types of SR: Rayleigh and Raman scattering.

In *Raman SR* we consider a Λ system with a pump pulse coupling the populated ground state to an empty ground state via an excited state. The SR radiation pulse is emitted on the undriven leg of the Λ system, thus we get a change of the internal atomic state between two ground states [Yoshikawa04, Schneble04]. Note that here the intensity of the drive pulse determines the time scale, unlike in early SR experiments in which the time scale was set by the excited state life time.

In *Rayleigh SR* instead of transferring between two different internal atomic states the coupling is between atomic momentum states mediated by Rayleigh scattering. Here an off resonance probe produces spontaneous scattering events leading to atoms being translated in momentum space, in which a photon is emitted along the high optical depth axis of the sample and the atom recoil according to the momentum difference of the incident and scattered light. For example, if we probe along the long axis of the sample then the SR photon will be emitted in the backward direction and the atom will receive twice the photon momentum ($\hbar k$) [Inouye99, Schneble03]. This microscopic picture implies that one expects to find a one-to-one correlation in the number of backscattered photons and recoiling atoms.

3.1   Classical picture of Rayleigh superradiance

In this thesis we are interested in the Rayleigh SR, and describe it using the "Bragg" grating or "matter wave grating" picture [Ketterle01]. Identifying the collective sample wave function as Ψ then the Rayleigh scattering event perturbs it
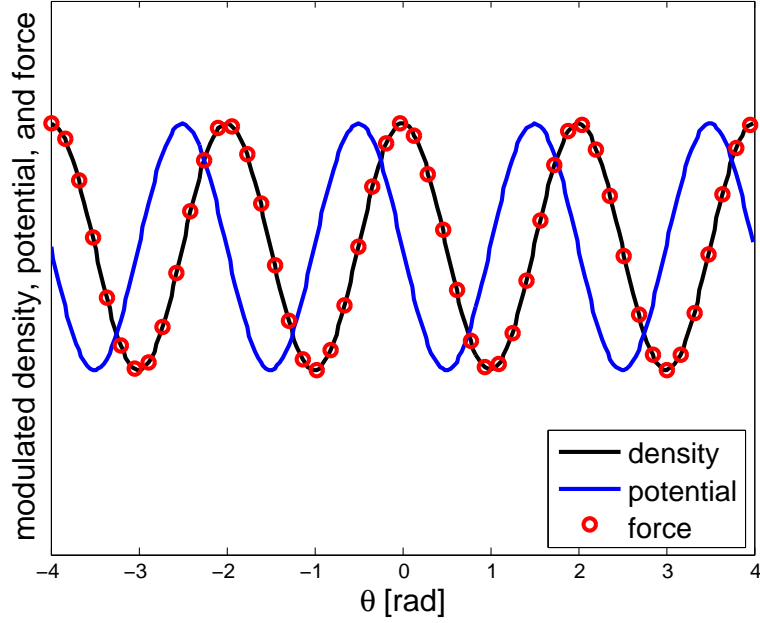
Figure 3.1: The matter-wave and light modulations for the phase difference $\phi_l - \phi_a = \pm\pi/2$ for blue/red detuning. Black line is the density around the initial value (dashed magenta). Blue is the light-atom dipole potential around the density profile. Red circles is the light dipole force shifted around the mean density value.

to $\Psi = \Psi_0 + \Psi_2 e^{-i(\omega_a t - \mathbf{k_a} \cdot \mathbf{r} + \phi_a)}$, where Ψ_0 is the wave function of the unperturbed atoms (or atoms at rest), Ψ_2 is the wave function of the perturbed atom with $2\hbar k$ momentum[1], $\omega_a t - \mathbf{k_a} \cdot \mathbf{r}$ is the dynamic part of the phase given to the perturbed atoms and is fixed by energy and momentum conservation, and ϕ_a is the phase difference. For probing along the high optical axis we have $\mathbf{k_a} = 2\mathbf{k_p}$ and $\omega_a = 4\omega_r$. With $\mathbf{k_p}$ the probe wavenumber, and $\omega_r = \hbar k_p^2/(2M) = 2\pi \times 3.6\text{kHz}$ the recoil frequency. The sample density is found from,

$$n(\mathbf{r}) = |\langle \Psi | \Psi \rangle| = |\Psi_0|^2 + 2\left|\Psi_0 \Psi_2^*\right| \cos\left(\omega_a t - \mathbf{k_a} \cdot \mathbf{r} + \phi_a\right) + |\Psi_2|^2 \quad (3.1)$$

The resulting density has a slowly moving density modulation forming a sinusoidal grating[2] due to the interference term between the two momentum modes. The grating maxima and minima initial position is determined by the initial phase ϕ_a. This grating increases the backward scattered light thus increases the grating contrast, which in turn amplifies the reflected light. Thus, this is a self amplifying process that grows exponentially with time.

We can now examine the complementary picture of a light grating that diffracts matter waves. We write the light-atom dipole potential from the incident probe light (E_p) and the scattered light (E_s) after adiabatically eliminating the excited states as,

$$U_{dip} \propto I/\Delta \propto \left|E_p\right|^2/\Delta + 2\left(\left|E_p E_s\right|/\Delta\right) \cos\left(\omega_a t - \mathbf{k_a} \cdot \mathbf{r} + \phi_l\right) + |E_s|^2/\Delta \quad (3.2)$$

with I the total intensity, Δ the probe detuning, and ϕ_l the phase difference between the probe light and the scattered field. The main contribution to the force changing the atomic momentum distribution comes from the interference term, as it is both amplified by the probe field and has a modulation with the short length scale (optical wavelength).

---

[1]Note here we explicitly assume that the emitted photons are in the backward direction therefore the atoms get two momentum kicks ($\hbar k$)

[2]Sometime this is also called a "walking" standing wave

For the case $\phi_l - \phi_a = \pm\pi/2$ with blue/red detunings[3] (positive sign for blue detuning) we get that both the light grating and matter-wave grating are enhanced. To see this we examine the contribution to the dipole force due to the interference part[4], $\mathbf{F_{inter}} = \mathbf{k_a} \left(2 \left| E_p E_s \right| / |\Delta| \right) \cos \left(\omega_a t - \mathbf{k_a} \cdot \mathbf{r} \right)$ and in Fig. 3.1 we show the density modulation, dipole potential and F_{inter} around the mean density value for this case. The total force acting on a single wavelength of the sample is pointing in the direction of $\mathbf{k_a}$, since there are more atoms in the interference maxima than in the interference minima ($\int \mathbf{F_{inter}} n d\mathbf{r} > 0$). This means that more atoms are transferred to the $2\hbar\mathbf{k_a}$ momentum state which increases Ψ_2 and increases the density modulation. In turn each atom that gains the extra momentum corresponds to an additional scattering event, i.e. increasing E_s. The mutual increase of both Ψ_2 and E_s enhances the matter-wave and light gratings. A more detailed description including the interaction between the light and atoms is given in section 5.3, where we derive the equations of motion for the light and atoms from the Maxwell-Schrödinger equations.

The required phase difference for maximum gain $\phi_l - \phi_a = \pm\pi/2$ is, actually, automatically realized. When looking at the atomic phase difference for the first scattering event its value can be set to $\phi_a = 0$, by setting the coordinate system on that unknown atom that emits the first spontaneous photon. We are allowed to do this since we can neglect any evolution of the atom during the Rayleigh scattering event, as the time scale for any such evolution is set by the natural life time which is about 30ns. This means that the atomic grating peak is at the location of the first scattering event which is random and changes from realization to realization. For the scattered light field at far off resonance we have $\phi_l = \pm\pi/2$. This can be seen as we drive a dipole with an off resonant oscillating force (the probe). The phase of the dipole response as a function of detuning follows an arctangent function with the needed asymptotic values. Note that the direction of the emission of the photon is random. Thus we require enough Rayleigh scattering events to get the first photon along the right direction. In addition, as in any real system, there are also losses. Thus, the SR threshold is not due to a single scattering event but requires more events in order to overcome the losses in the system.

From the above picture two points are evident:

1. SR is sensitive to the quantum fluctuations of spontaneous scattering events.

2. SR has a built in red/blue detuning symmetry.

The first point has been investigated in [Hilliard08b]. There has also been a considerable effort to detect directly the one-to-one correlation between the number of backward scattered photons and atoms in the excited momentum state ($2\hbar k$) [Hilliard08b, Kaminski12b]. Successful detection of the correlation would also enable to generate useful entanglement between the backward scattered light and the recoiling atoms [Moore00].

The second point, red/blue detuning symmetry, is at the heart of this part of the thesis. Apparently, even though Rayleigh SR has been studied for many years, all of the experiments in BECs until 2010 were done using red detuned probes only, and no one had tested the detuning symmetry.

---

[3]Here we define red detuning as $\Delta = \omega_p - \omega_a < 0$, i.e. the probe energy is lower than the transition energy.

[4]Here, for convenience, we take the $\phi_a = 0$ and $\phi_l = \pm\pi/2$.

3.2 The detuning asymmetry

In late 2009 Deng *et al.* have put on the arXiv the draft of a theory paper which was published February 2010 [Deng10b], claiming to "...explain why matter-wave superradiance can occur only when the pump laser is red detuned". This strong claim, was quickly supported with experimental evidence put at the end of 2010 in [Deng10a].

These two papers have started a debate on the source of the asymmetry. The theory given in [Deng10b] has encountered lots of criticism summarized in the comment [Ketterle11] and a reply [Deng11]. Our interest has started since we did not agree with the explanations put forth in [Deng10b, Deng11, Deng10a], and we had a different explanation in mind. But before we continue with the discussion on how to approch the problem, we first take a closer look on how the dipole force depends on the detuning as given in Eq. 3.2. Specifically we are interested in the onset process when the scattered field (E_s) is on the level of a single scattering event. As we require that the scattering rate (R) is constant regardless of the used detuning and define $R = E_p^2/(\Delta^2 a^2)$, with a a constant for dimensions, and rewrite the dipole potential as:

$$U_{dip} \propto 2aR^{1/2}\left|E_s\right|\cos\left(\omega_a t - \mathbf{k_a}\cdot\mathbf{r} + \phi_l\right) + a^2 R\Delta + \left|E_s\right|^2/\Delta \qquad (3.3)$$

Here we have ordered the terms of the above equation by the dipole force magnitude. The biggest contribution is from the interference (or SR) term with both big amplification proportional to $R^{1/2}$ and a big derivative as it changes with an optical wavelength scale (k_a). The other two terms are significantly smaller, though which of them is bigger then the other depends on the actual realization of the probe light. For any reasonable realization the next term in size is the radial dipole force due to the probe beam[5]. It is proportional to the gradient of the intensity distribution and increases linearly with detuning, $\propto \nabla R\Delta$. The smallest contribution to the dipole force, comes from the scattered light $\nabla\left|E_s\right|^2/\Delta$ since it is both multiplied by a single scattering event (during the SR onset) and the spatial derivative is proportional to the sample length[6]. The derivative is proportional to the sample length, since it is more likely that the scattering event will occur at the beginning of the sample. A more detailed analysis including propagation along the sample gives a mode shape described by a modified Bessel function[7] leading to the same length scale for the variation of the scattered field.

From the above dipole force estimation the two extra terms for the dipole force have inherent detuning asymmetry, but are significantly smaller. The effect of the first one, $\propto \nabla R\Delta$, is to change the trapping potential and increases with increasing detuning. In past measurements of the Rayleigh SR performance spanned over a wide rage of red detunings (from $\Delta = -2\text{GHz}$ till $\Delta = -8\text{GHz}$). No significant deviation from a simple constant scattering rate was observed [Hilliard08a]. Therefore this term can not explain the detuning asymmetry observed by Deng *et al.*.

The model given by Deng *et al.*, suggests that the SR asymmetry is due to the dipole force for the single scattering event ($\nabla\left|E_s\right|^2/\Delta$). The scattered field is amplified upon propagation through the medium and is assumed to change the structure factor for light scattering by modifying the sample mean field energy [Deng10b, Deng10a]. Since the structure factor depends sensitively on interac-

---

[5]We explicitly assume here that the probe beam waist is much bigger than the probe wavelength.

[6]Here we assume that the sample length is much longer than an optical wavelength.

[7]A similar problem it was analytically solved (and shown) in [Raymer81, Mishina07]

tion and correlation properties of the constituent particles, this suggestion appears entirely unfounded without a detailed look at the microscopic properties. Note that in this model only the effect of the amplified scattered field is considered while the much bigger effect of the interference term (the grating) is neglected. Moreover the mean field energy is a nonlinear contribution, which means that it affects the time evolution of the SR only at later stages and not at the onset, we show this using a more detailed calculation in section 5.3.

Instead of approaching the problem from a macroscopic point of view, we examine the problem from a microscopic point of view, by adding to the typical far-field dipole-dipole interaction between atoms, the contribution of light scattering for atom pairs in their respective near-field. This mechanism is well studied in the context of photoassociation spectroscopy [Weiner99, Jones06], in which two close atoms are excited to a molecular state via an external photon. This process is inherently detuning asymmetric, as for red detuning there are bound excited states (photoassociation resonances) while for blue detuning there is a continuum of states. The influence of the excitation to the blue continuum on radiative trap loss has been observed by Vuletić *et al.* [Vuletić99], where the pair excitation rate has been modified by tuning the scattering length, and hence the node of the ground state pair correlation function, to the Condon point.

Our goal is to find the signature of the molecular potential as the cause for the additional loss of matter-wave coherence existing when probing with blue detuning. Typically, a photoassociation event leads to a direct loss of the two atoms forming the excited state molecule, since the pair gains kinetic energy during the dissociation [Burnett96]. Besides the loss of the two atoms, there is also the photon which is shifted towards the atomic resonance during the life time of the excited molecule. Here we find that with high probability ($\sim 90\%$) this photon will be emitted at the atomic resonance, and as the molecule is produced inside the sample so will the resonant photon. Since the sample is optically thick the resonant photon will be reabsorbed by neighboring atoms and will "slowly" diffuse out. During this time the light-matter coherent grating will be destroyed [Kampel12], thus inhibiting the SR process by increasing the dephasing rate.

3.3   Outline of experimental and theoretical work

In chapter 4 we present our experimental results. Here we concentrate on finding the onset of the SR at different probe light blue detuning $\Delta \leq 35$GHz and compare them to the threshold at red detuning $\Delta = -2.57$GHz. The results are presented in section 4.1, in which we also derive the expected threshold dependence for a general detuning dependent loss mechanism, from a simple rate equation model.

Then we turn to examine the influence of the probe light dipole force, i.e. second term on the left hand side of Eq. 3.3. Here the probe acts as a repulsive dipole "anti"-trap, with increasing strength as we increase the detuning. In section 4.2 we find that the cloud is expanding as expected due to the probe.

After examining the experimental results we develop a quantitative model for the measured increase in the threshold. The model is based on three ingredients, 1) production rate of the excited molecules; 2) the light emitted during the dissociation of the molecule on the atomic resonance; and 3) the number of reabsorption events (diffusion time) of the resonant photon. These are combined to a loss rate in section 5.1.

In section 5.2 we calculate the effect of the probe dipole force on the density of the atomic cloud and the change of the probe intensity due to the density dependent refractive index of the atomic sample. When combining these two effects we get a second order correction of the SR threshold. We finish in section 5.3 with a derivation of the well known Maxwell-Schrödinger equations for Rayleigh superradiance [Zobay05, Zobay06, Bar-Gill07, Hilliard08a, Hilliard08b]. The motivation for reproducing the calculation here is to show that a condensate mean-field term does not influence the threshold for SR to first order, contrary to the claims of Deng *et al.*.

Experimental results

In our experiments, Rayleigh SR scattering is induced in a trapped BEC by illuminating it with an off-resonant light pulse along the axial direction of the condensate. We use a $100\mu s$ rectangle pulse and vary the pulse intensity to explore the SR onset. In the experiments we prepared prolate condensates containing 2.2×10^5 atoms with in-trap Thomas-Fermi radii of $r_\perp \approx 6\mu$m and $r_\parallel \approx 60\mu$m in the radial and axial directions, with no discernible thermal fraction. The probe light is detuned from the $|F_0 = 1, m_F = -1\rangle \rightarrow |F = 2, m_{F'} = -2\rangle$ transition on the D_1 line of ^{87}Rb at 795nm and is circularly polarized. We measure the probe detuning ($\Delta = -2.57 \rightarrow 35$GHz) using a wave meter (with ~ 300MHz resolution) and a Fabry-Perot resonator (1.5GHz FSR) referenced to a laser stabilized to saturated absorption features of the ^{85}Rb D_1 line. The probe beam is focused to a waist radius of 20μm (at e^{-2}) on the atoms. The probe pulse duration is chosen long enough to suppress backward (Kapitza-Dirac) scattering of atoms and short enough to neglect decoherence due to decaying overlap of matter wave packets. The range of explored probe detunings is chosen such as to have negligible light depletion at low detunings and is limited by our available laser power at high detunings.

4.1 Threshold dependence

The populations of atomic momentum modes ($0\hbar k$ and $2\hbar k$) are extracted from absorption images taken after time-of-flight of 45ms. At each detuning we measure the population transfer for different single atom Rayleigh scattering rates R, which determines the dynamics time scale. We fit a straight line to the results with low scattering rate to extract a phenomenological threshold probe rate $R_{th}(\Delta)$ where superradiant gain exceeds linear losses enough to start significant population transfer during the interaction time. Figure 4.1 shows an example of transfer efficiency measurements at a blue detuning $\Delta = 5.24$GHz. Here the scattering rate is normalized to the measured threshold rate $R_0 = 2\pi \times 80$Hz at a red detuning of $\Delta = -2.57$GHz [1]. A detuning asymmetry in the threshold and a saturation of the transfer efficiency at high scattering rates is visible.

In Fig. 4.2 we present measured threshold rates as a function of probe laser detuning. A threshold increase up to a factor of three is evident for low values of the blue detuning. Also shown in the figure is the expected threshold increase due to light assisted collisions calculated from the model presented in chapter 5
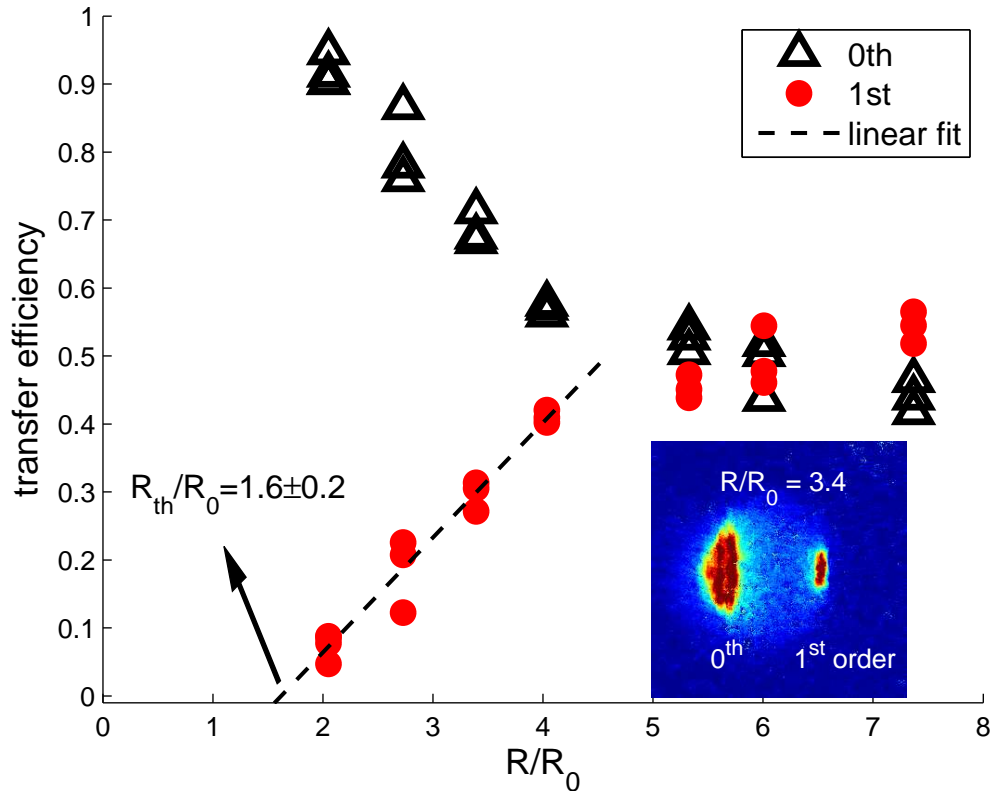
Figure 4.1: The transfer efficiency as a function of normalized single atom Rayleigh scattering rate at $\Delta = 5.24\text{GHz}$. Open triangles: population of the $0\hbar k$ momentum mode; filled circles: population of the $2\hbar k$ momentum mode; dashed line: linear fit; inset: TOF image of the atomic momentum distribution.

(section 5.1).

The starting point for the description of the coherent part of the SR process are the coupled Maxwell-Schrödinger equations [Zobay05, Zobay06]. Both from these equations[2] and as was shown in [Ketterle01], a simple rate equation for the number of atoms N_2 appearing in the recoil mode $\dot{N}_2 = G \cdot (N_2 + 1)$, is sufficient to describe the early stages of the dynamics where depletion of condensate atoms N_0 and probe light are not important. The rate constant for growth $G = Rd_0$ depends for a fixed sample geometry linearly on the single atom Rayleigh scattering rate R and on the resonant optical depth d_0 of the sample along the propagation direction of the superradiant light mode [Ketterle01]. Since the Rayleigh scattering rate varies symmetrically with laser detuning no asymmetry is predicted by this model[3].

At this level of description, Rayleigh SR, does not have a threshold probe rate. To have a more realistic model of the onset, damping mechanisms for the coherence grating need to be accounted for. We include loss rates $L_R = R$ to describe removal of N_2 atoms by spontaneous Rayleigh scattering, $L_{gg}(n_0)$ to describe damping by incoherent ground state collisions between (N_0, N_2) pairs[4], and a loss rate L_{ge} to account for light assisted collisions followed by radiation trap-

---

[1]For red detuning above 2GHz SR dynamics has been shown previously to be independent of detuning [Hilliard08a].

[2]We show this in section 5.3

[3]We arrive in section 5.3 to the same conclusion also for a 1-D model containing propagation effects.

[4]A loss term describing coherence loss due to wavepacket separation can be freely added to this term, but is smaller than the collision term for our axial excitation geometry.
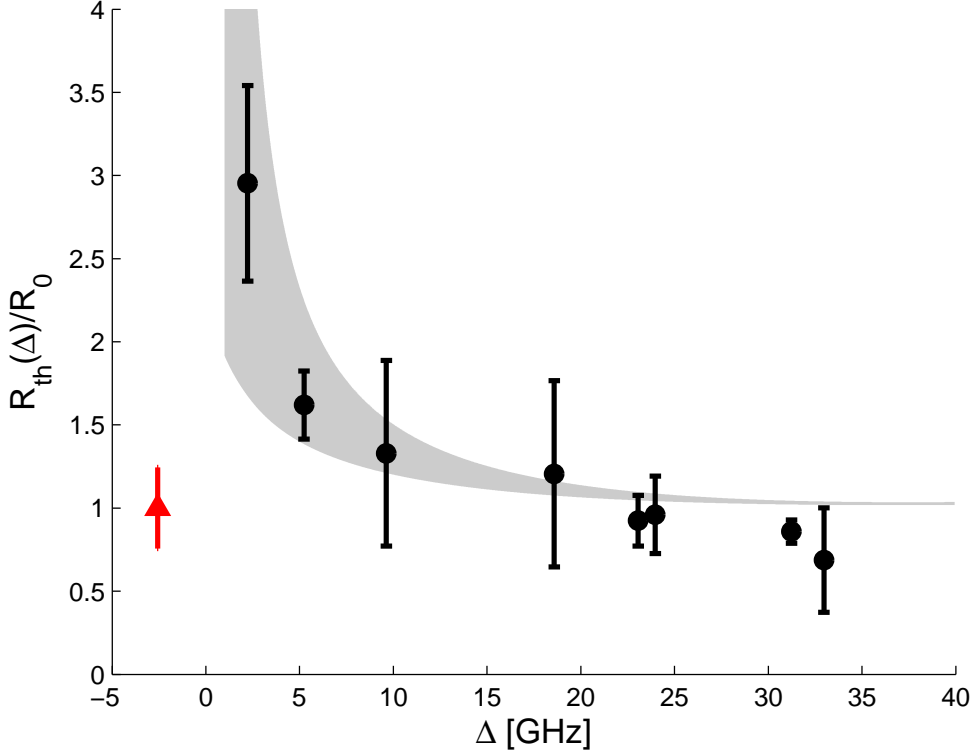
Figure 4.2: Normalized threshold scattering rate vs. detuning. Filled symbols show the measured threshold increase; Error bars designate 95% confidence level; Gray shaded region depicts the expected threshold due to close range dipole-dipole interaction; The borders of the gray area are calculated with $\left|\delta L_{ge}/L_{ge}\right| \leq 0.33$.

ping, that will be discussed in detail in section 5.1. We also add a nonlinear loss rate $L_{nl}(N_0,\Delta)$, to account for processes that depend nonlinearly on the population of the superradiant modes as those suggested in [Deng10a]. This nonlinear term could come, for example, from the mean field contribution as we show in section 5.3. The resulting rate equation

$$\dot{N}_2 = G(N_2 + 1) - (L_R + L_{gg} + L_{ge})N_2 - L_{nl}N_2^2 \tag{4.1}$$

shows initial exponential growth when gain exceeds linear losses, i.e. $G > L_R + L_{gg} + L_{ge}$. Equality of gain and linear losses defines the threshold for SR scattering in this model and the threshold does not depend on L_{nl}. Similar to a depletion term, L_{nl} clamps the growth rate later during the evolution when the population in the recoil mode becomes significant.

Here we are interested in finding the threshold dependence as a function of the loss term L_{ge}. We start by denoting the threshold gain (Rayleigh rate) in the absence of the L_{ge} term as G_0 (R_0) and isolating the ground state collisions loss term L_{gg}

$$L_{gg} = G_0 - L_R = R_0\,(d_0 - 1) \tag{4.2}$$

Before we find the threshold dependence on the light assisted collision term we parameterize it as $L_{ge} = R\tilde{L}_{ge}(n_0,\Delta)$ where n_0 is the density and Δ is the detuning. While the correct functional dependence will be worked out later in section 5.1, a linear dependence on both the scattering rate and density is expected as these parameters describe the relevant basic components for the
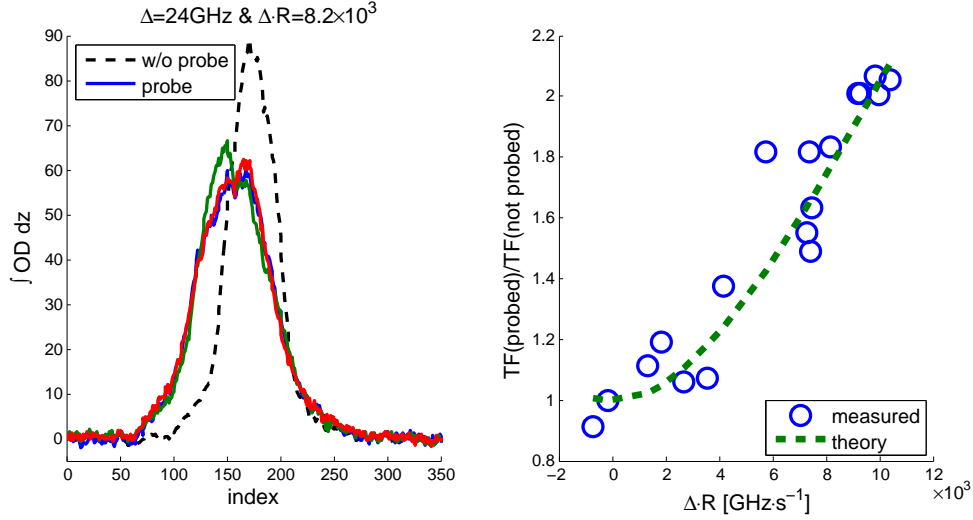
Figure 4.3: Left: Absorbtion images integrated along the longitudinal axis, after a TOF of 45ms at a detuning $\Delta = 24\text{GHz}$; dashed black line represents the cross section without probing the atoms, and the blue, green and red full lines represents single experimental realization with a probe pulse. Right: The fitted Thomas-Fermi radii from the experiments with probing the atoms normalized the Thomas-Fermi radius from the experiments without probing, as a function of the detuning times the single atom scattering rate; blue circles represents experiments and the green dashed lines represents the expected ratio using the Castin-Dum model given in section 5.2.

process. The threshold can now be expressed as

$$G_{th} = R_{th}d_0 = R_{th} + R_0\left(d_0 - 1\right) + R_{th}\tilde{L}_{ge},$$
$$R_{th}\left(d_0 - 1 - \tilde{L}_{ge}\right) = R_0\left(d_0 - 1\right),$$
$$\frac{R_{th}(\Delta)}{R_0} = \left(1 - \frac{\tilde{L}_{ge}(n_0,\Delta)}{d_0 - 1}\right)^{-1} \tag{4.3}$$

which is the quantity determined in our experiment. Thus from the measurements shown in Fig. 4.2 we can test the predictions of $\tilde{L}_{ge}$ as described in section 5.1, and shown as the gray area of the figure.

4.2   Effect of the probe beam dipole force

In chapter 3 we have shown from first principles that, in SR experiments, the probe beam dipole force affects only to second order due to a trap/"anti"-trap action. The forces due to the probe will increase as one increases the detuning[5]. Since in our experiments the probe light is focused we expect a significant variation of the dipole potential over the cloud.

The motivation to test changes in the cloud shape and position due to the probe light comes from the additional loss term for blue detuned probe, in which resonance light is produced inside the sample and then diffuses out. In an independent atom picture, this resonant light should give a recoil kick to each atom as it is absorbed and re-emitted. This additional recoil kick should be visible as an increase in the cloud size. Hence by testing the cloud size we can distinguish between an independent atom picture from a collective many atom picture in which the photon energy is distributed over many atoms when leaving the cloud.

---

[5]see second term on the left of Eq. 3.3
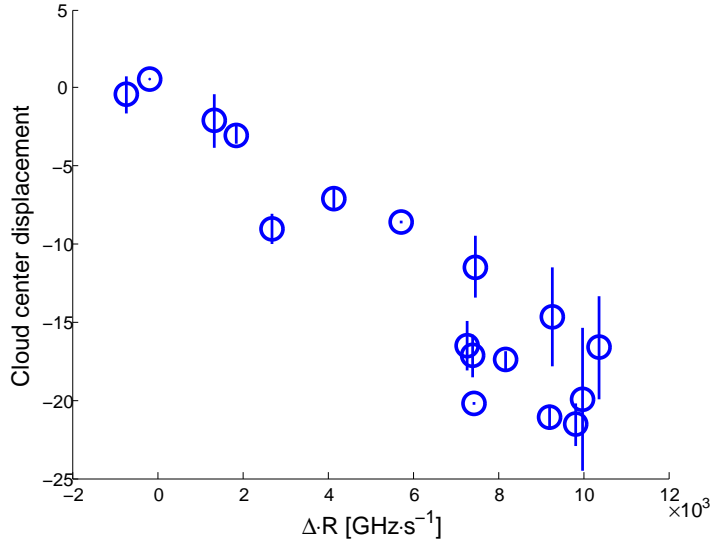
Figure 4.4: The change in the center of the cloud as function of the detuning times the single atom scattering rate. The points represents mean value over the experiments at that detuning and scattering rate, and the error is one standard deviation.

We measure the Thomas-Fermi radii of the atomic samples for the experiments with low percentage of atom transfer into the first order ($2\hbar k$). Using absorption images after integration over the longitudinal axis, we fit a bimodal cloud function to the experiments with detunings $\Delta \leq 10$GHz and for the experiments with higher detunings we fit a pure BEC function. Examples for cross sections at $\Delta = 24$GHz are given in Fig. 4.3-left. The dashed black line shows a cross section of an unprobed cloud. From the plot we see that the cloud has been stretched and that the center has been moved.

The relevant quantity to describe the above behavior is the dipole potential, which is proportional to scattering rate times the detuning (see Eq. 3.3). Therefor, in Fig. 4.3-right, we present the measured normalized Thomas-Fermi radii from the experiments with probing the atoms in the blue circles, and compare this increase to the expected one due to the trapping potential of the probe using the Castin-Dum model [Castin96] reviewed in subsection 5.2.1. We find that the expected values from the model, fit the measured expansion of the cloud. Note that we also see a reduction of the peak amplitude, in Fig. 4.3-left, which fits the predicted reduction by the model.

An additional observation is that the cloud position has been shifted. This could come from a small misalignment of the probe beam. For a position shift after *TOF* due to a dipole force a linear dependence on the strength of the dipole force, proportional to the product of the detuning and the scattering rate, is expected. We test this and indeed find a linear displacement, as is visible in Fig. 4.4.

In this section we have seen a good match between the measured cloud expansion and the expected expansion due to the Castin-Dum model [Castin96]. We do not see an additional heating (expansion) due to the resonant photon inside the cloud, i.e. a single atom picture is not compatible with the observed data. Since there is an overlap of the de Broglie wavelength of the atoms inside the condensate, we expect that the photon will actually give a recoil kick to a bunch of atoms and not a single atom. In this case the recoil is significantly less, as the effective mass increases, and we do not expect to observe its effect.

Models

In this chapter we model the two different effects presented in the previous chapter. We start, in section 5.1, by deriving a quantitative model for the asymmetric loss term, $\tilde{L}_{ge}$. In section 5.2 we examine how the probe beam is affected by the cloud, specifically the change in probe beam intensity (scattering rate), and how the cloud density is affected by the probe due to the dipole potential. The combination of both changes the estimated threshold and the expected light assisted collision rate, as presented in subsection 5.1.3.

Last, in section 5.3 we derive the full propagation and time evolution equations, i.e. the coupled Maxwell-Schrödinger equations. Even though this was done several times before [Zobay05, Zobay06, Bar-Gill07, Hilliard08a], we rederive this result putting emphasis on the threshold. The motivation is to dismiss the claim by Deng *et al.* in [Deng10b] that if one takes both the time and propagation effects including the mean field term, then the detuning asymmetry can be shown. Here we, of course, show that the detuning symmetry is conserved when keeping the mean field term.

5.1 Effects of light assisted collisions

Modeling off-resonant light scattering as purely elastic ceases to be a good approximation at high atom densities when the probability to excite close pairs of atoms becomes significant. To include this a molecular point of view description is necessary. Here we consider long range molecules that are produced in a collision of two atoms mediated by an external photon [Weiner99, Jones06]. These molecular potentials have the form of $1/R^3$ and can be either attractive or repulsive, as depicted in Fig. 5.1. While the attractive potentials support bound states (photoassociation resonances) that are addressed by red detuned light, the repulsive potentials allow for a continuous spectrum that is addressed by blue detuned light (radiative heating).

These molecules have a clear detuning asymmetry and therefore a loss mechanism that entails production of molecules will be inherently asymmetric. Therefor this was our initial motivation to test the hypothesis, whether light assisted collisions could be the cause of the SR detuning asymmetry?

For explaining the threshold asymmetry the additional loss term $\tilde{L}_{ge}$ should be comparable to the optical depth (d_0), as seen from Eq. 4.3. As shown below the rate for light assisted collisions and Rayleigh scattering are comparable at typical condensate densities of $10^{13} - 10^{14} \text{cm}^{-3}$. This implies that transient molecule formation alone cannot account quantitatively for the observed detuning asym-
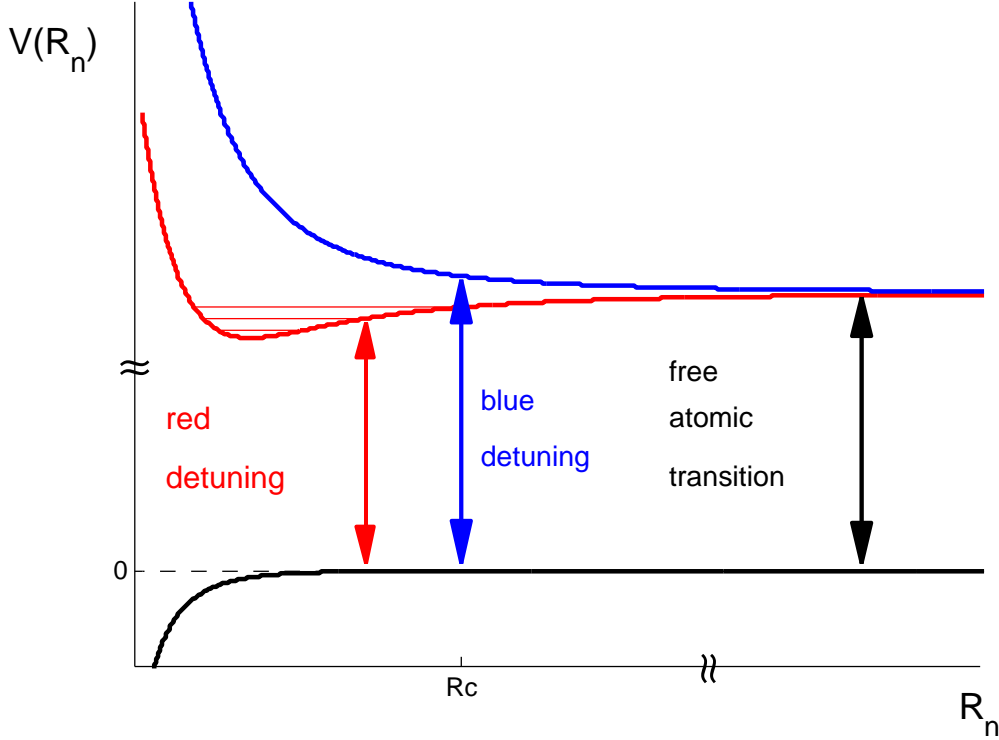
Figure 5.1: Typical ground and excited state potentials for cold collisions in light fields in the detuning regime where the excited state structure is dominated by resonant dipole-dipole interaction. Red detuned light excites pairs to bound states (free-bound transition), while blue detuned light excites to a continuum (free-free transition).

metry given the high optical depth of the BEC clouds[1].

Typically, when examining the loss rate of atoms from optical traps due to light assisted collisions [Burnett96, Julienne96] it is the loss of two atoms after the molecule has dissociated since the atoms gained enough kinetic energy to escape the trap. In our case this loss of atom pairs from the cloud has negligible influence, since the vast majority of light assisted collisions in the cloud happens without participation of N_2 atoms. The actual damage to the SR comes from the photon emitted during the dissociation process.

The emitted photons can be scattered with a significant frequency shift such that the outgoing photon is close to the atomic resonance. This resonant photon will repeatedly scatter off spectator atoms before leaving the cloud spoiling the mutual coherence of the matter wave and light gratings.

This reduction in coherence is modeled by the loss term $\tilde{L}_{ge}$ in the rate equation Eq. 4.3, and parameterized as $L_{ge} = R\tilde{L}_{ge} = R\chi n_0 (1 + F\bar{n})$, where $R\chi n_0$ is the light assisted collision rate, with n_0 the condensate density and χ the molecular production rate parameter, F is the fraction of resonant photons produced in a collision, and $\bar{n}$ is the average number of subsequent scattering events for a resonant photon inside the cloud. Note that the 1 in the brackets of $\tilde{L}_{ge}$ indicates the loss of a single N_2 atom assuming that the collision process is between a N_0 atom and an N_2 atom.

To allow for a comparison between model predictions and our experimental data, we now turn to a more detailed discussion of the three-step process leading

---

[1]This can be seen immediately from Eq. 4.3, by $\left(1 - \frac{\chi n_0}{d_0 - 1}\right)^{-1} \longrightarrow 1 + \frac{\chi n_0}{d_0 - 1} \simeq 1$ for $\chi n_0 \ll d_0$

to the coherence loss rate $\tilde{L}_{ge}$. In subsection 5.1.1 we derive the light assisted collision rate $(R\chi n_0)$, and in subsection 5.1.2 we estimate the probability of the emitted photon to be within the atomic resonance (F) and the average number of scattering events the photon undergoes before leaving the sample $(\bar{n})$. In subsection 5.1.3 we discuss the resulting SR threshold increase as depicted in the gray area of Fig. 4.2.

5.1.1 Light assisted collisions (molecular production) rate

The initial light assisted collision step in the three-step process has been used in the past to assess light induced atom loss rates from condensates [Burnett96]. To estimate quantitatively the event rate coefficient for binary light assisted collisions $R\chi n_0$ appearing in L_{ge} we switch to a microscopic description of the collision employing the methods outlined in [Julienne96].

The probability rate to excite a molecule per density is given by:

$$R\chi(\Delta, R_n) = \frac{\pi\hbar}{\mu k_\infty} \times \left| S_{eg} \right|^2 \tag{5.1}$$

$$S_{eg} = -2\pi i \left\langle \Psi_e^- (E + \hbar\Delta) \left| V_{eg}(R_n) \right| \Psi_g^+ (E) \right\rangle \tag{5.2}$$

Here, μ is the reduced mass for a ^{87}Rb atom pair, $\hbar k_\infty$ is the relative momentum in the entrance channel with corresponding kinetic energy E, R_n is the distance between the two atoms, Δ is the photon detuning from the atomic resonance, S_{eg} is the quantum matrix element to excite a molecule, Ψ_g (Ψ_e) is the ground (excited) scattering wave function, and V_{eg} is the radiative coupling potential.

We write the radiative coupling potential as $V_{eg}(R_n) = b_C(R_n)\hbar\Omega_A$, where Ω_A is the atomic Rabi frequency and $b_C(R_n)$ is a molecular parameter reflecting the change of the electronic wavefunction with internuclear distance R_n, and assume that it varies only little in the range of atomic distances relevant here. Thus we can extract V_{eg} out of the matrix element (integral) and write it as $V_c = V_{eg}$. For internuclear distances that we are interested in ($R_n > 70a_0$ where a_0 is Bohr radius), we can use the reflection approximation[2] to get:

$$R\chi = \frac{\pi\hbar}{\mu k_\infty} \times 4\pi^2 V_c^2 \times \frac{1}{D_C} \left| \Psi_g(R_c, E) \right|^2 \tag{5.3}$$

Here, R_c is the Condon radius[3] where the molecule tunes into resonance. The Franck-Condon factor[4] $\left| \Psi_g(R_c, E) \right|^2 / D_C$, with D_c the difference in potential slopes, regulates the detuning dependence. The ground state scattering wave function is numerically evaluated by solving the Milne equation[5]. In the inset of Fig. 5.2 we show the results of the ground wave function.

Now we are missing the C_3 coefficient and the value of b_C in order to be able to calculate χn_0. These molecular parameters are found from the simple model explicitly given in [Movre77, Movre80] that does not take into consideration hyperfine splitting. Under this approximation, we identify two repulsive potentials and fit a C_3/R_n^3 to find the potential coefficient and get $C_3(0_g^+) = 11.9$a.u.

---

[2]The reflection approximation is valid as long as the ground state wave function does not rapidly oscillate, see inset of Fig 5.2. For ^{87}Rb it is valid for internuclear distances bigger than $50a_0$.

[3]In which $\hbar\Delta = C_3/R_c^3$, with C_3 the molecular potential energy.

[4]The free-free Franck-Condon factor has units of J^{-2}.

[5]For more details see Appendix A in [Julienne96] equations 60-62.
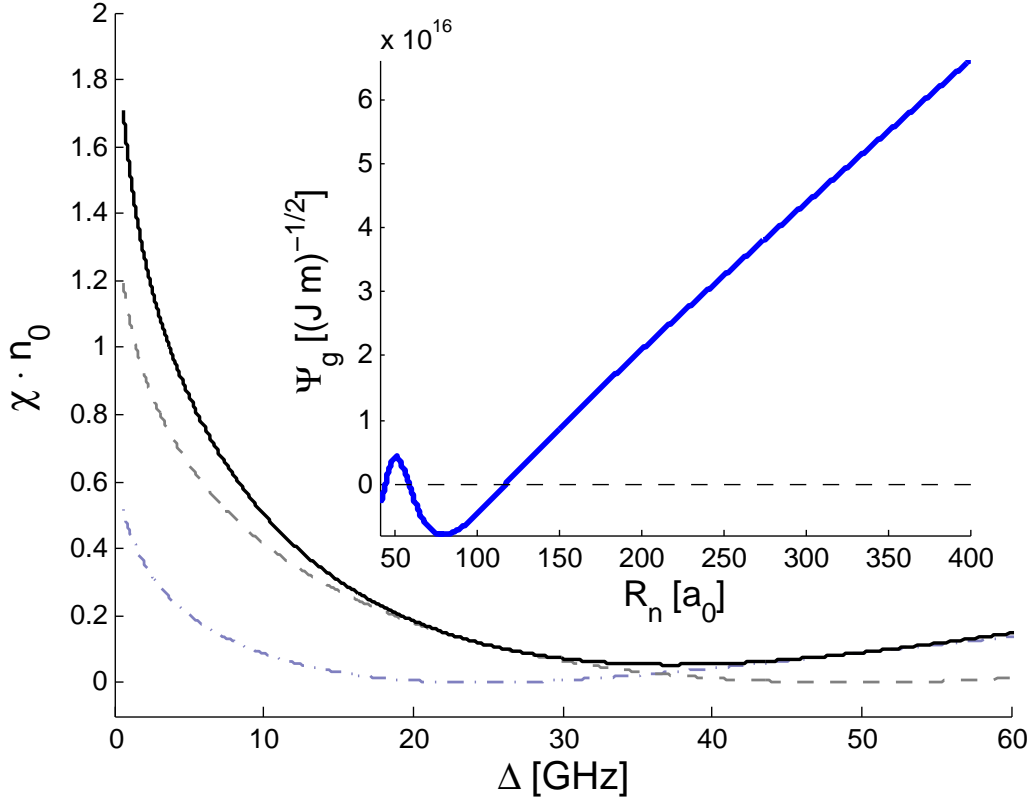
Figure 5.2: Ratio of pair collision rate to Rayleigh scattering rate (χn_0) for an atomic density of 10^{14}cm^{-3} as a function of detuning. Dashed and dash-dotted lines: Separate contributions from the 0_g^+ and 1_u molecular potentials; Solid line: total ratio. Inset: the ground state wave function versus the internuclear distance

and $C_3(1_u) = 5.89$a.u.. This allows us to calculate D_C, knowing the C_6 coefficient for the ground state potential from [Marte02]. The b_C coefficient is found from [Movre80] as the square root of the ratio of molecular and atomic oscillator strength.

In the main panel of Fig. 5.2, we give the result of the ratio between light assisted collision rate and isolated atom Rayleigh scattering rate (χn_0) at a typical BEC density of $n_0 = 10^{14}$cm^{-3}.

5.1.2 Estimating the emitted photon frequency

To get the frequency spectrum of the photons produced in binary collisions, we use the Ehrenfest theorem to calculate by classical mechanics the trajectory of the excited state wave packet in the repulsive molecular potential. Knowing the kinetic energy as a function of time along the trajectory, allows to transform the probability distribution for decay as a function of time to the spectral distribution. The wave packet approach is justified by the same stationary phase argument that is used to calculate the Franck-Condon factor for the upward transition. The calculation is completely analogous to the survival probability estimate used in the Gallagher-Pritchard model for binary collisions in red detuned light fields [Gallagher89].

We start by considering the total energy E available in a generic two-body (half-)

collision in a repulsive R_n^{-3} potential,

$$E = T + V \tag{5.4}$$

$$\hbar\Delta = \frac{\mu}{2}\dot{R}_n^2 + \frac{C_3}{R_n^3}, \tag{5.5}$$

where T and μ are the kinetic energy and reduced mass, respectively. We do not consider a centrifugal potential term. The ground state scattering wave function has s-wave symmetry, while the electronic angular momentum coupling in the non-centrosymmetric dipole potential is accounted for by the designation of the molecular state, parametrized by C_3. The energy of accessible (l=0, l=1) rotational state continua differs for the smallest Condon radii by less than the atomic natural line width $\hbar\Gamma$ which is dwarfed by the total collision energy $\Delta \gg \Gamma$. The detuning is defined as $\Delta = \omega_L - \omega_0$, where ω_L is the probe (laser) frequency and ω_0 is the atomic line resonance frequency.

Simple algebraic manipulation allow us to derive the differential equation describing the temporal change of kinetic energy along the trajectory as

$$\dot{R}_n = \left(\frac{2T}{\mu}\right)^{1/2},$$

$$\dot{V} = -3V\dot{R}_n/R_n = -3C_3^{-1/3}\dot{R}_n V^{4/3},$$

$$\dot{T} = \left(\frac{18}{\mu C_3^{2/3}}\right)^{1/2} T^{1/2}(E-T)^{4/3}, \tag{5.6}$$

which can be integrated by separation of variables. Introducing scaled variables $u = T/E$ and $\tau = \Gamma_m t$, where $1/\Gamma_m$ is the radiative lifetime of the excited molecular state, we write the solution as:

$$\tau(u) = \frac{\Gamma_m}{\alpha\Gamma} \int_0^u \frac{dx}{x^{1/2}(1-x)^{4/3}} \cdot \tag{5.7}$$

The coefficient $\alpha = 6(\Delta/\Gamma)^{5/6}(2\omega_r/\Gamma)^{1/2}(\hbar\Gamma/(C_3 k^3))^{1/3}$ contains all physical parameters of the specific system, while the integral can be expressed in terms of hypergeometric functions. Here ω_r is the recoil frequency and k is the wave number. When evaluated numerically, care must be taken to treat the singularities of the integrand correctly.

The probability density for decay to the electronic ground state of the colliding atom pair is given by

$$\frac{dP}{dt} = \Gamma_m \exp(-\Gamma_m t). \tag{5.8}$$

Moving to the scaled kinetic energy as the independent variable and transforming the differential accordingly we arrive at

$$\frac{dP}{du} = \frac{\Gamma_m}{\alpha\Gamma} \frac{1}{u^{1/2}(1-u)^{4/3}} \exp\left[-\frac{\Gamma_m}{\alpha\Gamma} \int_0^u \frac{dx}{x^{1/2}(1-x)^{4/3}}\right]. \tag{5.9}$$

Recognizing that the variable $u \in [0..1]$ maps the energy of the outgoing photon on the interval $[\omega_0 + \Delta..\omega_0]$ the fraction F of photons emitted in a frequency interval of width Γ above the atomic resonance can be written as

$$F = \frac{1}{2}\left(1 - \int_0^{1-\Gamma/\Delta} \frac{dP}{du} du\right),$$

$$F = \frac{1}{2}\exp\left[-\frac{\Gamma_m}{\alpha\Gamma} \int_0^{1-\Gamma/\Delta} \frac{dx}{x^{1/2}(1-x)^{4/3}}\right]. \tag{5.10}$$
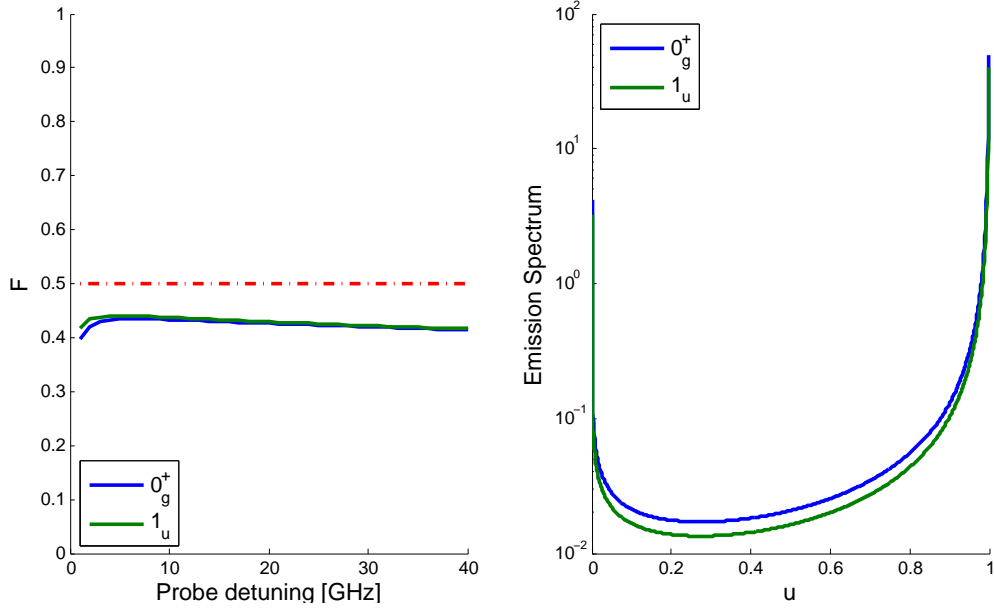
Figure 5.3: Left figure: Fraction of photons emitted in a frequency interval of width Γ above the atomic resonance as a function of detuning; red dot-dashed is the maximum fraction of resonance photons possible. Right figure: emission spectrum ($\frac{dP}{du}$) as a function of $u = (\omega_l - \omega)/\Delta$, evaluated at $\Delta = 3GHz$.

solving the integral by identifying that the integrant ($\frac{dP}{du}$) is the derivative of the exponent (trivially seen from Eq. 5.8). Here we added a factor $1/2$ due to hyperfine branching, since there is $50 - 50$ change for the photon to decay to the atomic state $|F_0 = 2\rangle$ and $|F_0 = 1\rangle$.

The spectrum of fluorescence for excitation at $\Delta = 500\Gamma$ as well as the fraction F as a function of detuning are shown in Fig. 5.3. Note that around 43% of the emitted light is fully resonant with the hosting cloud for all $\Delta > 0$ used in the experiment. The additional (small) broadening due to the finite emission time Γ_m^{-1} is not taken into account in this simple calculation.

We finish this calculation with the remark, that the recoil shift for the emitted radiation which is, of course, negligibly small compared to the red shift compensating the change of relative kinetic energy, must be evaluated using the total mass of the composite radiating system, i.e. twice the atomic mass. Providing the answer to the equivalent questions about deposited energy and recoil for the case of resonant radiation incident on a whole group of close atoms, is an interesting but highly nontrivial task, in our view.

As the third ingredient to assess the damping of the matter wave coherence we need to find the average number of scattering events $\bar{n}$ for resonant photons before leaving the cloud. Neglecting further frequency redistribution we use a simplified Holstein model, essentially a diffusive transport equation for light intensity in a medium of high optical depth, to describe radiation trapping [Fioretti98]. We use the decay time of the slowest Holstein mode $\tau_0^{el} = \gamma d^2 \tau_{nat} \simeq \bar{n}\tau_{nat}$ to calculate $\bar{n}$ [Labeyrie03]. Here, γ is a geometry parameter, τ_{nat} is the radiative lifetime of the excited atomic state, and d is the optical depth. For a simple estimate we assume a Gaussian spherical geometry ($\gamma \simeq 0.06$) with an optical depth equivalent to the geometric mean along the different condensate axes. For our parameters we find $\bar{n} > 1000$.

Due to the strong dependence of $\bar{n}$ on optical thickness the threshold increases

remarkably for dense and optically thick clouds, while it is unaltered in the limit of low density and optically dilute clouds, in accordance with the experimental observations in [Deng10a].

5.1.3 The change in SR threshold

In Eq. 4.3 we derived how an additional loss term changes the threshold, and write it as $L_{ge} = R\tilde{L}_{ge} = R\chi n_0 (1 + F\bar{n})$. This parametrization of L_{ge} puts emphasis on the role of N_2 atoms for the contrast and spatial coherence of the matter wave grating responsible for the amplified directed SR scattering. The matter wave grating amplitude can decrease or dephase either by direct participation and subsequent loss of an N_2 atom in a binary light assisted collision or by interaction of an N_2 atom with a resonant photon produced in any light assisted collision within the cloud. This second mechanism is far more important than direct loss of N_2 atoms[6]. Since in a fully quantum mechanical picture of SR scattering recoiling atoms and backscattered photons are created as correlated pairs contributing on equal footing to the gain, it is interesting to ask how important the loss of photon coherence due to inelastic collisions is for the net reduction of SR gain. The vast majority of binary collisions, which are the source for nearly isotropic incoherent resonant radiation, happens between N_0 atom pairs assisted by probe light photons. As long as depletion of the probe light is negligible, the direct influence of the frequency shifted radiation on the coherence of the light grating is marginal. It is the strong response of atoms to even minute amounts of resonant light which spoils the coherence of the matter wave and this way also the mutual coherence between light and matter waves.

The gray area in Fig. 4.2 depicts the calculated threshold increase via Eq. 4.3 for the experiment. Given the several rather crude assumptions in the calculation of the microscopic model parameters, together with smaller systematic uncertainties in the experimental parameters atom number and density, we allow an uncertainty δL_{ge} in the loss rate L_{ge}. The borders of the gray area in Fig. 4.2 are calculated with $|\delta L_{ge}/L_{ge}| \leq 0.33$. We note that the exact spectral signature is sensitive to molecular hyperfine structure, which is not taken into account in our model potentials. While the qualitative and near quantitative agreement between data and prediction is satisfying to see, the rate equation and radiation trapping model applied does not do full justice to the underlying complicated many-body physics. Simple inspection of the threshold condition reveals that at our highest observed threshold increase more than 60% of the atoms should have interacted with a trapped resonant photon. The little observed recoil heating in the experiment is clearly incompatible with a picture of individual atoms receiving random recoil kicks from an isotropic radiation field. In fact, at resonance and high density photonic and atomic degrees of freedom mix strongly, forming polariton type excitations with an effective mass very different from the bare atomic mass [Svistunov90]. In using the radiation diffusion model we implicitly assume that the dephasing rate is still governed by the bare atomic decay rate Γ.

Whatever the precise nature of the trapped excitations is, their incoherent production by collisions and slow diffusion implies the presence of electronic excitation inside the cloud many natural lifetimes after the probe light has left the cloud. Photoionization out of the excited state can provide a critical test of the model but also a tool to study the temporal dynamics of the polaritons in detail.

---

[6]In the experiment we do not observe pronounced loss of atoms at any of the tested probe detuning values.
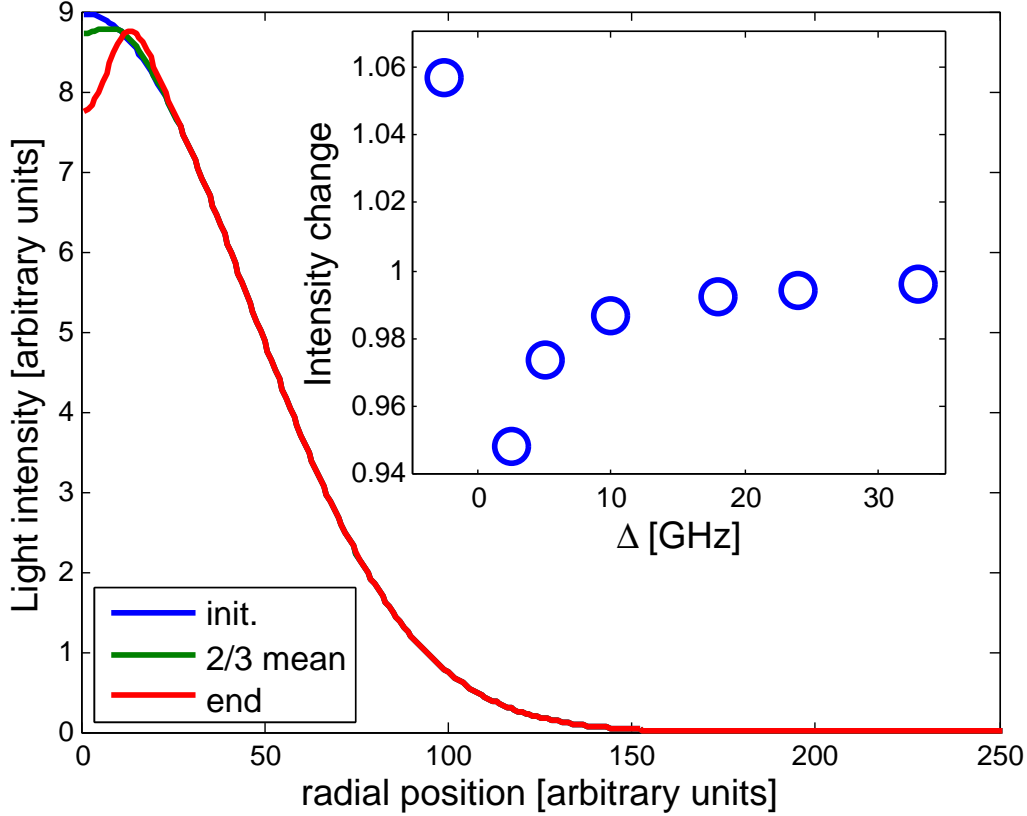
Figure 5.4: The light intensity radial profile at three different cases, entering into the sample, mean over the first 2/3 of the sample and exiting the sample. This intensity profile is given for a detuning of 5GHz In the inset we show the mean intensity change over the first 2/3 of the sample at the center of the sample as function of detuning.

5.2   Effects of the probe light

In the previous section we have explicitly assumed that both the probe light intensity profile and the atom density distribution are not changed due to the interaction, while in this section we examine how these effects change the threshold. There are two main effects that change the experimental conditions: 1) the dipole force changes the sample density, thus changes $\tilde{L}_{ge}$ and 2) the sample changes the light intensity distribution, thus changes R. The change in the sample density comes due to the variation of the dipole potential ($U_{dip} \propto R\Delta$). The change in the light intensity comes from the atomic ensemble index of refraction, which is inversely proportional to the detuning.

Since these effects are small and influence at opposite detuning limits, here we are correcting one while ignoring the other and vice versa. For correcting the light we have used a $3D$ simulations[7] done by Anna Grodecka-Grad [Zeuthen11] which show that the light intensity change is less than 10%. Note that since the SR process starts at the beginning of the sample [Hilliard08b] we consider the average center intensity change over the first 2/3 of the sample length. In Fig. 5.4 we show an example of the resulting intensity profile at detuning of +5GHz. As expected for blue (positive) detuning, the light is refracted radially outward and the total intensity decreases. For estimating the change in intensity we take the worst case, i.e. evaluating the intensity at the center. The inset of Fig. 5.4 shows the relative intensity change as function of detuning.

---

[7]This was done for our experimental conditions.

The change in beam intensity changes the actual scattering rate for the atoms. This means that our initial estimate for the threshold scattering rate, as given in figures 4.1 and 4.2, should be modified accordingly.

In the next step we need to examine the change in the atomic sample density. Then we can reevaluate the threshold increase, shown in Fig. 4.2, with a slightly different scattering rate axis, and with modified density values used in estimating $\tilde{L}_{ge}(n_0, \Delta)$

5.2.1 Estimating the clouds density after probing

We estimate the change in the sample density using a semi-classical model first presented by Castin and Dum in [Castin96], in which the BEC cloud evolution in a harmonic potential is calculated. Here the cloud size is scaled by a factor $r_i(t) = \lambda_i(t)r_i(0)$, with $i(= 1, 2, 3)$ an axis index. The time dependent density distribution is therefore given as

$$n_0(\mathbf{r}, t) = \frac{1}{\lambda_1(t)\lambda_2(t)\lambda_3(t)} \times n_0(\{r_i/\lambda_i(t)\}_{i=1,2,3}, t = 0). \qquad (5.11)$$

The time evolution of the scaling factors is governed by Newton's second law,

$$\frac{d^2}{dt^2}\lambda_i = \frac{\omega_i^2(0)}{\lambda_i\lambda_1\lambda_2\lambda_3} - \omega_i^2(t)\lambda_i \qquad (5.12)$$

where the first term on the right hand side stems from the clouds mean field potential energy[8], and the second term comes from the time varying of the trapping potential. In our case there are two relevant axis radial ($\lambda_\perp$) and axial (λ_z) giving

$$\frac{d^2}{dt^2}\begin{pmatrix} \lambda_z \\ \lambda_\perp \end{pmatrix} = \begin{pmatrix} -\omega_z^2(t) & \frac{\omega_z^2(0)}{\lambda_\perp^3\lambda_z^2} \\ \frac{\omega_\perp^2(0)}{\lambda_\perp^3\lambda_z^2} & -\omega_\perp^2(t) \end{pmatrix} \begin{pmatrix} \lambda_z \\ \lambda_\perp \end{pmatrix} \qquad (5.13)$$

These equations can be solved analytically in the case of time independent trap frequency, e.g. when turning off the trap and doing a time of flight measurement. For a time evolving trap, we reduce the set of second order differential equations to first order by increasing the number of equations, to get:

$$\frac{d}{dt}\begin{pmatrix} \lambda_z \\ \lambda_\perp \\ \dot{\lambda}_z \\ \dot{\lambda}_\perp \end{pmatrix} = \begin{pmatrix} 0 & 0 & 1 & 0 \\ 0 & 0 & 0 & 1 \\ -\omega_z^2(t) & \frac{\omega_z^2(0)}{\lambda_\perp^3\lambda_z^2} & 0 & 0 \\ \frac{\omega_\perp^2(0)}{\lambda_\perp^3\lambda_z^2} & -\omega_\perp^2(t) & 0 & 0 \end{pmatrix} \begin{pmatrix} \lambda_z \\ \lambda_\perp \\ \dot{\lambda}_z \\ \dot{\lambda}_\perp \end{pmatrix} \qquad (5.14)$$

This allows us to use a modified Simpson algorithm (Runge-Kutta method). This mathematical exercise gave us the ability to use a stable and fast algorithm to solve the above set of equations.

In our case during the probing the trap frequency is changed to $\omega^2(0 < t \leq t_p) = \omega_B^2 + \omega_p^2$, with probing time of $t_p = 100\mu s$, ω_B the magnetic trap frequency, ω_p the probe trap frequency, as estimated by Eq. A.10 and Eq. A.11.

The results of this model have been used to evaluate the dashed green line of Fig. 4.3-right, in which we plot the evaluated scaled factor with different probe parameters normalized to the scaled factor without probing ($\omega_p = 0$).

---

[8]Using here the fact that initially the cloud density is set by the potential of the magnetic trap.
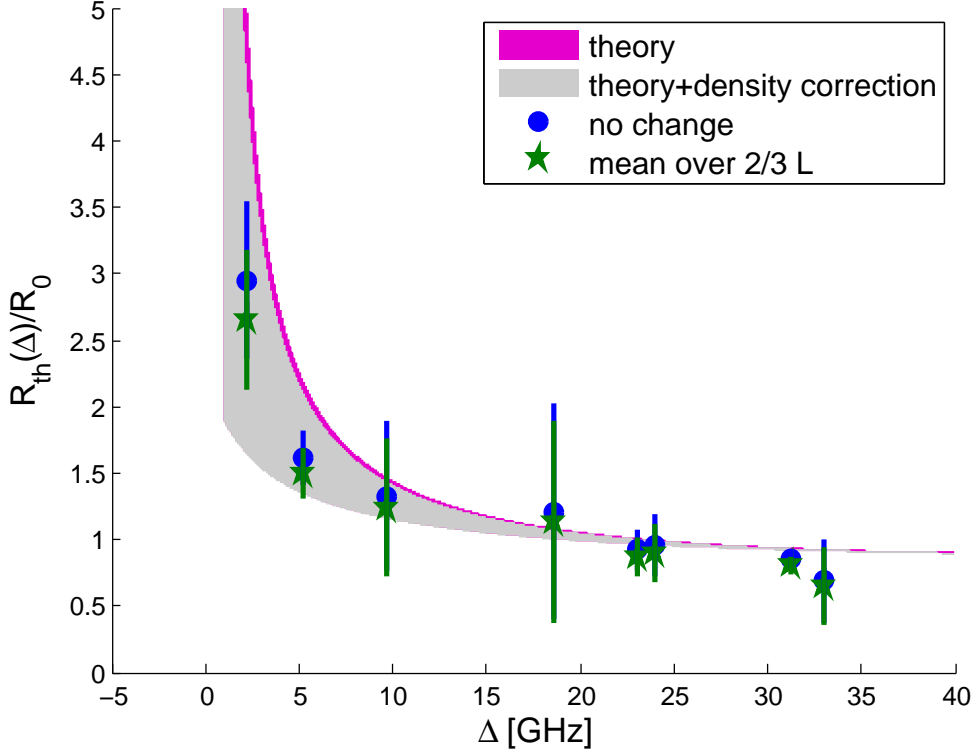
Figure 5.5: Normalized threshold scattering rate vs. detuning. Filled symbols show the measured threshold increase, round (star) the uncorrected (corrected) determined scattering rates; Error bars designate 95% confidence level; Purple (Gray) shaded region depicts the density uncorrected (corrected) expected threshold due to close range dipole-dipole interaction; The borders of the gray area are calculated with $\left|\delta L_{ge}/L_{ge}\right| \leq 0.33$.

5.2.2 The new threshold dependence

Above we have estimated both the change in the scattering rate due to the atomic cloud, and the change in the cloud density due to the probe intensity. Note that as the cloud density is changed the most for far detuning, the scattering rate modification is biggest at small detuning. In Fig 5.5 we include both corrections into the estimation of the threshold dependence measurements. Here we have corrected the measured threshold scattering rate, see green stars (corrected) verses the blue circles (not corrected). The correction to the cloud density influences directly the loss rate $\tilde{L}_{ge}$, and the effect is shown as the difference between the two shaded areas. Note that since the density reduces as we increase the detuning, we can get a threshold ratio smaller than 1.

5.3 Detuning symmetry from Maxwell-Schrödinger equations

Above we use a simplified rate equation for the number of recoiling atoms to describe the onset of superradiance (SR) in the absence of incoherent losses. Here, we sketch the steps to arrive at the rate equation, which averages over propagation effects, starting from Maxwell-Schrödinger equations, which include all propagation effects. The basic coupled evolution equations for light and matter fields have been presented in the literature already several times [Zobay05, Zobay06, Hilliard08a, Bar-Gill07]. On the way to the rate equation we discuss, in particular, the various approximations that enter the derivation, also

in view of recent attempts to explain the detuning asymmetry in superradiance based on approximate analytic solutions of the Maxwell-Schrödinger equations and modifications thereof [Deng10b, Deng10a].

The starting point are the mean-field Gross-Pitaevski equation for the matter field ψ in the electronic ground level including an effective coupling term to the light field and a classical wave equation for the propagating electric field $\mathbf{E}$ with a polarization term to describe the coherent radiation by the driven atoms:

$$i\hbar \frac{\partial}{\partial t}\psi = -\frac{\hbar^2}{2M}\nabla^2\psi + \frac{\left(\mathbf{d}^+ \cdot \mathbf{E}^-\right)\left(\mathbf{d}^- \cdot \mathbf{E}^+\right)}{\hbar\Delta}\psi + g_0 \left|\psi\right|^2 \psi \qquad (5.15)$$

$$\left(\nabla^2 - \frac{1}{c^2}\frac{\partial^2}{\partial t^2}\right)\mathbf{E}^\pm = \frac{1}{c^2\epsilon_0}\frac{\partial^2}{\partial t^2}\mathbf{P}^\pm. \qquad (5.16)$$

Here, superscripts $\pm$ denote positive and negative frequency components, M is the atomic mass for ^{87}Rb, $\hbar$ is the reduced Planck constant, $\mathbf{d}$ is the atomic dipole matrix element on the driven electronic transition, c is the speed of light, and ϵ_0 is the free space permittivity. The nonlinear term proportional to g_0 describes the mean field energy from ground state van der Waals interaction. The macroscopic polarization is given by $\mathbf{P}^\pm = -\left|\psi\right|^2 \mathbf{d}\left(\mathbf{d} \cdot \mathbf{E}^\pm\right)/(\hbar\Delta)$. Several approximations have already been applied to arrive at this form of the equations. The trapping potential for the atoms has been dropped, since it has negligible influence on the dynamics on the time scale of the interaction with the probe pulse. Implicitly the effect of the trapping potential is, of course, contained in the initial density distribution of the cloud. Only the Rayleigh scattering channel back into the initial Zeeman sublevel is considered for the superradiant dynamics, since the inhomogeneous magnetic field destroys rapidly the coherence between different sublevels. More importantly, the dipole response of the atoms is calculated in second order perturbation theory for an isolated atom in a rotating wave and low saturation approximation to eliminate excited states adiabatically. The radiative damping term $i\Gamma/2$, which formally needs to be added to the detuning Δ, has negligible influence for the range of detunings considered later on, and is thus left out. Doing the adiabatic elimination at the single atom level, the light mediated interaction between atoms in their near-field and its impact on the scattering properties are neglected. We choose to take these effects into account later by switching to a molecular picture for close pairs of atoms. Effective macroscopic descriptions including the near-field interaction, derived several times in the literature, have many subtleties [Sokolov09, You96]. In particular, frequency redistribution processes and radiation trapping, invoked as a source of decoherence, are buried deep under the formalism and are only hard to recognize in the macroscopic treatment, which concentrates on the stationary linear response of the scattering medium.

At this stage, as long as the Maxwell-Schrödinger equations are solved simultaneously, all coherent light mediated interaction between driven dipoles in their far-field and all dipole forces are still fully accounted for. Keeping the full 3-D description throughout is cumbersome, so the next step is a reduction to 1-D. Two potentially important effects, depending on the specific geometry of an experiment, that are lost in a 1-D description are the transverse components of the dipole force exerted by the light field distribution on the atoms and the corresponding back action on the light (diffraction and lensing). In sections 4.2 and 5.2 we have showen that these effects have small effect on the SR dynamics, even for our experimental parameters in which the probe dipole potential was made relatively big.

We simplify the above equations by going to an effective 1-D geometry assuming a constant transverse cross section A of the interaction region. This keeps

longitudinal components of interaction and dipole forces only. To simplify the equations further we split the electric field into forward and backward propagating modes and introduce slowly varying envelope functions for the modes denoted by subscripts $\pm$ in the following. Likewise, the matter wave function is split into recoil modes with slowly varying envelopes as

$$\psi(z,t) = \sum_{m=2n} \psi_m(z,t) e^{-i(\omega_m t - mkz)} \tag{5.17}$$

where $m = 2n$ and n is an integer number (SR order number), $\omega_m = m^2\omega_r$, $\omega_r = \frac{\hbar k^2}{2M}$ is the recoil frequency, and k is the wave number. Since the condensates used in the experiments are much longer than an optical wavelength ($L \simeq 100\lambda$) the mode functions are orthogonal to a very good approximation. As the next step we transform the equations to dimensionless form, by defining electric field, time and length units via $\mathbf{E}_\pm = \varepsilon_\pm \sqrt{\frac{\hbar\omega}{2\epsilon_0} \cdot \frac{2\omega_r}{cA}}$, $\tau = 2\omega_r t$ and $\xi = kz$. Using the slowly varying envelope approximation the transformed equations read:

$$\frac{\partial \varepsilon_+}{\partial \xi} = -i\Lambda \sum_m \left\{ \varepsilon_+ |\psi_m|^2 + \varepsilon_- \psi_{m-2}^* \psi_m e^{-2i(m-1)\tau} \right\} \tag{5.18}$$

$$\frac{\partial \varepsilon_-}{\partial \xi} = i\Lambda \sum_m \left\{ \varepsilon_+ \psi_{m+2}^* \psi_m e^{2i(m+1)\tau} + \varepsilon_- |\psi_m|^2 \right\} \tag{5.19}$$

$$\frac{\partial \psi_m}{\partial \tau} = \frac{i}{2} \frac{\partial^2 \psi_m}{\partial \xi^2} - m \frac{\partial \psi_m}{\partial \xi} - i\Lambda \left(|\varepsilon_+|^2 + |\varepsilon_-|^2 \right) \psi_m$$
$$- i\frac{\omega_{MF}}{2\omega_r} \sum_n \sum_l \psi_n^* \psi_{n-l} \psi_{m+l} e^{-il(m-n+l)\tau}$$
$$- i\Lambda \varepsilon_+^* \varepsilon_- e^{-2i(m+1)\tau} \psi_{m+2} - i\Lambda \varepsilon_-^* \varepsilon_+ e^{2i(m-1)\tau} \psi_{m-2}. \tag{5.20}$$

The coupling constant is expressed as $\Lambda = 1/4 \cdot \sigma_0 / A \cdot \Gamma / \Delta$ and ω_{MF} denotes the mean-field ground state interaction. The ratio of atomic absorption cross-section σ_0 to sample cross section A and the detuning Δ in units of the linewidth Γ determine the strength of the effective atom-light interaction. The first two terms on the r.h.s. of Eq. 5.20 describe wave packet spreading and recoil induced drift of the matter wave envelopes, which ultimately leads to coherence loss by spatial separation. In our experiments the influence of these terms is small due to the short interaction time and long sample length, hence we drop them in the following.

To connect the equations more directly to observable quantities we switch to density matrix elements instead of mode amplitudes. Since we are interested mainly in the onset of superradiance we restrict the number of recoil modes for the matter wave to the first two. This makes the system formally equivalent to a coherent two-level amplifier/absorber, with a weak nonlinear contribution due to the mean field interaction.

$$\frac{\partial |\psi_0|^2}{\partial \tau} = i\Lambda \left(\varepsilon_-^* \varepsilon_+ e^{2i\tau} \psi_0 \psi_2^* - \varepsilon_+^* \varepsilon_- e^{-2i\tau} \psi_0^* \psi_2 \right) \tag{5.21}$$

$$\frac{\partial |\psi_2|^2}{\partial \tau} = -i\Lambda \left(\varepsilon_-^* \varepsilon_+ e^{2i\tau} \psi_2^* \psi_0 - \varepsilon_+^* \varepsilon_- e^{-2i\tau} \psi_2 \psi_0^* \right) \tag{5.22}$$

$$\frac{\partial}{\partial \tau} \psi_0^* \psi_2 = i\Lambda \varepsilon_-^* \varepsilon_+ e^{2i\tau} \left(|\psi_2|^2 - |\psi_0|^2 \right) + i\frac{\omega_{MF}}{2\omega_r} \left(|\psi_2|^2 - |\psi_0|^2 \right) \psi_0^* \psi_2 \tag{5.23}$$

The last term in Eq. 5.23 stems from the extra energy cost to create a density modulation in the interacting cloud and describes e.g. the mean field shift of a

Bragg resonance. The light flux propagation equations read:

$$\frac{\partial |\varepsilon_+|^2}{\partial \zeta} = i\Lambda \left(\psi_2^* \psi_0 e^{2i\tau} \varepsilon_-^* \varepsilon_+ - \psi_0^* \psi_2 e^{-2i\tau} \varepsilon_+^* \varepsilon_- \right) \quad (5.24)$$

$$\frac{\partial |\varepsilon_-|^2}{\partial \zeta} = i\Lambda \left(\psi_2^* \psi_0 e^{2i\tau} \varepsilon_-^* \varepsilon_+ - \psi_0^* \psi_2 e^{-2i\tau} \varepsilon_+^* \varepsilon_- \right) \quad (5.25)$$

$$\frac{\partial}{\partial \zeta} \varepsilon_-^* \varepsilon_+ = -i\Lambda \psi_0^* \psi_2 e^{-2i\tau} \left(|\varepsilon_+|^2 + |\varepsilon_-|^2 \right) - 2i\Lambda \left(|\psi_0|^2 + |\psi_2|^2 \right) \varepsilon_-^* \varepsilon_+. \quad (5.26)$$

The last term in Eq. 5.26 reflects the modification of light wavelength due to the refractive index of the cloud. Writing the complex coherences in polar form as $\varepsilon_-^* \varepsilon_+ = \rho_l e^{i\phi_l}$ and $\psi_0^* \psi_2 = \rho_a e^{i\phi_a}$ brings the equations into a form suitable for further discussion.

$$\frac{\partial}{\partial \tau} |\psi_2|^2 = -\frac{\partial}{\partial \tau} |\psi_0|^2 = 2\Lambda \rho_l \rho_a \sin \left(2\tau + \phi_l - \phi_a \right) \quad (5.27)$$

$$\frac{\partial}{\partial \zeta} |\varepsilon_-|^2 = \frac{\partial}{\partial \zeta} |\varepsilon_+|^2 = -2\Lambda \rho_l \rho_a \sin \left(2\tau + \phi_l - \phi_a \right) \quad (5.28)$$

$$\frac{\partial}{\partial \zeta} \rho_l = -\Lambda \left(|\varepsilon_+|^2 + |\varepsilon_-|^2 \right) \rho_a \sin(2\tau + \phi_l - \phi_a) \quad (5.29)$$

$$\frac{\partial}{\partial \tau} \rho_a = \Lambda \left(|\psi_0|^2 - |\psi_2|^2 \right) \rho_l \sin \left(2\tau + \phi_l - \phi_a \right) \quad (5.30)$$

One can recognize the first equality in Eq. 5.27 as the local conservation of atom number, which is a consequence of neglecting wavepacket drift and spread. Similarly, the first equality in Eq. 5.28 expresses a continuity equation for the photon density, a necessary consequence of the adiabatic elimination of excited atomic states.

We note that the terms describing the mean-field interaction and the refractive index drop from the magnitude and coherence equations. These terms will weakly influence the evolution of the phase of matter and light gratings (ϕ_a & ϕ_l). With our choice of the probe laser frequency as the carrier frequency for both forward and backward propagating light modes, the time dependence of ϕ_l acquires the recoil shift of the backscattered light and compensates the explicit time dependence in Eqs. (5.27-5.30).

To model the onset of superradiant scattering we make use of the specific initial and boundary conditions in the experiments, i.e. $|\psi_0|^2 \gg |\psi_2|^2$ and $|\varepsilon_+|^2 \gg |\varepsilon_-|^2$. At first sight the equations seem to imply an odd symmetry in the dependence on the sign of probe laser detuning ($\Lambda \propto \Delta^{-1}$), and hence to explain the observed asymmetry in the SR threshold. A closer inspection reveals, that this is not the case. Due to the sinusoidal dependence on the relative phase of light and matter wave gratings, Eqs. (5.27-5.30) support runaway solutions, growing nearly exponentially in time and in space, for both signs of the parameter Λ (Δ). The SR is triggered by spontaneous Rayleigh scattering that creates random gratings and provides a seed for the growth [9]. Note that this derivation supports the intuitive picture given in the introduction (chapter 3), where both the cloud and the light support a grating with exponential growth of the coherence.

If boundary conditions are such that both $|\varepsilon_-|^2$ and $|\varepsilon_+|^2$ are strong light fields incident on the sample, the coupled equations describe just Bragg diffraction of matter waves in a (walking) standing wave including the backaction of atoms onto the light field. Similarly, for initial conditions such that both atomic recoil

---

[9]For analytic solutions of completely analogous quantum dynamics see e.g.[Raymer81, Mishina07].

modes are macroscopically populated, reflection of light from a density grating is described.

Returning to SR scattering, in a minimalistic approach the equations can be reduced to a zero dimensional system leading to the rate equation for the number of atoms appearing in the recoil mode. To do this we assume initial homogeneous matter wave coherence $\rho_a(\tau = 0)$ over the sample corresponding to one delocalized atom in the recoil mode and perfect phase matching conditions $\sin(2\tau + \phi_l - \phi_a) \simeq 1$ which is valid in the early stages of the dynamics. Now, Eq. 5.29 is solved subject to the boundary condition that $\rho_l(\xi_{max}) = 0$. The result is inserted into Eq. 5.27, leading to[10]:

$$\frac{\partial}{\partial \tau} |\psi_2|^2 = 2\Lambda^2 |\epsilon_+|^2 \rho_a^2 \xi_{max} \left(1 - \frac{\xi}{\xi_{max}} \right). \tag{5.31}$$

Integrating this over the appropriate dimensionless length, such that we get back the sample atom number ($\int_0^{\xi_{max}} d\xi\, |\Psi_0|^2 = N_0$), renders a rate equation for the number of atoms in the recoil mode as:

$$\frac{\partial}{\partial \tau} N_2 = \Lambda^2 N_0 |\epsilon_+|^2 (N_2 + 1). \tag{5.32}$$

Here we have added one in the brackets for getting the appropriate initial conditions[11], that come from the spontaneous emission event which is not included in this simple model.

Next we restore physical units to get:

$$\frac{\partial}{\partial t} N_2 = \left(\frac{\sigma_0}{A} N_0 \right) \left(\frac{\Gamma}{2} \frac{I}{I_{sat}} \left(\frac{\Gamma}{2\Delta} \right)^2 \right) (N_2 + 1)$$

$$\frac{\partial}{\partial t} N_2 = G (N_2 + 1) \tag{5.33}$$

Here we have used the relations for the intensity $I = \epsilon_0 c |E_+|^2 / 2$ and saturation intensity $I_{sat} = (\Gamma/2)\hbar\omega/\sigma_0$. Note that here we retain the result used in section 4.1, for the SR gain coefficient $G = R d_0$, with R the single atom Rayleigh rate and d_0 the on-resonance optical depth.

---

[10]Note that in the supplementary material of [Kampel12] there is a miss print, the ξ_{max} is missing.

[11]This allows starting the process, else a stable solution of $N_2 = 0$ will be the case

Part II

# Off-resonant Raman memory in a magnetic trap

CHAPTER 6

Memory introduction

In this part we move to forward scattering (memory) experiments instead of backward scattering (superradiance) experiments as presented in the previous part. In a typical memory experiment a weak probe light is swaped into the sample atomic state when a strong coupling (drive) beam is turned on, then the coupling bean is turned off and at a later time when the coupling (drive) beam is turned on again the weak probe is swaped out of the sample. At first sight the physics is very similar. The difference is in the Raman (memory) the transfer is between two internal states instead of transferring between two different momentum states. The actual difference is more inherent as the basic Hamiltonian describing the two systems is different, but both share the same coupling strength; the sample optical depth (OD) times the scattering rate. The superradiance is described by the parametric amplifier Hamiltonian [Hilliard08a], and the memory process is described by the beam splitter Hamiltonian [Hammerer10].

Another difference between the superradiance and the memory experiments is in the control over the process, i.e. in the memory experiment we are interested in starting the process and then to reverse it "on demand". This control is a key ingrideient in a memory protocol (or experiment) [Simon10]. The idea is to map an incoming signal pulse into a long-lived atomic coherence, so that it can be later retrieved "on demand" with the highest possible efficiency. This key feature is what makes the memory such a useful tool in (or a requirement for) many quantum information and communications protocols [Duan01, Lukin03, Hammerer10], such as quantum repeaters and entanglement swapping [Sangouard11]. Another conceptually simple example with a useful practical application, is to send a single heralded photon to a memory and thus producing a true single photon source on demand.

To get a high coupling between the photons and the atoms there are mainly two approaches: 1) ensemble based i.e. using a large number of atoms, and 2) multi-pass i.e. use a high finesse cavity. In the ensemble based approach the weak interaction between the photon and the atom is increased using high OD [Gorshkov07b, Mishina07, Simon10], as was also shown in the previous chapters. The second option is using a single system (atom, or ion, or a quantum dot) in a high finesse cavity and in this way increasing the coupling [Gorshkov07a, Specht11, Ritter12].

Memories are also identified by what they can store: 1) single photon, 2) Qubit, and 3) continuous variable (CV) [Simon10]. With the single photon means that only one excitation can be made, but both quadratures are stored. A Qubit memory is an inherent a two-mode memory in which there are two possible
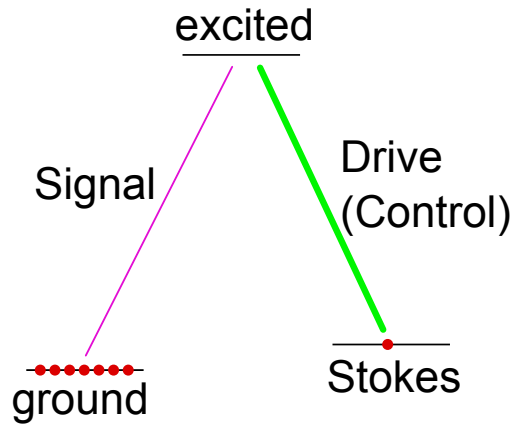
Figure 6.1: A three level Λ system.

target state[1]. In continuous variable type one can store many excitations, thus the source of the name continuous variables. Here as we used a sample with many atoms we are implementing a continues variable type of memory.

6.1   A memory protocol in a Λ system

The simplest system to realize a memory is a two level system, but it suffers from the big disadvantage of lack of control over the process. Adding a third level allows control over the process. In such a system, two long lived states are coupled via a third level[2]. An oversimplifying, but useful, way to think about the memory is to consider a STIRAP process [Bergmann98] only instead of transferring all the atoms from one ground level to the other we are interested in transferring a small fraction.

A three level system in a Λ-configuration, couples the ground state to a second ground level typically referred to as the Stokes level via an excited level. The coupling is mediated with two light sources the "signal" and the "drive", as sketched in Fig. 6.1.

A memory protocol has three stages: writing, storage, and reading. The *writing* stage, in a naive picture, a small fraction of atoms in the ground level are Raman transferred to the Stokes level. In a more complete picture, the two quadratures of the electric field of the signal beam are coherently mapped into the atomic coherence with the signal beam excitations being annihilated and the drive light excitations are created. Here, first the strong (classical) drive beam is turned on, then the weak signal beam (or quantum signal) is coherently absorbed in the sample; while the drive light is turned off again. The coupling of the two beams gives rise to a coherence between the two ground levels: ground and Stokes in Fig. 6.1. Additionally, it is important to notice that the atomic medium is initially transparent for the drive light as there are no atoms in the Stokes level.

The *storage* stage starts when the signal beam (SB) and the drive light (DL) are turned off. A low dephasing between the two ground levels is important at this stage, as the coherence between the ground and Stokes levels should not be modified. Typically there are three major causes for loss of coherence in atomic

---

[1]We note that one can also produce a qubit memory with one target state with two time bins.

[2]Here the concept of the third level is used very loosely. One can even use a two level system where after storing the excitation the two levels are moved off-resonance and thus the coupling is effectively turned off.

ensembles, magnetic field inhomogeneity, atoms moving out of the interaction region, and collisional spin relaxation [Zhao09].

In the *read* stage, the DL is turned on and the spin coherence that was initially stored is converted back to SB photons. One can look at the outgoing SB as an amplified emission of a phased array of optical dipoles. In Fig. 6.1 we have named the beam coupling the Stokes level to the excited state as the drive light, even though it is sometimes called the control beam; as turning it on/off controls the different stages.

While we described the memory process using a semi-classical picture, we can also describe the process using a quantum mechanical model. During the write process a SB photon is annihilated ($\hat{a}_{SB}$), a DL photon is created ($\hat{a}_{DL}^{\dagger}$) and an atomic excitation is created ($\hat{b}_a^{\dagger}$). This results in a term to the Hamiltonian as $H \sim \hat{a}_{SB}\hat{a}_{DL}^{\dagger}\hat{b}_a^{\dagger}$. Similarly the read process Hamiltonian is described by the Hermitian conjugate $H \sim \hat{a}_{SB}^{\dagger}\hat{a}_{DL}\hat{b}_a$, i.e. we create a SB photon, annihilate a DL photon and annihilate the atomic excitation. Here the DL is in a high amplitude coherent state, so that $\hat{a}_{DL}$ ($\hat{a}_{DL}^{\dagger}$) can be replaced by a complex number χ (χ^*), and the whole process can be described by the beam splitter Hamiltonian, i.e. $\hat{H}_{BS} = \chi_{BS}\left(\hat{a}_{SB}\hat{b}_a^{\dagger} + \hat{a}_{SB}^{\dagger}\hat{b}_a\right)$ [Hammerer10].

To compare to the experiments discussed in the first part of the thesis, the super-radiance process is described by the parametric amplifier (or two-mode squeezing) Hamiltonian. In this case we annihilate a single probe photon, create a backward propagating photon ($\hat{a}_{bs}^{\dagger}$) and create an atomic excitation with $2\hbar k$ momentum ($\hat{b}_a^{\dagger}$). In the limit of a classical probe this results in $\hat{H}_{PA} = \chi_{PA}\left(\hat{a}_{bs}\hat{b}_a + \hat{a}_{bs}^{\dagger}\hat{b}_a^{\dagger}\right)$ [Hammerer10].

6.2   Characterizing the memory performance

There are several criteria for evaluating the memory performance [Simon10]:

1. **Efficiency** is defined as the ratio between the number of signal photons retrieved to the number of photons sent. To date the highest efficiency that was measured is 87% in a ^{87}Rb hot vapor cell [Hosseini11b]. To the best of our knowledge, the highest efficiency using ultra-cold atoms is about 50% [Riedl12].

   While not all applications require high efficiency, some require as high efficiency as possible like quantum repeater. This is since the time to distribute an entangled pair drastically reduces as function of the memory efficiency. For example for a quantum repeater with fidelity of 90% and distribution distance of 600km a reduction in the memory efficiency from 90% to 89% leads to an increase in the entanglement distribution time by $10\% - 14\%$, depending on the protocol [Sangouard11].

2. **Fidelity** is defined as the wave function overlap between the input state and the output state, $\mathfrak{F} = |\langle\psi_{in}|\psi_{out}\rangle|$. For a single photon source sometimes conditional fidelity is used, i.e. the fidelity is evaluated only for the case a photon is detected. Fidelity as high as 1.000 ± 0.004 has been shown [Riedl12] using ultra-cold atoms.

3. **Storage time** is the time we can store the input signal before we lose the information, due to decoherence processes. To date the largest storage time is 180s in a donor spins of ^{28}Si [Steger12].

For the cases of atomic ensembles the limitation is different to warm cells which are limited by collisional spin relaxation and is less than 10ms [Julsgaard04]. For ultra-cold atoms the limitation comes from the relative movement of the atoms in the ground state from the atoms in the Stokes state by about a de Broglie wavelength [Zhang09, Riedl12], and could be longer than 1s. It should be noted, though, that in most experiments the magnetic field inhomogeneity determines the actual storage time [Zhao09].

4. **Bandwidth** determines the achievable repetition rate. An important parameter here is the time-bandwidth product of a memory, that quantifies the number of distinct time bins available for computational operations in a hypothetical quantum processor using the memory. The highest memory bandwidth achieved exceeds 1GHz, with a time-bandwidth product of about 2×10^3 [Reim11], with a pulse width of about 1ns.

5. **Capacity to store multiple orthogonal modes**. This is naturally relevant only for ensemble type of implementations and not for a single atom based implementation. The general criterion is the maximum number of orthogonal spatial modes that can be stored [Zeuthen11], for generating quantum holograms. Storing images has been shown either using atomic samples [Shuker08, Firstenberg09], or in doped solids [Heinze10].

6. **Wavelength** of the outgoing signal beam is important for different realizations. For example for long distance communication one would prefer to work with telecom wavelength, such has been shown by Lauritzen *et al.* at 1.5μm wavelength using an erbium-doped Y_2SiO_5 crystal with storage time of 0.6μs and total efficiency of 0.2% [Lauritzen10]. At the wavelength of 1.3μm it has also been realized by Radnaev *et al.* with a life time of 165ms and total efficiency of less than 5% [Radnaev10].

6.3   Different types of memory implementations

In this section we are going to describe the main different memory schemes without discussing the actual experimental requirements. There are five main types of ensemble based memories that are commonly used [Simon10, Hammerer10, Lvovsky09] which are called: electromagnetically induced transparency (EIT), off-resonance Raman, controlled reversible inhomogeneous broadening (CRIB), atomic frequency combs (AFC), and Faraday rotation. The first three memory types are conceptually very similar, with the EIT and Raman are different by the single photon detuning (Δ) and the CRIB is similar to the EIT only operates in momentum space. The AFC is based on the reversible absorption by a periodic structure of narrow absorption peaks. The Faraday interaction based memory has an inherent difference as it couples only one of the two light quadratures to the sample, hence for a two quadrature memory one is required to measure the other quadrature and to feedback it into the atoms [Julsgaard04, Hammerer10].

The way each of these memory schemes work is:

1. *EIT* type coupling is achieved when the weak signal beam and the classical drive (control) beam interact such that the transition probability to the excited level vanishes. A more mathematical way to express this is that the two beams form a stationary eigenstate of the three level system that contains only the ground and Stokes levels. Populating a dark polariton causes a typically opaque medium to become transparent, and is therefore

called electromagnetically induced transparency [Lukin03]. This happens when the two beam are on resonance with the excited level.

Another way to look at EIT is that the DL beam changes the atomic index of refraction (or the susceptibility), such that the group velocity for the signal light is significantly reduced. A group velocity as low as 10m/s was measured [Zhang09]. This can be used for storing the SB light pulse. By turning off the DL we adiabatically transfer the SB photons into a dark state polariton. Then at a later time, by turning back on the DL we transfer back this dark state polariton into the SB photons.

2. *Off-resonance Raman* is achieved when the SB and DL beams are on the two photon resonance with a large detuning from the excited state. When only the DL alone is on, it is transparent to the sample but when the SB arrives it fulfills the two-photon resonance condition and the SB mode is coherently transferred into the sample. Formally this requires that the single photon detuning (Δ) is much larger than the natural line width (Γ) times the optical depth of the sample (OD), i.e. $\Delta \gg OD \cdot \Gamma$ [Gorshkov07b].

3. *CRIB* is known as controlled reversible inhomogeneous broadening. It results from the observation that a pulse of light, absorbed in an inhomogeneously broadened medium with small homogeneous linewidth, can be forced to reemerge from the medium at some later time as an echo [Tittel10]. This involves controlled broadening an initially narrow absorption line using either linear Stark effect or a linear magnetic field (based on Zeeman splitting of the excited states) [Simon10, Hosseini11a]. In this case the memory acts in similar to the EIT memory just in momentum space.

4. *AFC* the atoms are described by a periodic comb-like structure that has absorption lines spaced by multiples of Δ. Repetitive rephasing occurs at times $2\pi/\Delta$, when the phases accumulated by atomic dipoles in different "teeth" differ by multiples of 2π. This condition is well satisfied in crystals doped with rare-earth-ions [Lvovsky09]. To inhibit re-emission after one fixed cycle and to allow for long storage time with on-demand retrieval, the excited optical coherence can be transferred temporarily to a coherence between other atomic levels where the comb structure is not present [Timoney12].

5. *Faraday* rotation or sometimes also called the quantum non-demolition coupling is different from the other coupling schemes presented above [Hammerer10, Kurucz08]. Here one of the SB quadratures is rotated into the atomic sample. It can be used for a memory protocol when combined with measurement and feedback, since only one of the SB quadratures is coupled [Julsgaard04, Jensen10].

6.4   Optimal pulse shape

Above we did a naive analogy between the memory process and the STIRAP process. While this analogy is over simplifying, it captures several important points, such as the counter-intuitive pulse sequence. For optimal storage efficiency the SB pulse shape should be tailored to the experimental conditions, i.e. to the sample OD and DL power. In the off resonance Raman memory it is conceptually easy to understand that in a dense medium the SB will be transformed into an atomic excitation at the beginning of the sample, and then propagating through the sample as long as the DL is on.
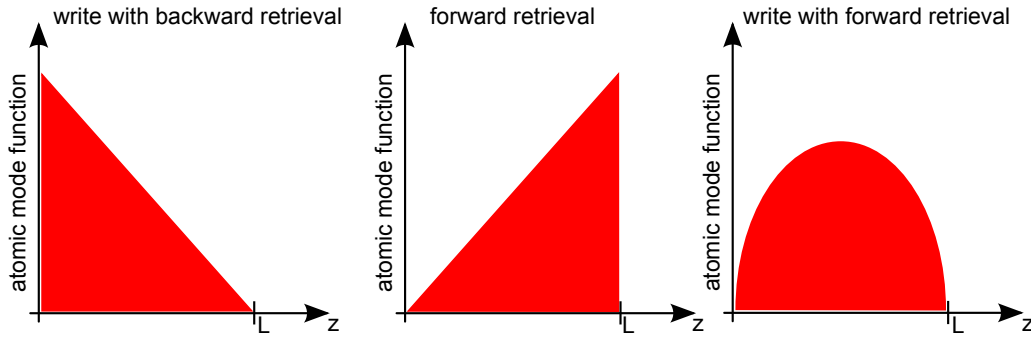
Figure 6.2: Optimal atomic excitation mode function for a cylindrical sample with a length L.

With this in mind for an optimum writing efficiency the excitation mode shape in the sample is a right angle triangle along the sample with its peak at the beginning of the sample, see Fig. 6.2-left. Similarly, for optimum forward retrieval efficiency the excitation mode shape is a triangle shape along the sample with a peak now at the end of the sample, see Fig. 6.2-middle. In the limit of high OD and for forward writing and retrieval the optimal spatial shape of the storage mode of the excitation is an inverted parabola in the sample [Gorshkov07b], see Fig. 6.2-right.

6.5 Scope of the experimental and theoretical work

After describing different types of memory schemes and their realization, we move to describe our realization of the off-resonance Raman memory. We start, in chapter 7, with the experimental apparatus. In chapter 8, as a first test for our detection scheme, we explored Rabi oscillations between the ground and Stokes levels. We use the results to find the two photon resonance.

We have decided to implement the memory inside the magnetic trap. We have realized a magnetic servo-loop to effectively eliminate the gravitational sag. This provides a symmetric environment for the atoms and reduces undesired initial mixture of the ground and Stokes levels. In chapter 9 we give a brief description of the servo-loop performance, with the full details are given in appendix G.

Next, in chapter 10, we characterize the setup performance and optimization steps. We then take a side track to derive a $1D$ model to allow us both to design the input parameters and to compare to the experimental results. The model is described in chapter 11 and the implementation of the numerical simulation is given in chapter 12.

Then after having both the experimental setup optimized and a $1D$ model to compare experimental results to, in chapter 13 we characterize the memory performance using bucket detection. In chapter 14 we characterize the temporal-spatial retrieved signal beam. We finish this part of the thesis with chapter 15, in which we describe what experimental changes should be done when considering the results we have got.

Overview of setup

In this chapter we describe our memory experimental system, using ultra-cold ^{87}Rb Bose gas utilizing the relatively high on axis optical depth ($OD \sim 200$). We identify a Λ-system, see Fig. 6.1 in which the ground level is the trapped level $\left|F_0 = 1, m_f = -1\right\rangle$, the Stokes level is the anti-trapped level $\left|F_0 = 1, m_f = +1\right\rangle$, and the excited level is $\left|F = 1, m_f = 0\right\rangle$. Here F_0 (F) is the hyperfine ground (excited) quantum number and m_f is the Zeeman quantum number. Choosing to work with this Λ-system we have defined the polarization for the signal beam (SB) to be circularly polarized (σ_+) and for the drive light (DL) to have the opposite circularly polarization (σ_-).

The DL induces a differential light shift on the two ground state levels used for the memory, $\left|F_0 = 1, m_f = \pm 1\right\rangle$. This light shift is dependent on the single photon detuning (Δ), and means that we have different two-photon resonance condition depending on the DL power. While we can overcome this by a smart design of the SB phase, it gives an inherent dependence on the DL power and its noise. This dependence can be canceled by working with the so-called "magic" detuning in which there is no differential light shift, at $\Delta \cong -200$MHz for the case of ^{87}Rb utilizing the $D1$-line with $F_0 = 1$ hyperfine ground state. A different way to describe this effect is that the atomic ensemble has a different index of refraction for the different circular light polarization components that causes a differential phase shift to the light beams. This effect known as Faraday rotation and is canceled at the "magic" detuning.

For efficient detection we have chosen to work with balanced heterodyne or homodyne detection [Garrison08], that allows detection of a single excitation in the right mode with a signal-to-noise ratio of one. In addition, since in our setup both the SB and DL are co-propagating this type of detection allows for further suppressing of the DL leak light by choosing a different spatial mode to the SB and DL. In this detection scheme the weak signal is amplified by an external beam called local oscillator (LO). We have designed and built our balanced detector with a bandwidth of 20MHz. The detection is shot noise limited for LO powers higher than 40μW.

In section 7.1 we describe the light setup, focusing on the production of the different beams and the detection. Then in section 7.2, we analyze the heterodyne detection system, i.e. how we extract from the measure signal the two electric field quadratures. We have used two types of detections: time dependent and integrating over the spatial coordinates (with a brick-wall corner frequency of 460kHz), and position resolved ($\sim 3\mu$m^2 resolution) and time integrated over 1μs. In section 7.3 we describe the design and realization of the 20MHz DC balanced detectors for the heterodyne detection.
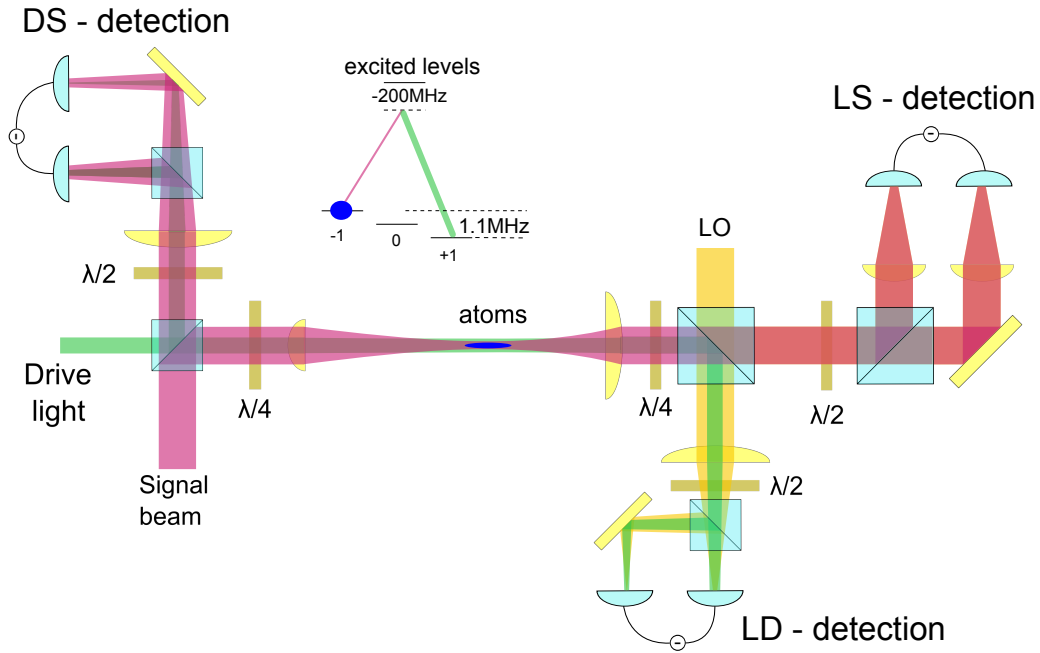
Figure 7.1: The memory experimental setup. The inset shows the atomic level schematic.

7.1 The setup

In this section we describe the probing setup and assume a prolate sample that its production is described in chapter 2. At this point we remind the reader that the optical axis along the long axis of the cloud is limited by a 4mm hole at a 100mm from the atoms, due to the magnetic trap we use (see chapter 2). This is important as it limits the focusing of the input beam.

The light is produced from a diode laser phased locked to a second laser locked on a ^{85}Rb $D1$ line via saturation absorbtion. This allows to detune the laser over a range of about 9GHz around the ^{87}Rb transition $|F_0 = 1\rangle \longleftrightarrow |F = 2\rangle$ [Kaminski12b, Appel09]. Then we clean the spatial mode and decouple the locking setup from the rest via a 2m polarizing maintaining fiber.

We split the light exiting from the fiber to three different beams using half-wave plates and polarizing beam splitters (PBS), for the SB, DL and LO beams. Each beam is then passed through a double pass Acousto-Optic Modulator (AOM) setup and coupled into a 2m polarizing maintaining fiber. We control the AOM frequency shift and phase using a Direct Digital Synthesizer (DDS), with a 250MHz bandwidth, a $14 - $bit amplitude resolution and a $16 - $bit phase resolution.

The single photon detuning is set by the phase lock with a 5MHz resolution, referenced to the transition $|F_0 = 1\rangle \longleftrightarrow |F = 1\rangle$ (see inset of Fig. 7.1). The fine tune is achieved with the AOM as the DDS allows for a 2Hz resolution. Note that the DDS frequency is determined by an external clock, in our case a 1GHz Voltage Controlled Oscillator (VCO). Since our data acquisition is done with an oscilloscope, we tune the VCO such that both will have the same time base combined to give $\Delta f / f \cong 10^{-4}$.

A schematic of the memory apparatus and the detection is given in Fig. 7.1, in which the SB and DL have different beam diameter before we combine them on a PBS and set their circular polarization using a quarter wave plate. This
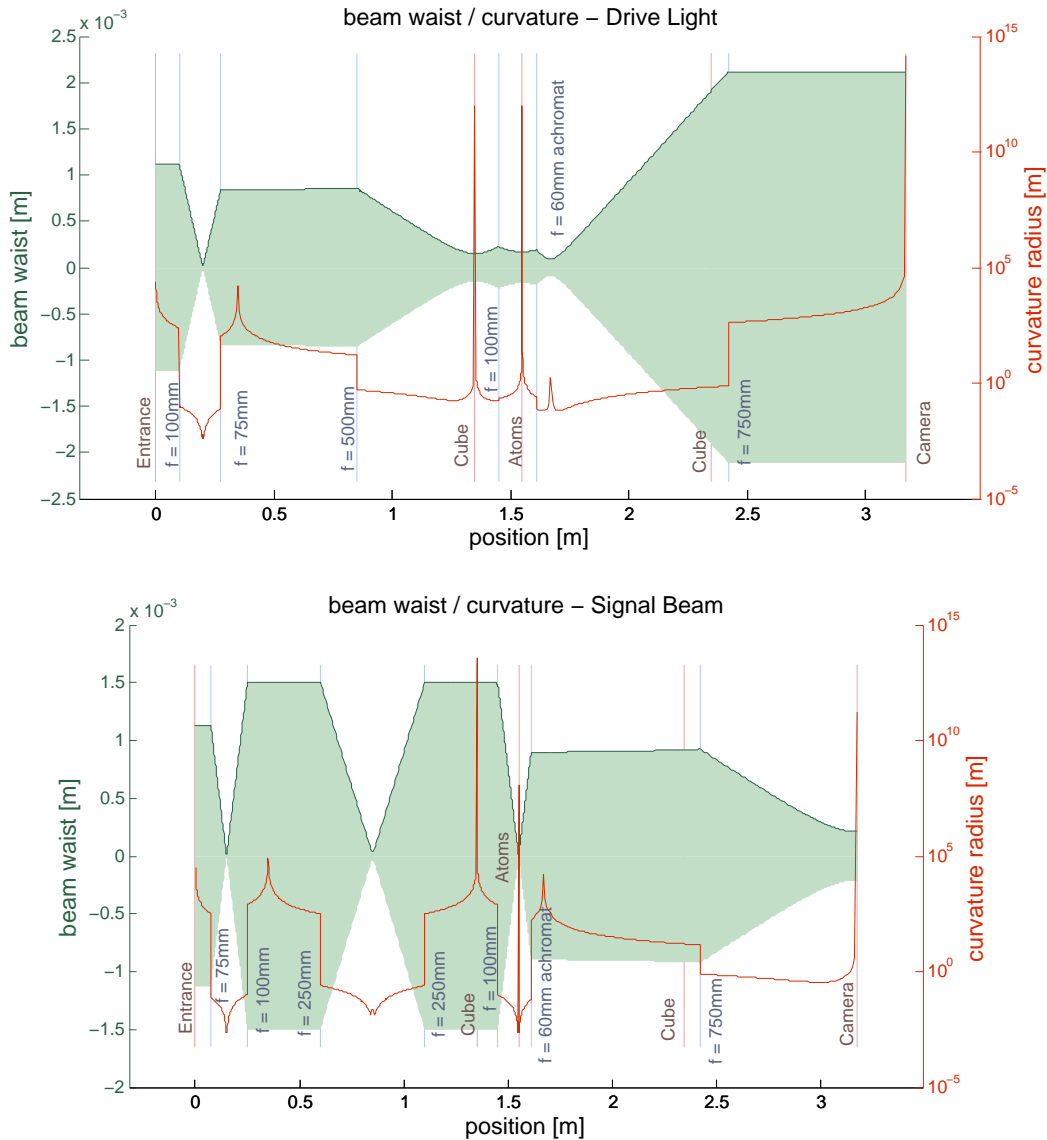
Figure 7.2: Design of beam and waist curvature for the DL (top) and SB (bottom). Here we start at an output of a fiber coupler (entrance) then the beams pass through two lenses (telescope). The two beams are combined at a polarizing beam splitter. Then we focus the beams on the atoms ($f = 100$mm). The outgoing beams pass through an achromat lens and separated on a beam splitter cube. The SB can be imaged onto a CCD camera.

is done such that the SB will be mode matched to the atoms[1], and the DL will be a plain wave. As the light source originates from a fiber we implement a telescope configuration to set the initial beam diameters. The full setup (waist and curvature) for the SB and DL is given in Fig. 7.2. We end up with the SB focused to 20μm ($1/e^2$) at the atoms and the DL has 140μm ($1/e^2$) waist radius with a large radius of curvature at the atoms.

We have chosen to work with a balanced heterodyne detection and measure both quadratures of the electric field [Garrison08], as it is a well established method in quantum information experiments [Lvovsky09, Hammerer10]. The big advantage of working with heterodyne is that the weak signal is interfered with an external local oscillator (LO), and the noise is dominated by the LO noise. This means that for a strong enough LO we get a shot noise limited

---

[1]Actually we have focused the beam to have the smallest focused that we can achieved. Then we have set the cloud external diameter to fit the SB.

detection[2]. In addition we measure the SB projection to the LO mode, since this is an interference measurement and the LO is much stronger than the SB. By combining a post-processing lockin analysis, as described in section 7.2, we simultaneously measure both quadratures of the SB electric field [Garrison08]. For an optimum the LO needs to be mode matched to the measured signal. In our case we do not have the physical space to mode match the LO beam to both the SB and the DL, therefore we only mode match it to the SB (see Fig. 7.1). We measure a visibility of 90% between the LO and the SB. Note that the low visibility between the LO and the DL also helps in suppressing the contribution of the DL leak light into the SB channel.

The detection setup, given in Fig. 7.1, is designed to measure both field quadratures of the SB and DL. From the two heterodyne detectors after the atoms we measure the field amplitude of the SB and DL and their relative phases to the LO. The phase difference between the SB and DL before the atoms is directly measured from the input (DS) heterodyne detector, see Fig. 7.1. Thus using these three detectors and assuming interferometrically stability of the optical setup[3] over the experiment time scale (less than $100\mu s$) we can get the information about all the different quadratures.

Next we turn to the alignment of the experiment, i.e. setting the input polarization, aligning the SB on the atoms and separating the SB and the DL. The SB and DL input polarization need to be circular with opposite rotation direction, which is achieved by setting the quarter wave plate before the atoms. We aligned it by putting a pre aligned quarter wave plate after the atoms[4] (see Fig. 7.1) and with a PBS we can find the two axis of the quarter wave plate. This way we get circularly polarized light but do not know which is the σ_- and which is the σ_+ light. To find this we use Rayleigh superradiance experiments as the transition $|F_0 = 1, m_f = -1\rangle \rightarrow |F = 2, m_f = -2\rangle$ is stronger than the transition $|F_0 = 1, m_f = -1\rangle \rightarrow |F = 1, m_f = 0\rangle$. This allowed us to set the right circular polarization, i.e. DL has σ_- polarization and SB has σ_+ polarization. Later, a more sensitive fine tuning of the quarter wave plate alignment was done (see section 10.2).

Before each experimental sequence we have aligned the spatial overlap between the SB and the atomic sample. As both SB and the atomic sample have similar small size, we are sensitive to slow alignment drifts over several days. By resonant absorption imaging along the long (probe) axis we find the atoms position and by direct imaging find the SB and DL positions. The imaging setup is described in detail in [Kaminski12b].

In order to measure the different contribution of the SB and of the DL we separate them after the atoms, by initially transforming their polarization from circular to linear polarization using a quarter wave plate. Then the two beams are split by a PBS and the SB is transmitted by the PBS and the DL is reflected by the PBS, see Fig. 7.1. A crucial point here is to suppress the leak DL on the SB channel (on the LS-detector in Fig. 7.1), since typically the DL photon flux is about five order of magnitude larger than the SB photon flux. Here we achieve six order of magnitude suppression ratio of the DL in the SB channel, due to the PBS and to the low visibility between the DL and the LO. This suppression is measured on the LS-detector (see Fig. 7.1), for example in a typical situation[5] we measure

---

[2]Here we explicitly assume that the LO light source has no classical noise sources bigger than the shot noise, this was verified in section 7.3.

[3]We measured the setup stability to be on the order of a second.

[4]Naturally, this was done without the atoms.

[5]This is typical and not best!

40mV signal when sending 420μW DL power and 300mV signal when sending 5nW SB power. Thus the suppression is given by $(40\text{mV} \cdot 5\text{nW}/300\text{mV})/420\mu$W that gives a 1.6×10^{-6} suppression ratio.

Imaging the SB

Here the goal is to measure the spatial mode of the outgoing SB, during the retrieval stage. For this we have replaced the LS-detector in Fig. 7.1 by a CCD camera, with both ports of the balancing beam splitter detected on distinct regions of the CCD chip. The focusing of two different beams on the camera such that we image the end of the atomic sample with a resolution of 3.5μm is described in detail in [Kaminski12b].

As the camera cannot be gated with fast enough time resolution[6] and integrates the signal over time we use homodyne detection instead of the heterodyne. Since in homodyne there is no frequency difference between the LO and the SB, the signal will not be averaged out. The disadvantage is that we measure a single quadrature of the electric field that changes for each experimental realization, as we don't have control over the phase difference. Therefore we square the detected signal on the camera signal and average over many realizations assuming fair random sampling of the LO phases on the unit circle. This allows as to measure the sum of the two squares of the mean electric field quadratures, see section 7.2.4.

7.2 The heterodyne signal and post analysis (lock-in)

In section 7.1 we described the measurement setup and motivated the use of heterodyne detection. Here we are going to derive the expected signal for our experimental situation and define the post measurement analysis, i.e. extracting the two electric field quadratures using a lock-in procedure. In the last subsection we go over the expected signal when we image the SB using homodyne. While the approach used in this section is fully classical, it is straight forward to generalize it to a quantum description [Garrison08].

7.2.1 Deriving the heterodyne signal

Here we are going to analyze the signal coming to the different heterodyne detectors, shown in Fig. 7.1. For simplicity we are going to assume a regular beam splitter in the analysis and not a PBS. We start by writing the electric field components for the SB-LO:

$$E_t(\tau, x, y) = tE_{SB}e^{-i\omega_{SB}t} + tE_{DL}e^{-i\omega_{DL}t} + rE_{LO}e^{-i\omega_{LO}t} \tag{7.1}$$

$$E_r(\tau, x, y) = rE_{SB}e^{-i\omega_{SB}t} + rE_{DL}e^{-i\omega_{DL}t} + tE_{LO}e^{-i\omega_{LO}t} \tag{7.2}$$

where r and t are the complex transmission and reflection coefficients of the beam splitter, E is the electric field component before the beam splitter, ω is the carrier frequency with the subscript identifying the field component. For brevity reasons we wrote the position (x, y) and time (τ) only on the left hand side.

Here, E_{DL} is the leak DL electric field and has the same polarization as the SB, while the LO has the opposite polarization. Next, we express the electric field in polar coordinates, thus intruducing amplitude and phase e.g. $E = \rho e^{i\phi}$. We

---

[6]Gating time is several to tens of milliseconds that is longer than the experiment duration

write the measured intensity[7] at each photodiode port to be

$$I_r(\tau, x, y) \equiv \mathbf{E}_r^* \mathbf{E}_r = |r|^2 \rho_{SB}^2 + |r|^2 \rho_{DL}^2 + |t|^2 \rho_{LO}^2 +$$
$$2 |r|^2 \rho_{SB} \rho_{DL} \cos(\Delta\omega_{DL-SB} t - \Delta\phi_{DL-SB}) -$$
$$2\rho_{SB}\rho_{LO} |t| |r| \sin(\Delta\omega_{LO-SB} t - \Delta\phi_{LO-SB}) -$$
$$2\rho_{DL}\rho_{LO} |t| |r| \sin(\Delta\omega_{LO-DL} t - \Delta\phi_{LO-DL}) \tag{7.3}$$

$$I_t(\tau, x, y) \equiv \mathbf{E}_l^* \mathbf{E}_l = |t|^2 \rho_{SB}^2 + |t|^2 \rho_{DL}^2 + |r|^2 \rho_{LO}^2 +$$
$$2 |t|^2 \rho_{SB} \rho_{DL} \cos(\Delta\omega_{DL-SB} t - \Delta\phi_{DL-SB}) +$$
$$-2 |r| |t| \rho_{SB}\rho_{LO} \sin(\Delta\omega_{LO-SB} t - \Delta\phi_{LO-SB}) +$$
$$-2 |r| |t| \rho_{DL}\rho_{LO} \sin(\Delta\omega_{LO-DL} t - \Delta\phi_{LO-DL}) \tag{7.4}$$

We invock energy conservation to state that $tr^* = |t| |r| e^{-i\pi/2}$, and for a 50/50 beam splitter we have $|t| = |r| = 1/\sqrt{2}$. The frequency and phase differences are given in the subscripts.

For a balanced heterodyne detection we get:

$$S_{hete}(\tau, x, y; SB - LO) = I_t - I_r = \left(|t|^2 - |r|^2\right)\left(\rho_{SB}^2 + \rho_{DL}^2 + \rho_{LO}^2\right) +$$
$$\left(|t|^2 - |r|^2\right) 2\rho_{SB}\rho_{DL} \cos(\Delta\omega_{DL-SB} t - \Delta\phi_{DL-SB}) +$$
$$-2 |r| |t| 2\rho_{SB}\rho_{LO} \sin(\Delta\omega_{LO-SB} t - \Delta\phi_{LO-SB}) +$$
$$-2 |r| |t| 2\rho_{DL}\rho_{LO} \sin(\Delta\omega_{LO-DL} t - \Delta\phi_{LO-DL}) \tag{7.5}$$

As is evident, when using a 50/50 beam splitter $\left(|t|^2 - |r|^2\right) \to 0$ and $2 |r| |t| \to 1$, which gives the main two advantages of balanced heterodyne detection:

1. The common mode noise (classical) is canceled; this can also be achieved when measuring only one port by mixing the signal with an appropriate modulated signal and low pass the result, as is the typical situation with heterodyne measurements.

2. There is an extra factor of two that is unique to the balanced detection.

From a similar calculation we find the signal for the DL-LO balanced detector to be:

$$S_{hete}(\tau, x, y; DL - LO) = \left(|t|^2 - |r|^2\right)\left(\rho_{SB}^2 + \rho_{DL}^2 + \rho_{LO}^2\right) +$$
$$\left(|t|^2 - |r|^2\right) 2\rho_{SB}\rho_{LO} \cos(\Delta\omega_{LO-SB} t - \Delta\phi_{LO-SB}) +$$
$$-2 |r| |t| 2\rho_{DL}\rho_{LO} \sin(\Delta\omega_{LO-DL} t - \Delta\phi_{LO-DL}) +$$
$$-2 |r| |t| 2\rho_{SB}\rho_{DL} \sin(\Delta\omega_{SB-DL} t - \Delta\phi_{SB-DL}) \tag{7.6}$$

and for the DL-SB detector the result is:

$$S_{hete}(\tau, x, y; DL - SB) = \left(|t|^2 - |r|^2\right)\left(\rho_{SB}^2 + \rho_{DL}^2\right) +$$
$$-2 |r| |t| 2\rho_{SB}\rho_{DL} \sin(\Delta\omega_{SB-DL} t - \Delta\phi_{SB-DL}) \tag{7.7}$$

At this point we remind the reader that these signals need to either be integrated over the spatial coordinates in the case of a bucket detector or integrated over time as in the case of detection with a CCS camera.

---

[7]Up to a dimension constants.

det. / par.	LD	DS	LS
ω_1	$\Delta\omega_{LO-DL}$	$\Delta\omega_{SB-DL}$	$\Delta\omega_{LO-SB}$
ω_2	$\Delta\omega_{SB-DL}$	—	$\Delta\omega_{LO-DL}$
ω_3	$\Delta\omega_{LO-SB}$	—	$\Delta\omega_{DL-SB}$
A	$2\,\lvert r\rvert\,\lvert t\rvert\,\rho_{DL}\rho_{LO}$	$2\,\lvert r\rvert\,\lvert t\rvert\,\rho_{SB}\rho_{DL}$	$2\,\lvert r\rvert\,\lvert t\rvert\,\rho_{SB}\rho_{LO}$
B	$2\,\lvert r\rvert\,\lvert t\rvert\,\rho_{SB}\rho_{DL}$	—	$2\,\lvert r\rvert\,\lvert t\rvert\,\rho_{DL}\rho_{LO}$
C	$\left(\lvert t\rvert^2-\lvert r\rvert^2\right)\rho_{SB}\rho_{LO}$	—	$\left(\lvert t\rvert^2-\lvert r\rvert^2\right)\rho_{SB}\rho_{DL}$

Table 7.1: This table summarizes the different parameters used in Eq. 7.8 (par.) and correlates it to the appropriate detector (det.). The detectors names are: LD for measuring the DL, DS for measuring the differences between the DL and the SB, and LS for measuring the SB. Here we ignored the contribution of the D coefficient.

7.2.2 The post processing: lock-in analysis and filtering

Here we describe how to extract the two electric field quadratures from the balanced heterodyne signals. We parameterize the signals as:

$$S = 2A\sin(\omega_1 t + \phi_1) + 2B\sin(\omega_2 t + \phi_2) + 2C\cos(\omega_3 t + \phi_3) + D \qquad (7.8)$$

with A, B, and C the electric field amplitudes, D the missbalance of the detection, and ϕ_1, ϕ_2, and ϕ_3 the phase differences. Our goal is to extract out of the signal A and ϕ_1, and remove B, C, D, ϕ_2, and ϕ_3. Note that C is the coefficient includes $\left(\lvert t\rvert^2 - \lvert r\rvert^2\right)$ and is inherently smaller than A. On the other hand for the LS-detector, the B coefficient indicates the DL leak light and could be as big as A, as both are amplified by the external LO. Later we will discuss the influence of a comparable B coefficient. The correlation between the different coefficients and the frequencies to the detectors is given in table 7.1.

To extract the wanted parameters we multiply the signal by $\sin\omega_1 t$ and $\cos\omega_1 t$ that gives

$$
\begin{aligned}
Sc = S \times \cos(\omega_1 t) = {} & A\left\{-\sin\phi_1 + \sin(2\omega_1 t - \phi_1)\right\} + \\
& B\left\{\sin\left[(\omega_2-\omega_1)t - \phi_2\right] + \sin\left[(\omega_2+\omega_1)t - \phi_2\right]\right\} + \\
C\left\{\cos\left[(\omega_3-\omega_1)t - \phi_3\right]\right. & \left. + \cos\left[(\omega_3+\omega_1)t - \phi_3\right]\right\} + D\cos(\omega_1 t) \qquad (7.9) \\
Ss = S \times \sin(\omega_1 t) = {} & A\left\{\cos\phi_1 - \cos(2\omega_1 t - \phi_1)\right\} + \\
& B\left\{\cos\left[(\omega_2-\omega_1)t - \phi_2\right] - \cos\left[(\omega_2+\omega_1)t - \phi_2\right]\right\} + \\
C\left\{-\sin\left[(\omega_3-\omega_1)t - \phi_3\right]\right. & \left. + \sin\left[(\omega_3+\omega_1)t - \phi_3\right]\right\} + D\sin(\omega_1 t) \qquad (7.10)
\end{aligned}
$$

if we low pass filter these signals we get:

$$Sc = -A\sin\phi_1 \qquad (7.11)$$
$$Ss = A\cos\phi_1 \qquad (7.12)$$

from which we can evaluate the amplitude (A) and phase (ϕ_1). For all filters the lowest frequency that is needed to efficiently suppress is $\omega_{DL} - \omega_{SB}$ (see table. 7.1 and table 7.2), which is the Zeeman splitting of the hyperfine ground level. For our experimental parameters the Zeeman splitting is about one megahertz.

As a low pass filter we are interested in a filter that suppresses each one of the oscillation frequencies in Eq. 7.9 and Eq. 7.10. In order to suppresses these frequencies we consecutively run several rectangular window running average filter each corresponding to one full cycle ($T = 2\pi/\omega$) of the frequency needed

detector \ frequency	LD	DS	LS
$2\omega_1$	$2(LO - DL)$	$2DL$	$2LO$
$\omega_2 - \omega_1$	$LO - 2DL$	DL	DL
$\omega_2 + \omega_1$	LO	—	$2LO - DL$
$\omega_3 - \omega_1$	DL	—	$LO - DL$
$\omega_3 + \omega_1$	$2LO - DL$	—	$LO + DL$
ω_1	$LO - DL$	—	LO

Table 7.2: This table summarizes the different frequencies used in the filter. The detectors names are: LD for measuring the DL, DS for measuring the differences between the DL and the SB, and LS for measuring the SB. The different frequencies are given referenced to the SB frequency, i.e. $LO = 5\text{MHz}$ and $DL = 1.1\text{MHz}$.

to be suppressed. In the frequency domain each rectangular window running average filter spectrum is a sinc-function with a node at the frequency needed to be suppressed. The total filters response in the frequency domain is a multiplication of sinc-functions with nodes at each of the oscillating frequencies of Eq. 7.9 and Eq. 7.10. In table 7.2 we give the relevant frequencies defining each of the rectangular window in the filter for each of the detectors.

Here we have used twice the DL frequency difference i.e. $\omega_{DL} - \omega_{SB}$. The frequency response of the low-pass filter crosses the $3dB$ point at 430kHz and the $6dB$ point at 600kHz. For the noise estimation we are interested in the equivalent brick-wall filter [Horowitz01] which is at 460kHz, and needs to be compared to the 1.1MHz Zeeman splitting.

Sensitivity to the DL leak light

Here we test the analysis procedure and focus on the effects of the DL leak light on the LS-detector which is parameterized by the B and ϕ_2 coefficients. We test this on three different synthetic envelope signals: constant, Gaussian, and the experimental input. In the case of constant envelop we find six order of magnitude suppression, of the unwanted parameters (B, C, and D). For the time dependent pulses that have frequency components at frequencies above 460kHz we expect that the pulse will be deformed and the signal could depend on the ϕ_2 initial phase. In the right panel of Fig. 7.3 we test a Gaussian signal envelop with a time constant of $\sqrt{2}\mu s$ ($1/e$), and find a negligible time dependence on the ϕ_2 phase.

Next we have tested the effect of the different ϕ_2 phases on a synthetic experimental SB input pulse, as shown in Fig. 7.3 on the left panel. Here we find that the signal has a non-trivial phase dependence which is due to the non-trivial phase of the filter transformation. In addition we find that the filter reduces the total area of the signal to about 70% of the input signal area.

7.2.3   Estimating the signal to noise ratio

In heterodyne detection the detection is shot noise limited when the LO power is sufficiently high. For our employed photodetectors the LO power required to equalize the electronic noise and light shot noise is $40\mu W$, and in our experiments a $300 - 400\mu W$ LO power is used. Therefore the detection noise is
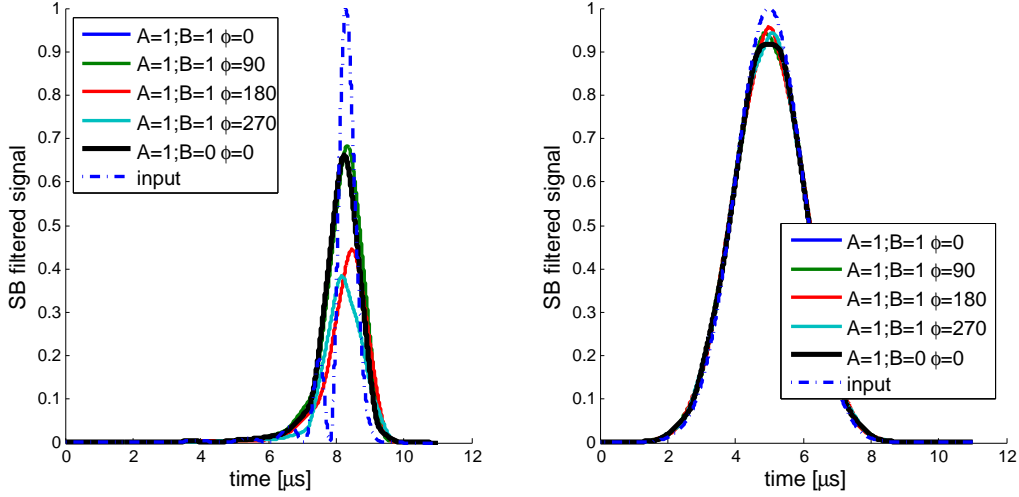
Figure 7.3: The result of the lock-in analysis on synthetic signals, of a functional form given by Eq. 7.8. The input envelope is given in the dashed blue line, and the full lines are the filtered outputs. The legend indicates the differing A, B, and ϕ_2 coefficient of Eq. 7.8. The left hand panel shows pulses envelopes as used in the experiment, and the right hand panel shows results for a Gaussian envelope input pulse.

dominated by the noise of the LO[8]. From evaluating the noise levels we get the SB excitation, and the noise-normalized-signal (NNS) gives the square root of the photon flux in a given bandwidth [Hobbs09].

To estimate the NNS in the experiments with the bucket detector, we have added an additional long 250μs pulse with no SB to determine the noise level. Then on the amplitude quadrature of the detected signal we have used a decimating algorithm with different time separation to remove correlation between adjacent bins due to oversampling[9] and limited filter bandwidth. The relevant correlation time difference is given by the filter equivalent brick-wall bandwidth, which is 460kHz.

For a given decimating time separation we get a number of correlated arrays each containing uncorrelated points used to evaluate the variance. The resulted variance of the correlated arrays is given in Fig. 7.4, using different decimating time constant ($0.5, 1, 2, 4\mu$s). In the case of 4μs the points are independent, as the separation time is larger than the filter bandwidth (corresponding to $\simeq 2\mu$s), while in the case of 0.5μs there is correlation between two adjacent points. Even though there is some correlation in the data when examining the average variance for all time separation cases we get the same result to within 2%. Therefore we work with 1μs and average the results in order to find the variance for each experimental realization, i.e. we find the noise level (N^2).

Next we extract out of the signals amplitude ρ_{SB} by normalizing to the square root of the LO power. Now the signal (S) has unit is $V/\sqrt{\mu W}$ and the noise-normalized-signal (NNS) is given by

$$NNS = \frac{S - \langle bi \rangle}{N} \tag{7.13}$$

with bi is the background value of the signal, which is subtracted since the amplitude quadrature is positive definite. Thus we get that the NNS is around zero,

---

[8]Which is shot noise.

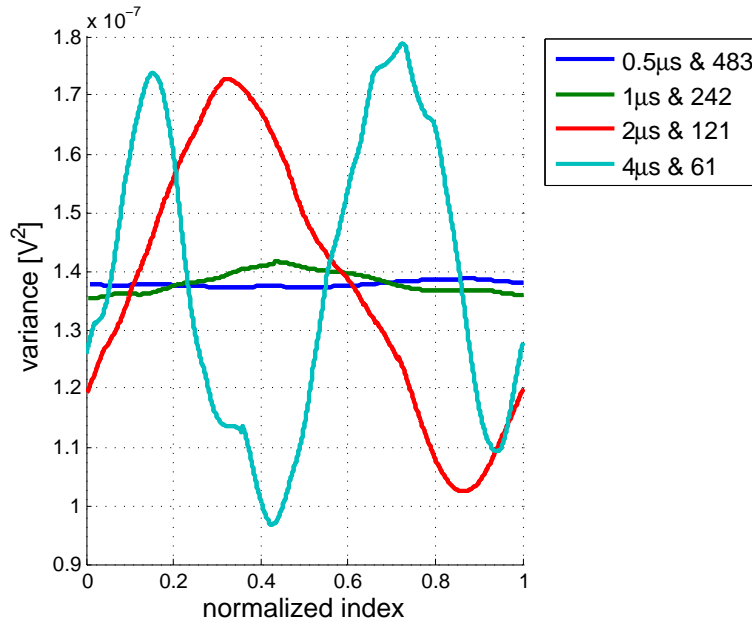[9]The data acquisition is done using a resolution of $1 - 4$ns between neighboring points.

Figure 7.4: The evaluated variance from each decimated array calculated for the amplitude quadrature of a 250μs pulse signal without the SB. For each decimating time constant we get a different number of arrays, and show their evaluated variance as a function of a normalized index. The left number in the legend gives the time constant used for decimating, which results in an array with a length given by the right number in the legend.

and has units of square root of the number of photons in the filter bandwidth (460kHz).

7.2.4 Analyzing the balanced homodyne images

In this subsection we describe the analysis procedure in the experiments where the goal is to measure the spatial mode of the outgoing SB, using balanced homodyne imaging. The analysis is composed of three steeps: centering the two ports such that we can faithfully subtract/add them, analyze the images to extract the field quadrature, and to average the square of the signal over many realizations. The last step is important as the homodyne signal is sensitive to the phase difference between the LO and the SB which has a random value in each realization.

The camera has no fast gating option, therefore to get time resolution we have gated the LO pulse. In order to minimize the influence of the DL leak light, we choose the LO pulse duration to be one cycle of the LO-DL frequency difference. In addition throughout this section we explicitly assume a 50/50 beam splitter, i.e. $|r| = |t| = 1/\sqrt{2}$.

We have imaged the outgoing SB at two different DL leak intensities. In the chronological first batch the DL leak was measurable and we needed to subtract the contribution of it. In the second experimental batch the input polarization was carefully optimized and the leak light from the DL fell below the detection sensitivity. Therefore for this experimental batch the DL removal step was left out of the analysis to avoid unnecessary additional noise.

Centering the images

The imaging setup is done such that we image both output ports of the beam-splitter with the CCD camera. Then we cut from the single image the transmitted

and reflected ports of the PBS. For the homodyne we need to faithfully subtract the two images pixel by pixel; for this we require to know the center of the atomic cloud on each of the two images. Utilizing the fact that when sending only the DL (with fast rise time) we measure SB photons that come from the atomic sample and have its integrated density profile. This can be understood such that during the turn on and off of the DL it also has frequency components that satisfy the two photon resonance condition and thus we can measure the Raman transfer. More details about this effect are given in sections 10.1 and 10.2. From the measured sample density profile we find the center of the cloud and can now center the two port such that they have the same position of the cloud to sub pixel resolution. Note that due to modulating the cloud position along the gravitational axis (see chapter 9) along that axis, we get a common mode deviation of two pixels (that corresponds to 2μm) in the cloud position.

Evaluating the mean SB field from the homodyne images

We start by re-writing Eq. 7.5 for the imaging case:

$$S_{im}(x,y) = \int_0^T dt \left(I_t(x,y) - I_r(x,y) \right) = \left(|t|^2 - |r|^2 \right) \int_0^T dt \left(\rho_{SB}^2 + \rho_{DL}^2 + \rho_{LO}^2 \right) +$$

$$2\rho_{LO} \int_0^T dt \rho_{SB} \sin\left(\Delta\phi_{LO-SB} \right) - 2\rho_{LO} \int_0^T dt \rho_{DL} \sin\left(\Delta\omega_{LO-DL}t - \Delta\phi_{LO-DL} \right) \tag{7.14}$$

assuming that the LO pulse is constant over the integration time and sets the integration limits, which is valid due to the fast rise time and fall time of the pulse[10]. We set the integration time, $T = 2\pi/\Delta\omega_{LO-DL} \cong 1\mu$s, to be one cycle such that we minimize the contribution of the DL leak light.

Here in each realization we have taken four different images:

1. *at* - performing the full memory sequence with the atoms (S_{at}).

2. *bg* - performing the full memory sequence without the atoms, i.e. a background pulse (S_{bg}).

3. *LO* - measuring the LO light pulse (L_{LO}).

4. *bi* - measuring the bias count level without any light pulses.

From the raw images we subtract the bias images[11] then subtract the two ports of the PBS to get the homodyne image as given by Eq. 7.14. Next we are interested in removing the measured leak light, i.e. the first term on the right hand side of Eq. 7.14 that comes from a small misbalancing of the beam splitter. This term has two components to it, first we subtract the LO light that is directly measured. In order to subtract the DL and SB leak light we have taken many (~ 20) realizations without the LO, in which we only measure this contribution $\langle L_{DL,SB} \rangle$ and subtract that as well. We note that in one of the experimental configurations this leak light was not detectable, i.e. $\langle L_{DL,SB} \rangle = 0$.

We divide the signal by twice the square root of the LO to get,

$$\bar{S}_{im}(x,y) = \frac{S_{im} - L_{LO} - \langle L_{DL,SB} \rangle}{2\rho_{LO}\sqrt{T}} =$$

$$\int_0^T dt \rho_{SB} \sin \Delta\phi_{LO-SB} - \int_0^T dt \rho_{DL} \sin\left(\Delta\omega_{LO-DL}t - \Delta\phi_{LO-DL} \right) \tag{7.15}$$

---

[10]The rise time is 40ns out of a pulse of 1μs.

[11]We note that these picture are homogeneous and are at the read background level.

the contribution of the last term on the right hand side is negligible as we set the LO pulse time to integrate over a full cycle. Even though there is the additional term that comes from the wrong polarization of the DL, that was motivated above and discussed in details in section 10.2. This term has the same polarization as the SB, thus the analyzed signal for each realization is:

$$\bar{S}_{im}(x,y) = \int_0^T dt \rho_{SB} \sin \Delta\phi_{LO-SB} + \int_0^T dt \rho_{wp} \sin \Delta\phi_{LO-wp} \qquad (7.16)$$

Averaging the signal over many realizations

Since in each experimental realization the phase ϕ_{LO-SB} is different and unknown we cannot extract the electric field amplitude from a single realization. In order to overcome this, we have repeated each experiment more than 20 times using the same conditions, and square the results then averaged all the different realizations.

For brevity we start by evaluating,

$$\left\langle \left(\int_0^T dt \rho \sin \Delta\phi \right)^2 \right\rangle_r = \left\langle \int_0^T dt \int_0^T dt' \rho(t)\rho(t') \sin \Delta\phi(t) \sin \Delta\phi(t') \right\rangle_r =$$

$$\left\langle \frac{1}{2} \int_0^T dt \int_0^T dt' \rho(t)\rho(t') \left\{ \cos\left[\Delta\phi(t) - \Delta\phi(t')\right] - \cos\left[\Delta\phi(t) + \Delta\phi(t')\right] \right\} \right\rangle_r =$$

$$\frac{1}{2} \left\langle \int_0^T dt \int_0^T dt' \rho(t)\rho(t') \cos\left[\phi(t) - \phi(t')\right] \right\rangle_r \qquad (7.17)$$

here in the last step we dropped the contribution of the cosine with the addition of the phase difference, as this term goes to zero in the limit of infinite number of realizations. Here we assume that 20 realizations is sufficient. In addition we have dropped the phase difference notation (Δ), this comes from the fact that the LO phase is constant through the $1\mu s$ pulse. Thus we find

$$\left\langle \left(\int_0^T dt \rho \sin \Delta\phi \right)^2 \right\rangle_r =$$

$$\frac{1}{2} \left\langle \left(\int_0^T dt \rho(t) \cos \phi(t) \right)^2 \right\rangle_r + \frac{1}{2} \left\langle \left(\int_0^T dt \rho(t) \sin \phi(t) \right)^2 \right\rangle_r \qquad (7.18)$$

Now we can write the full (not so nice) expression for the signal

$$\left\langle \bar{S}_{im}(x,y)^2 \right\rangle_r =$$

$$\frac{1}{2} \left\langle \left(\int_0^T dt \rho_{SB} \cos \phi_{SB} \right)^2 \right\rangle_r + \frac{1}{2} \left\langle \left(\int_0^T dt \rho_{SB} \sin \phi_{SB} \right)^2 \right\rangle_r +$$

$$\frac{1}{2} \left\langle \left(\int_0^T dt \rho_{wp} \cos \phi_{wp} \right)^2 \right\rangle_r + \frac{1}{2} \left\langle \left(\int_0^T dt \rho_{wp} \sin \phi_{wp} \right)^2 \right\rangle_r +$$

$$\frac{1}{2} \left\langle \int_0^T dt \int_0^T dt' \rho_{SB}(t)\rho_{wp}(t') \cos\left[\phi_{SB}(t) - \phi_{wp}(t')\right] \right\rangle_r \qquad (7.19)$$

Later in the text we measure this signal in two different experimental conditions, first when $\rho_{wp} = 0$ and second when $\rho_{wp} \cong \rho_{SB}$. When interpreting the first case care should be taken, as we measure the square average of two orthogonal electric field quadratures. Which is not the mean photon number, but only a
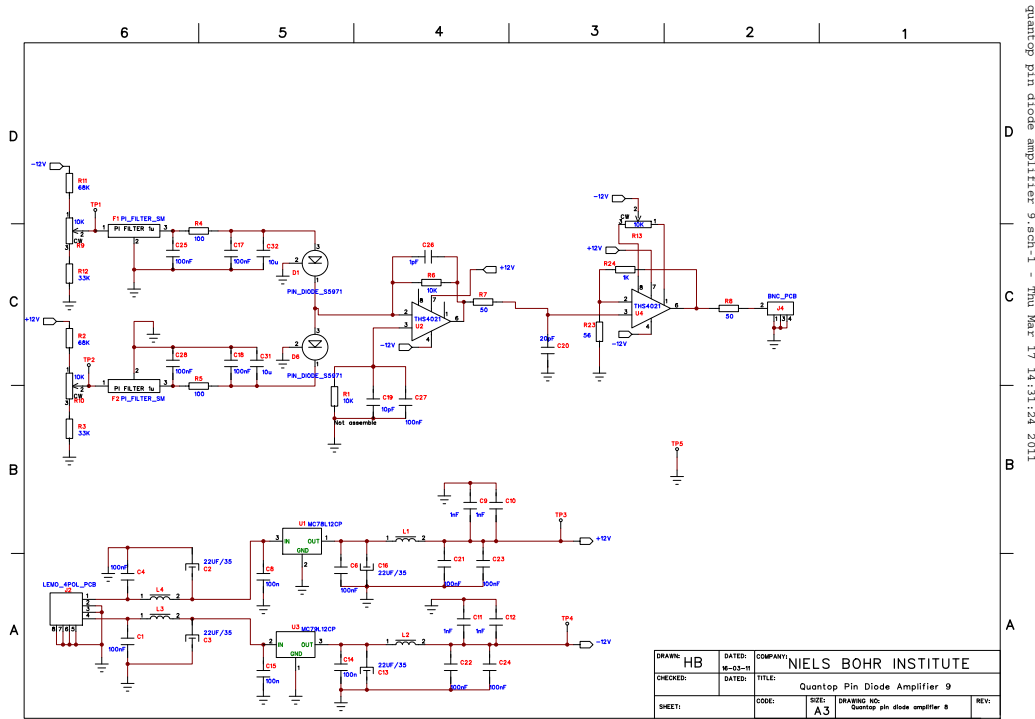
Figure 7.5: The balanced detector schematic.

lower boundary of it. This is since the SB phase can (and do) significantly change during the LO pulse. When measuring the signal in the second condition we also measure the mean contribution without any SB sent, i.e. setting $\rho_{SB} = 0$, and subtract that result. Here we are sensitive to the interference term (last line in Eq. 7.19), and in section 14.2 we further discus this interference term. We note that if the two phases are independent the interference term should drop out when averaging over many different realizations.

7.3   The DC balanced detectors

Here we present the design and characterization of the of the balanced detector that we used. The design for measuring the current difference from the diodes is based on [Hobbs09], and the voltage filtering is based on the work done by [Windpassinger09]. The actual circuit schematic is given in Fig. 7.5. Here in the first stage we convert the current difference to voltage, then in the second stage we amplify voltage by about 20. Note that we have also tried a configuration with an additional amplification stage but that introduces oscillations.

We have measured the detector bandwidth using a fast pulse and compare the $10 - 90$ rise time measured by our detector to a 150MHz Thorlabs detector. Here we have measured with both detectors a rise time of 20ns that corresponds to a bandwidth above $BW = 0.35/\Delta t_{10-90} = 17$MHz. This explicitly assumes that the gain profile is the same as an RC-low pass filter[12]. Note that since both detector measure the same rise time we can only conclude here that our detector bandwidth is higher or equal to 17MHz.

Next we turn to characterize the detector noise behavior for this we send a 1μs pulse to a balanced detector. We evaluate the signal using a two sided mean,

---

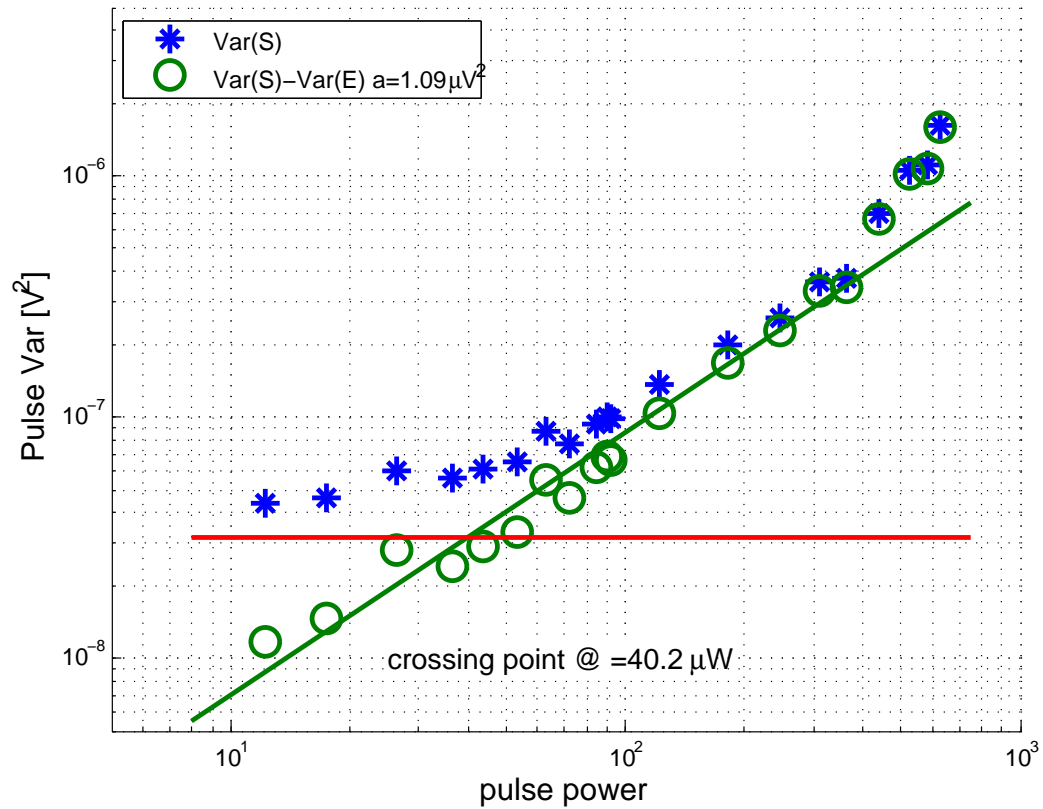[12]A good review is given in the wikipedia page under "rise time".

Figure 7.6: The balanced detector noise profile, as a function of a 1μs pulse at different powers. The blue stars are the measured variance; The green circles are the variance after removing the electronic level. The red line shows the electronic noise level.

to remove noise contribution at zero frequency [Windpassinger09]. For each pulse power we have repeated the measurement about 400 times, and show the resulted variance in Fig. 7.6. The red line shows the electronic noise level, the blue shows the measured variance, and the green circles show the variance subtracted the electronic noise. At the crossing point between the electronic noise level (red line) and the signal subtracted the electronic noise (green circles), the electronic noise contribution is equal to the light (LO) shot noise. For our detector this is at $P = 40\mu$W.

From Fig. 7.6 we can see that the classical noise start to overcome that shot noise at higher powers[13] (above 400μW). This means that for this detector a good working point is $300 - 400\mu$W, as the noise is dominated by light shot noise and it is with the biggest amplification before saturating the detector.

---

[13]This is an indication for saturating the detectors.

CHAPTER 8

Rabi oscillations

As a first test to the detection setup we have started with a Rabi oscillation experiment. The idea is to start testing the heterodyne detection scheme using a system with relativly big signals and less sensitive to misalignment.

Rabi oscillations occur when a two level system is coherently driven between the two states via an external field [Garrison08]. In our system the effective two level system is between two Zeeman sublevels (m_f) in a single hyperfine ground state ($F_0 = 1$), $|m_f = -1\rangle \langle m_f = -1|$ and $|m_f = +1\rangle \langle m_f = +1|$. Unlike in a classical Rabi oscillation we couple the two levels with a two photon transition which has, using the memory notation: the signal beam (SB) that couple the initially occupied level to a virtual level and the drive light (DL) that couple the second ground level to the same virtual level. Here the virtual level is red detuned by $\Delta = -200$MHz from the electronically excited level. The detuning Δ is called the single photon detuning. The electronically excited level can be adiabatically eliminated [Bergmann98]. Note that here we are using the same two level system as we will use in the memory experiment (see inset of Fig. 7.1). The main difference to the memory experiment is that here we are interested in coherently transferring all the atoms between the two ground levels, while in the memory experiments we are interested in transferring a small fraction (one percent or less). The Rabi oscillations in these experiments can be detected either by directly measuring the photons or by measuring the atoms in the trapped state[1] ($|-1\rangle \langle -1|$). As we are interested in testing the heterodyne detection scheme we only focused on the light detection. For each atom transferred from the ground level ($|-1\rangle \langle -1|$) to the Stokes level ($|+1\rangle \langle +1|$) we expect an absorption of a SB photon and emission of a DL photon. Thus the slowly varying envelope of the electric field of the SB and of the DL will oscillate with a $\pi/2$ phase shift between them. Note that the spatial mode shape of the emitted/absorbed photons will be determined by the atomic density spatial profile and in general will be different from the incoming spatial light mode. This is important for our heterodyne detection specifically on the DL channel.

The actual oscillation frequency is a function of both the resonant Rabi frequency (Ω_{R0}) and of the two photon detuning ($\delta - \delta_0$). We define the two photon detuning as the DL detuning difference from the virtual level given by the SB. Here $\hbar\delta_0$ is the energy difference between the two ground state levels. Using this notation

---

[1]We can do this by stopping the process and just hold the atoms for enough time such that all the atoms in the $|+1\rangle \langle +1|$ will be accelerated out of the trap.
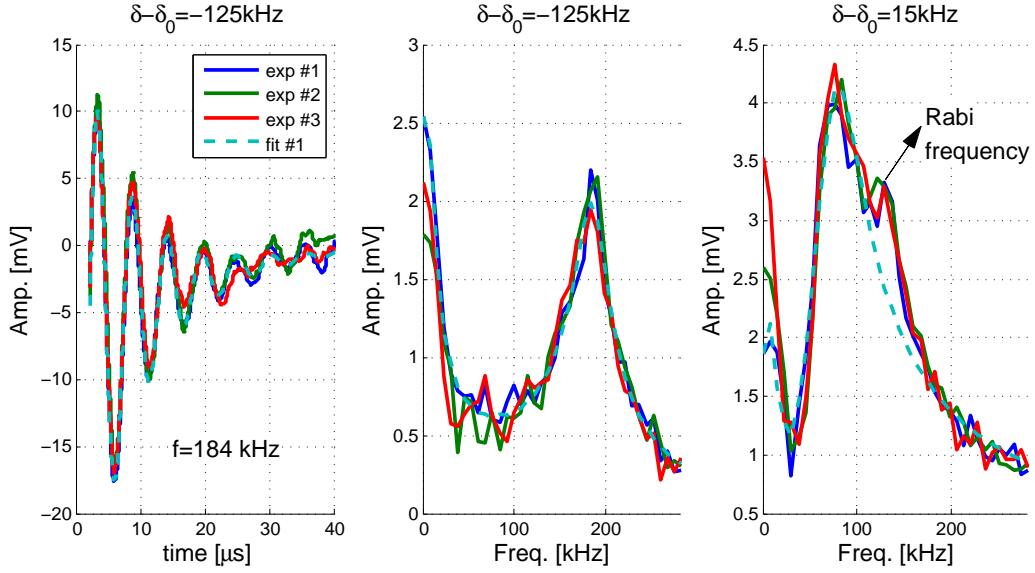
Figure 8.1: The SB amplitude analyzed as explained in the main text. Left: The time evolution at a two photon detuning of 125kHz, with fitted frequency of 184kHz. Middle: The Fourier transform as function of frequency at two photon detuning of 125kHz. Right: The Fourier transform as function of frequency at two photon detuning of −15kHz. The dashed light blue line is the fitted curve to exp #1 by Eq. 8.4.

we can now write the effective Rabi oscillation frequency as,

$$\Omega_R = \sqrt{|\Omega_{R0}|^2 + (\delta - \delta_0)^2} \tag{8.1}$$

$$\Omega_{R0} = \frac{\Omega_{SB}\Omega_{DL}^*}{\Delta} \tag{8.2}$$

$$\Omega_{xx} = \frac{\langle \mathbf{d} \cdot \mathbf{E}_{xx} \rangle}{\hbar} = \frac{\langle \mathbf{d} \rangle}{\hbar}\sqrt{\frac{I}{2\epsilon_0 c}} \tag{8.3}$$

where $\langle \mathbf{d} \rangle$ is the dipole element for the given transition, $\mathbf{E}_{xx}$ is the electric field of a given beam (xx), I is the beam intensity, $\hbar$ is the Planck's constant divided by 2π, c is the speed of light, and ϵ_0 is the vacuum permittivity.

Here we have measured the Rabi oscillations for different two photon detuning $(\delta - \delta_0)$ over a time span much longer than the coherence time. We fit to the end part of the signals a linear fit, corresponding to times $t \geq 40\mu s$. The results of the SB amplitude at $\delta - \delta_0 = -125$kHz are given in Fig. 8.1-left. In this plot we show three different realizations and in the dashed light blue a fit to one realization. For the fit we use the following functiona,

$$f(t) = A_s e^{-t/\tau_s} + A_r e^{-t/\tau_r}\sin\left(\Omega_R t + \phi\right) + B \tag{8.4}$$

where τ_s (A_s) is the optical pumping decay time (amplitude) constant, and τ_r (A_r) is the Rabi coherence decay time (amplitude) constant, B is the offset, Ω_R is the effective Rabi frequency and ϕ is the initial phase. To the experimental data and to the fit we have performed Fourier transforms for all different two photon detunings; two examples are given in Fig. 8.1-middle and right. From the middle plot at a "big" two photon detuning we can see that the fit and the experiments are in good agreement for finding the Rabi frequency. On the other hand in the right plot of Fig. 8.1 we can see that, at a "low" two photon detuning, there are two distinct frequency component: one which is dominant at "low" frequency and a second at a higher frequency with a smaller amplitude . The
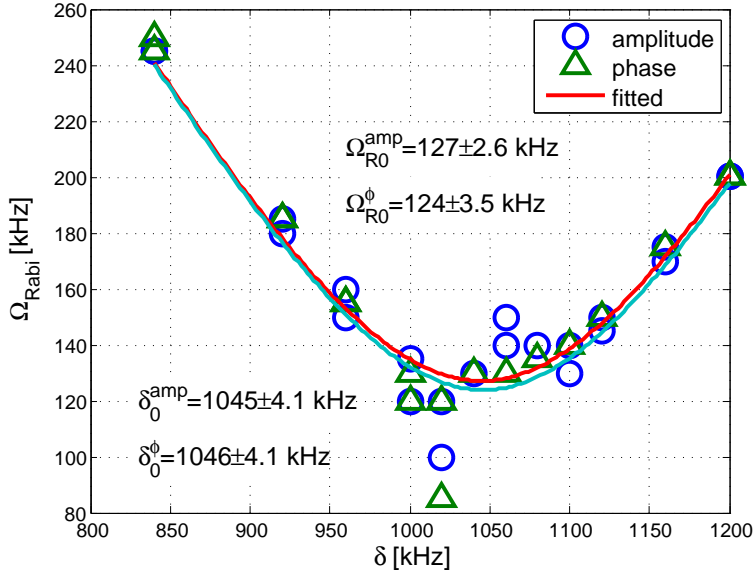
Figure 8.2: The Rabi frequency as measured from the Fourier transform of the signals as function of the two photon detuning. The blue circles indicates the points from the amplitude and the green triangles the points from the phase measurements. The full curves are the best fit for the data.

two frequencies in the spectrum appear only close to the two photon resonance, where the smaller amplitude (at higher frequency) corresponds to the expected effective Rabi frequency. Possible reasons for this could come from the radial change in the sample OD and the change in the beam intensity due to depletion. That said we do not have, at present, a good model explaining the emergence of the extra frequency components when driving the atoms close to the two-photon resonance.

For each two photon detuning we have extracted the Rabi frequency, as described above, and fitted to the data the functional given in Eq. 8.1. The results are given in Fig. 8.2, and from the fit we find a resonant Rabi frequency of $\Omega_{R0} = 2\pi \times 126 \pm 5\text{kHz}$.

The above experiments were done with total atom numbers of 1.3×10^6, at temperature of 430nK which is 1.6 times above the critical temperature, with radial cloud width of $\sigma_\perp = 19.6\mu\text{m}$ ($1/e^2$). To estimate the expected resonant Rabi frequency we use Eq. 8.2. No correction is needed to the estimated DL peak Rabi frequency due to the large beam waist at the atoms compared to the atomic radial width. But for the SB we need to average over the radial direction as the SB waist is comparable to the atomic cloud. Using the cloud density (n),

$$p = 2\pi \int_0^\infty n(\rho)e^{-\rho^2/w^2}\rho d\rho = \left(1 + \sigma_\perp^2/(2w^2)\right)^{-1} \tag{8.5}$$

$$n(\rho) = 2/\left(\pi\sigma_\perp^2\right)e^{-2\rho^2/\sigma_\perp^2} \tag{8.6}$$

with ρ the radial coordinate, p the radial average normalized to the peak prefactor for the SB calculated effective Rabi frequency. For the beam and sample parameters of the experiment $p = 0.72$. Using this and the experimental data we estimate the resonance Rabi frequency to be 130kHz which fits the measured value.

Magnetic feedback – canceling the gravitational sag

In this chapter we discuss the effects of the gravitational potential on the magnetic trap. While the magnetic trap potential is fully symmetric once the gravitational potential is added the symmetry is broken. The actual effect of the gravitational potential is to pull the atoms vertically downwards away from the magnetic field minimum. Here we dynamically change the vertical magnetic field thus shifting the magnetic field minimum without allowing the atoms time to move to the new trap minimum. This operation restores the symmetry of the trap.

When changing the position of the magnetic trap minimum the atoms will start sloshing around the new trap minimum. The sloshing time is given by the radial trap frequency $\omega_\perp$ which is not changed as we apply a homogeneous magnetic field. Therefore we want to change the magnetic field faster than $2\pi/\omega_\perp = 10$ms, such that the atoms will not start sloshing. On the other hand we want to change the magnetic field slow with respect to the Larmor precession frequency ($\omega_B/2\pi$). This ensures that the atoms total angular momentum will not start precessing around the new magnetic field direction. These two requirements means that we would like to change the trap minimum in a time scale, $10\text{ms} \cong 2\pi/\omega_\perp \gg T \gg 2\pi/\omega_B \cong 2\mu\text{s}$.

9.1 Canceling the effect of the gravitational potential

We start by writing the total potential energy of an atom in the presence of the magnetic trap and gravity

$$V(\mathbf{r}) = \mu B_0 + \frac{1}{2}M\omega_\perp^2\left(x^2 + y^2\right) + \frac{1}{2}M\omega_z^2 z^2 + Mgx =$$
$$\mu B_0 - M\frac{g^2}{2\omega_\perp^2} + \frac{1}{2}M\omega_\perp^2\left(\tilde{x}^2 + y^2\right) + \frac{1}{2}M\omega_z^2 z^2 \qquad (9.1)$$

where μ is the magnetic moment[1], M is the rubidium 87 mass, $\omega_\perp$ and ω_z are the trap frequencies, B_0 is a constant magnetic field, g is the gravitational acceleration constant, and $\mathbf{r} = (x, y, z)$ is the position with the gravity pointing along the vertical $\hat{x}$ direction and the light propagates along the $\hat{z}$ axis. In the second line of Eq. 9.1 we have used $\tilde{x} = x + g/\omega_\perp^2$, which directly shows the gravitational sag. Note that the gravitation potential also effectively modifies the value of the

---

[1]The magnetic moment is $\mu = m_f g_f \mu_B$, with m_f is the Zeeman sublevel quantum number, g_f is the Landé g-factor, and μ_B is Bohr magnetron constant.
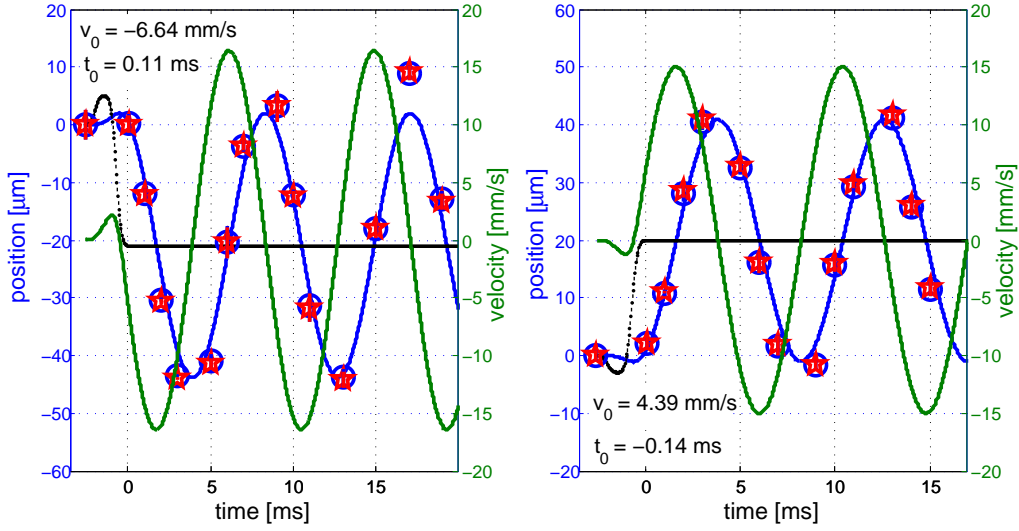
Figure 9.1: Here we show the atoms measured position (red stars and blue circles) as a function of time, after changing the trap center as indicated in the black line. The blue line is the expected cloud position (left axis) and in the greed line the expected cloud velocity (right axis). Left: changing the trap center to -20μm, and right: changing the trap center to $+20\mu$m.

constant magnetic field. For our experimental parameters the gravitational sag is $g/\omega_\perp^2 = 19\mu$m and the effective constant modification to the total magnetic field is $Mg^2/(2h\omega_\perp^2) = 20$kHz with h is the Planck's constant.

Here we move the trap center by changing the magnetic field along the gravitation direction. During this time the atomic internal state follows adiabatically the change in the magnetic field without precessing, while the atoms start sloshing around the new trap center. We model the sloshing movement of the atoms by solving the time evolution of a single atom in a harmonic potential around the trap center (x_c) set at time t_0. Thus the atoms position and velocity for $t \geq t_0$ is

$$x(t) = A\cos\omega_\perp t + B\sin\omega_\perp t \tag{9.2}$$
$$v(t) = -\omega A\sin\omega_\perp t + \omega B\cos\omega_\perp t \tag{9.3}$$
$$x(t) \equiv pos(t) - x_c(t_0) \tag{9.4}$$

where A and B are constants to match the initial condition from the previous step, $\omega_\perp$ is the trap radial frequency, and pos is the actual atomic position. We calibrate x_c to the change in the vertical offset field by slowly varying the magnetic field and measuring the change of the equilibrium position.

We measure the cloud position by absorbtion imaging of the atoms using the DL as the probe light along the long axis of the cloud, such that we can see the movement along the vertical axis. Utilizing the strong transition ($|F_0 = 1, m_f = -1\rangle \leftrightarrow |F = 2, m_f = -2\rangle$) and the big waist of 140μm of the DL, allows to measure large changes in the cloud position. In our imaging system we have a magnification such that each pixel is equivalent to one micrometer. Even though our imaging resolution is limited to 3.5μm for each experimental realization we find the atomic center to better than a pixel, by fitting the cloud density profile. The actual position resolution is limited by the shot-to-shot fluctuations that are 2μm along the vertical axis and 0.2μm along the other direction. We observe that the additional fluctuations along the vertical axis are due to the magnetic feedback.

We verify this by measuring the cloud position without the magnetic feedback and find the same statistical error of 0.2μm in the cloud position along both axes.

Since our servo-loop is not fast enough to change the trap center by the needed amount (19μm) in less than 1ms, we have designed a more elaborate temporal trajectory of the magnetic field minimum such that the atoms will stay at the same place as the trap center is moved to its new hight. The position/velocity profile is given in Fig. 9.1 for both directions. The black dotted line shows the programmed trap center that the servo-loop follows, the red stars and blue circles indicates the measured atoms position, and the blue (green) line indicates the calculated position (velocity) of the atoms using the above harmonic model. From Fig. 9.1 we can see good agreement between the model and the measured atom position. We note that in the reminder of the thesis all of the experiments are done using this pulse and are at time $t = 0$ in the plot, i.e. when the trap center is at -19μm and the atoms are still at position 0μm.

9.2 Properties of the magnetic servo-loop

In this section we summarize the details of the servo-loop used to change the trap minimum center position. It is designed to stabilize the magnetic field to below 1mGauss while holding the atoms in a dipole trap but due to time constraints the dipole trap was not realized. The basic ingredients [Bechhoefer05] for the servo-loop are: Controlling the magnetic field, Measuring the magnetic field, and the Feedback circuitry. In the following subsection we summarize the performance of each of these ingredients and in appendix G we give the full details.

Controlling the magnetic field

The magnetic field at the cloud position is controlled by three sets of Helmholtz coils, that were build to provide a constant homogeneous magnetic field. Therefore they are big with a high number of windings, which is good for having good optical access. The coils have a relatively high inductance of $16 - 25$mH and a DC resistance of $12 - 16\Omega$. With this combination of parameters the inductance starts to dominate the coil impedance already at low frequencies ($f > 250$Hz). This requires a careful design of the current supply for the coils to avoid oscillation of the servo loop. To drive the coils we have built a current controller that would allow changing the current through the coils without inducing oscillations. Here we chose a modified push-pull configuration for the current driver controller scheme, which is described in detailed in appendix G.1.

The gain phase performance of the coils with the current controller were measured. We find that the coils peak gain is at about 250Hz and decays to zero at frequencies above 700Hz, and the phase delay is changing by 90 degrees at 250Hz.

Measuring the magnetic field

We have chosen to measure the magnetic field using a commercial sensor[2], based on a metallic strap that changes its resistivity due to an external magnetic field. This magnetoresistive sensor is made from a nickel-iron (Permalloy) thin film deposited on a silicon wafer. The variation in the resistance is measured using a Wheatstone bridge, i.e. $\Delta R/R$.

The range of the sensor is ± 2Gauss and it has a resolution of 50μGauss (and a second detector with 150μGauss) which corresponds to 50μV (and 150μV).

---

[2]HMC1001 and HMC1002.

The bandwidth of the sensor is 150kHz with no appreciable phase delay up till 10kHz and 90 degrees phase delay at 100kHz.

The magnetic servo-loop

We have realized a proportional integrate differential (PID) type feedback circuit. The circuit can either be controlled externally or internally[3], with an additional internally controlled feed forward. We use the combination of internal and external control of the circuit to slowly move the magnetic field from the initial value to the external control value. This prevents an initial jump in the magnetic field, and allows a small error in the initial set value. To characterize the feedback performance we have measured the Bode plot for the amplitude and phase of the feedback. We find a bandwidth (gain bigger than 0.5) higher than 3kHz, with no appreciable phase delay for frequencies below 2kHz for all axes.

Details of the implementation and characterization are given in appendix G.

---

[3]By using a micro-processor ATMEGA-168PA.

Characterizing the setup performance

In the previous chapters 7-9 we have: introduced the memory experimental setup, how we have tested the heterodyne detection, and how we cancel the gravitational sag. In this chapter we go over the performance and sensitivity of the memory apparatus.

We start by introducing the raw signals after the lockin analysis, in section 10.1. In section 10.2, we go over the optimization of the drive light (DL) input polarization. In section 10.3 we optimize the timing of the signal beam (SB), to minimize retrieval of SB photons during the write stage.

We finish with section 10.4 examining the effect of optical pumping, due to the DL power, from the populated ground state $|F_0 = 1, m_f = -1\rangle$ into the hyperfine ground state $|F_0 = 2, m_f = -2\rangle$ and $|F_0 = 2, m_f = -1\rangle$ with F_0 is the hyperfine ground state quantum number, and m_f is the Zeeman sublevel quantum number.

10.1   The detected signals

Here we examine the signal for a single realization of the memory experiment. In Fig. 10.1 we present the time evolution of the SB signal after evaluating the NNS (left axis) using Eq. 7.13. The green dashed line shows the time evolution of the DL (normalized to the LO power) on the right axis. The first pulse indicates the writing stage with a duration of about $5\mu s$, then for a duration of $6\mu s$ we turn the DL off, which is the storage time. During the retrieval (read) stage we turn on the DL for a relatively long time duration of about $25\mu s$. Here, the DL signal is not constant and is evolving with time, we attribute this to optical pumping and the change in the DL beam shape (DL-LO visibility) due to different atomic conditions (index of refraction). The SB signal is given in the blue lines, were the dashed line indicates the input signal[1] and the full line indicates the output signal[2].

When examining the left plot of Fig. 10.1 we can see that about 10% of the SB photons leak through the atomic sample already during the writing stage. In the retrieval step ($t \geq 10\mu s$) about 10% of the photons sent are retrieved from the sample.

The two plots of Fig. 10.1 present experiments done at two different conditions. On the left (right) the sample OD is 170 (120), the cloud statistical $1/e^2$ waist

---

[1]This is measured without atoms, and sometimes is referred to as the background signal.
[2]This is measured with atoms, and sometimes is referred to as the atom signal.
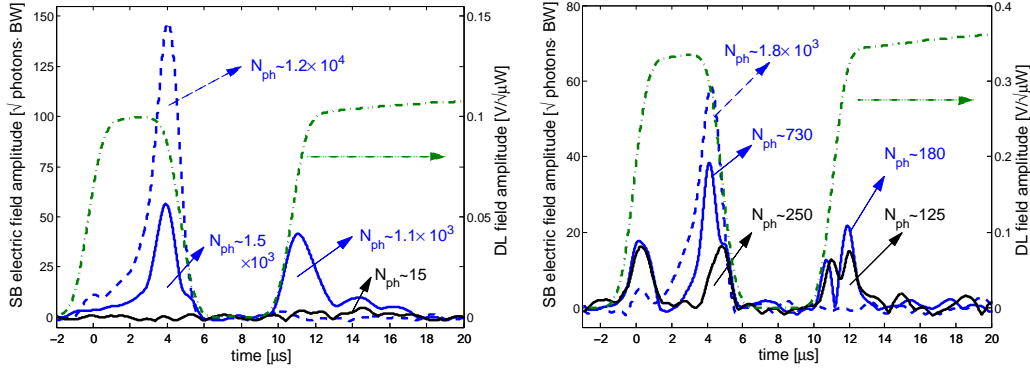
Figure 10.1: The measured amplitude (after the lockin procedure) of a single experimental realization of the SB and DL signals time evolution; the left (right) plot is without (with) wrong polarization contribution. Left axis: the SB input signal (dashed blue line); the SB out going signal (full blue line); the wrong polarization contribution (full black line). Right axis: DL signal (green dot-dashed line). The SB is converted to NNS as explained in section 7.2.3, with bandwidth of $BW = 460$kHz.

is 10.5μm (8μm), and the cloud reduced temperature is $T/T_c = 1.2$ (1.5). The total efficiency in the experiment presented in Fig. 10.1-left is $\sim 10\%$ and in the experiment in Fig. 10.1-right it is $\sim 3\%$. The different efficiencies can be attributed to the different sample OD.

Before we have mentioned that when running the memory experiment sequence without any incoming SB we measure SB photons leaving the atomic sample, this effect is shown as the full black line in Fig. 10.1. We attribute these photons to storage of DL photons, and discuss their origin in the next section. These retrieved photons are measured by the LS-heterodyne detector (see Fig. 7.1) and cannot be distinguished from the SB. We measure the contribution of the wrong polarization electric field by blocking the input SB and later subtract the average result from each measurement that contains both the SB and the wrong polarization contributions.

The experiments presented in this thesis are done in two different regimes: with a comparable contribution of the wrong polarization and of the SB as seen in Fig. 10.1-right, and with a negligible contribution of the wrong polarization as seen in Fig. 10.1-left. All the results using bucket detection presented in this thesis are with negligible contribution of the wrong polarization unless explicitly stated otherwise.

10.2   Purification of the input polarization

In this section we discuss in details how we optimized the input polarization of the DL and SB. Ideally the input polarization is purely circular in the frame defined by the orientation of the atoms (which coincides with the direction of the magnetic field). In the experimental situation there is a small mixture of the wrong circular polarization component to each of the beams and is modeled by a small mixture angle. One can think of this mixture angle as a rotation from the ideal case (containing only one circular component) to a mixture of the right circular polarization component and a small contribution of the wrong circular polarization. We control this angle with the $\lambda/4$ just before the atoms, see Fig. 7.1. Note that the output is nicely orthogonal to the input polarization regardless of the alignment of the input $\lambda/4$ as we optimize the alignment of the
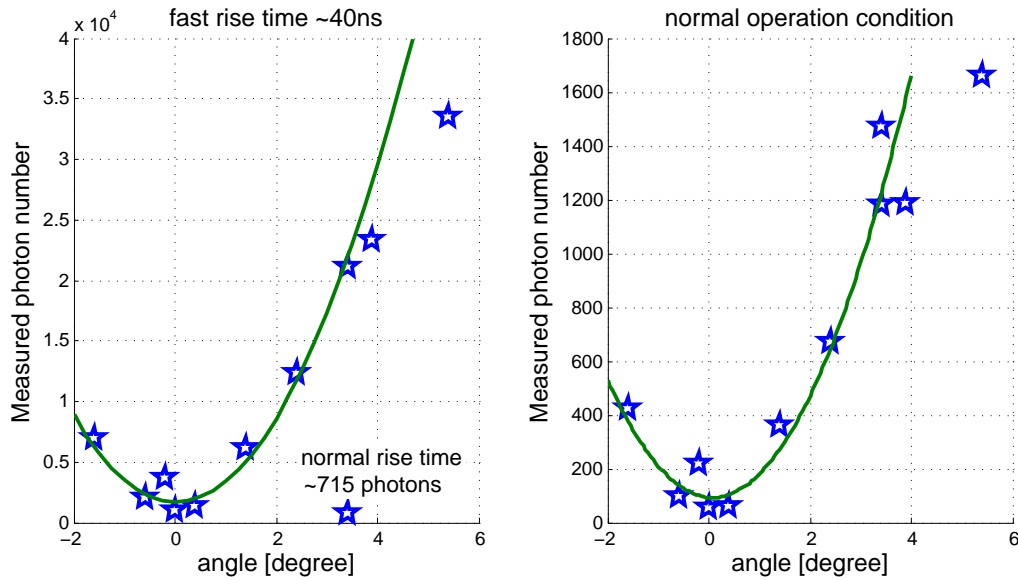
Figure 10.2: The number of measured wrong polarization photons as function of the input $\lambda/4$ wave plate angle. Left: the number of photons with a turn on DL pulse with a rise time of 40ns. Right: the number of photons with normal condition turning on and off the DL pulse.

$\lambda/4$ wave plate after the atoms to suppress the DL leak on the SB detection to better than six orders of magnitude.

The effect of the misalignment is that the DL has also a contribution of the wrong polarization (similar to the SB polarization), which is off from the two-photon resonance. Therefore it does not influence the experiment while the DL power is constant, but during turning on and off the DL it has also spectral components which are resonant on the two photon transition. This means, that even when there is no SB present we can store part of the DL wrong polarization photons. These wrong polarization photons are sensitive to the DL rise time and fall time, to the purity of the input polarization, and to the sample OD. The OD influences indirectly since for a higher OD the storage and retrieval are more efficient and therefore more evident.

In chapter 7 we have described how we initially coarsely aligned the input polarization. From this alignment procedure we have got a comparable contribution from the wrong polarization photons and from the SB photons, as shown in Fig. 10.1-right. To enhance the effect we have increased the DL rise time to 40ns, then by fine adjusting the input $\lambda/4$ wave plate we have minimized the contribution of the wrong polarization photons. The result of this procedure as function of the wave plate angle is given in Fig. 10.2.

The optimization has reduced the number of wrong polarization photons by a factor of about 25, reducing the number to below 50 photons for the maximum DL powers used in the memory experiments. This reduction has made the contribution of the wrong polarization photons negligible, as can be seen from the black line in Fig. 10.1-left.
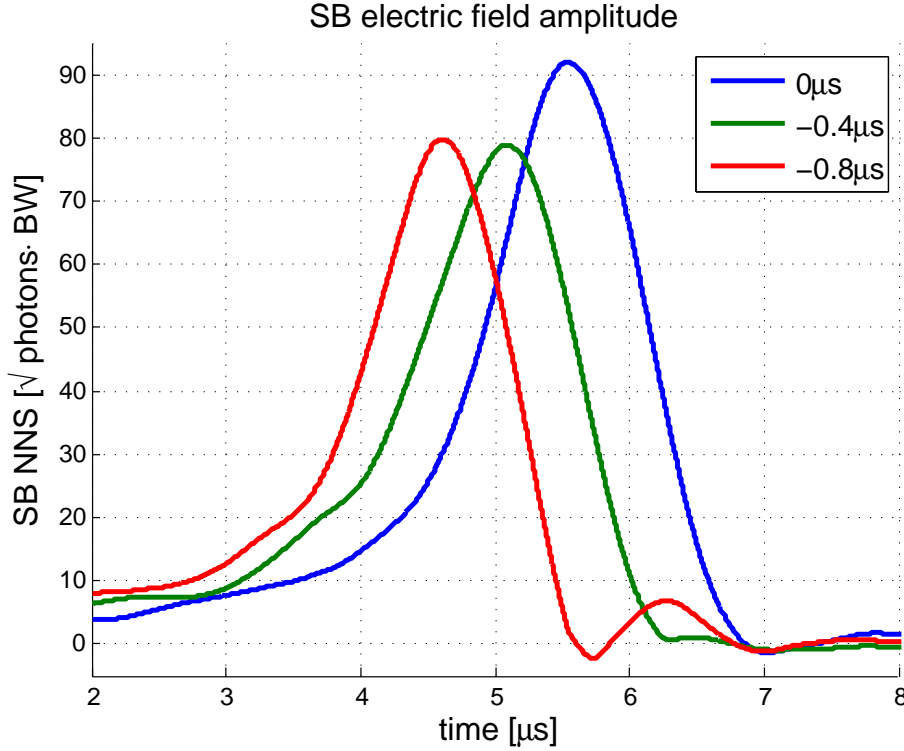
Figure 10.3: The SB electric field amplitude (NNS) in units of $\sqrt{\text{photons} \cdot BW}$ output during the writing step. The legend gives the SB pulse start time delay with respect to the DL.

10.3 The signal beam's timing

In this section we examine the sensitivity of the SB timing with respect to the DL. Here we find the right timing such that non of the stored SB photons will not be retrieved during the writing stage. This was done with a cloud OD of 25, and before we have optimized the DL input polarization. The results of the SB NNS at different time delays are given in Fig. 10.3, with the time delay defined between the peak SB pulse and the 50% DL fall time.

When examining the leak SB electric field amplitude in Fig. 10.3, we look for two things: the peak leak light (which we want to minimize), and whether light start to be retrieved. From the peak signals we see that the timing corresponding to the blue line (0μs) is sent too late as there is more leak light than in the other signals, which means that the DL is turned off too early. On the other hand, when examining the red curve we can see that the SB starts to be retrieved[3]. Here the green curve (-0.4μs) gives the best result.

These experiments were done at relatively low OD, but even when we have improved the OD to 120 the optimal timing has not changed. Only later, when we improved the OD even more to 180 we get a small contribution of retrieved light during the writing stage. Because this contribution is small we have not changed the timing. It should be noted that the given OD here are for similar reduced temperature (T/T_c).

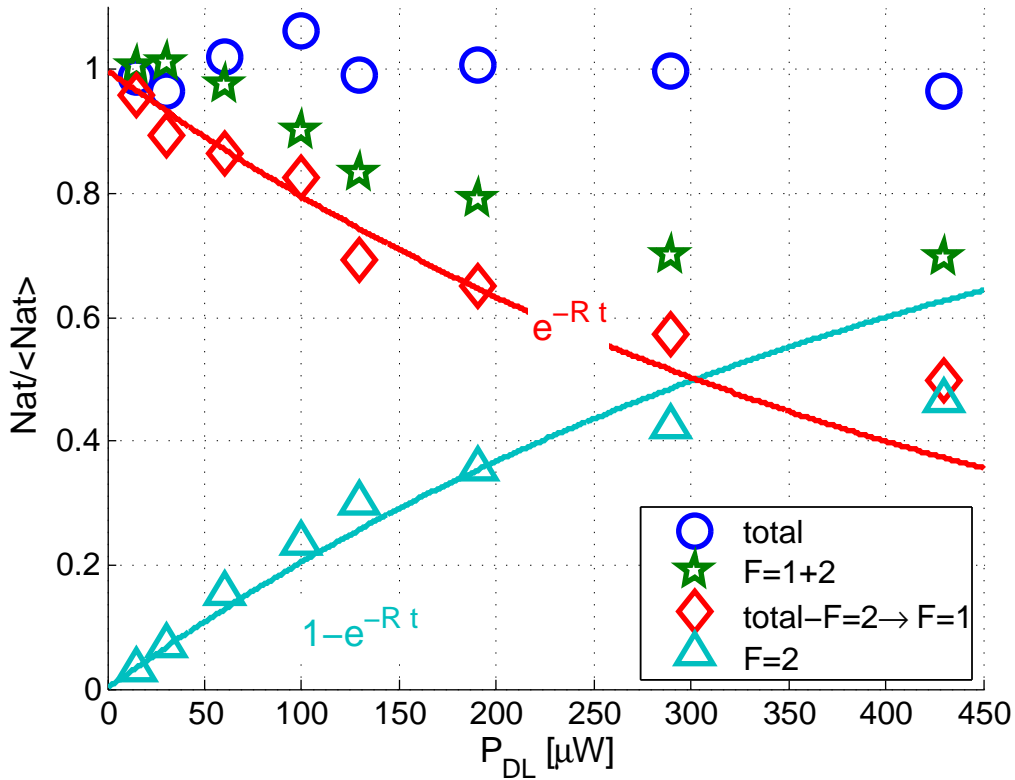
[3]The retrieved pulse starts at 5.75μs and ends at 7μs

Figure 10.4: The relative atom number as a function of the DL power for probing duration of 30μs. We normalize to the average total number of atoms measured without probing. The solid lines are curves evaluated using the formulas in their color on the plots.

10.4 Optical pumping into the $F_0 = 2$ hyperfine ground state

Up to now we have only considered our system as a Λ-system for which the DL beam sees an optically thin sample, i.e. the DL does not couple the populated ground level to any excited level. For ^{87}Rb atoms the DL does couple the populated ground level to an excited level $|F = 2, m_f = -2\rangle$ with F the excited hyperfine quantum number and m_f the Zeeman sublevel quantum number, with a detuning of $\Delta_p \cong -1000$MHz, for our case. Note that this detuning is five times bigger than the relevant one for the memory ($\Delta \cong -200$MHz).

The extra coupling of the DL causes an optical pumping of atoms from the ground level $|F_0 = 1, m_f = -1\rangle$ into the hyperfine levels $|F_0 = 2, m_f = -2\rangle$ and $|F_0 = 2, m_f = -1\rangle$ where F_0 is the ground level hyperfine quantum number. In this section we examine the effect of optical pumping in the memory experiments for different DL powers, for 30μs duration. We use the atomic absorption imaging to measure the total number of atoms in $F_0 = 1$ and $F_0 = 2$ and by blocking the imaging repump pulse we also measure only the atom number in $F_0 = 2$. Using these two measurements with a third reference measurement of the total number of atoms, we can find the fraction of atoms left in $F_0 = 1$ and fraction of atoms transferred into $F_0 = 2$. The result of these measured fractions are given in Fig. 10.4.

The optical pumping has an exponential behavior e^{-Rt} with R the scattering rate,

and $t = 30\mu$s the probing time. The scattering rate is calculated using,

$$R = \frac{\Gamma}{2} \frac{I}{I_{sat}} \frac{1}{1 + I/I_{sat} + \left(2\Delta_p/\Gamma\right)^2} CG^2,$$

$$(10.1)$$

where Γ is the natural line decay rate, Δ_p is the detuning, I_{sat} is the saturation intensity, I is the probe intensity, and CG is the Clebsch-Gordan coefficient. We use the known experimental parameters to evaluate R, plot the results in Fig. 10.4 and find good agreement between the scattering rate model and the experimental data for powers lower or equal to 200μW. For higher powers we find that we loose atoms and that the results do not fit the simple scattering model. This could be due to atoms scattering more than one time and get out of the image range and with low density such that it is below the detection resolution, or due to "high" density effects such as photoassociation.

The influence of optical pumping on the performance of the memory comes from depleting the ground state during the writing stage, and thus reducing the sample OD. Note that this means that actually this is a small effect even for the highest used DL power in which $40 - 50\%$ of the atoms are transferred into $F = 2$ since this is after both the writing and retrieval stage. Our writing stage is only 6μs therefore during the writing stage we expect only about 2% of the atoms to be optically pumped[4]. Besides this relatively small effect the transferred atoms do not influence the evolution of the experiments, since the light probe is 6.8GHz off resonance.

---

[4]This comes from $50^{6/30} \simeq 2\%$.

Theoretical description of the ensemble a multi-Level model

After describing the experimental setup and how the signals look like, we are also interested in a model to compare the experimental results to. Therefore in the next two chapters we take a sidetrack from the experimental results, and derive a model that describe our system and write a numerical simulation to evaluate the time evolution of the system. In this chapter we derive the effective Hamiltonian for the light-atom interaction, the interaction Hamiltonian for the atoms with an external magnetic field, and derive the coupled propagation equations for atoms and light. In chapter 12 we present our numerical simulation.

In the introduction to this part of the thesis, chapter 6, we have used a three level system in order to explain the memory. While a lot of the theoretical descriptions assumes a three level system [Gorshkov07a, Zeuthen11], the real system has more levels that could influence the evolution. When considering ^{87}Rb coupled to the D1-line light field a more appropriate system is a W-system with an extra ground state that atoms can only be pumped into but do not evolve in time than a Λ-system. In such a system the two extreme excited levels of the W-system are from $|F = 2\rangle$ and the center one is $|F = 1\rangle$, with F the excited hyperfine quantum level. From the two extra levels at $|F = 2\rangle$ the pumping into the extra ground state is achieved. The additional levels means that when solving such a system one needs a very fine numerical grid since the evolution equations contain terms oscillating at the hyperfine splitting frequency $\Delta_{hf} = 2\pi \times 815MHz$. This term is removed by adiabatically eliminate the excited state, since we are working off resonant $\Delta/\Gamma \gg 1$, where Δ is the detuning with respect to the excited level $F = 1$ and Γ is the natural level life width. For a system where all the excited levels are adiabatically eliminated we can write the effective Hamiltonian for all ground Zeeman sublevels, and thus get a more general system than the W-system. Therefore in this chapter we describe the more general case, and do not present the derivation of a W-system.

In section 11.1 we give the effective light-atom Hamiltonian using the irreducible tensor notation, and leave the derivation details to appendix D. The derivation of the Hamiltonian follows the work described in [Kupriyanov05]. Then in section 11.2 we write the atom-magnetic field interaction Hamiltonian. In section 11.3, we derive from the Heisenberg equation the coupled light atoms equations in time and space. Here we start with spherical coordinates, and then transfer the equations to cartesian coordinates. We end, in section 11.4, by reducing the three level system (8×8) set of equations to a two level system (3×3) set of equations, resulting in the off-resonant Raman memory case that

was also derived and analytically solved in [Mishina07]. We note here that while the Hamiltonian and propagation equations follows the work in [Kupriyanov05, Mishina07], here we have extended the propagation equations from a two level system to a three level system.

11.1   The light-atom Hamiltonian

In this section we sketch the derivation steps for an effective off resonant light-atom interaction. Assuming that only the dipole interaction is relevant, we utilize the rotating wave approximation (RWA), adiabatic elimination of all excited states, and that the evolution can be fully described by one hyperfine ground state[1].

Our goal is to write both the light-atom interaction Hamiltonian and the magnetic field Hamiltonian, for each there is a different natural quantization axis. For the light-atom it is natural to define the quantization axis along the light propagation, thus removing any π-polarization light component, while for the magnetic field interaction it is natural to define the quantization axis along the magnetic field direction[2]. Here we choose to define the quantization axis along the light propagation axis, thus simplifying the effective light-atom Hamiltonian and writing the atom-magnetic field interaction Hamiltonian with a general quntization direction. In general this complicates both the notation for the atomic initial condition and the propagation equations (by the addition of two more magnetic field components). Note, that we have designed our system such that both the light and the magnetic field direction will be aligned to each other. Due to the gravitational sag there is a small angle that we minimize, as described in chapter 10.

We start with the light-atom interaction Hamiltonian in the dipole approximation, $H_{int} = -\mathbf{d} \cdot \hat{\mathbf{E}}$, where $\mathbf{d}$ is the dipole moment operator operating as raising and lowering the atomic state, and $\hat{\mathbf{E}}$ is the electric field. We decompose the electric field for positive ($\hat{\mathbf{E}}^+$) and negative ($\hat{\mathbf{E}}^-$)frequency components [Garrison08]:

$$\hat{\mathbf{E}} = \hat{\mathbf{E}}^- + \hat{\mathbf{E}}^+ \tag{11.1}$$

$$H_{eff} = -\hat{E}_i^- \alpha_{i,j} \hat{E}_j^+ \tag{11.2}$$

After using the RWA and adiabatically eliminating all the excited states one get the description for the above effective light-atom interaction Hamiltonian (Eq. 11.2). With α is the atomic polarizibility (defined in appendix D.1) and is a function of the detuning. The subscripts i and j indicate cartesian coordinates and we invoke the Einstein sum rule. In the polarizibility definition we only describe light scattered in the forward direction. The steps to arrive to arrive at the effective Hamiltonian have been described several times in the literature. A good presentation can be found in [Kupriyanov05, Geremia06, Hammerer10] and was also shown in F. Kaminski Ph.D. thesis [Kaminski12b].

The mathematical steps transforming the effective Hamiltonian from Eq. 11.2 to a notation using the Stokes and collective spin operators are not well documented in [Kupriyanov05]. Therefore we describe the actual mathematical steps

---

[1]Here we also explicitly neglect any coherences between two hyperfine states. This is valid since our light couples two Zeeman sublevels and the two hyperfine levels are separated by 6.8GHz.

[2]It is natural to choose the magnetic field quantization axis since it simplifies the initial conditions. Specifically in our case, since the sample is prepared by evaporation cooling it will be in a pure $\left| F_0 = 1, m_f = -1 \right\rangle \left\langle F_0 = 1, m_f = -1 \right|$ state, with F_0 the ground hyperfine quantum number and m_f is the Zeeman sublevel quantum number.

in appendix D and give here a few intermediate points that give insight into the system.

The polarizibility tensor operator (defined by Eq. D.3) includes the different atomic coherences, i.e. $|F_0, m\rangle \langle F_0, m'|$ with F_0 the ground state hyperfine quantum number and m and m' the Zeeman sublevel quantum numbers. We can describe the coherence using the angular momentum algebra and decompose it into irreducible groups, where each irreducible group is closed with respect to spatial rotations. Specifically, we write the coherence using the irreducible tensor notation $\hat{T}_{K,Q}$ [Varshalovich88, Kupriyanov05]. Note that using this notation is useful since it allows us to distinguish between scalar ($K = 0$), vector ($K = 1$), and rank-2 tensor ($K = 2$) operators. From a closer investigation of Eq. 11.2 we can see that the left hand side is scalar (the Hamiltonian), and the right hand side contains two vectors each with total angular momentum one (the electric fields) therefore the polarizibility operator must be such that the combination of it and the two vectors will give a scalar. Which means that, already at this stage, we can expect that the end results will contain irreducible tensors with rank $K \leq 2$.

The irreducible tensor is defined as:

$$\hat{T}_{K,Q} = \sqrt{\frac{2K+1}{2F_0+1}} \sum_{m',m} C^{F_0,m'}_{F_0,m,K,Q} |F_0, m'\rangle \langle F_0, m| \qquad (11.3)$$

$$|F_0, m'\rangle \langle F_0, m| = \sum_{K,Q} \sqrt{\frac{2K+1}{2F_0+1}} C^{F_0,m'}_{F_0,m,K,Q} \hat{T}_{K,Q} \qquad (11.4)$$

where $C^{...}_{...}$ is the Clebsch-Gordan coefficient, and K and Q are two quantum numbers of the irreducible tensors. One can work with them using angular momentum theory as K corresponds to the total angular momentum and Q is the projection of the angular momentum.

We insert the above decomposition of the atomic density operator elements into the polarizibility and sum over all the different axis combinations. The result is polarizibilities that correlate either to no change in the angular momentum (α_{0+} given by Eq. D.26 and α_{0-} given by Eq. D.27) or to a change of two in the angular momentum (α_{2+} given by Eq. D.28 and α_{2-} given by Eq. D.29). Thus we get an effective Hamiltonian:

$$H_{eff} = -\frac{\hbar}{2} \sum_F \sum_{K=0}^2 \left(\tilde{\alpha}_{0+} \hat{\Xi}_0 + \tilde{\alpha}_{0-} \hat{\Xi}_\sigma \right) \hat{T}_{K,0} +$$
$$\frac{\hbar}{2} \sum_F \left(\sqrt{2} \tilde{\alpha}_{+2} \hat{\Xi}_- \hat{T}_{2,2} + \sqrt{2} \tilde{\alpha}_{-2} \hat{\Xi}_+ \hat{T}_{2,-2} \right) \qquad (11.5)$$

where $\hat{\Xi}$ are the Stokes parameters describing the photon flux ($1/s$) defined in appendix C, and F is the excited state hyperfine quantum number. Here we absorb additional common factors into the polarizibilities such that they are dimensionless and rewrite them as $\tilde{\alpha}$. Note that when examining the units here the irreducible tensor is dimensionless and the Hamiltonian is written for a single atom. To move to an ensemble of atoms we need to redefine the irreducible tensors, we do this in section 11.3 and discuss different possible ways to redefine the atomic coherence in appendix F.

From examining the above Hamiltonian one gets an insight about the different polarizibility terms. From the atoms "point of view" $\alpha_{0\pm}$ describe the light shift of the atomic levels: $K = 0$ is the scalar, $K = 1$ is the vector, and $K = 2$ is the tensor light shift. The $\alpha_{\pm 2}$ describe a Raman transfer between atomic levels with $\Delta m =$

± 2. From the light "point of view" $\alpha_{0,+}$ is correlated to the refractive index, $\alpha_{0,-}$ is the Faraday rotation term[3] also known as the circular birefringence, and $\alpha_{\pm 2}$ describe annihilation/creation of a circular photons (i.e. linear birefringence).

At this stage each of the polarizibilities explicitly sums over all possible Zeeman sublevels (ground and excited). When summing over the different sublevels we can use the symmetry of the Clebsch-Gordan coefficients to further simplify the polarizibility, which explicitly assumes degeneracy of all Zeeman sublevels. This assumption is valid only for small magnetic field amplitude. In our case we have a magnetic field of about one gauss that changes the ground Zeeman sublevel by about ± 0.7MHz which is negligible compared to the 200MHz detuning. Note that if a more correct description with respect to an external magnetic field is needed, this simplification should not be done.

Summing over all levels reduces to three polarizibilities α_0, α_1, and α_2, where the subscript indicates the total angular momentum change (see appendix D.4.1). Using this we get the following effective Hamiltonian:

$$H_{eff} = -\frac{\hbar}{2} \left(\tilde{\alpha}_0 \hat{\Xi}_0 \hat{T}_{0,0} + \frac{1}{\sqrt{6}} \tilde{\alpha}_2 \hat{\Xi}_0 \hat{T}_{2,0} + \tilde{\alpha}_1 \hat{\Xi}_\sigma \hat{T}_{1,0} \right) +$$
$$\frac{\hbar}{2} \frac{\tilde{\alpha}_2}{\sqrt{2}} \left(\hat{\Xi}_- \hat{T}_{2,2} + \hat{\Xi}_+ \hat{T}_{2,-2} \right) \qquad (11.6)$$

$$H_{eff} = -\frac{\hbar}{2} \left(\tilde{\alpha}_0 \hat{\Xi}_0 \hat{T}_{0,0} + \frac{1}{\sqrt{6}} \tilde{\alpha}_2 \hat{\Xi}_0 \hat{T}_{2,z} + \tilde{\alpha}_1 \hat{\Xi}_\sigma \hat{T}_{1,z} \right) +$$
$$\frac{\hbar}{2} \frac{\tilde{\alpha}_2}{\sqrt{2}} \left(\hat{\Xi}_{HV} \hat{T}_{HV} + \hat{\Xi}_{45} \hat{T}_{45} \right) \qquad (11.7)$$

Here we wrote it in both the spherical basis (Eq. 11.6) and in the cartesian basis (Eq. 11.7).

11.1.1   cgs ver. SI units

In this subsection we work out the constants entering the modified polarizibility $\tilde{\alpha}$, and see how they change between cgs and SI units. We start by examining Eq. 11.2, and notice the Hamiltonian has been transformed from $H \propto \alpha \hat{E}^2 \hat{T}$ to $H \propto \hbar \tilde{\alpha} \hat{\Xi} \hat{T}$. The electric field has been rewritten in terms of the Stokes vector components, the atomic density operator elements have been factored out of the polarizability tensor and the remainding constans have been absorbed into the dimensionless polarizability coefficients $\tilde{\alpha}$. Here the positive frequency part of the electric field is defined as

$$\hat{\mathbf{E}}^{(+)} = i\mathbf{e} g \hat{a} e^{-i\omega_{sb}t} \qquad (11.8)$$

where $\mathbf{e}$ is a unit polarization vector, $\hat{a}$ is the annihilation operator, and g is a constant. The Stokes parameters are defined as $\hat{\Xi} \sim (c/L)\hat{a}^\dagger \hat{a}$ and when written using the electric field it is $\hat{\Xi}_0 \sim c/(Lg^2)\hat{\mathbf{E}}^{(-)}\hat{\mathbf{E}}^{(+)}$, where L is the length of the quantization volume. Therefore, as is shown in appendix D, the prefactor that multiplies the polarizability is $g^2 L/c$ and we can rewrite the modified polarizibility as,

$$\tilde{\alpha} = \frac{2}{\hbar} \frac{g^2 L}{c} \alpha \qquad (11.9)$$

This combination gives us a dimensionless modified polarizibility with leaving the $\hbar$ outside the Hamiltonian and an extra factor of 2 for convenience when

---

[3]Leading to a rotation of linear polarization.

deriving the propagation equations. Now we write the factors for both cgs to SI units as,

$$g_{cgs} = \sqrt{\frac{2\pi\hbar\omega}{AL}} \; ; g_{SI} = \sqrt{\frac{\hbar\omega}{2\epsilon_0 AL}} \tag{11.10}$$

$$\tilde{\alpha}_{cgs} = \frac{4\pi\omega}{Ac}\alpha \; ; \tilde{\alpha}_{SI} = \frac{\omega}{\epsilon_0 Ac}\alpha \tag{11.11}$$

where A is the sample cross section and L is the sample length (AL is the quantization volume), $\hbar$ is Planck's constant divided by 2π, ω is the light radial frequency, and ϵ_0 is the vacuum permeability. The reduced dipole operator in the modified polarizibility can also be expressed using the natural line width of the level Γ [Steck08] and thus we can write the modified polarizibility as

$$\tilde{\alpha} \propto \frac{\sigma_0}{A}\frac{\Gamma}{2\Delta} \tag{11.12}$$

with σ_0 ($= 3\lambda^2/(2\pi)$) the atomic absorption cross-section, λ the laser wavelength, and Δ the detuning.

11.2 The atom-magnetic field interaction Hamiltonian

Here we are interested in presenting the atom-magnetic field interaction Hamiltonian using the irreducible tensor notation, defined in Eq. 11.3. Before writing the Hamiltonian we introduce the relation between the angular momentum vector and the irreducible tensor [Varshalovich88]:

$$\hat{T}_{1,q} = \sqrt{\frac{3}{F_0(F_0 + 1)(2F_0 + 1)}}\hat{j}_q \equiv \beta_0\hat{j}_q \tag{11.13}$$

with $q = -1, 0, 1$ represents the spherical basis component, β_0 a constant ($\beta_0 = 1/\sqrt{2}$ for $F_0 = 1$), and $\hat{j}$ the angular momentum operator for a single atom.

The atom-magnetic field interaction Hamiltonian is:

$$\hat{H}_B = g_F\mu_B\mathbf{j} \cdot \mathbf{B} = \hbar\left(-\omega_+\hat{j}_+ + \omega_-\hat{j}_- + \omega_z\hat{j}_z\right) =$$
$$\hbar/\beta_0\left(-\omega_+\hat{T}_{1,1} + \omega_-\hat{T}_{1,-1} + \omega_z\hat{T}_{1,0}\right) \tag{11.14}$$

with g_F the Landé g-factor for the hyperfine ground level, μ_B the Bohr magneton, $\mathbf{B}$ the magnetic field, and $\hbar\boldsymbol{\omega} = g_F\mu_B\mathbf{B}$. Here we used the following base transformation

$$B_\pm = \frac{B_x \mp iB_y}{\sqrt{2}} \; ; \omega_\pm = \frac{\omega_x \mp i\omega_y}{\sqrt{2}} \tag{11.15}$$

11.3 Propagation equations

In this section we derive the propagation equations for the collective atomic spin operators ($\hat{T}_{K,Q}$) and for the Stokes operators ($\hat{\Xi}$). First we transform the atomic operator (the irreducible tensor) from an operator of a single atom to describe a collective excitation of many atoms at a specific location. This allows to derive the equations describing the system both in time and space using the Heisenberg equation. We start, in subsection 11.3.1, with the derivation of the Stokes parameters propagation along the sample. Then we derive the atomic time evolution equations. We derive the equations in spherical basis (subsection 11.3.2), next we

move to cartesian coordinate system (subsection 11.3.3), and then we generalize the equations to include two light sources with different frequencies (subsection 11.3.4). We finish this section with a short discussion about the resulting equations.

Up till now the atomic operator, the irreducible tensor, described the internal state of a single atom. To move to a collective description for both spatial and internal degrees of freedom we need to sum over all atoms inside a thin slice. For this we assume that the number of atoms in each slice is large enough such that it contains much more than a single atom yet the thickness of each slice is small enough so that we can consider our system with continuous variables [Kupriyanov05, Mishina07, Gorshkov07b]. There are several different ways that we can normalize the atomic operator which will affect the commutation relations. This point is discussed in more detail in appendix F. Here we have decided to keep the convention chosen in [Kupriyanov05] which defines the atomic operators as densities, i.e. the irreducible tensor will have unit of number of atoms per length (in cgs this gives $1/\text{cm}$), and is redefined as

$$\hat{T}_{K,Q}(z,t) = \frac{1}{\Delta z} \sum_{z < z_a \leq z + \Delta z} \hat{T}_{K,Q}(z_a, t) \tag{11.16}$$

With this change we move from a Hamiltonian describing a single atom to a density Hamiltonian with units of energy per unit length. The irreducible tensors commutation relation [Varshalovich88, Kupriyanov05] is given by,

$$\left[T_{K,Q}(z,t), T_{K',Q'}(z',t) \right] = \sqrt{(2K+1)(2K'+1)} \sum_{K'',Q''} \left[1 - (-1)^{K+K'+K''} \right] \times$$

$$\begin{Bmatrix} K & K' & K'' \\ F_0 & F_0 & F_0 \end{Bmatrix} (-1)^{2F_0+K''} C_{K,Q;K',Q'}^{K'',Q''} T_{K'',Q''}(z,t) \delta(z - z') \tag{11.17}$$

where $\{\}$ is the 6-j symbol, $C_{\cdots}^{\cdots}$ is the Clebsch-Gordan coefficient, and $\delta(z - z')$ is the Dirac delta function. Note that the Dirac delta function enters from the way we have decided to redefine the irreducible tensors and it has units of one over length.

The coupled propagation equations for light and atoms [Kupriyanov05, Mishina07, Gorshkov07b] are given by the Heisenberg equation,

$$\left(c \frac{\partial}{\partial z} + \frac{\partial}{\partial t} \right) \hat{\Xi} = \frac{i}{\hbar} \left[H_B + H_{eff}, \hat{\Xi} \right] \tag{11.18}$$

$$\frac{\partial}{\partial t} \hat{T}_{K,Q} = \frac{i}{\hbar} \left[H_B + H_{eff}, \hat{T}_{K,Q} \right] \tag{11.19}$$

and are derived in the next subsections.

11.3.1 Stokes parameter propagation equations

In Eq. 11.18 we have written the Heisenberg equation for the Stokes operators. We start by showing that the radiation Hamiltonian, $\hat{H}_R = \hbar\omega(\hat{a}^\dagger \hat{a} + 1/2)$, gives rise to a spatial derivative of the Stokes operator, which appears in the first term on the left hand side of Eq. 11.18. To see this we write the Heisenberg equation for the annihilation operator and Fourier transform the results and Fourier transform back, i.e.

$$\frac{\partial}{\partial t} \hat{a} = \frac{1}{\sqrt{2\pi}} \int dk \frac{i}{\hbar} \left[\hat{H}, \hat{a} \right] e^{ikz} = \frac{1}{\sqrt{2\pi}} \int dk (-i) ck \hat{a} e^{ikz} = -c \frac{\partial}{\partial z} \hat{a} \tag{11.20}$$

thus (using $\omega = ck$) we get Eq. 11.18.

The $\partial/(c\partial t)$ term in the propagation equation can be neglected, since in our case the sample length is very short in comparison to the time it takes the light to pass through the sample $\partial z << c\partial t$. This time scale is $L/c \approx 10^{-4}/10^8\text{s} = 10^{-12}\text{s}$ which is much shorter than any other time scale in our system which would be about 10^{-6}s.

The atom-magnetic field interaction Hamiltonian does not influence the light directly since the Stokes operators commute with the atomic operator, i.e. $[H_B, \hat{\Xi}] = 0$. We still need to evaluate the commutation relation for $[H_{eff}, \hat{\Xi}]$. For this we write the commutation relation for the Stokes parameters [Mishina07]

$$\left[\hat{\Xi}_i(z,t), \hat{\Xi}_j(z',t)\right] = 2i\varepsilon_{i,j,k}c\delta(z-z')\hat{\Xi}_k \tag{11.21}$$

where $\varepsilon_{i,j,k}$ is the Levi-Civita totally anti-symmetric tensor, i,j,k are the running indices $\{i,j,k\} = \{45,\sigma,HV\}$, c is the speed of light, and $\delta(z-z')$ is Dirac delta function that ensures the position of the light. Now we write the light propagation equation as:

$$\frac{\partial}{\partial_z}\hat{\Xi}_i = \frac{i}{\hbar c}\left[H_{eff}, \hat{\Xi}_i\right] = -\tilde{\alpha}_1 \hat{T}_{1,0}\left[\hat{\Xi}_\sigma, \hat{\Xi}_i\right]\frac{i}{2c} +$$
$$+\frac{1}{\sqrt{2}}\tilde{\alpha}_2\left(\hat{T}_{HV}\left[\hat{\Xi}_{HV}, \hat{\Xi}_i\right]\frac{i}{2c} + \hat{T}_{45}\left[\hat{\Xi}_{45}, \hat{\Xi}_i\right]\frac{i}{2c}\right) \tag{11.22}$$

Which gives the end result,

$$\frac{\partial}{\partial_z}\begin{pmatrix} \hat{\Xi}_{45} \\ \hat{\Xi}_\sigma \\ \hat{\Xi}_{HV} \end{pmatrix} = \begin{pmatrix} 0 & -\frac{\tilde{\alpha}_2}{\sqrt{2}}\hat{T}_{HV} & \tilde{\alpha}_1\hat{T}_{1,0} \\ \frac{\tilde{\alpha}_2}{\sqrt{2}}\hat{T}_{HV} & 0 & -\frac{\tilde{\alpha}_2}{\sqrt{2}}\hat{T}_{45} \\ -\tilde{\alpha}_1\hat{T}_{1,0} & \frac{\tilde{\alpha}_2}{\sqrt{2}}\hat{T}_{45} & 0 \end{pmatrix}\begin{pmatrix} \hat{\Xi}_{45} \\ \hat{\Xi}_\sigma \\ \hat{\Xi}_{HV} \end{pmatrix} \tag{11.23}$$

This equation can also be written as $(\partial/\partial z)\hat{\Xi} = \tilde{T}_R \times \hat{\Xi}$, with an effective atomic vector $\tilde{T}_R$. This means that the light Stokes operator vector is rotating along the sample around the atomic coherence operator ($\tilde{T}_R$).

11.3.2   Atomic time evolution - in the spherical basis

Here we solve the propagation Eq. 11.19 for the case of $F_0 = 1$, as this is the hyperfine ground state that we are using. The Heisenberg equation includes the commutation relations between the different irreducible tensors, we evaluate them using Eq. 11.17, and give the results in appendix E. Next we solve and write the evolution equations due to the magnetic field and due to the light-atom interaction.

Atomic time evolution due to the magnetic field

The time evolution equation due to the magnetic field is:

$$\frac{\partial}{\partial t}\hat{T}_{K,Q} = \frac{i}{\hbar}\left[H_B, \hat{T}_{K,Q}\right] = -\frac{i\omega_+}{\beta_0}\left[\hat{T}_{1,1}, \hat{T}_{K,Q}\right] + \frac{i\omega_-}{\beta_0}\left[\hat{T}_{1,-1}, \hat{T}_{K,Q}\right] +$$
$$+\frac{i\omega_z}{\beta_0}\left[\hat{T}_{1,0}, \hat{T}_{K,Q}\right] \tag{11.24}$$

We represent the result in a matrix form as:

$M_{B,sph} =$

	$\hat{T}_{1,0}$	$\hat{T}_{1,1}$	$\hat{T}_{1,-1}$	$\hat{T}_{2,0}$	$\hat{T}_{2,1}$	$\hat{T}_{2,-1}$	$\hat{T}_{2,2}$	$\hat{T}_{2,-2}$
$\hat{T}_{1,0}$	0	$i\omega_+$	$i\omega_-$	0	0	0	0	0
$\hat{T}_{1,1}$	$i\omega_-$	$i\omega_z$	0	0	0	0	0	0
$\hat{T}_{1,-1}$	$i\omega_+$	0	$-i\omega_z$	0	0	0	0	0
$\hat{T}_{2,0}$	0	0	0	0	$i\sqrt{3}\omega_+$	$i\sqrt{3}\omega_-$	0	0
$\hat{T}_{2,1}$	0	0	0	$i\sqrt{3}\omega_-$	$i\omega_z$	0	$i\sqrt{2}\omega_+$	0
$\hat{T}_{2,-1}$	0	0	0	$i\sqrt{3}\omega_+$	0	$-i\omega_z$	0	$i\sqrt{2}\omega_-$
$\hat{T}_{2,2}$	0	0	0	0	$i\sqrt{2}\omega_-$	0	$i2\omega_z$	0
$\hat{T}_{2,-2}$	0	0	0	0	0	$i\sqrt{2}\omega_+$	0	$-i2\omega_z$

$$(11.25)$$

Atomic time evolution due to the light atom interaction

The time evolution equation due to the light matter interaction using the effective Hamiltonian given in Eq. 11.6 gives,

$$\frac{\partial}{\partial t}\hat{T}_{K,Q} = -\frac{i}{2}\tilde{\alpha}_0\hat{\Xi}_0\left[\hat{T}_{0,0},\hat{T}_{K,Q}\right] - \frac{i}{2\sqrt{6}}\tilde{\alpha}_2\hat{\Xi}_0\left[\hat{T}_{2,0},\hat{T}_{K,Q}\right] +$$

$$+\frac{i}{2}\tilde{\alpha}_1\hat{\Xi}_\sigma\left[\hat{T}_{1,0},\hat{T}_{K,Q}\right] + \frac{i}{2\sqrt{2}}\tilde{\alpha}_2\left(\hat{\Xi}_-\left[\hat{T}_{2,2},\hat{T}_{K,Q}\right] + \hat{\Xi}_+\left[\hat{T}_{2,-2},\hat{T}_{K,Q}\right]\right) \qquad (11.26)$$

We define the following parameters:

$$\hat{\Omega}_\sigma = \frac{1}{2}\beta_0\tilde{\alpha}_1\hat{\Xi}_\sigma \qquad (11.27)$$

$$\epsilon = \frac{1}{2\sqrt{2}}\beta_0\tilde{\alpha}_2 \qquad (11.28)$$

For our case with the ground state hyperfine quantum number $F_0 = 1$, we get $\epsilon = \tilde{\alpha}_2/4$. Next we write the evolution matrix as,

$M_{T,sph} =$

i

	$\hat{T}_{1,0}$	$\hat{T}_{1,1}$	$\hat{T}_{1,-1}$	$\hat{T}_{2,0}$	$\hat{T}_{2,1}$	$\hat{T}_{2,-1}$	$\hat{T}_{2,2}$	$\hat{T}_{2,-2}$
	0	0	0	0	0	0	$-2\epsilon\hat{\Xi}_-$	$2\epsilon\hat{\Xi}_+$
	0	$\hat{\Omega}_\sigma$	0	0	$-\epsilon\hat{\Xi}_0$	$\sqrt{2}\epsilon\hat{\Xi}_+$	0	0
	0	0	$-\hat{\Omega}_\sigma$	0	$-\sqrt{2}\epsilon\hat{\Xi}_-$	$\epsilon\hat{\Xi}_0$	0	0
	0	0	0	0	0	0	0	0
	0	$-\epsilon\hat{\Xi}_0$	$-\sqrt{2}\epsilon\hat{\Xi}_+$	0	$\hat{\Omega}_\sigma$	0	0	0
	0	$\sqrt{2}\epsilon\hat{\Xi}_-$	$\epsilon\hat{\Xi}_0$	0	0	$-\hat{\Omega}_\sigma$	0	0
	$-2\epsilon\hat{\Xi}_+$	0	0	0	0	0	$2\hat{\Omega}_\sigma$	0
	$2\epsilon\hat{\Xi}_-$	0	0	0	0	0	0	$-2\hat{\Omega}_\sigma$

$$(11.29)$$

With the total propagation equation given by:

$$\frac{\partial}{\partial t}\hat{\mathbf{T}} = \left(M_{B,sph} + M_{T,sph}\right)\hat{\mathbf{T}} \qquad (11.30)$$

where $\hat{\mathbf{T}}^T = \left(\hat{T}_{1,0}, \hat{T}_{1,1}, \hat{T}_{1,-1}, \hat{T}_{2,0}, \hat{T}_{2,1}, \hat{T}_{2,1}, \hat{T}_{2,-1}, \hat{T}_{2,2}, \hat{T}_{2,-2}\right)$, $M_{B,sph}$ is given by Eq. 11.25 and $M_{T,sph}$ is given by Eq. 11.29.

11.3.3 Transforming to Cartesian coordinate system

Here we transform the above equations from a spherical basis to a cartesian basis. The transformation is:

$$\hat{T}_{HV} = \frac{\hat{T}_{2,2} + \hat{T}_{2,-2}}{\sqrt{2}} \; ; \hat{T}_{45} = \frac{\hat{T}_{2,2} - \hat{T}_{2,-2}}{i\sqrt{2}} \tag{11.31}$$

$$\hat{T}_{2,2} = \frac{\hat{T}_{HV} + i\hat{T}_{45}}{\sqrt{2}} \; ; \hat{T}_{2,-2} = \frac{\hat{T}_{HV} - i\hat{T}_{45}}{\sqrt{2}} \tag{11.32}$$

$$\hat{\Xi}_{+} = \frac{\hat{\Xi}_{HV} + i\hat{\Xi}_{45}}{\sqrt{2}} \; ; \hat{\Xi}_{-} = \frac{\hat{\Xi}_{HV} - i\hat{\Xi}_{45}}{\sqrt{2}} \tag{11.33}$$

$$\hat{\Xi}_{HV} = \frac{\hat{\Xi}_{+} + \hat{\Xi}_{-}}{\sqrt{2}} \; ; \hat{\Xi}_{45} = \frac{\hat{\Xi}_{+} - \hat{\Xi}_{-}}{i\sqrt{2}} \tag{11.34}$$

$$\hat{T}_{1,1} = -\frac{\hat{T}_{1,x} + i\hat{T}_{1,y}}{\sqrt{2}} \; ; \hat{T}_{1,-1} = \frac{\hat{T}_{1,x} - i\hat{T}_{1,y}}{\sqrt{2}} \tag{11.35}$$

$$\hat{T}_{1,x} = -\frac{\hat{T}_{1,1} - \hat{T}_{1,-1}}{\sqrt{2}} \; ; \hat{T}_{1,y} = -\frac{\hat{T}_{1,1} + \hat{T}_{1,-1}}{i\sqrt{2}} \tag{11.36}$$

$$\hat{T}_{2,1} = -\frac{\hat{T}_{2,x} + i\hat{T}_{2,y}}{\sqrt{2}} \; ; \hat{T}_{2,-1} = \frac{\hat{T}_{2,x} - i\hat{T}_{2,y}}{\sqrt{2}} \tag{11.37}$$

$$\hat{T}_{2,x} = -\frac{\hat{T}_{2,1} - \hat{T}_{2,-1}}{\sqrt{2}} \; ; \hat{T}_{2,y} = -\frac{\hat{T}_{2,1} + \hat{T}_{2,-1}}{i\sqrt{2}} \tag{11.38}$$

Note that here the definition for $\hat{T}_{HV}$ and $\hat{T}_{45}$ is different from the one given in [Kupriyanov05, Mishina07] by a factor of $\sqrt{2}$. This factor is important to keep the equation in an anti-symmetric form, and for consistency when defining the total atom number by $\hat{\mathbf{T}}^{\dagger}\hat{\mathbf{T}}$.

We rewrite the propagation matrix, for both the magnetic and atom-light parts, which gives:

$M_{car} = M_{B,car} + M_{T,car} =$

	$\hat{T}_{1,x}$	$\hat{T}_{1,y}$	$\hat{T}_{1,z}$	$\hat{T}_{2,x}$	$\hat{T}_{2,y}$	$\hat{T}_{2,z}$	$\hat{T}_{HV}$	$\hat{T}_{45}$
$\hat{T}_{1,x}$	0	$-\hat{\Omega}_{\sigma,z}$	ω_y	$\epsilon\hat{\Xi}_{45}$	$\epsilon(\hat{\Xi}_0 - \hat{\Xi}_{HV})$	0	0	0
$\hat{T}_{1,y}$	$\hat{\Omega}_{\sigma,z}$	0	$-\omega_x$	$-\epsilon(\hat{\Xi}_0 + \hat{\Xi}_{HV})$	$-\epsilon\hat{\Xi}_{45}$	0	0	0
$\hat{T}_{1,z}$	$-\omega_y$	ω_x	0	0	0	0	$-2\epsilon\hat{\Xi}_{45}$	$2\epsilon\hat{\Xi}_{HV}$
$\hat{T}_{2,x}$	$-\epsilon\hat{\Xi}_{45}$	$\epsilon(\hat{\Xi}_0 + \hat{\Xi}_{HV})$	0	0	$-\hat{\Omega}_{\sigma,z}$	$\sqrt{3}\omega_y$	$-\omega_y$	ω_x
$\hat{T}_{2,y}$	$-\epsilon(\hat{\Xi}_0 - \hat{\Xi}_{HV})$	$\epsilon\hat{\Xi}_{45}$	0	$\hat{\Omega}_{\sigma,z}$	0	$-\sqrt{3}\omega_x$	$-\omega_x$	$-\omega_y$
$\hat{T}_{2,z}$	0	0	0	$-\sqrt{3}\omega_y$	$\sqrt{3}\omega_x$	0	0	0
$\hat{T}_{HV}$	0	0	$2\epsilon\hat{\Xi}_{45}$	ω_y	ω_x	0	0	$-2\hat{\Omega}_{\sigma,z}$
$\hat{T}_{45}$	0	0	$-2\epsilon\hat{\Xi}_{HV}$	$-\omega_x$	ω_y	0	$2\hat{\Omega}_{\sigma,z}$	0

$$\tag{11.39}$$

with

$$\hat{\Omega}_{\sigma,z} = \omega_z + \hat{\Omega}_{\sigma} \tag{11.40}$$

11.3.4 Two different light sources

In the previous sections we have used only one light mode with different polarization components, here we are going to assume that each polarization component has a different wavelength. This case is interesting since it enables to effectively cancel out the magnetic field along the propagation direction by tuning to the two-photon resonance, i.e. effectively setting $\hat{\Omega}_{\sigma,z} \rightarrow 0$ in Eq. 11.39.

Changing to a two different frequencies for the light means the following transformation: $\hat{a}_{+} = \hat{a}_{+}^{s}$ (corresponding to the SB with σ_{+} polarization) and $\hat{a}_{-} =$

$\hat{a}^s_- e^{2i\delta t}$ (corresponding to the DL with σ_- polarization). Here the superscript s stands for slowly varying and δ is half the frequency difference between the two light sources. Entering this transformation into the Stokes parameters in Eq. C.2- C.4 gives:

$$\hat{\Xi}_\sigma = \hat{\Xi}^s_\sigma \tag{11.41}$$

$$\begin{pmatrix} \hat{\Xi}_{HV} \\ \hat{\Xi}_{45} \end{pmatrix} = \begin{pmatrix} \cos 2\delta t & \sin 2\delta t \\ -\sin 2\delta t & \cos 2\delta t \end{pmatrix} \begin{pmatrix} \hat{\Xi}^s_{HV} \\ \hat{\Xi}^s_{45} \end{pmatrix} \tag{11.42}$$

In order to absorb the time varying dependence we need to move to a rotating frame at a frequency δ, by defining:

$$\begin{pmatrix} \hat{T}_{HV} \\ \hat{T}_{45} \end{pmatrix} = \begin{pmatrix} \cos 2\delta t & \sin 2\delta t \\ -\sin 2\delta t & \cos 2\delta t \end{pmatrix} \begin{pmatrix} \hat{T}^s_{HV} \\ \hat{T}^s_{45} \end{pmatrix} \tag{11.43}$$

$$\begin{pmatrix} \hat{T}_{1,x} \\ \hat{T}_{1,y} \end{pmatrix} = \begin{pmatrix} \cos \delta t & \sin \delta t \\ -\sin \delta t & \cos \delta t \end{pmatrix} \begin{pmatrix} \hat{T}^s_{1,x} \\ \hat{T}^s_{1,y} \end{pmatrix} \tag{11.44}$$

$$\begin{pmatrix} \hat{T}_{2,x} \\ \hat{T}_{2,y} \end{pmatrix} = \begin{pmatrix} \cos \delta t & \sin \delta t \\ -\sin \delta t & \cos \delta t \end{pmatrix} \begin{pmatrix} \hat{T}^s_{2,x} \\ \hat{T}^s_{2,y} \end{pmatrix} \tag{11.45}$$

and the magnetic field is transformed as:

$$\begin{pmatrix} \omega_x \\ \omega_y \end{pmatrix} = \begin{pmatrix} \cos \delta t & \sin \delta t \\ -\sin \delta t & \cos \delta t \end{pmatrix} \begin{pmatrix} \omega^s_x \\ \omega^s_y \end{pmatrix} \tag{11.46}$$

with $\hat{T}_{1,z} = \hat{T}^s_{1,z}$ and $\hat{T}_{2,z} = \hat{T}^s_{2,z}$. Now we rewrite the full time evolution equations as:

$M_{s,car} = M_{B^s,car} + M_{T^s,car} =$

	$\hat{T}^s_{1,x}$	$\hat{T}^s_{1,y}$	$\hat{T}^s_{1,z}$	$\hat{T}^s_{2,x}$	$\hat{T}^s_{2,y}$	$\hat{T}^s_{2,z}$	$\hat{T}^s_{HV}$	$\hat{T}^s_{45}$
$\hat{T}^s_{1,x}$	0	$-\hat{\Omega}_{\sigma,z}-\delta$	ω^s_y	$\epsilon\hat{\Xi}^s_{45}$	$\epsilon(\hat{\Xi}_0-\hat{\Xi}^s_{HV})$	0	0	0
$\hat{T}^s_{1,y}$	$\hat{\Omega}_{\sigma,z}+\delta$	0	$-\omega^s_x$	$-\epsilon(\hat{\Xi}_0+\hat{\Xi}^s_{HV})$	$-\epsilon\hat{\Xi}^s_{45}$	0	0	0
$\hat{T}^s_{1,z}$	$-\omega^s_y$	ω^s_x	0	0	0	0	$-2\epsilon\hat{\Xi}^s_{45}$	$2\epsilon\hat{\Xi}^s_{HV}$
$\hat{T}^s_{2,x}$	$-\epsilon\hat{\Xi}^s_{45}$	$\epsilon(\hat{\Xi}_0+\hat{\Xi}^s_{HV})$	0	0	$-\hat{\Omega}_{\sigma,z}-\delta$	$\sqrt{3}\omega^s_y$	$-\omega^s_y$	ω^s_x
$\hat{T}^s_{2,y}$	$-\epsilon(\hat{\Xi}_0-\hat{\Xi}^s_{HV})$	$\epsilon\hat{\Xi}^s_{45}$	0	$\hat{\Omega}_{\sigma,z}+\delta$	0	$-\sqrt{3}\omega^s_x$	$-\omega^s_x$	$-\omega^s_y$
$\hat{T}^s_{2,z}$	0	0	0	$-\sqrt{3}\omega^s_y$	$\sqrt{3}\omega^s_x$	0	0	0
$\hat{T}^s_{HV}$	0	0	$2\epsilon\hat{\Xi}^s_{45}$	ω^s_y	ω^s_x	0	0	$-2\hat{\Omega}_{\sigma,z}-2\delta$
$\hat{T}^s_{45}$	0	0	$-2\epsilon\hat{\Xi}^s_{HV}$	$-\omega^s_x$	ω^s_y	0	$2\hat{\Omega}_{\sigma,z}+2\delta$	0

$$\tag{11.47}$$

By moving to the rotating frame, and introducing a frequency difference between the two polarizations components, we have changed the time evolution (Eq. 11.39) from $\hat{\Omega}_{\sigma,z}$ to $\hat{\Omega}_{\sigma,z}+\delta$. Thus by setting the right frequency difference between the two beams (SB and DL) we can set $\hat{\Omega}_{\sigma,z}+\delta \to 0$. Now the propagation equations are,

$$\frac{\partial}{\partial t}\hat{\mathbf{T}}^s = M_{s,car}\hat{\mathbf{T}}^s \tag{11.48}$$

$$\hat{\mathbf{T}}^T = \left(\hat{T}^s_{1,x}, \hat{T}^s_{1,y}, \hat{T}^s_{1,z}, \hat{T}^s_{2,x}, \hat{T}^s_{2,y}, \hat{T}^s_{2,z}, \hat{T}^s_{HV}, \hat{T}^s_{45} \right) \tag{11.49}$$

11.3.5　Discussion about the propagation equations

When examining the evolution equations Eq. 11.23 and Eq. 11.47 we can identify two things: the evolution is set by rotation matrices and they are antisymmetric. The rotation matrix means that the atomic coherence operators will

rotate around the light operators and the magnetic field. In the limit that only a subspace can be examined we can write the equation as a cross product, similar to what we showed for the light at the end of section 11.3.1. For the atoms we can look at two interesting cases, restricting to the angular momentum vector and to the Raman transfer coherence terms. Up to a numerical constant the angular momentum vector is $\hat{\mathbf{T}}_v^T = \left(\hat{T}_{1,x}, \hat{T}_{1,y}, \hat{T}_{1,z} \right)$ and in the case that $(\partial/\partial t)\hat{T}_{2,Q} = 0$, we get the well known result $(\partial/\partial t)\hat{\mathbf{T}}_v = \tilde{\mathbf{B}} \times \hat{\mathbf{T}}_v$ with the definition of the effective magnetic field as $\tilde{\mathbf{B}}^T = \left(\omega_x^s, \omega_y^s, \hat{\Omega}_{\sigma,z} + \delta \right)$. For the Raman transfer we are interested in $\hat{\mathbf{T}}_R^T = \left(\hat{T}_{1,z}, \hat{T}_{HV}, \hat{T}_{45} \right)$ and assume that the rest of the irreducible tensors are constant of motion. Thus we again can write the time evolution as $(\partial/\partial t)\hat{\mathbf{T}}_R = \mathbf{B_l} \times \hat{\mathbf{T}}_R$ with $\tilde{\mathbf{B}}_l^T = 2 \left(\hat{\Omega}_{\sigma,z} + \delta, \epsilon \hat{\Xi}_{HV}^s, \epsilon \hat{\Xi}_{45}^s \right)$.

This means that under certain requirements from the system we can get two coupled equations of the form:

$$\frac{\partial}{\partial t} \hat{\mathbf{T}}_R = \mathbf{B_l} \times \hat{\mathbf{T}}_R \tag{11.50}$$

$$\frac{\partial}{\partial z} \hat{\mathbf{\Xi}} = \tilde{\mathbf{T}}_R \times \hat{\mathbf{\Xi}} \tag{11.51}$$

These equations, at certain conditions, give rise to the memory or entanglement protocols [Mishina07]. For the case of the Raman memory we show this in the next section, but a similar procedure can be done with $\hat{\mathbf{T}}_v$ to get a memory protocol [Kupriyanov05].

The second point that we want to emphasize is that the evolution matrices are antisymmetric, which states that they conserve energy (atom and photon number). The conservation law is tested by examining the derivative of the number of atoms or photons, i.e.

$$\frac{\partial}{\partial t} \mathbf{T}^\dagger \mathbf{T} = (\frac{\partial}{\partial t} \mathbf{T}^\dagger) \mathbf{T} + \mathbf{T}^\dagger \frac{\partial}{\partial t} \mathbf{T} = \mathbf{T}^\dagger \left(M^\dagger + M \right) \mathbf{T} \tag{11.52}$$

Here M is some general matrix describing the evolution, which we can split (without loss of generality) to $M = M_{as} + M_s$ where M_{as} is an anti-symmetric matrix and M_s is a symmetric matrix. Using that $M_{as}^\dagger = -M_{as}$ and $M_s^\dagger = M_s$ we get,

$$\frac{\partial}{\partial t} \mathbf{T}^\dagger \mathbf{T} = 2\mathbf{T}^\dagger M_s \mathbf{T} \tag{11.53}$$

This means that if these equations contains a symmetric part they would not conserve energy! We point out that due to the way $\hat{T}_{HV}$ and $\hat{T}_{45}$ are defined in [Kupriyanov05, Mishina07] their equations do not explicitly show this conservation law.

11.4   2-level system - off-resonant Raman memory

In this section we examine the special case where we neglect any population of the sublevel $|F = 1, m_f = 0\rangle$, which is a good approximation in our case. This reduces the problem such that we can describe the system as an evolution of a vector undergoing rotation, and describe the propagation equations as a cross product (Eq. 11.50 and Eq. 11.51). Now the atomic time evolution equations are

reduced from a 8×8 matrix to a 3×3 matrix, i.e. they are

$$\frac{\partial}{\partial t} \begin{pmatrix} \hat{T}_{1,z} \\ \hat{T}_{HV} \\ \hat{T}_{45} \end{pmatrix} = 2 \begin{pmatrix} 0 & -\epsilon \hat{\Xi}_{45} & \epsilon \hat{\Xi}_{HV} \\ \epsilon \hat{\Xi}_{45} & 0 & -\hat{\Omega}_{\sigma,z} - \delta \\ -\epsilon \hat{\Xi}_{HV} & \hat{\Omega}_{\sigma,z} + \delta & 0 \end{pmatrix} \begin{pmatrix} \hat{T}_{1,z} \\ \hat{T}_{HV} \\ \hat{T}_{45} \end{pmatrix} \quad (11.54)$$

$$\frac{\partial}{\partial z} \begin{pmatrix} \hat{\Xi}_{45} \\ \hat{\Xi}_{\sigma} \\ \hat{\Xi}_{HV} \end{pmatrix} = \begin{pmatrix} 0 & -\frac{\tilde{\alpha}_2}{\sqrt{2}} \hat{T}_{HV} & \tilde{\alpha}_1 \hat{T}_{1,0} \\ \frac{\tilde{\alpha}_2}{\sqrt{2}} \hat{T}_{HV} & 0 & -\frac{\tilde{\alpha}_2}{\sqrt{2}} \hat{T}_{45} \\ -\tilde{\alpha}_1 \hat{T}_{1,0} & \frac{\tilde{\alpha}_2}{\sqrt{2}} \hat{T}_{45} & 0 \end{pmatrix} \begin{pmatrix} \hat{\Xi}_{45} \\ \hat{\Xi}_{\sigma} \\ \hat{\Xi}_{HV} \end{pmatrix} \quad (11.55)$$

Here, we also wrote the full propagation equations for the light for completeness. Writing both evolution and propagation equations makes it a bit easier to see how the memory and entanglement protocols arise [Mishina07]. For both protocols one prepares the atomic state such that $\hat{T}_{1,z}$ is classical and does not evolve in time and similarly for the circular light Stokes parameter, i.e. $\hat{T}_{1,z} \to T_{1,z}$ and $\hat{\Xi}_{\sigma} \to \Xi_{\sigma}$ are now c-numbers and their derivatives are zero. Considering these two assumptions we can write the propagation equations as:

$$\frac{\partial}{\partial t} \begin{pmatrix} \hat{T}_{45} \\ \hat{T}_{HV} \end{pmatrix} = 2 \left(\hat{\Omega}_{\sigma,z} + \delta \right) \begin{pmatrix} 0 & 1 \\ -1 & 0 \end{pmatrix} \begin{pmatrix} \hat{T}_{45} \\ \hat{T}_{HV} \end{pmatrix} - 2\epsilon T_{1,z} \begin{pmatrix} 0 & 1 \\ -1 & 0 \end{pmatrix} \begin{pmatrix} \hat{\Xi}_{45} \\ \hat{\Xi}_{HV} \end{pmatrix}$$
$$(11.56)$$

$$\frac{\partial}{\partial z} \begin{pmatrix} \hat{\Xi}_{45} \\ \hat{\Xi}_{HV} \end{pmatrix} = \tilde{\alpha}_1 T_{1,z} \begin{pmatrix} 0 & 1 \\ -1 & 0 \end{pmatrix} \begin{pmatrix} \hat{\Xi}_{45} \\ \hat{\Xi}_{HV} \end{pmatrix} - \frac{\tilde{\alpha}_2}{\sqrt{2}} \Xi_{\sigma} \begin{pmatrix} 0 & 1 \\ -1 & 0 \end{pmatrix} \begin{pmatrix} \hat{T}_{45} \\ \hat{T}_{HV} \end{pmatrix}$$
$$(11.57)$$

Here we use these equations with $\tilde{\alpha}_1 \to 0$ and $\hat{\Omega}_{\sigma,z} + \delta \to 0$. In this case (for memory) when the light enters into the sample its quantum state is "swapped" onto the atomic variables from which it can later be "swapped" back onto the outgoing light. These equations are examined in two regions: $T_{1,z}\Xi_{\sigma} < 0$ gives rise to memory, and $T_{1,z}\Xi_{\sigma} > 0$ that gives rise to entanglement. These sets of equations have been analytically solved in [Mishina07] and are governed by an integral over a Bessel function of the first kind, with $\tilde{\alpha}_2^2 T_{1,z} \cdot \Xi_{\sigma}$ the amplification prefactor.

These coupled equations are closely related to the coupled equations derived for the superradiance case, in section 5.3. Also here these coupling constant is proportional to the total scattering rate times the OD. To show this we use the modified polarizibility as expressed by Eq. 11.12, and the scattering rate as expressed by Eq. 10.1 in the limit of big detuning,

$$R = \frac{\Gamma}{2} \frac{I}{I_{sat}} \left(\frac{\Gamma}{2\Delta} \right)^2 = \frac{\sigma_0}{A} \left(\frac{\Gamma}{2\Delta} \right)^2 \Xi_0 \quad (11.58)$$

$$\tilde{\alpha}_2^2 T_{1,z} \cdot \Xi_{\sigma} = \left(\frac{2J+1}{2J_0+1} \tilde{C}_2 \right)^2 \frac{\sigma_0}{A} T_{1,z} R \quad (11.59)$$

Here we use that $\Xi_0 \sim \Xi_{\sigma}$. The constants are defined in section 11.1.1 (Eq. 11.12), with $I_{sat} = (\Gamma/2)(\hbar\omega/\sigma_0)$, and $I = \hbar\omega/A\Xi_0 \sim \hbar\omega/A\Xi_{\sigma}$ the total intensity. Next, for our hyperfine ground level $T_{1,z} = N_a/(2\sqrt{2}L)$ with N_a the total atom number and L the sample length. We assume a homogeneous sample as $T_{1,z}$ is up to a constant the atom density at a certain location. We thus get,

$$\tilde{\alpha}_2^2 T_{1,z} \cdot \Xi_{\sigma} \sim R \cdot OD/L. \quad (11.60)$$

Simulations

In this chapter we explain how we solve the coupled propagation equations for light and atoms, described in Eq. 11.23 and Eq. 11.47, using two different numerical implementations. We then discuss the convergence of the numerical solution and how to set the initial conditions from the experimental ones. We finish this chapter by showing the optimal pulse shape, by simulating a retrieval when we write an ideal mode [Gorshkov07b].

In section 12.1 we explain the different numerical implementations. Here we solve the equations either by explicitly calculating the exponential matrix or by backward/forward propagating method. For each type of a solution we use a two step approximation in order to improve the convergence. In section 12.2 we test the numerical convergence of the different numerical implementations.

In section 12.3 we express the experimental conditions in terms appropriate for the simulation. Here two points are relevant: rotating the atomic state from the initial known state along the magnetic axis to the chosen quantization axis along the light propagation, and determining the drive light (DL) photon flux through the sample. The first point allows us to simulate configurations with the magnetic field not aligned to the light propagation axis. The second point is important since the DL waist is much larger than the atomic sample, thus the photon flux used in the simulation is less than the one we actually used.

In section 12.4 we use the simulation in order to design the SB input pulse shape. The idea is based on the time inversion principle given in [Gorshkov07a, Gorshkov07b]. We run the simulation with initially distributing atoms in the $|+1\rangle\langle+1|$ state with a spatial parabolic distribution, and from the results of the outgoing SB photons flux, we get the optimal input pulse shape by time inverting the retrieved output pulse.

12.1 The numerics

The employed numerical method needs to solve two coupled equations of the type,

$$\frac{d}{dt}\mathbf{T}(z,t) = M_t(z,t,\varXi)\mathbf{T}(z,t) \tag{12.1}$$

$$\frac{d}{dz}\varXi(z,t) = M_z(z,t,\mathbf{T})\varXi(z,t) \tag{12.2}$$

where $\mathbf{T}$ is the atomic collective spin vector and $\varXi$ is the Stokes parameter vector, M_t and M_z are the evolution matrices. Note that here we have removed

the hat symbol and treat all the operators as a c-number[1]. We solve the above coupled equations with two types of algorithms: 1) exponential matrix, and 2) backward/forward propagation. Since the logic is the same for the time propagation (solving the atomic evolution) and for the propagation along the sample (solving the light evolution) we show here only the solution for the time propagation (atomic states). The exact solution of the equations during a small time step of Δt is

$$\mathbf{T}(z,t) = e^{\int_{t-\Delta t}^{t} dt' M_t(z,t')} \mathbf{T}(z,t-\Delta t) \qquad (12.3)$$

$$\mathbf{T}(z,t) = \left(\mathbb{1} - M_t(z,t)\frac{\Delta t}{2}\right)^{-1} \left(\mathbb{1} + M_t(z,t-\Delta t)\frac{\Delta t}{2}\right) \mathbf{T}(z,t-\Delta t) \qquad (12.4)$$

Here we have dropped the additional notation of the Stokes parameter in the evolution matrix for the atomic state, for brevity. Equation 12.3 describes the exponential matrix type of solution, and Eq. 12.4 the backward/forward propagating. In the backward/forward method we use the definition of the differential to evaluate the half step from both directions, with the advantage of utilizing higher order corrections. While the above equations are exact, we can not evaluate them since we do not know $M_t(z,t)$. The better the approximation of $M_t(z,t)$ the larger time step we can take (Δt) and reduce the run time. Here we either use a one step approximation, in which we assume that the matrix is constant over the time step, or a two step solution where we use the result of the first step as a guess for the matrix value at time t. For the exponential matrix approach, the full sequence is,

$$\mathbf{T}_0(z,t) = e^{\Delta t M_t(z,t-\Delta t)} \mathbf{T}(z,t-\Delta t) \qquad (12.5)$$

$$\Xi_0(z,t) = e^{\Delta z M_z(z-\Delta z,t)} \Xi(z-\Delta z,t) \qquad (12.6)$$

then, using this as a guess we get

$$\mathbf{T}(z,t) = e^{(\Delta t/2)\left(M_t(z,t-\Delta t)+M_t^0(z,t)\right)} \mathbf{T}(z,t-\Delta t) \qquad (12.7)$$

$$\Xi(z,t) = e^{(\Delta z/2)\left(M_z(z-\Delta z,t)+M_z^0(z,t)\right)} \Xi(z-\Delta z,t) \qquad (12.8)$$

Here the matrices with the superscript zero need to be interpreted as $M_t^0(z,t,\Xi_0)$ and $M_z^0(z,t,\mathbf{T}_0)$. Note that this second step almost doubles the run time, but it can reduce the grid size by more than a factor of four (for our case), for a similar convergence of the simulation. The solution for the backward/forward type is similar therefore we do not explicitly write it here.

12.2   Convergence of the numerics

In this section we tests of the convergence of the numerical solution, by testing the conservation of atom number and of photon number[2] and testing the Raman transfer of atoms from the $|+1\rangle \langle+1|$ state into the $|-1\rangle \langle-1|$ using only the DL pulse. For our numerical implementation the conservation of atom number or photon number is "easily" achieved due to the construction of the solution, while for the Raman transfer we require a much finer grid resolution.

Here we have tested four different run configurations at two different grid resolutions. These configurations correspond to the backward/forward and exponential matrix. For each method we used the single-step and two-step solution.

---

[1]From the way we have constructed the equations the results will be real numbers and not complex.
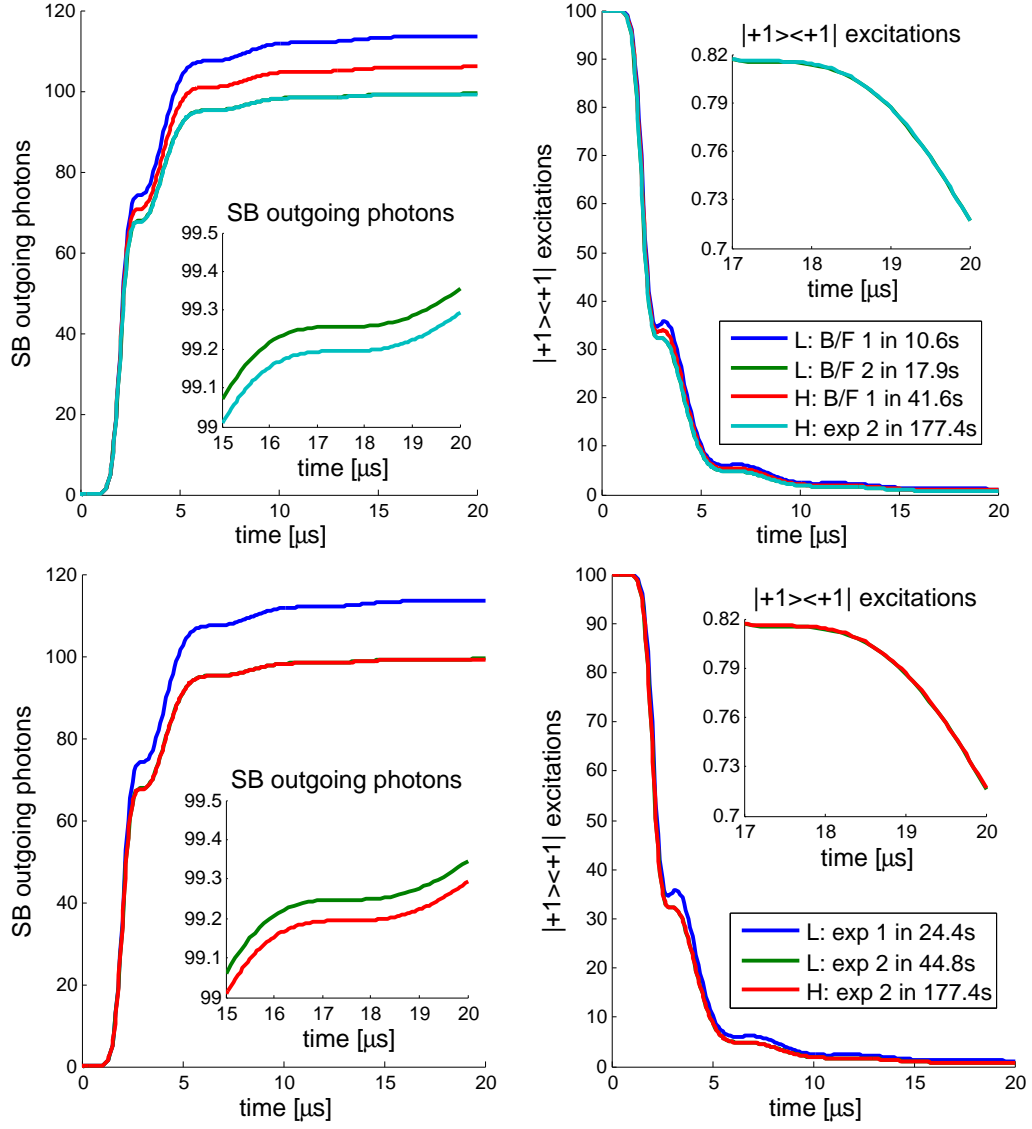
[2]As discussed in section 11.3.5

Figure 12.1: Simulation results output for a retrieval operation of $100 \left|+1\right\rangle \left\langle +1\right|$ excitations written in a parabolic distribution along the sample. Top subplots show the results of backward/forward numeric method; and the bottom subplots show the results of the exponential matrix approach. Left subplots show the SB outgoing photons; right subplots show the number of $\left|+1\right\rangle \left\langle +1\right|$ excitations. In the legend we report the run time and state the simulation method and resolution: B/F is the backward/forward method; exp is the exponential matrix method; the number 1 or 2 stands for the number of steps used in evaluating each cell; L or H represents the simulation resolution with L means $\Delta t = 100$ns and $\Delta z = 0.8\mu$m, and H means $\Delta t = 50$ns and $\Delta z = 0.4\mu$m.

The resolution of the run is $\Delta t = 100$ns and $\Delta z = 800$nm. We test the convergence by comparing to a run with half the step size $\Delta t = 50$ns and $\Delta z = 400$nm using the exponential matrix and two-step configuration.

For all configurations the conservation of atom number and photon number is better than 10^{-14}. We have also tested this conservation using a lower resolution by a factor of 10 for both time and space coordinates, and got the same result. This is due to the construction of the numerical algorithm.

The Raman transfer convergence is tested by using a sample with 100 excitations of $\left|+1\right\rangle \left\langle +1\right|$ states in a parabolic spatial distribution. The results of the different run configurations are given in Fig. 12.1. Here we assume that the two-step expo-

nential result with the high resolution has converged and use it as the reference. The results show that using the second evaluation step significantly improves the convergence without having to increase the grid size. Moreover, as is shown for the backward/forward method the two-step solution increases the run time by 80% and approaches the reference solution to better than 0.2%. While the single-step does not converge even after increasing the grid size resolution by a factor of two in both axis (increasing the run time by a factor of four), and the simulation result over estimate the total output SB photons by about 6%. The two-step exponential method (with the low resolution) is slightly closer to the reference run than the two-step backward/forward method. On the other hand the run time of 45s is significantly longer for the exponential method compared to a run time of 18s for the backward/forward method.

12.3   Setting the initial input states for the simulation

In this section we discuss two points, first how to translate the experimental drive light (DL) photon flux to the one usd in the simulation, and secondly how to rotate the collective atomic spin from the direction of the magnetic field to the light propagation direction.

Overlapping the atomic sample and the drive light beam

In the experiments we used a DL beam that is much larger than the atomic sample, as this gives a good approximation to a plane wave. The Stokes parameters, that are used in the simulation, are defined as the photon flux that passes through the cloud. To match the DL photon flux as measured with a power-meter to the Stokes parameter we need to determine the geometrical overlap of DL beam and atomic sample.

Since both the atomic cloud and the DL beam are characterized by a Gaussian distribution the overlap factor is:

$$OVL = 1 - e^{\frac{n^2 \sigma_a^2}{2\sigma_{DL}^2}} \tag{12.9}$$

where σ_a is the *rms* radius of the Gaussian atomic cloud, σ_{DL} is *rms* radius of the DL beam, and n is the number of standard deviations of the atomic cloud that we use. Since in our $1D$ model we explicitly assume a cylindrical sample shape, we take the sample area as the equivalent flat top distribution which sets $n^2 = 2$ $(2\pi\sigma_a^2/(\pi\sigma_a^2))$.

Rotating the collective atomic spin

We produce our atomic sample using evaporative cooling and therefore the initial atomic state along the magnetic field is a pure $|-1\rangle \langle -1|_B$ (with the subscript B indicating the magnetic axis). In our model we have used the quantization axis along the light propagation, which means that we need to rotate the collective atomic spin by an angle (θ) between the magnetic field direction and the light propagation direction. Here we do not derive the general concept of rotating an angular momentum, and send the interested reader to [Sakurai94]. To rotate an angular momentum we use the Wigner D function in their irreducible form. This means that the rotation only mixes irreducible tensor with the same K quantum number, i.e. $\hat{T}_{1,q}$ and $\hat{T}_{2,q'}$ will not mix. Here we use the notation of [Varshalovich88] (page 59), and find the rotated components of the Irreducible tensors:

$$\hat{T}_{F,m'} = \Sigma_m d^F_{m',m}(\theta) \hat{T}^{(B)}_{F,m} \tag{12.10}$$

where $d^F_{m',m}(\theta)$ is the small Wigner D-function, θ is the Euler angle around the y axis, and $\hat{T}_{F,m}$ is the irreducible tensor. The explicit form of $d^F_{m',m}(\theta)$ for the case $F = 1$ [Varshalovich88] is:

$$d^{(1)}_{m',m}(\theta) = \begin{pmatrix} \frac{1}{2}(1+\cos\theta) & -\frac{1}{\sqrt{2}}\sin\theta & \frac{1}{2}(1-\cos\theta) \\ \frac{1}{\sqrt{2}}\sin\theta & \cos\theta & -\frac{1}{\sqrt{2}}\sin\theta \\ \frac{1}{2}(1-\cos\theta) & \frac{1}{\sqrt{2}}\sin\theta & \frac{1}{2}(1+\cos\theta) \end{pmatrix} \tag{12.11}$$

and for $F = 2$ we have,

$$d^2_{m',m}(\theta) =$$

m, m'	2	1	0	-1	-2
2	$\frac{1}{4}(1+\cos\theta)^2$	$-\frac{1}{2}\sin\theta(1+\cos\theta)$	$\frac{1}{2}\sqrt{\frac{3}{2}}\sin^2\theta$	$-\frac{1}{2}\sin\theta(1-\cos\theta)$	$\frac{1}{4}(1-\cos\theta)^2$
1	$\frac{1}{2}\sin\theta(1+\cos\theta)$	$\frac{1}{2}(2\cos^2\theta+\cos\theta-1)$	$-\sqrt{\frac{3}{2}}\sin\theta\cos\theta$	$-\frac{1}{2}(2\cos^2\theta-\cos\theta-1)$	$-\frac{1}{2}\sin\theta(1-\cos\theta)$
0	$\frac{1}{2}\sqrt{\frac{3}{2}}\sin^2\theta$	$\sqrt{\frac{3}{2}}\sin\theta\cos\theta$	$\frac{1}{2}(3\cos^2\theta-1)$	$-\sqrt{\frac{3}{2}}\sin\theta\cos\theta$	$\frac{1}{2}\sqrt{\frac{3}{2}}\sin^2\theta$
-1	$\frac{1}{2}\sin\theta(1-\cos\theta)$	$-\frac{1}{2}(2\cos^2\theta-\cos\theta-1)$	$\sqrt{\frac{3}{2}}\sin\theta\cos\theta$	$\frac{1}{2}(2\cos^2\theta+\cos\theta-1)$	$-\frac{1}{2}\sin\theta(1+\cos\theta)$
-2	$\frac{1}{4}(1-\cos\theta)^2$	$\frac{1}{2}\sin\theta(1-\cos\theta)$	$\frac{1}{2}\sqrt{\frac{3}{2}}\sin^2\theta$	$\frac{1}{2}\sin\theta(1+\cos\theta)$	$\frac{1}{4}(1+\cos\theta)^2$

$$\tag{12.12}$$

For our initial conditions, the only non zero collective spin are $\hat{T}_{1,0} \neq 0$ and $\hat{T}_{2,0} \neq 0$ which include the state $|-1\rangle\langle-1|_B$.

For $\hat{T}_{K=1,m}$ this gives:

$$\hat{T}_{1,m'=\pm 1} = \pm\frac{1}{\sqrt{2}}\sin\theta\hat{T}_{1,0} \tag{12.13}$$

$$\hat{T}_{1,m'=0} = \cos\theta\hat{T}_{1,0} \tag{12.14}$$

and in the cartesian coordinates it is:

$$\hat{T}_{1,x'} = -\frac{\hat{T}_{1,m'=1} - \hat{T}_{1,m'=-1}}{\sqrt{2}} = -\sin\theta\hat{T}_{1,z} \tag{12.15}$$

$$\hat{T}_{1,y'} = -\frac{\hat{T}_{1,1} + \hat{T}_{1,-1}}{i\sqrt{2}} = 0 \tag{12.16}$$

$$\hat{T}_{1,z'} = \cos\theta\hat{T}_{1,z} \tag{12.17}$$

For $\hat{T}_{K=2,m}$ this gives:

$$\hat{T}_{2,m'=0} = \frac{3\cos^2\theta - 1}{2}\hat{T}_{2,0} \tag{12.18}$$

$$\hat{T}_{2,m'=\pm 1} = \pm\frac{\sqrt{3}}{2\sqrt{2}}\sin 2\theta\hat{T}_{2,0} \tag{12.19}$$

$$\hat{T}_{2,m'=\pm 2} = \frac{\sqrt{3}}{2\sqrt{2}}\sin^2\theta\hat{T}_{2,0} \tag{12.20}$$

and in the cartesian coordinates it is:

$$\hat{T}_{2,z'} = \frac{3\cos^2\theta - 1}{2}\hat{T}_{2,z} \tag{12.21}$$

$$\hat{T}_{2,x'} = -\frac{\sqrt{3}}{2}\sin 2\theta\hat{T}_{2,z} \tag{12.22}$$

$$\hat{T}_{2,y'} = 0 \tag{12.23}$$

$$\hat{T}_{HV} = \frac{\sqrt{3}}{2}\sin^2\theta\hat{T}_{2,z} \tag{12.24}$$

$$\hat{T}_{45} = 0 \tag{12.25}$$

Note, that for a non zero angle we find initially "stored" atomic excitations in the sample, i.e. non zero $\hat{T}_{HV}$.
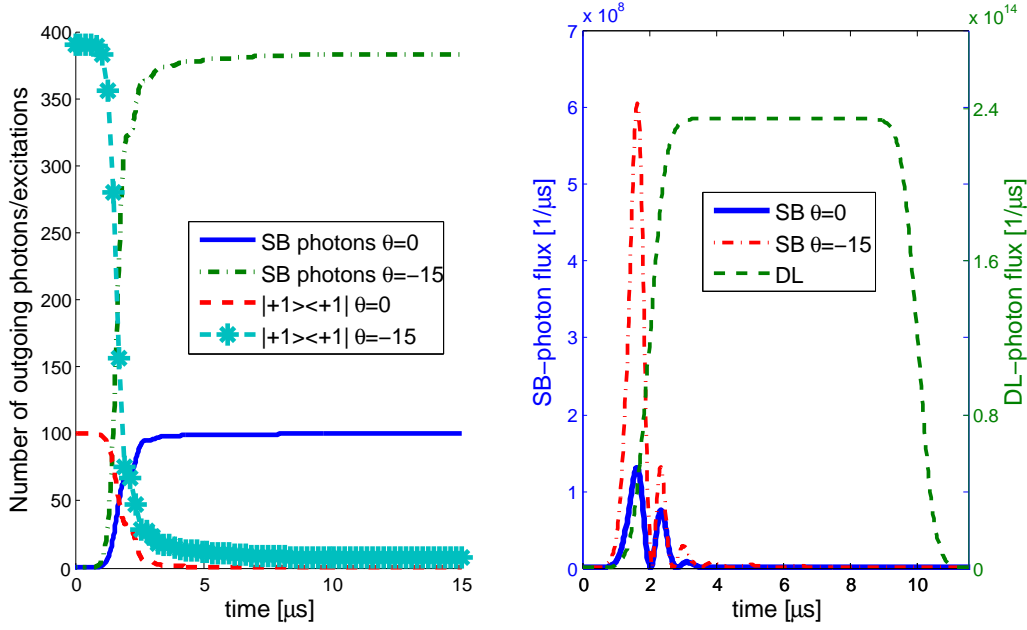
Figure 12.2: Simulating the retrieval stage after writing 100 atoms in a parabolic distribution into the sample. Left: the number of SB photons that leave the sample in full blue line (atoms aligned along the light propagation direction) and dot-dashed green line (atom with -15 degrees from the light propagation direction) and the number of atomic excitations $|+1\rangle\langle+1|$ in the sample in dashed red line (no angle) and in light blue dashed-asterisk line (-15 degree angle); Right plot: the SB photon flux on the left axis in the full blue line (0 degree angle) and in the dot-dashed red line (-15 degree angle), the DL photon flux on the right axis in dashed green line.

12.4   Pulse design

In this section we find the SB ideal pulse shape from a simulation where we initially enter a number of $|+1\rangle\langle+1|$ excitations in the atomic sample. For getting the ideal pulse shape for both writing and retrieval the excitations should be in a parabolic shaped spatial distribution [Gorshkov07b]. In Fig. 12.2 we present a simulation of a retrieval of such a distribution. On the left plot we present the SB outgoing photons (full blue line) and the atomic excitations (red dashed line). We find that after about 4μs most of the excitations are converted into SB photons.

Here we have also examined the influence of the magnetic field angle ($\theta = 0$ and $\theta = -15°$). From Fig. 12.2-left we can see that there are more than the 100 excitation that were entered, because of the extra excitations that come when we rotate the atoms, see Eq. 12.24. In Fig. 12.2-right we present the SB photon flux. Here the difference in the outgoing pulse shape when $\theta = -15°$ (dot-dashed red line) and when $\theta = 0°$ (full blue line) is evident. This is due to the different mode written in the cloud.

In most further experiments the time-reversed red-dashed pulse shape has been used. Several different pulse shapes have been tested, but no significant difference in storage efficiency was observed.

Time evolution of the signal beam

So far we have examined in chapter 10 the general performance of the experiment, and derived a $1D$ model to characterize the results in chapters 11 and 12. Our main goal was to achieve total (in-out) efficiencies as high as possible, aiming at 50% but this was not achieved experimentally. In this chapter we present the experimental characterization of the memory performance.

We start by examining the decoherence time, or storage time, of the system in section 13.1 and identify the main source of the decoherence. Next in section 13.2 we have varied both the sample OD and the DL power as these are the Raman coupling parameters[1]. Here we expect to find that as we increase the DL power (or the OD) we compress the time axis and the light should come out faster and thus above a certain DL power we would expect reaching the maximum feasible efficiency. Experimentally we find a more complicated behavior, and use our $1D$ model to explain our results in section 13.3.

As part of the memory performance tests we have also verified the linearity of the memory (section 13.4), and have tested the sensitivity to the two-photon detuning (section 13.5).

13.1 Storage time

In this section we present the measurements of the memory storage time, by varying the DL retrieval pulse starting time. The measured signals at different retrieval timing are shown in Fig. 13.1-left. The total (in-out) efficiency was measured for different storage time[2], and given in Fig. 13.1-right. Here we see that the dephasing happens on a timescale comparable to the input SB pulse duration.

There are three prominent sources for the decoherence: 1) dephasing due to magnetic inhomogeneity [Reim11, Zhao09], 2) reduction of the atomic wavepacket overlap[3] between atoms in the storage state and the initial state [Riedl12, Zhang09], and 3) collisional spin relaxation between atoms [HAPPER72] (typically relevant for room temperature experiments). In our case since we have done the experiments with cold ^{87}Rb cloud inside a magnetic trap and between two Zeeman

---

[1] We have shown in section 11.4 that the signal evolution is governed by $\tilde{\alpha}_2^2 T_{1,z} \cdot \Xi_{sigma}$ which can be expressed as $R \cdot OD$.

[2] We define here the storage time from the end of the input SB till the rise time of the DL (taken at 10%)

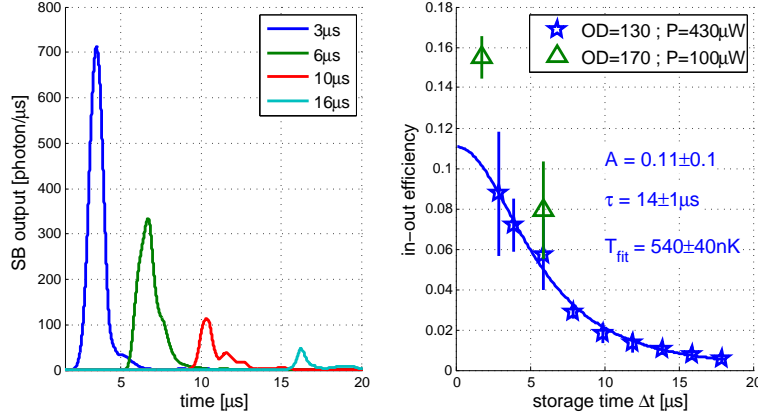[3] The appropriate length scale is the de Broglie wavelength.

Figure 13.1: Left: the SB retrieval pulses for different storage time. Right: the total memory efficiency as a function of the storage duration. The line represents a fit appropriate to a magnetic field inhomogeneity.

ground sublevels that are first order sensitive to the magnetic field potential. We examine how the magnetic field inhomogeneity and the loss of the wave function overlap influence the dephasing time. We find that the dephasing due to the magnetic field inhomogeneity is dominant for our experimental parameters.

Magnetic dephasing

Here we consider the magnetic dephasing of the Raman coherence due to external magnetic field, i.e. the Larmor precession of the coherence [Reim11]. For this we define a storing (or Raman) operator as $\hat{S} = a\mathbb{1} + b\hat{O}$, where $\mathbb{1}$ is the unit operator, $\hat{O}$ is the coherence operator, and a, b are the coefficients that are set by the experimental condition and have no relevance for the dephasing time. For our case $\mathbb{1} = |+1\rangle\langle+1| + |-1\rangle\langle-1|$ and $\hat{O} = C^{1,0}_{1,+1;1,-1}|+1\rangle\langle-1| + C^{1,0}_{1,-1;1,+1}|-1\rangle\langle+1|$. Here $C^{1,0}_{1,\mp1;1,\pm1}$ are the Clebsch-Gordan coefficients but for our case they are equal and therefore we absorb them into the b coefficient. $|\pm1\rangle$ are the atomic hyperfine ground sublevels of the $F_0 = 1$ state with ±1 denotes the Zeeman sublevel.

The coherence undergos Larmor precession due to the inhomogeneous magnetic field in the sample. In a suitably rotating frame the time evolution operator is written as:

$$\hat{U} = e^{i\Delta\omega t}|+1\rangle\langle+1| + e^{-i\Delta\omega t}|-1\rangle\langle-1| \tag{13.1}$$

with $\Delta\omega = g_F\mu_B(B(x,y,z) - B_0)$ the local Larmor frequency offset inside the sample, with g_F the Landé g-factor, μ_B Bohr magneton, B the position dependent magnetic field, and B_0 the bias magnetic field. In our case we can write the frequency components as the harmonic potential due to the magnetic trap [Hilliard08b], to get

$$\hbar\Delta\omega = \frac{1}{2}m\omega_\perp^2(x^2 + y^2) + \frac{1}{2}m\omega_z^2 z^2 = \frac{1}{2}k_B T\left(\tilde{x}^2 + \tilde{y}^2 + \tilde{z}^2\right) \tag{13.2}$$

where $\omega_\perp$ (ω_z) is the radial (axial) trap frequency, $\sigma_\perp$ (σ_z) is the thermal cloud *rms* radius, k_B is the Boltzmann constant, T is the sample temperature, and $\hbar$ is the Planck's constant divided by 2π. In addition we have redefined the coordinate system such that we can rewrite the harmonic oscillator as symmetric in all axes ($\tilde{x} = x/\sigma_\perp, \tilde{y} = y/\sigma_\perp, \tilde{z} = z/\sigma_z$).

The time evolution of the coherence is given by $\hat{U}^\dagger \hat{O} \hat{U}$, and $\hat{S}^\dagger |-1\rangle$ is the storage (Raman transfer) operation, therefore if we assume full retrieval after the writing and storage time we get that the total efficiency is proportional to:

$$\eta(t) \propto \left| \frac{\int d^3r n(r) \langle -1 | \hat{S} \hat{U}^\dagger \hat{O} \hat{U} \hat{S}^\dagger | -1 \rangle}{\int d^3r n(r)} \right|^2 =$$

$$= \frac{1}{\left| \int d^3r n(r) \right|^2} \left| 2\Re(ab^*) \int d^3r n(r) e^{2i\Delta\omega(r)t} \right|^2 \tag{13.3}$$

with $n(r)$ the atomic sample density distribution. Here we solve this for a thermal cloud to get:

$$\eta(t) \propto \left| (1 - 2i(k_B T/\hbar)t)^{-3/2} \right|^2 \tag{13.4}$$

Introducing the proportionality constant A we get the total efficiency as a function of time

$$\eta(t) = A \left(1 + 4 \left(k_B T/\hbar \right)^2 t^2 \right)^{-3/2} = A \left(1 + 4t^2/\tau^2 \right)^{-3/2} \tag{13.5}$$

with $\tau = \hbar/(k_B T)$. To this functional we fit the measured results, as shown in Fig. 13.1-right. This gives a typical time scale of $\tau/2 = 7\mu$s. Here we find that the coherence time is inversely proportional to the cloud temperature, as we decrease the temperature we increase the coherence time. For two data sets we compare the fitted temperature from the storage time measurements to the independent temperature measurements from the absorbtion imaging, and find an agreement to within the error bars. From the absorption imaging we find temperatures of 445 ± 10nK and 550 ± 10nK, and from the storage time we find temperatures of 470 ± 50nK and 545 ± 50nK respectively.

Overlap between the stored state and the initial state

Here we estimate the difference in motion between the atoms in the ground state $|-1\rangle$ and the storage level $|+1\rangle$. Since when the wavepackets in the two states separate in time it causes loss of coherence [Riedl12, Zhang09]. Here the important parameter is the de Broglie wavelength, i.e. we want that both wavepackets will overlap to within their de Broglie wave length.

In our case the state $|+1\rangle \langle +1|$ is anti-trapped and the stored atoms will be pushed away from the trapped atoms $|-1\rangle \langle -1|$. To find how long it takes the two wavepackets to separate, we solve the harmonic and repulsive time evolution ($\ddot{x}_- = -\omega^2 x_-$ and $\ddot{x}_+ = +\omega^2 x_+$). We start with the time evolution of the atoms in the state $|-1\rangle \langle -1|$

$$x_-(t) = x_0 \sin \omega t \tag{13.6}$$

with x_0 the edge of the cloud, and ω the trap radial frequency. Here we assumed initial conditions of the atoms at the center of the cloud without any lose of generality, since we will consider the evolution from any given time $t + \tau$ with τ the storage time and t sets the initial condition. Then at a certain time t we transfer an atom into the state $|+1\rangle \langle +1|$ which starts evolving in a potential with initial conditions given by $x_-(t)$, which gives:

$$x_+(t, \tau) = x_0 \left(\sin \omega t \cosh \omega \tau + \cos \omega t \sinh \omega \tau \right) \tag{13.7}$$

$$x_-(t, \tau) = x_0 \left(\sin \omega t \cos \omega \tau + \cos \omega t \sin \omega \tau \right) \tag{13.8}$$
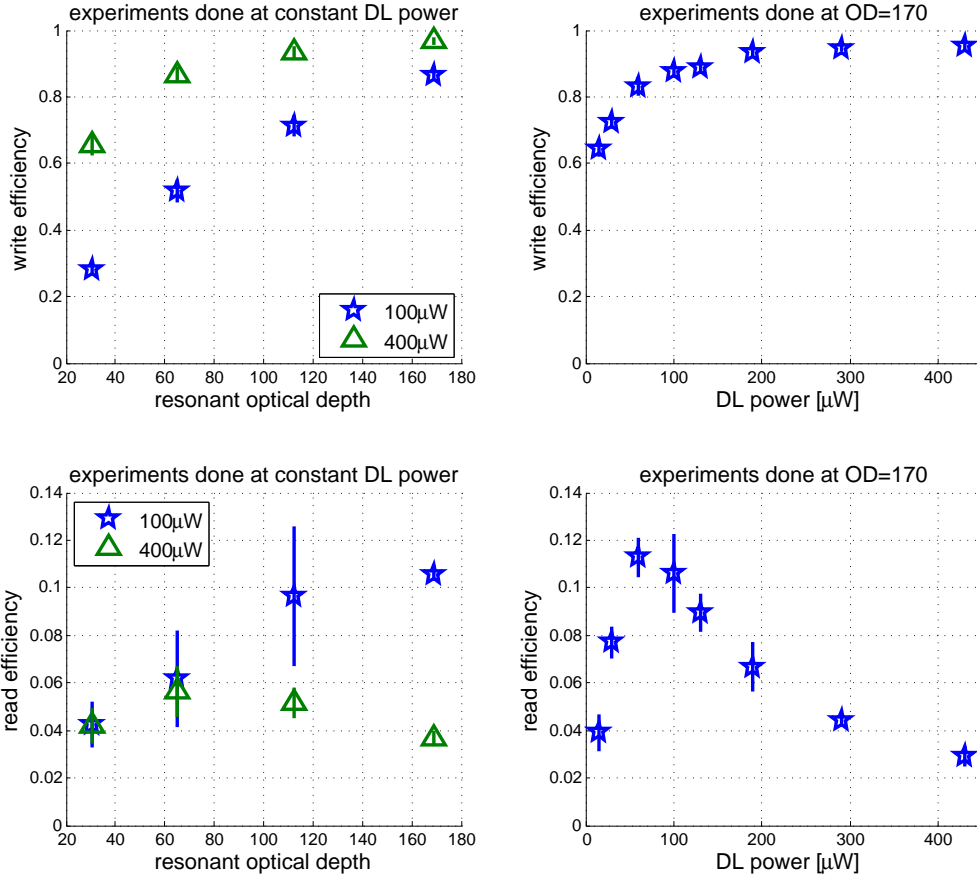
Figure 13.2: Top/bottom row: the write/retrieval efficiency as function of the OD for constant DL power (left plots) or as function of DL power for constant $OD = 170$ (right plots).

with

$$
\Delta x / x_0 = x_+(t, \tau)/x_0 - x_-(t, \tau)/x_0 =
$$
$$
\sin \omega t \left(\cosh \omega \tau - \cos \omega \tau \right) + \cos \omega t \left(\sinh \omega \tau - \sin \omega \tau \right) \tag{13.9}
$$

To estimate the appropriate coherence time we need to compare $\Delta x / \lambda_{dB} \approx \sigma / \lambda_{dB}$ as a function of time, with σ the cloud *rms* radius and $\lambda_{dB} = \sqrt{2\pi\hbar^2 / m k_B T}$ is the de Brolie wavelength depending on the cloud temperature. For our experimental parameters this gives $\sigma / \lambda_{dB} \approx 40$ and for $\sin \omega t = 1$ we find $\Delta x / \lambda_{dB} = 1$ at $\tau = 220 \mu$s.

From the above estimation it is clear that the loss of the overlap between the wave functions of the $|-1\rangle \langle -1|$ atoms and the stored atoms, $|+1\rangle \langle +1|$, does not cause for our observed decoherence mechanism.

13.2   Varying the Optical depth DL power

In this section we go over the experimental results in which we vary the sample OD or the DL power while keeping the other parameters constant. We present the at first sight surprising result that both increasing the OD and increasing the DL power reduces the total efficiency. Here we give an overview of the experimental results and explain the physical source of the effect while, in section 13.3 we show that a $1D$ simulation qualitatively reproduces the effect.
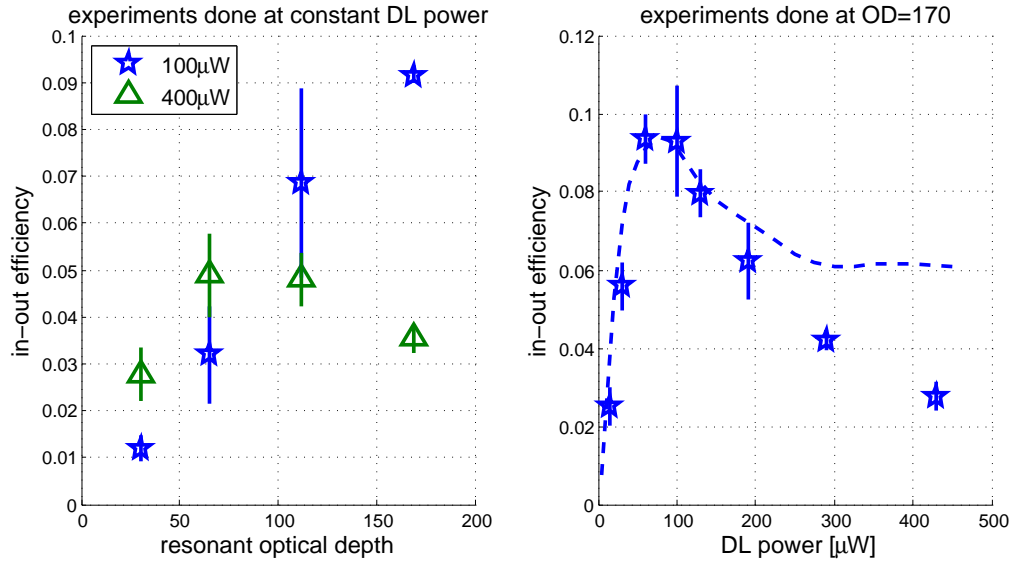
Figure 13.3: In-out efficiency when varying the OD (left plot) for two different DL powers, and for varying the DL power (right plot) for constant *OD*. The dashed line on the right plot represents numerical simulation using these experimental parameters.

In Fig. 13.2 we show the writing and retrieval efficiency of the memory for two different conditions: left plots shows the efficiency for constant DL power and varying the sample OD, and in the right plots we show the efficiency for constant sample OD (= 170) and changing the DL power. From the writing efficiency, as shown in Fig. 13.2-top we find as expected, that as we increase either the DL power or the sample OD the efficiency increases until it reaches saturation at 90%. On the other hand, when examining Fig. 13.2-bottom we find a different behavior. In Fig. 13.2-bottom-right we find a maximum retrieval efficiency at about 60μW DL power, where at lower powers the retrieval efficiency increases (as expected) but when increasing the DL power above 60μW instead of saturating the retrieval efficiency we see that it value reduces. A similar result is found in Fig. 13.2-bottom-left when changing the OD for a DL power of 400μW. Note that the retrieval efficiency results at constant power of 100μW monotonic increase as one would have expected.

In Fig. 13.3 we show the total (in-out) efficiency of the memory and find a similar result as in Fig. 13.2-bottom since the writing efficiency is saturated. To understand possible mechanism that could explain this result we examine the actual retrieved signals.

Even though we have a comparable decoherence time and input SB pulse duration, we still expect that as we increase the DL power the time axis will be compressed [Mishina07]. Which means that for higher DL power we should get the light to come out faster and thus get better efficiency in the retrieval stage. We do not observe this increase in the retrieval efficiency, and therefore examine the retrieved SB pulse shape with the different conditions. In Fig. 13.4-left we use the optimal DL power for the highest OD and varied the OD and find that the pulses become shorter with a higher peak photon flux and observe an improvement in both the write and retrieval efficiency. From the pulses shape we observe a combination of shrinking of the time axis with the ability to drive out more photons, as we expect. This is compatible with the assumption that a
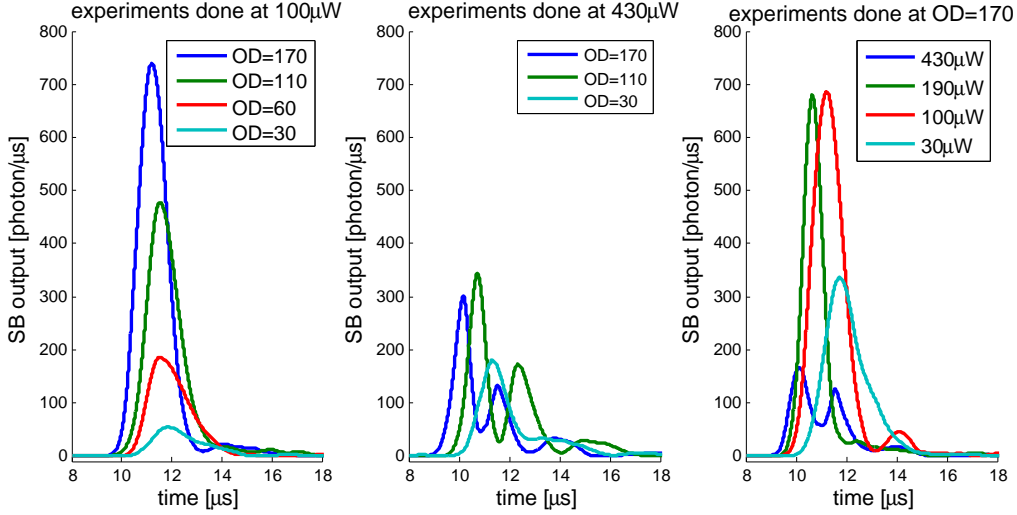
Figure 13.4: SB photon flux at the retrieval stage as function of time. Left: different OD and constant DL power of $P_{DL} = 100\mu W$; middel: different OD and constant DL power of $P_{DL} = 430\mu W$; right: different DL power and constant $OD = 170$.

similar mode has been written into the sample with different efficiency.

Next we examine Fig. 13.4-middle in which we have used a high DL power ($430\mu W$) and varied the OD. Except for the lowest OD ($= 30$) for all cases the writing efficiency is about 90%, but the retrieval efficiency drops as we increase the OD (see also Fig. 13.3-left). From the photon flux we see that for the higher OD the peak photon flux decreases between $OD = 110$ and $OD = 170$ and has more wiggles, i.e. has higher frequency components. This hints that as we increase the OD we actually get a lower photon flux that would come out over a longer time duration, and in the case of no losses both cases would give the same output photons but at a different time. This situation can only occur if for such a high DL power we actually write a different spatial mode into the sample, such that the outgoing photon flux is different. In Fig. 13.4-right we have used the highest OD ($= 170$) and varied the DL power. We see a similar effect as for Fig. 13.4-middle, this is compatible with the theory given in [Mishina07].

In this section we have suggested that the reduction of efficiency is due to the combination of high loss rate and writing different modes into the atomic sample. In the next section we show simulation results to support this explanation.

13.3   Simulating the OD and DL power results

When discussing the total (in-out) efficiency we need to separate the writing efficiency and the retrieval efficiency. For the writing efficiency we would expect that for a given OD there is a DL power above it the writing efficiency saturates. Then, at the retrieval stage, given a sufficiently high DL power we expect a change in the outgoing pulse shape but not in the retrieval efficiency. We remind here that the coupling parameter for the interaction is $R \cdot OD$ with R the Rayleigh scattering rate (see section 11.4), i.e. during the retrieval changing the DL power is equivalent to changing the OD. Contradictory to this picture we find that even when the writing efficiency is high (about 90%) and does not change when varying the DL power or the OD, the retrieval and total efficiency is reduced when increasing the DL power or the OD. In first sight this result is surprising, but as we show in this section it can be explained by combining a 1D model with an appropriate loss rate.
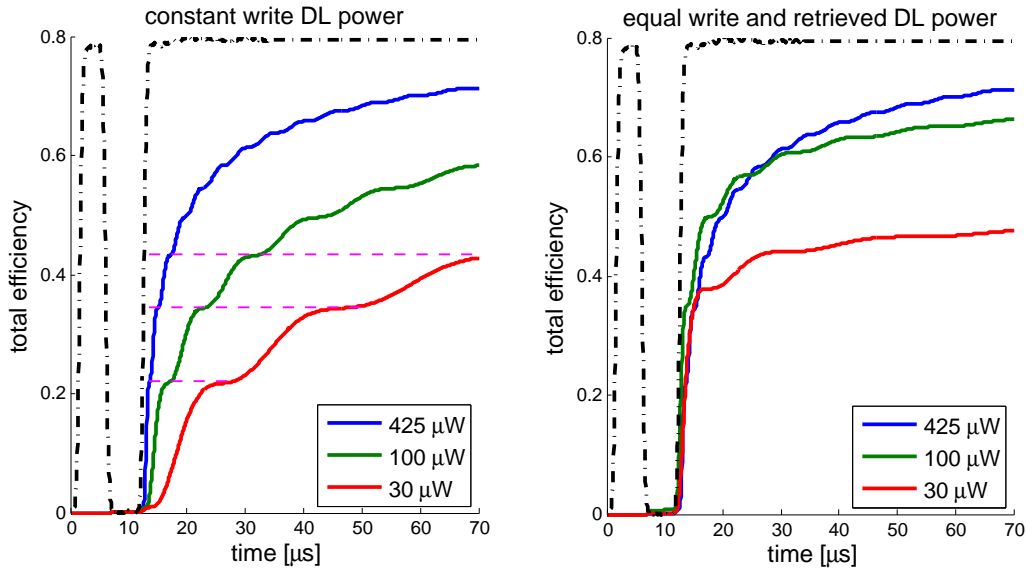
Figure 13.5: Simulation of the total (in-out) efficiency of the memory as function of time without any losses; in the black dot-dashed line the DL flux normalized to fit the axis scale. Left: constant DL power in the write stage and varying the DL power during the retrieval stage as indicated by the legend; Right: equal DL power in the write and retrieval stage as indicated by the legend. Note that the lines on the left plot are to show the compression of the time axis.

In the above picture the hidden assumption is that we write the same spatial mode into the sample, but when we change the DL power or the sample OD we also write a different mode in the sample. Therefore we retrieve a different pulse shape. To show this we have run two sets of simulations showing the retrieved SB photons from the sample as function of time. In the first case we present the situation of what we have expected to get by keeping the write stage DL power (425μW) constant and varying the retrieval DL power only, see Fig. 13.5-left. In the second set of simulations we use the same DL power for both the write and retrieval stages, similar to the experimental situation, and vary the DL power see Fig. 13.5-right. Note that at the end in both cases the total efficiency is similar though the temporal shape of the retrieved light pulses is different.

From Fig. 13.5-left we can see several things, first as one expects when changing the DL power we find compression or stretching of the time axis (see dashed lines). In addition as the photons come out faster we find higher total efficiency for any given time for the higher DL power, with maximum total efficiency of about 70% but after about 60μs. From Fig. 13.5-right in which we have kept the same DL power for both writing stage and the retrieval stage, we see that changing the DL power does not just compress or stretch the time axis yet the total efficiency is again about 70% after 60μs of retrieval time. When examining the SB pulse shapes (given from the total efficiency) the main difference is found at the initial stages, with more photons retrieved for the case of 100μW DL power than for the case of 425μW DL power at the initial 15μs. After those 15μs the situation is reversed and the total efficiency of the higher DL power is bigger.

To understand the source of the difference between Fig. 13.5-left and Fig. 13.5-right, we look at the mode shape that was actually written into the atoms. This is given in Fig. 13.6-left and shows the shape of the stored coherence ($|+1\rangle \langle-1|$) along the sample (at time 9μs). For the weak DL powers (30μW and 100μW) we actually get a trapezoidal shape with more excitations at the beginning of
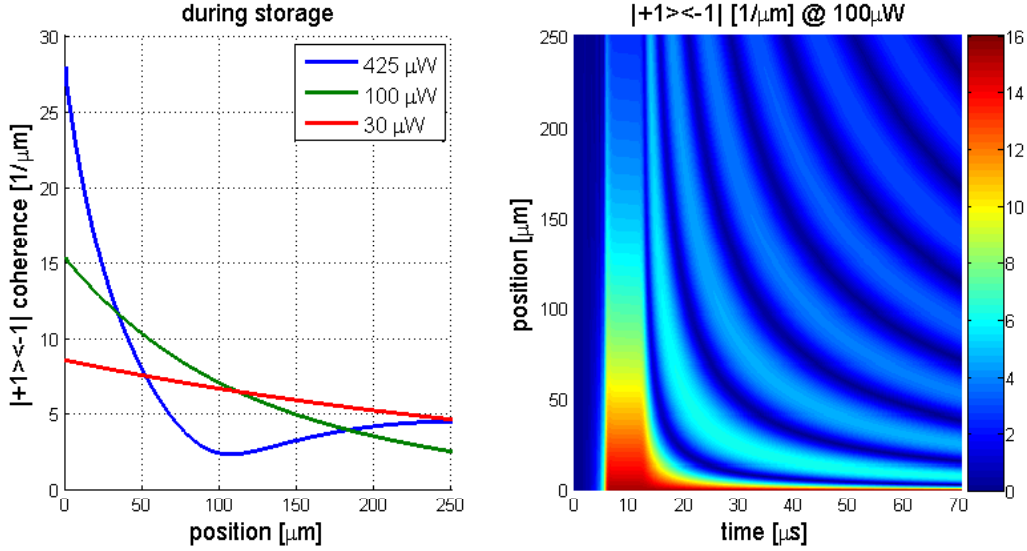
Figure 13.6: Left: The number of stored coherence $|+1\rangle\langle-1|$ per μm as function of position along the sample at different DL power at time 9μs corresponding to the storage stage. Right: position-time color map of the stored excitations $|+1\rangle\langle-1|$ at DL power of 100μW. For both plots we used $OD = 170$ and $\gamma_\pm = 0$.

the sample, and for the DL power of 425μW we have a minimum point in the middle of the sample. These shapes are closer to the ideal shape for the write stage and for backward retrieval, but are "bad" for a forward retrieval scheme [Gorshkov07b]. This difference between the stored shape explains the difference in shape of the outgoing SB mode.

Figure 13.6-right shows a color map of the stored coherence amplitude as a function of position-time, for the case of 100μW DL power. Here, the dynamics of extracting excitations from the sample during retrieval can be followed over a long time.

Another point that comes out from Fig. 13.5 and Fig. 13.6, is that the time scale for the SB light to come out is about 60μs which is much larger than the 7μs dephasing time we measured in section 13.1. Already from Fig. 13.5-right we can see that for a short retrieval pulse of about 5μs we get a higher total efficiency for the case with 100μW than for the case with 425μW. Therefore the next natural step is to take into account the losses by adding an external decay channel to the propagation equations on the two coherences $\hat{T}_{HV}$ and $\hat{T}_{45}$ similar to the work in [Gorshkov07a]. For brevity we write the change only on the time evolution equations representing the two level system (Eq. 11.56) to:

$$\frac{\partial}{\partial t}\begin{pmatrix} \hat{T}_{45} \\ \hat{T}_{HV} \end{pmatrix} = -\begin{pmatrix} \gamma_\pm & -\omega_{2p} \\ \omega_{2p} & \gamma_\pm \end{pmatrix}\begin{pmatrix} \hat{T}_{45} \\ \hat{T}_{HV} \end{pmatrix} + 2\epsilon T_{1,z}\begin{pmatrix} -\hat{\Xi}_{HV} \\ \hat{\Xi}_{45} \end{pmatrix} \qquad (13.10)$$

where $\omega_{2p} = 2\left(\hat{\Omega}_{\sigma,z} + \delta\right)$ is the difference from the two photon resonance, $\gamma_\pm$ is the additional loss term. Additionally, in the simulations done in this chapter we explicitly set the transverse magnetic field to zero. For simplicity the coherence decay, which is non-exponential (see Eq. 13.5) is modeled here by a single decay rate $\gamma_\pm$.

We set $\gamma_\pm = 2\pi \times 18$kHz, such that it reproduces the total efficiency at $OD = 170$, DL power of 100μW, and a storage time of 6μs. We have used this decoherence decay rate and the initial experimental conditions to compare the measured total efficiency and the simulated total efficiency at different DL powers.
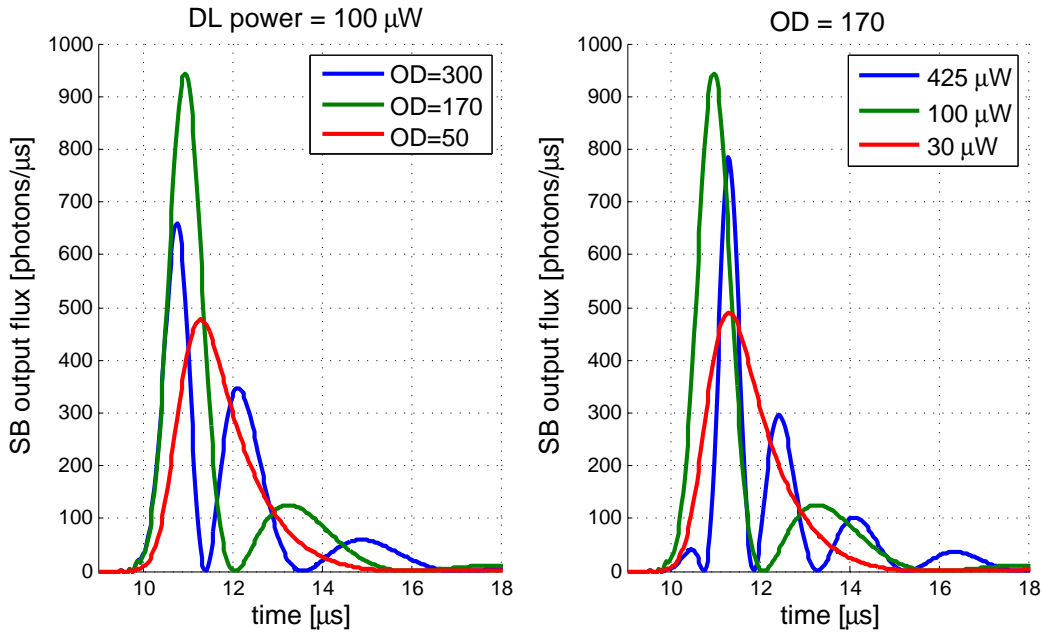
Figure 13.7: Simulating full memory stage sending 1.2×10^4 photons into a sample with different DL power or different OD, with the experimental pulse shapes and a loss rate of $\gamma_\pm = 2\pi \times 18$kHz. Here we zoom only on the SB output photon flux. Left: changing the optical depth and keeping the DL power constant at 100μW; Right: changing the DL power and keeping the OD constant at 170.

The result is given in Fig. 13.3-right, and we find that the simulation reproduce the measured total efficiency at DL powers below 150μW but overestimates the total efficiency for higher DL powers. The discrepancy could come from two sources, low detection efficiency of the higher frequency components that exists at higher DL power and the reduced visibility between the outgoing SB and LO[4] (each could contribute about 70% and thus explain the difference).

Next we examine the SB outgoing photon flux for the different conditions including the extra loss term. In Fig. 13.7-left we show the outgoing SB for different DL powers and in Fig. 13.7-right for different sample *OD*. We can see in both plots a similar behavior to the experimental data, i.e. when we increase the DL power from 30μW to 100μW we find that the peak photon flux increases and that the time scale is compressed. When increasing the DL power even further to 425μW we find that the peak photon flux reduces and more high frequency components appear for longer time. When we combine this effect with the additional loss term ($\gamma_\pm$) we get that when increasing the DL power we reduce the total memory efficiency. A similar result is found for the case of sample *OD* variation, as expected by the $1D$ theory [Mishina07]. We find here that as we increase the *OD* or the DL power we reduce the total memory efficiency, even though the writing efficiency is high in both cases.

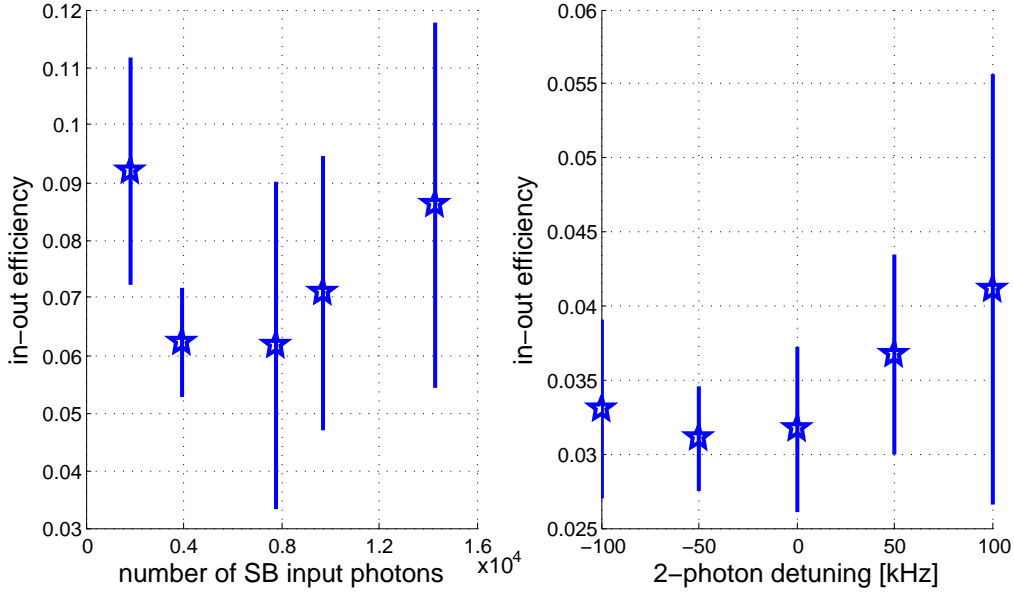
[4]We measure the SB outgoing mode shape in chapter 14

Figure 13.8: Total efficiency for the experiments testing the SB linearity (left plot) and the sensitivity to the two photon detuning (right plot).

13.4 Linearity

We test the linearity of the memory by varying the number of input photon of the SB. Here we expect the memory efficiency to be constant as the maximum number of photons sent through the atomic cloud is less than a percent of the total atom number. We note that these tests were done with an equal contribution of the wrong polarization and of the SB, i.e. before we have optimized the input polarization in section 10.2. In Fig. 13.8-left we show that the total efficiency is the same for SB photon numbers in the range $0.18 - 1.4 \times 10^4$ as expected. The experiments were done using a sample with 2×10^6 atoms, $OD = 100$, temperature of $T = 450$nK which is about 1.5 times above the condensation temperature, the storage time in these experiments is 5.5μs, with a cloud radial $1/e^2$ waist of $\sigma_\perp \sim 18.2\mu$m. We additionally note that here we used the "high" DL power region for our experiment, i.e. $P_{DL} = 400\mu$W with a write efficiency of about 85%.

13.5 Two-photon detuning

Here we are testing the sensitivity to the two photon resonance by changing the DL frequency. Being off the two photon resonance means that we don't cancel nicely the precession due to the main magnetic field, which sets $\hat{\Omega}_{\sigma,z} + \delta \neq 0$ in Eq. 11.47. This will start a coherent oscillation between the two quadratures of the stored coherence ($|-1\rangle \langle +1|$). Also these tests were done with an equal contribution of the wrong polarization and of the SB.

We find that for a few tens of kilohertz two photon detuning there is no change the total efficiency. The results are given in Fig. 13.8-right with the experimental conditions are: a sample with 4.2×10^6 atoms, $OD = 180$, temperature of $T = 530$nK which is about 1.35 times above the condensation temperature, the storage time in these experiments is 6μs, with a cloud radial $1/e^2$ waist of $\sigma_\perp \sim 19.6\mu$m. Here we used $P_{DL} = 430\mu$W with a write efficiency of about $\geq 90\%$.

The outgoing spatial mode evolution

In this chapter we describe the measurement of the spatial shape of the outgoing SB using the balanced homodyne imaging method presented in section 7.2.4. We measure the spatial mode of the SB in two regimes, without and with wrong polarization photons, as shown in Fig. 10.1. In section 14.1 measurements with pure input polarization are discussed. The effect of interfering DL wrong polarization are presented in section 14.2.

In these experiments we have changed the LO beam such that it is a close approximation to a plane wave with a gain region much bigger than the SB region. This allows us to also measure whether the SB diverges, for example due to diffraction as observed in Faraday rotation measurements with a BEC [Kaminski12b]. We note that even though in the Faraday rotation we have measured significant diffraction we do not observe it here, even when working with a pure BEC.

14.1   Pure input polarization

Here we are interested in measuring the amount of outgoing SB photons and their spatio-temporal evolution. The input SB and DL are prepared with no measurable contribution of the wrong polarization photons[1]. We repeat these measurements for two different cloud conditions.

We start by measuring the time evolution of the signal (with the large LO at the same day) using the bucket detection. In Fig. 14.1 we show the time evolution of the SB for the two different cloud parameters. The dashed black line shows the different LO pulse timing used for the spatially resolved measurements. Note that the observed time evolution is different from the pulse shapes presented in the preceding chapter. This difference is assigned to the different LO shape which defines the detection spatial mode.

In these experiments we used two thermal clouds with parameters: OD of 160 and 180, *rms* radius of 10.5μm and 9μm ($1/e^{0.5}$), 4.2×10^6 and 3.9×10^6 atoms, and reduced temperature $T/T_c = 1.5$ and $T/T_c = 1.2$. We use 1.87×10^4 total input SB photons with storage duration of 3.5μs, and DL power of 100μW which gave maximum efficiency for these parameters (see section 13.2).

Here we analyze the images as described in section 7.2.4. For the case with no

---

[1]This means that when evaluating $\bar{S}$ (defined by Eq. 7.16) we set $\rho_{wp} = 0$.
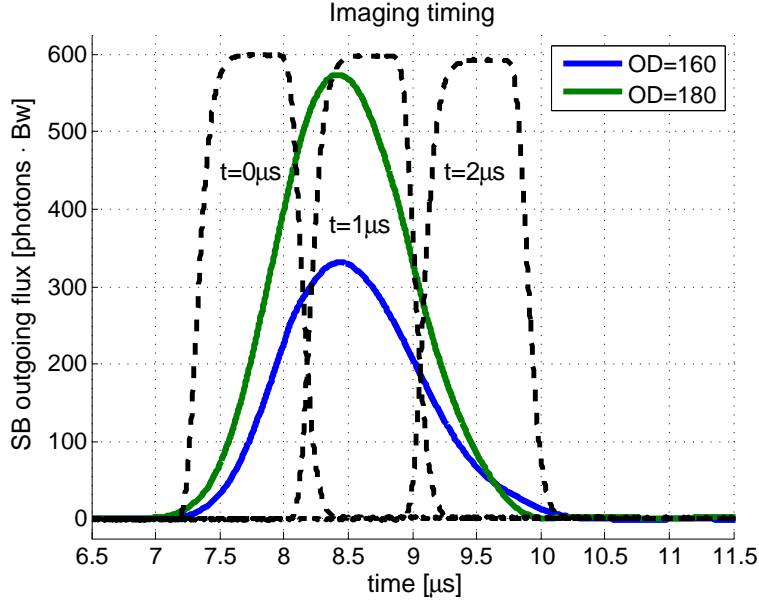
Figure 14.1: The SB output flux measured with the same LO used for the imaging. The dashed black lines represents the timing of the LO pulses, for $0\mu s$, $1\mu s$, and $2\mu s$ that are used in Fig. 14.2
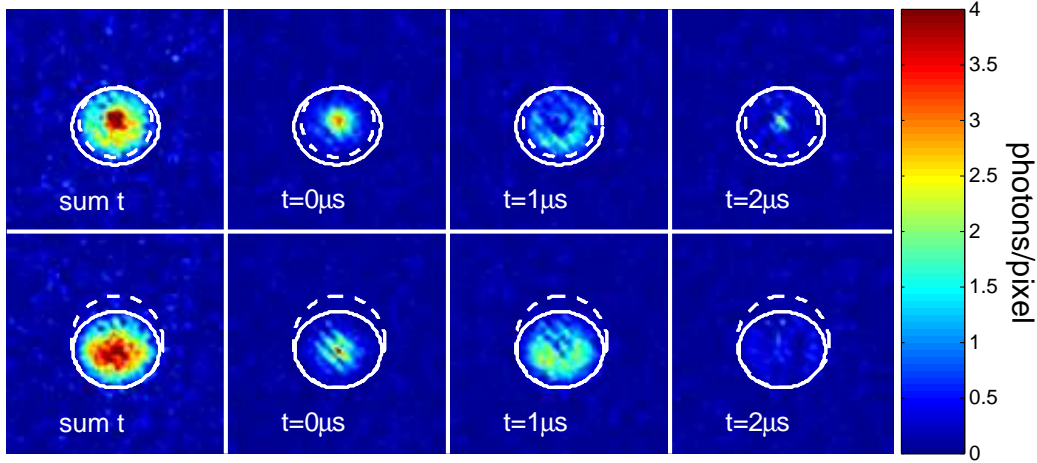

Figure 14.2: The SB outgoing photons at different times, with the left frame is the sum of all three other frames. The full white circle indicates the SB $1/e^2$ waist and the dashed white circle indicates the atoms $1/e^2$ waist.

wrong polarization photons we rewrite Eq. 7.19 to get:

$$2 \left\langle \bar{S}_{im}^2(x,y) \right\rangle_r = \left(\int_0^T dt \rho_S \cos \phi_S \right)^2 + \left(\int_0^T dt \rho_S \sin \phi_S \right)^2 \qquad (14.1)$$

The results are shown in Fig. 14.2. The presented signal is the average over many realization of the sum of the squares of the two electric field quadratures integrated over the LO pulse duration. From these measurement we can learn how the SB spatial mode evolves during the retrieval stage. As can be seen it changes with time. The light from the high OD regions comes out earlier than from the regions with lower OD, as evident in the ring shape at time $1\mu s$ in Fig. 14.2.

One of the motivations of these measurements was to test whether in these experiments the SB diffracts when leaving the sample similar to the effect mea-

	$OD = 160$	$OD = 180$
sum t	1850	1550
$t = 0\mu s$	540	580
$t = 1\mu s$	1045	690
$t = 2\mu s$	265	280

Table 14.1: The mean number of detected photons in the imaging for the different images. Counting in the SB $1/e^2$ waist region. In these experiments we used 1.87×10^4 input SB photons with storage time of $3.5\mu s$.

sured in [Kaminski12b]. Such diffraction of the SB results in a reduction of the LO-SB visibility when measuring with the bucket detection. A reduction in the visibility could partly explain the observed low retrieval efficiency. As it turns out we do not see evidence of diffraction of the outgoing SB even, with a pure BEC cloud, i.e. the total detected photon flux matches nicely the spatial shape of the atomic cloud. On the other hand we do see that the visibility is reduced and therefore the detection efficiency is less than we assume in chapter 13, and for a good detection we require a LO shaped in space and time.

From the spatial resolved images, as presented in Fig. 14.2, we get a lower bound on the photon number. We measure the lower boundary since we detect the square of the mean of the electric field and not the mean of the electric field square[2]. This means that if the electric field changes its phase during the measuring time (as one would expect from the bucket detection measurements) we will underestimate the photon number.

Table 14.1 gives the lower bound on the photon number (by pixel counting) for each frame. We find total efficiency of about 10%. This is a bit surprising, since we would have expected to get better efficiency using the images than with the heterodyne bucket detection. As in the homodyne imaging detection we are not sensitive to the lowered visibility between the SB and LO in the bucket detection measurements. We attribute this to the changing of the phase of the electric field during the $1\mu s$ LO gate pulse, as we expect the electric field value to change sign.

14.2 Interference with the drive light wrong polarization

In this section we investigate the interaction between the stored SB mode and the wrong polarization stored mode, done using the misaligned DL input polarization (see Fig. 10.2) such that we have a comparable contribution of the SB and wrong polarization outgoing photons[3]. When examining the square of the homodyne signal we are sensitive to the linear contribution of the light sources and to the additional interference term that depends on the phase difference between the two light sources, see Eq. 7.19. If the two phase sources are not correlated, then the interference term will average to zero over many realizations.

In Fig. 14.3 we present the signals analyzed using Eq. 7.19 (plotting twice the signal to compensate the factor of 0.5), at a time corresponding to $1\mu s$ in Fig. 14.2. We find that the spatial mode shape for the images measuring both the SB and the storage of the wrong polarization is different than the images measuring

---

[2]Mathematically this statement is: $\langle E \rangle^2 \leq \langle E^2 \rangle$, with E the electric field. Where $\langle E^2 \rangle$ is proportional to the number of photons, and we measure $\langle E \rangle^2$.

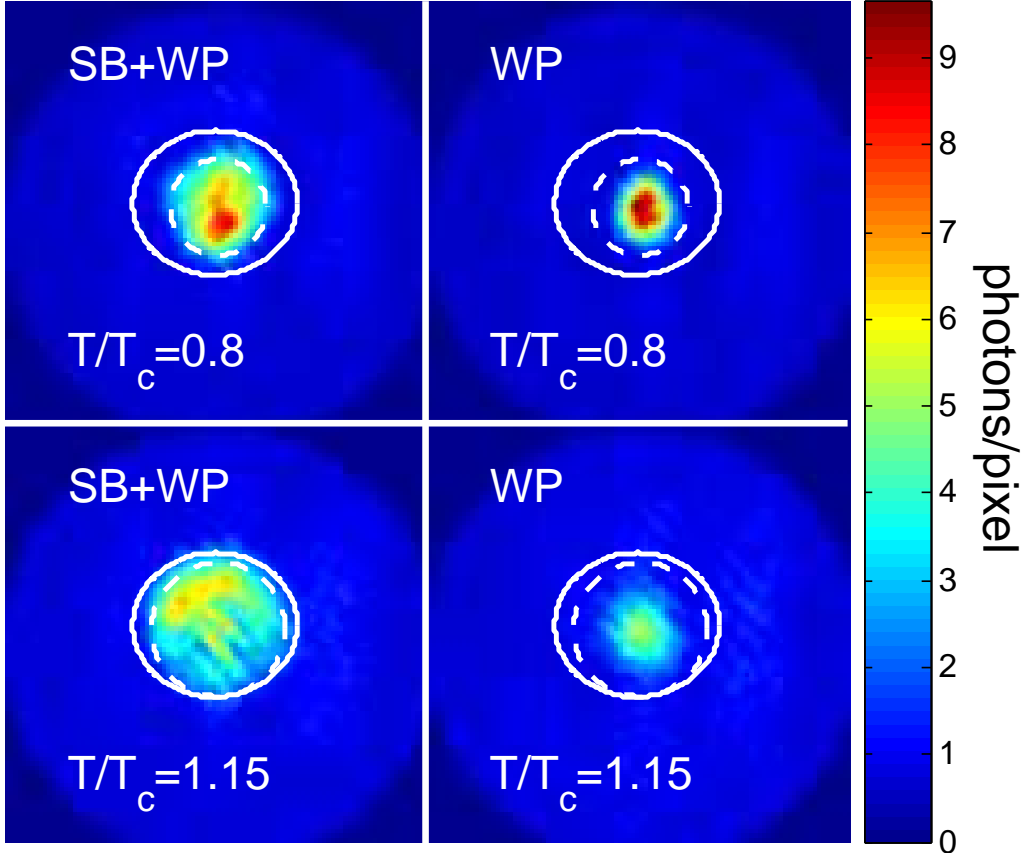[3]This corresponds to an angle of 3.5 degrees in Fig. 10.2.

Figure 14.3: The analyzed raw images presenting $2\left\langle \bar{S}^2_{im}(x,y)\right\rangle_r$ as defined by Eq. 7.19. On the left column the measurements with both the SB and wrong polarization photons and on the right column the measurements with only the wrong polarization photons. The top row shows the results down with a bimodal cloud and the bottom row for a thermal cloud just before condensing.

only the storage of the wrong polarization mode. It is also evident that the mode shape varies with the cloud temperature. From the two images with only the wrong polarization photons we measure a stronger signal for the higher OD cloud. To investigate if the interference term has a non zero contribution, we subtract the two images (left minus right frames in Fig. 14.3). The result is the combined contribution of the SB and the interference term, and are shown in Fig. 14.4 together with the cross sections with the sample OD.

Here we find, unexpectedly, that the difference images have negative values at the center, more pronounced as we increase the peak OD of the cloud. The negativity is due to the interference term of Eq. 7.19, and implies some locking mechanism between the two phases ($\phi_S - \phi_{wp} \approx$ const.), that becomes more dominant as the OD is increased. The source for such a mechanism is not clear to us.

Since this results implies a correlated phase difference, we take a closer look at the fair sampling assumption. The source of the wrong polarization comes from the DL, therefore we are interested in comparing the phase difference between the SB and the DL before interacting with the atoms. We do this by using the heterodyne detector measuring this phase difference using the bucket detection setup discussed in section 7.1. From this independent testing we find that the relative phase is stable only over several minutes. The actual measurements of each set took over one hour and 40 minutes, with each realization taking about 80s. This means that over the time it took to take 20 different realizations we had
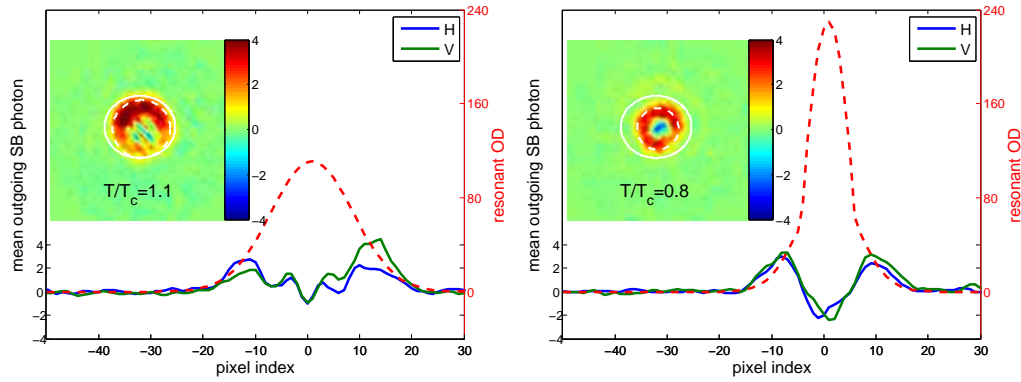
Figure 14.4: The cross-section and images (inset) of the difference between the outgoing SB and wrong polarization and only the wrong polarization. The cloud OD is overlapped with the cross-section as a right axis.

enough time to sample sufficiently different phases to assume fair sampling.

As the time it took to take the data is much larger than the phase stability of our setup and the fact that we see consistent results for the different peak OD, suggest a phase locking mechanism is present.

14.3 Potential for multimode memory

Our balanced homodyne imaging system is appropriate for measuring multimode memory. The high OD achieved here is good for storing many different spatial modes [Zeuthen11], and using our imaging system we can identify up to 30 different independent image patterns.

For utilizing our imaging system for a multimode memory, we need to add a phase lock on the different beams before the atoms. This will allow us to chose which quadrature of the SB electric field we measure in each realization, and will remove the need to average over many realizations.

Hindsight is 20/20

The phrase hindsight is 20/20 comes for the American vision test, and states that if you could see how an event would have turned out, you could have seen perfectly how to avoid its problems[1]. Similarly, this chapter is devoted to answer the question: Now after the experiments are done, what would one change to improve it?

The first thing we can improve is the storage time. In our setup we have measured, in section 13.1, a storage time of $7\mu s$ when using the Zeeman sublevels $\left| F_0 = 1, m_f = \pm 1 \right\rangle$ with F_0 the ground level hyperfine quantum number and m_f the Zeeman sublevel quantum number. The source for this dephasing is the first order sensitivity of the Zeeman sublevel splitting in the inhomogeneous field of the magnetic trap. One can drastically reduce this by replacing the target level $\left| F_0 = 1, m_f = +1 \right\rangle$ to $\left| F_0 = 2, m_f = +1 \right\rangle$ which results in first order insensitivity to the magnetic field. The level configuration is shown in Fig. 15.1-(A). In the group of A. Kuzmich at Atlanta a storage time of a few hundreds of milliseconds have been achieved using this configuration [Dudin10]. For our setup this change is expected to improve the storage time from $7\mu s$ to tens of milliseconds[2]. An additional improvement can be made by moving to a dipole trap and thus remove all together the different magnetic field values along the sample.

The new configuration given in Fig. 15.1-(A) requires changing the drive light (DL) frequency by $\Delta f = 6.8\text{GHz}$. This can be achieved with current technology [Appel09]. In addition to the fact that these two levels being first order magnetic insensitive, this new configuration also reduces the sensitivity to the wrong polarization of the DL beam (see section 10.2). Furthermore the optical pumping effect into $F_0 = 2$ from the inital populated ground state is significantly reduced as well (see section 10.4). This reduction is due to the larger DL detuning[3] and the reduction of DL power for the same coupling coefficient, i.e. $(\Delta_{new}/\Delta_{old})^2 \left(C^{1,0}_{2,1;1,-1}/C^{1,0}_{1,1;1,-1} \right)^2 = (6.4/1)^2 (12/4) = 125$ with $C^{...}_{...}$ the appropriate Clebsch-Gordan coefficient.

In Fig. 15.1-(B) we show an additional improvement to the configuration given in Fig. 15.1-(A), in which we have changed the roles of the initially populated

---

[1]Another interpretation for this phrase is that it is easy for one to be knowledgable about an event after it has happened.

[2]If one takes into account the next order correction in the magnetic field we expect an improvement of about $\mu_B B/\Delta E_{hf} \cong 5 \times 10^3$ that gives a time constant of about 35ms. Here μ_B is the Bohr magneton, B is the total magnetic field, and ΔE_{hf} is the ground hyperfine splitting.

[3]Here the detuning refers to between the initially populated ground state $\left| F_0 = 1, m_f = -1 \right\rangle$ and to the excited level $\left| F = 2, m_f = -2 \right\rangle$.
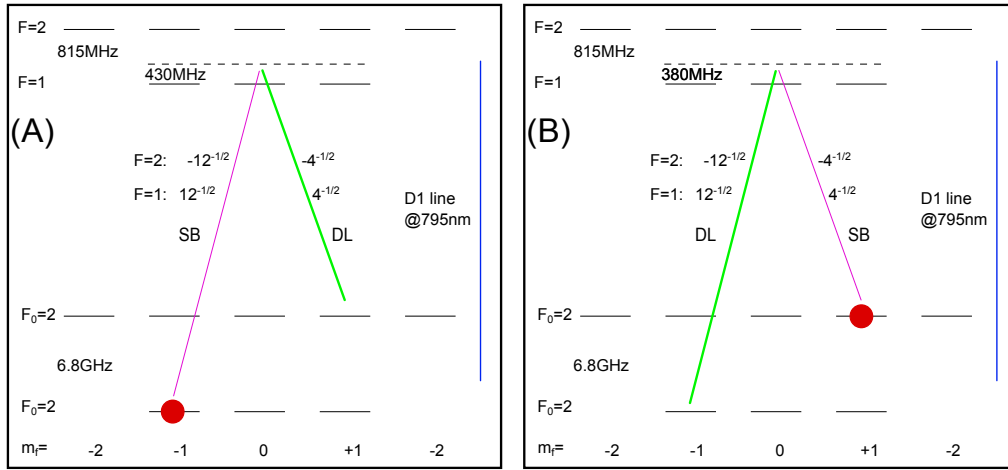
Figure 15.1: Full level scheme of Rubidium 87, used for a memory experiment. The relevant lines for the memory are shown with their Clebsch-Gordan coefficients. In (A) the initial populated ground level is $\left|F_0 = 1, m_f = -1\right\rangle$, and in (B) the initial populated ground level is $\left|F_0 = 2, m_f = +1\right\rangle$.

ground level and the target level[4]. This change improve the OD by a factor of three for the same number of atoms, due to the more favorable Clebsch-Gordan coefficients. For our parameters this will change the OD from 180 to 540 which is significantly higher than the benchmark of $OD = 200$ given in [Gorshkov07b].

In the experiments presented in this thesis we used a "magic" detuning in which there is no differential light shift to the levels due to the DL[5] (see chapter 7). To find the "magic" detuning value, we match the light shift of the two levels for the two new configurations and find:

$$\frac{1}{4\Delta} + \frac{1}{4(\Delta - \delta_h)} = \frac{1}{2(\Delta - \delta_h - \Delta_h)} \qquad \Rightarrow \Delta = \delta_h \frac{1 + \delta_h/\Delta_h}{2 + \delta_h/\Delta_h} \qquad (15.1)$$

$$\frac{1}{12\Delta} + \frac{1}{12(\Delta - \delta_h)} = \frac{1}{6(\Delta - \delta_h + \Delta_h)} \qquad \Rightarrow \Delta = \delta_h \frac{1 - \delta_h/\Delta_h}{2 - \delta_h/\Delta_h} \qquad (15.2)$$

where Δ is the detuning referenced to $F = 1$, F is the excited hyperfine quantum number, $\delta_h = 814.5$MHz is the excited hyperfine splitting, and $\Delta_h \cong 6.8$GHz is the ground hyperfine splitting. Equation 15.1 treats the case depicted in Fig. 15.1-(A) and leads for a detuning $\Delta = 2\pi \times 430$MHz. The case shown in Fig. 15.1-(B) resulting in a detuning $\Delta = 2\pi \times 380$MHz.

The second change would be to reduce the transverse dependence on the optical depth (OD). In chapter 14 we have seen that when the signal beam (SB) is mode matched to the transverse inhomogeneous sample it results in a spatial-temporal changing output SB mode. The motivation for such a design was utilizing all the atoms in the sample. This introduces a detection problem when using homodyne (or heterodyne) detection, as the visibility changes with time. One can overcome this problem by either time dependent shaping off the local oscillator such that it fits the SB output mode using similar techniques as used in [Jack09], or a sampling transverse homogenous sample.

There are several several ways to sample a transverse homogenous sample. The most simple one is to focus the SB tighter, such that the beam waist is much

---

[4]Using this level will reduce less the effect of optical pumping from 125 to 40.

[5]This could also be thought of as canceling the Faraday term in the Hamiltonian.

smaller than the sample similar to the approach used in [Riedl12]. The problem with this approach is that the coherence time is proportional to the time it takes the atoms to move out of the beam region. Another approach is to use a spatial homogeneous trap, for example by combining the trap with an additional blue detuned circular trap. This change is a significant change to the experimental apparatus. If we allow a different experimental setup then a $3D$ Mott-insulator setup is preferable in which the atoms are trapped in an optical lattice with occupation of one atom per site. This freezes the atomic motion and still have high optical depth with long coherence time. Which was demonstrated in the group of I. Bloch with a coherence time of 240ms [Schnorrberger09]. Another promising setup could be using a nano-fiber where the atoms are trapped near the fiber by the evanescent field [Dawkins11].

Part III

Summary

Summary

In this thesis we have presented two projects:

1. Detuning asymmetry in Rayleigh superradiance, in part I of this thesis.

2. First steps (in our lab) towards producing multimode high efficiency memory using ultra-cold atomic ensemble, in part II of this thesis.

In part I we have started by presenting the commonly used physical model describing Rayleigh superradiance, i.e. how the initial spontaneous scattering event produces a Bragg grating which in turn amplifies the probability of getting the next spontaneous scattering event and thus leads to an exponential increase of the scattering rate. Since this mechanism depends on the Rayleigh scattering rate, $R \propto 1/\Delta^2$ with Δ is the detuning, we were surprised and puzzled when claims appeared in the literature that superradiance can only occur when using red detuning probe light ($\Delta < 0$) [Deng10a], but proposed explanations remained controversial [Ketterle11, Deng11].

We have developed a different model for the asymmetry based on the idea that the source of the asymmetry lies in light-assisted collisions followed by radiation trapping. To support this we have measured the threshold as function of detuning, and correlate it to the additional losses. We have derived a quantitative model that evaluates the extra losses. In addition we have repeated the well known derivation of the superradiance onset when including propagation effects, starting from the Maxwell-Schrödinger equations with an additional mean-field term, showing the detuning symmetry of that model. The motivation for this was to answer one of the claims put forth in [Deng10b], which states that if one takes into account both the mean-field energy and the propagation effects than the asymmetry will show up.

The second project, presented in part II, describes the first steps towards realizing a high efficiency multimode off-resonance Raman memory. Here after describing the experimental setup and detection system, we have identified the technical problems and how these have been overcome. We have derived a simple $1D$ model and have realized a numerical simulation of the full propagation equations in time and space. This model has been used to design the input signal beam temporal mode shape.

We have examined the dependence of the system to different parameters. Here we have found that the dephasing time scale for our configuration in the magnetic trap is 7μs. Next we have tested the system sensitivity to the sample optical depth and drive light power, and have found that instead of saturating the total efficiency we get a reduction of the total efficiency. This is due to a combination

of the high dephasing rate and of writing to a non optimal mode for retrieval, in the sample. To get higher efficiency and longer storage time one can either change the memory ground levels to levels that are first order magnetic insensitive (expected increase of the storage time by $\sim 10^3$) or transfer the atoms into a dipole trap.

As a first step towards multimode memory and to test the heterodyne detection efficiency we have used the dual port imaging system used to measure the spatial Faraday rotation angle [Kaminski12a, Kaminski12b] to measure the spatio-temporal shape of the retrieved signal beam mode. Here the imaging system can detect up to 30 independent modes in the region of the atomic sample. From these measurements we have found that the retrieved signal beam has a spatial dependence corresponding to the spatial dependence of the sample optical depth. The signal in the region at higher optical depth is retrieved earlier than the signal at the region with lower optical depth. This effect reduces the visibility of the signal beam and local oscillator interference and thus reduces the efficiency of our heterodyne detection. We have suggested different approaches to reduce the sensitivity to this effect.

Part IV

Appendices

Evaluating the dipole trap frequencies

Here we are interested in finding the dipole trap depth and the appropriate trap frequencies. Starting with an atom in the ground stat angular momentum F_0 and an excited angular momentum F. We consider the off resonance light with a detuning Δ interacting with an atom via the interaction Hamiltonian H_{int}. The atomic and interaction Hamiltonians are given by:

$$H_{at} = -\hbar\Delta\sum_n |F,n\rangle\langle F,n| - \hbar(\omega_r + \Delta)\sum_m |F_0,m\rangle\langle F_0,m| \qquad (A.1)$$

$$H_{int} = -\mathbf{d}\mathbf{E} \qquad (A.2)$$

Where ω_r is the atomic resonance frequency, m (n) stands for an ground (excited) Zeeman sublevel quantum number. Since we are considering far off resonance interaction we can adiabatically eliminate the excited states, and by using the Schrödinger equation we get,

$$i\hbar\frac{\partial}{\partial t}|F,n\rangle = (H_{at} + H_{int})|F,n\rangle = 0 \qquad (A.3)$$

$$-\hbar\Delta\sum_{n_s} |F,n_s\rangle\langle F,n_s|F,n\rangle - \mathbb{1}\mathbf{d}\mathbf{E}\mathbb{1}|F,n\rangle = 0$$

$$-\hbar\Delta|F,n\rangle - \sum_{n_s}\sum_{m_s} |F_0,m_s\rangle\langle F_0,m_s|\mathbf{d}\mathbf{E}|F,n_s\rangle\langle F,n_s|F,n\rangle = 0$$

$$\hbar\Delta|F,n\rangle = -\sum_{m_s}\langle F_0,m_s|\mathbf{d}\mathbf{E}|F,n\rangle|F_0,m_s\rangle \qquad (A.4)$$

In the second line of Eq. A.3 we have added to the interaction Hamiltonian the unit matrix $\mathbb{1}$, and then write it as a sum over all ground or excited levels. Note that in general the sum also need to be over all ground hyperfine levels (F_0). Rewriting the interaction Hamiltonian and adding the above result gives,

$$H_{int} = -\mathbb{1}\mathbf{d}\mathbf{E}\mathbb{1} = -\sum_{n_s}\sum_{m_s}\langle F,n_s|\mathbf{d}\mathbf{E}|F_0,m_s\rangle|F,n_s\rangle\langle F_0,m_s|,$$

$$H_{int} = \frac{1}{\hbar\Delta}\sum_{n_s}\sum_{m_s,m}\langle F,n_s|\mathbf{E}\mathbf{d}|F_0,m_s\rangle\langle F_0,m|\mathbf{d}\mathbf{E}|F,n_s\rangle|F_0,m\rangle\langle F_0,m_s| \qquad (A.5)$$

In this thesis we are using the electric field defined as, $\mathbf{E} = \mathbf{E}^+ + \mathbf{E}^-$, where the plus sign is for positive frequencies and the annihilation operator ($\hat{a}$) and the minus sign is for the negative frequencies and the creation operator ($\hat{a}^\dagger$). Thus after the RWA (rotating wave approximation) we are left with

$$H_{int} = \frac{1}{\hbar\Delta}\sum_{n_s}\sum_{m_s,m}\mathbf{E}^-\langle F,n_s|\mathbf{d}^-|F_0,m_s\rangle\langle F_0,m|\mathbf{d}^+|F,n_s\rangle|F_0,m\rangle\langle F_0,m_s|\mathbf{E}^+ \quad (A.6)$$

Next we move to the reduce dipole matrix elements [Steck08] to get:

$$H_{int} = \frac{1}{\hbar\Delta} |\langle J \|d\| J_0\rangle|^2 \times$$

$$\sum_{n_s} \sum_{m_s,m} \sum_{q_1,q_2} E_{q_1}^- \tilde{c}_{F_0,m_s;1,q_1}^{F,n_s} \tilde{c}_{F,n_s;1,q_2}^{F_0,m} E_{q_2}^+ |F_0, m\rangle \langle F_0, m_s| \tag{A.7}$$

where $\tilde{c}_{\cdots}^{\cdots}$ is the reduction coefficient, and J_0 (J) is the total angular momentum of the ground (excited) state. The definition of the electric field is related to the intensity by $I = 2\epsilon_0 c\mathbf{E}^- \cdot \mathbf{E}^+$, with ϵ_0 is the vacuum permittivity and c is the speed of light.

A.1   Solving for a specific transition

Here we are interested in evaluate the dipole trap for the case of circular polarized light for a specific transition. Since in the superradiance experiments the atomic sample is fully polarized, i.e. all atoms are in the ground state $|F_0 = 1, m_f = -1\rangle$, and are probed by a circularly polarized light corresponding to the excited sate $|F = 2, n_s = -2\rangle$. For this case we get,

$$U_{dip} = \langle F_0 = 1, m_f = -1| H_{int} |F_0 = 1, m_f = -1\rangle,$$

$$U_{dip} = \left(\tilde{c}_{F0=1,m_f=-1;1,-1}^{F=2,n_s=-2}\right)^2 \frac{|\langle J \|d\| J_0\rangle|^2}{2\epsilon_0 c\hbar\Delta} I \tag{A.8}$$

with $\tilde{c}_{F0=1,m_f=-1;1,-1}^{F=2,n_s=-2} = 1/\sqrt{2}$.

A.2   Evaluating the trap frequencies

Expressing the dipole potential as an harmonic oscillator, by expanding the potential around the beams focus. Therefor we explicitly write the intensity into Eq. A.8, and get

$$U_{dip} = \frac{U_0}{\Delta} \frac{2P}{\pi w_0^2(1+z^2/z_r^2)} e^{-\frac{2\rho^2}{w_0^2(1+z^2/z_r^2)}} =$$

$$\approx \frac{U_0}{\Delta} \frac{2P}{\pi w_0^2} \left(1 - z^2/z_r^2 - \frac{2}{w_0^2}\rho^2\right) \tag{A.9}$$

where $z_r = \pi w_0^2/\lambda$ is the Rayleigh range, P is the beam power, w_0 is the beam waist at the focal point, λ is the beam wavelength, and $U_0 = U_{dip}\Delta/I$ is a constant of units given by Eq. A.8, and ρ and z are the transverse and axial coordinates. We write it as an harmonic potential $V = \frac{1}{2}m\omega_\perp^2\rho^2 + \frac{1}{2}m\omega_z^2 z^2$, thuse we find

$$\omega_\perp^2 = -\frac{U_0}{\Delta} \frac{8P}{\pi m w_0^4} \tag{A.10}$$

$$\omega_z^2 = -\frac{U_0}{\Delta} \frac{4P}{\pi m w_0^2 z_r^2} = -\frac{U_0}{\Delta} \frac{4P\lambda^2}{\pi^3 m w_0^4} \tag{A.11}$$

Electric field in free space

Here we are interested in examining the difference in describing the electric field using a single cavity mode and a free space mode[1] [Gorshkov07a, Gorshkov07b]. Note that the end result is the same for both descriptions.

We start with the usual description of positive and negative frequency electric field [Garrison08],

$$\mathbf{E} = \mathbf{E}^{(+)} + \mathbf{E}^{(-)} \tag{B.1}$$

$$\mathbf{E}^{(+)} = i\mathbf{g}\hat{a}e^{-i\omega_m t} \tag{B.2}$$

Here $\mathbf{g}$ is the electric field coefficient given by Eq. 11.10, ω is the frequency, and $\hat{a}$ is the annihilation operator of the cavity mode. The quantization of the field is done inside a close box with a volume of AL, with A is the cross section and L is the length. When moving to a free space one takes $L \to \infty$ which means a continuum of modes, thus we want to use only the cross section to get discrete (quanta of) modes [Gorshkov07b]. In such a case the electric field is defined as [Gorshkov07b],

$$\mathbf{E}^{(+)}(z) = i\mathbf{g}\sqrt{\frac{L}{2\pi c}} \int d\omega \hat{a}_\omega e^{i\omega z/c} = i\boldsymbol{\epsilon}\sqrt{\frac{\hbar\omega_m}{4\pi c\epsilon_0 A}} \int d\omega \hat{a}_\omega e^{i\omega z/c} \tag{B.3}$$

Here $\boldsymbol{\epsilon}$ is the electric field unit vector, ϵ_0 is the vacuum permeability, c is the speed of light, A is an effective area of the beam, and $\hbar\omega_m$ is the energy of a single photon. This result is a Fourier transform when the limits are taken to infinity. In the above transformation the annihilation operator was redefined and now its units has changed from square root of the number of photons to $[\hat{a}_\omega] = \sqrt{s \cdot \#_{ph}}$. The commutation relation is now given by,

$$\left[\hat{a}_\omega, \hat{a}_{\omega'}^\dagger\right] = \delta(\omega - \omega') \tag{B.4}$$

with $\delta(\omega - \omega')$ the Dirac delta function. Now we can define a slowly evolving annihilation operator

$$\hat{\varepsilon}(z) = \sqrt{\frac{L}{2\pi c}} e^{i(\omega_m - z/c)t} \int d\omega \hat{a}_\omega(t) e^{i\omega z/c}, \tag{B.5}$$

regaining the units of square root of the number of photons. With a commutation relation reducing to

$$\left[\hat{\varepsilon}_{sb}, \hat{\varepsilon}_{sb}^\dagger\right] = L\delta(z - z') \tag{B.6}$$

using this definition for the commutation relation and for the annihilation and creation operators reproduces the result for the cavity model, thus in Eq. 11.21 we have used the above commutation relation.

---

[1]In [Kupriyanov05, Geremia06, Mishina07] the electric field was not taken as free space one.

The Stokes parameters

In this appendix we define the Stokes parameters, which allows us a convenient way of redefine the electric field by intensity difference for different polarizations. There are several ways of defining them typically in quantum optics one defines them via the annihilation and creation operators. In this thesis we are following the notations given in [Kupriyanov05] with the units of photon flux, and not as number of photons [Geremia06]. Another very convenient way to define the Stokes parameters is using the Pauli matrices (σ) and define then as the number of photons, i.e. $\hat{\mathbf{S}} = \frac{1}{2}\hat{\mathbf{a}}^\dagger \sigma \hat{\mathbf{a}}$ [Koschorreck09] with $a \equiv [\hat{a}_+, \hat{a}_-]^T$ and $\hat{a}_+$, $\hat{a}_-$ are annihilation operators for left and right circular polarization respectively.

We define the Stokes parameters [Kupriyanov05, Mishina07] as:

$$\hat{\Xi}_0 = \frac{c}{L}\left(\hat{a}_+^\dagger \hat{a}_+ + \hat{a}_-^\dagger \hat{a}_-\right) \tag{C.1}$$

$$\hat{\Xi}_{45} = -\frac{c}{iL}\left(\hat{a}_+^\dagger \hat{a}_- - \hat{a}_-^\dagger \hat{a}_+\right) \tag{C.2}$$

$$\hat{\Xi}_\sigma = \frac{c}{L}\left(\hat{a}_+^\dagger \hat{a}_+ - \hat{a}_-^\dagger \hat{a}_-\right) \tag{C.3}$$

$$\hat{\Xi}_{HV} = -\frac{c}{L}\left(\hat{a}_+^\dagger \hat{a}_- + \hat{a}_-^\dagger \hat{a}_+\right) \tag{C.4}$$

where c is the speed of light, L is the sample length, and the subscript represents the analysis base i.e. HV - for the horizontal and vertical polarization basis, 45 - for the $\pm 45°$ degree with respect to the HV polarization basis, σ for the circular polarization basis, and 0 for the total photon flux. Note that here the the Stokes parameters have units of $1/s$, and $\Xi_0^2 = \Xi_{45}^2 + \Xi_\sigma^2 + \Xi_{HV}^2$.

Using the definition of the electric field given in Eq. 11.8, we can rewrite the Stokes parameters as:

$$\hat{\Xi}_0 = \frac{c}{g^2 L}\hat{\mathbf{E}}^-\hat{\mathbf{E}}^+ \tag{C.5}$$

$$\hat{\Xi}_{45} = \frac{c}{g^2 L}\left(\hat{E}_{+45°}^- \hat{E}_{+45°}^+ - \hat{E}_{-45°}^- \hat{E}_{-45°}^+\right) \tag{C.6}$$

$$\hat{\Xi}_\sigma = \frac{c}{g^2 L}\left(\hat{E}_{\sigma^+(R)}^- \hat{E}_{\sigma^+(R)}^+ - \hat{E}_{\sigma^-(L)}^- \hat{E}_{\sigma^-(L)}^+\right) \tag{C.7}$$

$$\hat{\Xi}_{HV} = \frac{c}{g^2 L}\left(\hat{E}_x^- \hat{E}_x^+ - \hat{E}_y^- \hat{E}_y^+\right) \tag{C.8}$$

$$\hat{\Xi}_\pm = \frac{1}{\sqrt{2}}\left(\hat{\Xi}_{HV} \pm i\hat{\Xi}_{45}\right) \tag{C.9}$$

with g the electric field dimension constant, in cgs we get $c/(g^2 L) = Ac/(2\pi\hbar\omega)$. Where A is the cross-section area of the light beam propagating through the

medium, ω is the laser radial frequency, and $\hbar$ is the Planck constant divided by 2π.

With the transformation base given by

$$\hat{E}_{45^o} = \frac{1}{\sqrt{2}} \left(\hat{E}_x + \hat{E}_y \right) \; ; \hat{E}_{-45^o} = \frac{1}{\sqrt{2}} \left(\hat{E}_x - \hat{E}_y \right) \tag{C.10}$$

$$\hat{E}_{\sigma^+} = -\frac{1}{\sqrt{2}} \left(\hat{E}_x + i\hat{E}_y \right) \; ; \hat{E}_{\sigma^-} = \frac{1}{\sqrt{2}} \left(\hat{E}_x - i\hat{E}_y \right) \tag{C.11}$$

It is useful to rewrite the Stokes parameters using the HV basis gives:

$$\hat{\Xi}_0 = \frac{c}{g^2 L} \left(\hat{E}_x^- \hat{E}_x^+ + \hat{E}_y^- \hat{E}_y^+ \right) \tag{C.12}$$

$$\hat{\Xi}_{45} = \frac{c}{g^2 L} \left(\hat{E}_x^- \hat{E}_y^+ + \hat{E}_y^- \hat{E}_x^+ \right) \tag{C.13}$$

$$\hat{\Xi}_\sigma = \frac{c}{g^2 L} i \left(\hat{E}_x^- \hat{E}_y^+ - \hat{E}_y^- \hat{E}_x^+ \right) \tag{C.14}$$

When evaluating the commutation relation of the Stokes parameters at free space using Eq. B.6 gives

$$\left[\hat{\Xi}_i(z), \hat{\Xi}_j(z') \right] = 2i\varepsilon_{i,j,k} \frac{c}{L} \hat{\Xi}_k L \delta(z - z') = 2i\varepsilon_{i,j,k} c \hat{\Xi}_k \delta(z - z') \tag{C.15}$$

Where $\varepsilon_{i,j,k}$ is the Levi-Civita unti-symmetric tensor, and i, j, k are running index $\{i, j, k\} = \{45, \sigma, HV\}$, and z and z' are the position in free space to evaluate the Stokes parameters. Thus we get the result of Eq. 11.21.

Expressing the effective Hamiltonian with the irreducible Tensors

Here we are starting with the effective Hamiltonian as derived (expressed) in [Kupriyanov05], and go through the derivation steps for describing the effective Hamiltonian using the irreducible tensors notation [Varshalovich88]. In showing the derivations steps we have two goals: 1) show how does the magnetic field changes the effective Hamiltonian as presented in [Kupriyanov05], and 2) show the actual derivation steps since they are not given in detail in [Kupriyanov05], and are important to get the right coefficients. As will be shown below, the convention of the reduced dipole matrix used could give a factor of $2F_0 + 1$ (where F_0 is the total angular momentum of the ground state).

Here in the derivation we are using the Stokes parameters as defined by Eq. C.5-C.8. Which leaves the transformation between SI units and cgs units simple.

D.1 The starting point - definitions

In this section we start with the effective Hamiltonian after using the RWA and adiabatically eliminating all the excited states one get the well known description for the effective light-atom interaction Hamiltonian [Kupriyanov05, Kaminski12b]:

$$H_{eff} = -\hat{E}_i^- \alpha_{i,j} \hat{E}_j^+ \tag{D.1}$$

$$\hat{\mathbf{E}}_0 = \hat{\mathbf{E}}_0^- + \hat{\mathbf{E}}_0^+ \tag{D.2}$$

$$\alpha_{i,j} = \sum_{m,m'} \sum_n \frac{\langle F_0, m' | d_i | F, n \rangle \langle F, n | d_j | F_0, m \rangle}{-\hbar(\omega - \omega_{n,m}) - i\hbar\Gamma/2} |F_0, m'\rangle \langle F_0, m| \tag{D.3}$$

where H_{eff} is the effective Hamiltonian, $\hat{\mathbf{E}}_0$ is the electric field, $\alpha_{i,j}$ is the polarizibility tensor, $\hat{\mathbf{E}}^+$ ($\hat{\mathbf{E}}^-$) is the electric field operator describing the positive (negative) frequency components, ω is the laser frequency, $\omega_{n,m}$ is the resonance line frequency, $\{i, j\}$ indicates $\{x, y\}$ cartesian coordinates, Γ is the line width (used to account for spontaneous emission losses), F_0 (F) is the ground (excited) state hyperfine total angular momentum with the ground (excited) sublevels m or m' (n), and $\mathbf{d} = e\mathbf{r}$ is the dipole moment with the corresponding matrix element $\langle F_0, m' | d_i | F, n \rangle$. Here we also invoke the sum rule ($\{i, j\} = \{1, 2\} = \{x, y\}$, and choose the quantization along the light propagation direction z thus we consider only transverse electric field. Note we got the same result in appendix A Eq. A.6.

Next we use the definition of the irreducible tensors [Varshalovich88],

$$|F_0, m'\rangle \langle F_0, m| = \sum_{K,Q} \sqrt{\frac{2K+1}{2F_0+1}} C_{F_0,m,K,Q}^{F_0,m'} \hat{T}_{K,Q} \tag{D.4}$$

$$\hat{T}_{K,Q} = \sqrt{\frac{2K+1}{2F_0+1}} \sum_{m',m} C_{F_0,m,K,Q}^{F_0,m'} |F_0, m'\rangle \langle F_0, m| \tag{D.5}$$

with $C_{F_0,m,K,Q}^{F_0,m'}$ the Clebsch-Gordan coefficient. Entering this definition into the polarizibility (Eq. D.3) we get,

$$\alpha_{i,j} = \sum_{K,q} \left(\sqrt{\frac{2K+1}{2F_0+1}} \sum_{m,m'} \sum_n \tilde{a}_{i,j}(m, m', n) \right) \hat{T}_{K,q} \tag{D.6}$$

$$\tilde{a}_{i,j}(m, m', n) = \frac{\langle F_0, m' |d_i| F, n\rangle \langle F, n |d_j| F_0, m\rangle}{-\hbar(\omega - \omega_{n,m}) - i\hbar\Gamma/2} C_{F_0,m,K,q}^{F_0,m'} \tag{D.7}$$

We define the detuning as $\Delta_{n,m} = \omega - \omega_{n,m}$, and for brevity we neglect Γ for the rest of this derivation.

D.2   Transforming into a circular basis

In this section we change the coordinate system from cartesian to a spherical (circular) basis. More specifically we simplify the brackets on the right side of Eq. D.6. The dipole operators transform into spherical coordinates as:

$$d_x = -\frac{d_+ - d_-}{\sqrt{2}} \; ; d_y = -\frac{d_+ + d_-}{i\sqrt{2}}, \tag{D.8}$$

The dipole matrix can be reduced such that

$$\langle F_0, m |d_\pm| F, n\rangle = \langle F_0 \|d\| F\rangle C_{F,n;1,\pm1}^{F_0,m} \tag{D.9}$$

$$\langle F, n |d_i| F_0, m\rangle = \left(\left(\langle F, n |d_i| F_0, m\rangle \right)^\dagger \right)^\dagger =$$

$$= \left(\left\langle F_0, m \left| d_i^\dagger \right| F, n \right\rangle \right)^\dagger = \left(\langle F_0, m |d_i| F, n\rangle \right)^\dagger \tag{D.10}$$

i can be either x or y, and using that in cartesian coordinates $d_i^\dagger = d_i$. Evaluating the different dipole matrix elements:

$$\langle F_0, m' |d_x| F, n\rangle = -\frac{1}{\sqrt{2}} \langle F_0 \|d\| F\rangle \left(C_{F,n;1,1}^{F_0,m'} - C_{F,n;1,-1}^{F_0,m'} \right) \tag{D.11}$$

$$\langle F_0, m' |d_y| F, n\rangle = -\frac{1}{i\sqrt{2}} \langle F_0 \|d\| F\rangle \left(C_{F,n;1,1}^{F_0,m'} + C_{F,n;1,-1}^{F_0,m'} \right) \tag{D.12}$$

$$\langle F, n |d_x| F_0, m\rangle = -\frac{1}{\sqrt{2}} \langle F_0 \|d\| F\rangle \left(C_{F,n;1,1}^{F_0,m} - C_{F,n;1,-1}^{F_0,m} \right) \tag{D.13}$$

$$\langle F, n |d_y| F_0, m\rangle = \frac{1}{i\sqrt{2}} \langle F_0 \|d\| F\rangle \left(C_{F,n;1,1}^{F_0,m} + C_{F,n;1,-1}^{F_0,m} \right) \tag{D.14}$$

We define the reduced dipole matrix element as

$$\mathbb{D}_{F,F_0} = \frac{|\langle F \|d\| F_0\rangle|^2}{-\hbar(\omega - \omega_{F,F_0})} = \frac{|\langle F \|d\| F_0\rangle|^2}{-\hbar\Delta_{F,F_0}} \tag{D.15}$$

D.3   Summing the transverse part in the effective Hamiltonian

Now we explicitly write the different components of $\tilde{a}$:

$$\tilde{a}_{x,x} = \frac{1}{2}\mathbb{D}_{n,m}\left(C^{F_0,m'}_{F,n;1,1} - C^{F_0,m'}_{F,n;1,-1}\right)\left(C^{F_0,m}_{F,n;1,1} - C^{F_0,m}_{F,n;1,-1}\right)C^{F_0,m'}_{F_0,m,K,q} \tag{D.16}$$

$$\tilde{a}_{y,y} = \frac{1}{2}\mathbb{D}_{n,m}\left(C^{F_0,m'}_{F,n;1,1} + C^{F_0,m'}_{F,n;1,-1}\right)\left(C^{F_0,m}_{F,n;1,1} + C^{F_0,m}_{F,n;1,-1}\right)C^{F_0,m'}_{F_0,m,K,q} \tag{D.17}$$

$$\tilde{a}_{x,y} = -\frac{1}{2i}\mathbb{D}_{n,m}\left(C^{F_0,m'}_{F,n;1,1} - C^{F_0,m'}_{F,n;1,-1}\right)\left(C^{F_0,m}_{F,n;1,1} + C^{F_0,m}_{F,n;1,-1}\right)C^{F_0,m'}_{F_0,m,K,q} \tag{D.18}$$

$$\tilde{a}_{y,x} = \frac{1}{2i}\mathbb{D}_{n,m}\left(C^{F_0,m'}_{F,n;1,1} + C^{F_0,m'}_{F,n;1,-1}\right)\left(C^{F_0,m}_{F,n;1,1} - C^{F_0,m}_{F,n;1,-1}\right)C^{F_0,m'}_{F_0,m,K,q} \tag{D.19}$$

From simple angular momentum conservation (addition) we can limit to two relations between m' and m, and writing these two cases as,

- $\Sigma^{q=0}_{\pm} = C^{F_0,m'}_{F,n;1,\pm1}C^{F_0,m}_{F,n;1,\pm1}C^{F_0,m'}_{F_0,m;K,q} \neq 0$ when $m' = m$ and $q = 0$.

- $\Sigma_{q=\pm2} = C^{F_0,m'}_{F,n;1,\pm1}C^{F_0,m}_{F,n;1,\mp1}C^{F_0,m'}_{F_0,m;K,q} \neq 0$ when $m' = m \pm 2$ and $q = \pm2$.

We note at this point that it is very tempting to use known relations and to sum over all of the excited and ground states, but this will directly assume degeneracy of the states. Since we are interested in showing the effect of the magnetic field that removes this degeneracy, at this point we do not do this simplification.

It is convenient to write the $\tilde{a}$ coefficients using the above Σ, thus we get:

$$\tilde{a}_{x,x} = \frac{1}{2}\mathbb{D}_{n,m}\left(\Sigma^{q=0}_{+} + \Sigma^{q=0}_{-} - \Sigma_{q=2} - \Sigma_{q=-2}\right) \tag{D.20}$$

$$\tilde{a}_{y,y} = \frac{1}{2}\mathbb{D}_{n,m}\left(\Sigma^{q=0}_{+} + \Sigma^{q=0}_{-} + \Sigma_{q=2} + \Sigma_{q=-2}\right) \tag{D.21}$$

$$\tilde{a}_{x,y} = -\frac{1}{2i}\mathbb{D}_{n,m}\left(\Sigma^{q=0}_{+} - \Sigma^{q=0}_{-} + \Sigma_{q=2} - \Sigma_{q=-2}\right) \tag{D.22}$$

$$\tilde{a}_{y,x} = \frac{1}{2i}\mathbb{D}_{n,m}\left(\Sigma^{q=0}_{+} - \Sigma^{q=0}_{-} - \Sigma_{q=2} + \Sigma_{q=-2}\right) \tag{D.23}$$

Next we look at the sum over the different transverse coordinates and get

$$\mathbf{E}^-_i\,\tilde{a}_{i,j}\mathbf{E}^+_j =$$

$$= \frac{1}{2}\mathbb{D}_{n,m}\left(\Sigma^{q=0}_{+} + \Sigma^{q=0}_{-}\right)\left(\hat{E}^-_x\hat{E}^+_x + \hat{E}^-_y\hat{E}^+_y\right) +$$

$$+ \frac{i}{2}\mathbb{D}_{n,m}\left(\Sigma^{q=0}_{+} - \Sigma^{q=0}_{-}\right)\left(\hat{E}^-_x\hat{E}^+_y - \hat{E}^-_y\hat{E}^+_x\right) +$$

$$- \frac{1}{2}\mathbb{D}_{n,m}\left(\Sigma_{q=2} + \Sigma_{q=-2}\right)\left(\hat{E}^-_x\hat{E}^+_x - \hat{E}^-_y\hat{E}^+_y\right) +$$

$$+ \frac{i}{2}\mathbb{D}_{n,m}\left(\Sigma_{q=2} - \Sigma_{q=-2}\right)\left(\hat{E}^-_x\hat{E}^+_y + \hat{E}^-_y\hat{E}^+_x\right) \tag{D.24}$$

Here we identify the electric field as the Stokes parameters, see Eq. C.12- C.14 in appndix C, and get:

$$\frac{c}{Lg^2}\mathbf{E}^-_i\,\tilde{a}_{i,j}\mathbf{E}^+_j =$$

$$= \frac{1}{2}\mathbb{D}_{n,m}\left(\Sigma^{q=0}_{+} + \Sigma^{q=0}_{-}\right)\hat{\Xi}_0 + \frac{1}{2}\mathbb{D}_{n,m}\left(\Sigma^{q=0}_{+} - \Sigma^{q=0}_{-}\right)\hat{\Xi}_\sigma +$$

$$- \frac{1}{2}\mathbb{D}_{n,m}\left(\Sigma_{q=2} + \Sigma_{q=-2}\right)\hat{\Xi}_{HV} + \frac{i}{2}\mathbb{D}_{n,m}\left(\Sigma_{q=2} - \Sigma_{q=-2}\right)\hat{\Xi}_{45} \tag{D.25}$$

with c is the speed of light, L is the sample length, and g is the electric field coefficient (see Eq. 11.10). The pre-factor is needed to set get the Stokes parameters.

Next we define the polarizibility for the different cases, and include the sum over all transitions,

$$\alpha_{0+} = \frac{1}{2}\sqrt{\frac{2K+1}{2F_0+1}}\sum_m\sum_n \mathbb{D}_{n,m}\left(\Sigma_+^{q=0} + \Sigma_-^{q=0}\right) \tag{D.26}$$

$$\alpha_{0-} = \frac{1}{2}\sqrt{\frac{2K+1}{2F_0+1}}\sum_m\sum_n \mathbb{D}_{n,m}\left(\Sigma_+^{q=0} - \Sigma_-^{q=0}\right) \tag{D.27}$$

$$\alpha_{+2} = \frac{1}{2}\sqrt{\frac{2K+1}{2F_0+1}}\sum_m\sum_n \mathbb{D}_{n,m}\Sigma_{q=2} \tag{D.28}$$

$$\alpha_{-2} = \frac{1}{2}\sqrt{\frac{2K+1}{2F_0+1}}\sum_m\sum_n \mathbb{D}_{n,m}\Sigma_{q=-2} \tag{D.29}$$

and get:

$$\sqrt{\frac{2K+1}{2F_0+1}}\frac{c}{Lg^2}\mathbf{E}_i^- \tilde{a}_{i,j}\mathbf{E}_j^+ =$$
$$\alpha_{0+}\hat{\Xi}_0 + \alpha_{0-}\hat{\Xi}_\sigma - \alpha_{+2}\left(\hat{\Xi}_{HV} - i\hat{\Xi}_{45}\right) - \alpha_{-2}\left(\hat{\Xi}_{HV} + i\hat{\Xi}_{45}\right) \tag{D.30}$$

D.4 The effective Hamiltonian

In this section we explicitly write the results for the effective Hamiltonian as written, using Eq. D.1 and Eq. D.6 and Eq. D.30. We start by writing the explicit for for a given level

$$H_{eff}(n,m) = -\hat{E}_i^- \alpha_{i,j}\hat{E}_j^+ = -\frac{Lg^2}{c}\sum_{K,F}\left(\alpha_{0+}\hat{\Xi}_0 + \alpha_{0-}\hat{\Xi}_\sigma\right)\hat{T}_{K,0}+$$

$$\frac{Lg^2}{c}\sum_{K,F}\left\{\alpha_{+2}\left(\hat{\Xi}_{HV} - i\hat{\Xi}_{45}\right)\hat{T}_{K,2} + \alpha_{-2}\left(\hat{\Xi}_{HV} + i\hat{\Xi}_{45}\right)\hat{T}_{K,-2}\right\} \tag{D.31}$$

Notice that K represent the change in angular momentum, therefore in the limit of second order perturbation it is limited to $K \leq 2$.

It is convenient to re-express the $\mathbb{D}_{n,m}$ constant reducing the dipole matrix to the total ground (excited) angular momentum J_0 (J) using the formulas given in [Steck08] to find

$$\mathbb{D}_{n,m} = -\frac{\hbar}{2}\frac{\Gamma}{2\Delta_{F,F_0}}\frac{\sigma_0}{A}\frac{c}{g^2L}(2J+1)(2F+1)\left\{\begin{array}{ccc} F & F_0 & I \\ J_0 & J & 1 \end{array}\right\}^2 \frac{1}{\frac{\Delta_{n,m}}{\Delta_{F,F_0}} + \frac{i\Gamma}{2\Delta_{F,F_0}}} \tag{D.32}$$

where A is the sample cross section, $\sigma_0(= 3\lambda^2/(2\pi))$ is the atomic absorption cross-section, λ is the laser wavelength, I is the nuclear spin, $\{\}$ is the 6-j symbol. We have explicitly included the atomic line with Γ. It is convenient to define the extra constant

$$\chi = \frac{1}{2}\sqrt{\frac{2K+1}{2F_0+1}}(2J+1)(2F+1)\left\{\begin{array}{ccc} F & F_0 & I \\ J_0 & J & 1 \end{array}\right\}^2 \tag{D.33}$$

and now we can define a dimensionless modified polarizibility

$$\tilde{\alpha} = \frac{2}{\hbar} \frac{g^2 L}{c} \alpha \tag{D.34}$$

$$\tilde{\alpha}_{0\pm} = -\left(\frac{\Gamma}{2\Delta_{F,F_0}}\right)\left(\frac{\sigma_0}{A}\right)\sum_m \sum_n \chi \frac{\Sigma_+^{q=0} \pm \Sigma_-^{q=0}}{\frac{\Delta_{n,m}}{\Delta_{F,F_0}} + \frac{i\Gamma}{2\Delta_{F,F_0}}} \tag{D.35}$$

$$\tilde{\alpha}_{\pm 2} = -\left(\frac{\Gamma}{2\Delta_{F,F_0}}\right)\left(\frac{\sigma_0}{A}\right)\sum_m \sum_n \chi \frac{\Sigma_{q=\pm 2}}{\frac{\Delta_{n,m}}{\Delta_{F,F_0}} + \frac{i\Gamma}{2\Delta_{F,F_0}}} \tag{D.36}$$

Thus we get the following effective Hamiltonian

$$H_{eff}(n,m) = -\frac{\hbar}{2}\sum_{K,F}\left(\tilde{\alpha}_{0+}\hat{\Xi}_0 + \tilde{\alpha}_{0-}\hat{\Xi}_\sigma\right)\hat{T}_{K,0} +$$

$$\frac{\hbar}{2}\sum_{K,F}\left\{\tilde{\alpha}_{+2}\left(\hat{\Xi}_{HV} - i\hat{\Xi}_{45}\right)\hat{T}_{K,2} + \tilde{\alpha}_{-2}\left(\hat{\Xi}_{HV} + i\hat{\Xi}_{45}\right)\hat{T}_{K,-2}\right\} \tag{D.37}$$

D.4.1   Summing over ground and excited states

Here we are interested in summing over all the levels, i.e. $\sum_{m,m'}\sum_n \Sigma_\pm^{q=0}$ and $\sum_{m,m'}\sum_n \Sigma_{q=\pm 2}$. For these sums we use the known relation [Varshalovich88] for these sums:

$$\sum_{m,m'}\sum_n \Sigma_\pm^{q=0} = \sum_{m,n} C_{F,n;1,\pm 1}^{F_0,m} C_{F,n;1,\pm 1}^{F_0,m} C_{F_0,m,K,0}^{F_0,m} = \tilde{c}_K C_{1,\pm 1;K,0}^{1,\pm 1} \tag{D.38}$$

$$\sum_{m,m'}\sum_n \Sigma_{q=\pm 2} = \sum_{m,m'}\sum_n C_{F,n;1,\mp 1}^{F_0,m} C_{F,n;1,\pm 1}^{F_0,m\pm 2} C_{F_0,m,K,\pm 2}^{F_0,m+\pm 2} = \tilde{c}_K C_{1,\mp 1;k,\pm 2}^{1,\pm 1} \tag{D.39}$$

with

$$\tilde{c}_K = (-1)^{F+1+F_0+K}\frac{(2F_0+1)^{3/2}}{\sqrt{3}}\left\{\begin{matrix} 1 & 1 & K \\ F_0 & F_0 & F \end{matrix}\right\} \tag{D.40}$$

Thus we get for the different polarizibility

$$\sum_{m,m'}\sum_n \alpha_{0+} = \mathbb{D}_{F,F_0}\tilde{c}_K\frac{C_{1,1;K,0}^{1,1} + C_{1,-1;K,0}^{1,-1}}{2} = \mathbb{D}_{F,F_0}\tilde{c}_K C_{1,1;K,0}^{1,1}\frac{1+(-1)^K}{2} \tag{D.41}$$

$$\sum_{m,m'}\sum_n \alpha_{0-} = \mathbb{D}_{F,F_0}\tilde{c}_K\frac{C_{1,1;K,0}^{1,1} - C_{1,-1;K,0}^{1,-1}}{2} = \mathbb{D}_{F,F_0}\tilde{c}_K C_{1,1;K,0}^{1,1}\frac{1-(-1)^K}{2} \tag{D.42}$$

$$\sum_{m,m'}\sum_n \alpha_{+2} = \frac{1}{2}\mathbb{D}_{F,F_0}\tilde{c}_K C_{1,-1;K,2}^{1,1} \tag{D.43}$$

$$\sum_{m,m'}\sum_n \alpha_{-2} = \frac{1}{2}\mathbb{D}_{F,F_0}\tilde{c}_K C_{1,1;K,-2}^{1,-1} \tag{D.44}$$

Note that here all levels have the same detuning ($\mathbb{D}_{n,m} \to \mathbb{D}_{F,F_0}$), and that from symmetry of the Clebsch-Gordan we also have $\alpha_{-2} = (-1)^K\alpha_{+2}$.

This result already tells us a lot about the way the effective Hamiltonian behaves (Eq. D.31), meaning that the circular polarized light will mainly interact with $\hat{T}_{1,0}$ and the contribution of $\tilde{\alpha}_{0-}\hat{\Xi}_\sigma\hat{T}_{0,0}$ is small[1]. Thus the propagation equations as written in Eq. 11.39 do not take all the effects of the magnetic field correctly.

---

[1]The contribution is equal to zero when the levels are degenerate.

We define a general polarizibility, with the subscript represents K:

$$\alpha_0 = \sum_F \sqrt{\frac{2K+1}{2F_0+1}} \mathbb{D}_{F,F_0} \tilde{c}_0 C^{1,1}_{1,1;0,0} \tag{D.45}$$

$$\alpha_1 = \sum_F \sqrt{\frac{2K+1}{2F_0+1}} \mathbb{D}_{F,F_0} \tilde{c}_1 C^{1,1}_{1,1;1,0} \tag{D.46}$$

$$\alpha_2 = \sum_F \sqrt{\frac{2K+1}{2F_0+1}} \mathbb{D}_{F,F_0} \tilde{c}_2 C^{1,1}_{1,-1;2,2} \tag{D.47}$$

For consistency with [Kupriyanov05] we enter into the polarizibility α_2 the Clebsch-Gordan coefficient $C^{1,1}_{1,-1;2,2}$ and not $C^{1,1}_{1,1;2,0}$. In addition we note that we get a different result by $2F_0 + 1$ due to a different convention in the reduction of the dipole matrix ($\mathbb{D}_{n,m}$). Next we write the modified polarizibilities as given by Eq. D.34,

$$\tilde{\alpha}_0 = \sum_F \left(\frac{\Gamma}{2\Delta_{F,F_0}}\right) \left(\frac{\sigma_0}{A}\right) C^{1,1}_{1,1;0,0} 2\chi(K=0)\tilde{c}_0 \frac{1}{1+\frac{i\Gamma}{2\Delta_{F,F_0}}} \tag{D.48}$$

$$\tilde{\alpha}_1 = \sum_F \left(\frac{\Gamma}{2\Delta_{F,F_0}}\right) \left(\frac{\sigma_0}{A}\right) C^{1,1}_{1,1;1,0} 2\chi(K=1)\tilde{c}_1 \frac{1}{1+\frac{i\Gamma}{2\Delta_{F,F_0}}} \tag{D.49}$$

$$\tilde{\alpha}_2 = \sum_F \left(\frac{\Gamma}{2\Delta_{F,F_0}}\right) \left(\frac{\sigma_0}{A}\right) C^{1,1}_{1,-1;2,2} 2\chi(K=2)\tilde{c}_2 \frac{1}{1+\frac{i\Gamma}{2\Delta_{F,F_0}}} \tag{D.50}$$

Combining these we rewriting the effective Hamiltonian as:

$$H_{eff} = -\frac{\hbar}{2} \sum_{K=0}^{1} \tilde{\alpha}_K \left(\frac{1+(-1)^K}{2}\hat{\Xi}_0 + \frac{1-(-1)^K}{2}\hat{\Xi}_\sigma\right) \hat{T}_{K,0} +$$

$$-\frac{\hbar}{2}\tilde{\alpha}_2 \frac{C^{1,1}_{1,1;2,0}}{C^{1,1}_{1,-1;2,2}} \left(\frac{1+(-1)^2}{2}\hat{\Xi}_0 + \frac{1-(-1)^2}{2}\hat{\Xi}_\sigma\right) \hat{T}_{2,0} +$$

$$+\frac{\hbar}{2}\frac{1}{\sqrt{2}}\tilde{\alpha}_2 \left\{\hat{\Xi}_{HV}\frac{\hat{T}_{2,2}+\hat{T}_{2,-2}}{\sqrt{2}} + \hat{\Xi}_{45}\frac{\hat{T}_{2,2}-\hat{T}_{2,-2}}{i\sqrt{2}}\right\} \tag{D.51}$$

Here the Clebsch-Gordan ratio $C^{1,1}_{1,1;2,0}/C^{1,1}_{1,-1;2,2} = 1/\sqrt{6}$, with the coherence $\sqrt{2}\hat{T}_{HV} = \hat{T}_{2,2} + \hat{T}_{2,-2}$ and $i\sqrt{2}\hat{T}_{45} = \hat{T}_{2,2} - \hat{T}_{2,-2}$.

D.5 Summary

In this appendix we have showed the last steps in the derivation of the effective Hamiltonian. Here we distinguish between two cases, when the Zeeman sub-leves are not degenerated and when they are degenerate. In this section we are going to give end result off the effective Hamiltonian for both cases.

The levels are split

$$H_{eff} = -\frac{\hbar}{2} \sum_{K=0}^{2} \sum_F \left(\tilde{\alpha}_{0+}\hat{\Xi}_0 + \tilde{\alpha}_{0-}\hat{\Xi}_\sigma\right) \hat{T}_{K,0} +$$

$$\frac{\hbar}{2} \sum_F \left(\tilde{\alpha}_{+2}\left(\hat{\Xi}_{HV} - i\hat{\Xi}_{45}\right)\hat{T}_{2,2} + \tilde{\alpha}_{-2}\left(\hat{\Xi}_{HV} + i\hat{\Xi}_{45}\right)\hat{T}_{2,-2}\right) \tag{D.52}$$

Where the polarizibility are defined by Eq. D.35- D.36, where one need to sum also over all possible hyperfine excited levels F.

The levels are degenerate

$$
H_{eff} = -\frac{\hbar}{2}\left(\tilde{\alpha}_0 \hat{\Xi}_0 \hat{T}_{0,0} + \frac{1}{\sqrt{6}}\tilde{\alpha}_2 \hat{\Xi}_0 \hat{T}_{2,0}\right) - \frac{\hbar}{2}\tilde{\alpha}_1 \hat{\Xi}_\sigma \hat{T}_{1,0} +
$$
$$
\frac{\hbar}{2}\frac{1}{\sqrt{2}}\tilde{\alpha}_2 \left(\hat{\Xi}_{HV} \hat{T}_{HV} + \hat{\Xi}_{45} \hat{T}_{45}\right) \qquad \text{(D.53)}
$$

Note that here the result is different than given in [Kupriyanov05, Mishina07] by a factor of $1/\sqrt{2}$ in front of $\tilde{\alpha}_2$, this is due to the different definition of the $\hat{T}_{HV}$ and $\hat{T}_{45}$.

The irreducible tensors commutation relation

Here we give the irreducible tensor commutation relation between any two tensors $\hat{T}_{K,Q}$ with $K \leq 2$. The results are summarized in table E.1 and in table E.2, for the case $F_0 = 1$ and $\beta_0 = 1/\sqrt{2}$.

	$\hat{T}_{0,0}$	$\hat{T}_{1,0}$	$\hat{T}_{1,1}$	$\hat{T}_{1,-1}$
$\hat{T}_{0,0}$	0	0	0	0
$\hat{T}_{1,0}$	0	0	1 (1,1)	-1 (1,-1)
$\hat{T}_{1,1}$	0	-1 (1,1)	0	-1 (1,0)
$\hat{T}_{1,-1}$	0	1 (1,-1)	1 (1,0)	0
$\hat{T}_{2,0}$	0	0	$\sqrt{3}$ (2,1)	$-\sqrt{3}$ (2,-1)
$\hat{T}_{2,1}$	0	-1 (2,1)	$\sqrt{2}$ (2,2)	$-\sqrt{3}$ (2,0)
$\hat{T}_{2,-1}$	0	1 (2,-1)	$\sqrt{3}$ (2,0)	$-\sqrt{2}$ (2,-2)
$\hat{T}_{2,2}$	0	-2 (2,2)	0	$-\sqrt{2}$ (2,1)
$\hat{T}_{2,-2}$	0	2 (2,-2)	$\sqrt{2}$ (2,-1)	0

Table E.1: The commutation relations $[\hat{T}_{K,Q}, \hat{T}_{K',Q'}] = const. \cdot \beta_0 \hat{T}_{(k,q)}$ for the case $F_0 = 1$ and $\beta_0 = 1/\sqrt{2}$, e.g. $[\hat{T}_{2,0}, \hat{T}_{1,1}] = \sqrt{3}\beta_0 \hat{T}_{2,1} = \sqrt{\frac{3}{2}}\hat{T}_{2,1}$.

	$\hat{T}_{2,0}$	$\hat{T}_{2,1}$	$\hat{T}_{2,-1}$	$\hat{T}_{2,2}$	$\hat{T}_{2,-2}$
$\hat{T}_{0,0}$	0	0	0	0	0
$\hat{T}_{1,0}$	0	1 (2,1)	-1 (2,-1)	2 (2,2)	-2 (2,-2)
$\hat{T}_{1,1}$	$-\sqrt{3}$ (2,1)	$-\sqrt{2}$ (2,2)	$-\sqrt{3}$ (2,0)	0	$-\sqrt{2}$ (2,-1)
$\hat{T}_{1,-1}$	$\sqrt{3}$ (2,-1)	$\sqrt{3}$ (2,0)	$\sqrt{2}$ (2,-2)	$\sqrt{2}$ (2,1)	0
$\hat{T}_{2,0}$	0	$\sqrt{3}$ (1,1)	$-\sqrt{3}$ (1,-1)	0	0
$\hat{T}_{2,1}$	$-\sqrt{3}$ (1,1)	0	-1 (1,0)	0	$\sqrt{2}$ (1,-1)
$\hat{T}_{2,-1}$	$\sqrt{3}$ (1,-1)	1 (1,0)	0	$-\sqrt{2}$ (1,1)	0
$\hat{T}_{2,2}$	0	0	$\sqrt{2}$ (1,1)	0	2 (1,0)
$\hat{T}_{2,-2}$	0	$-\sqrt{2}$ (1,-1)	0	-2 (1,0)	0

Table E.2: The commutation relations $[\hat{T}_{K,Q}, \hat{T}_{K',Q'}] = const. \cdot \beta_0 \hat{T}_{(k,q)}$ for the case $F_0 = 1$ and $\beta_0 = 1/\sqrt{2}$, e.g. $[\hat{T}_{2,0}, \hat{T}_{2,-1}] = -\sqrt{3}\beta_0 \hat{T}_{1,-1} = -\sqrt{\frac{3}{2}}\hat{T}_{1,-1}$.

Collective atomic operators

In the Hamiltonian derived in chapter 11 and appendix D, we have assumed a single atom picture. Here we describe how the operators are changed in order to sum over all atoms, which essentially means that the atomic excitation of a single atom is sheared by all atoms. A more mathematical formulation states, that the collective state is a superposition of a single excitation of one unknown atom. To keep the position information along the propagation direction (z), we sum the collective operator over all atoms in a small slice at position z. The requirement is that in each slice the number of atoms is much bigger to one, but thin enough that we can assume continues variables in space and time.

There is a freedom in choosing the normalization of the collective spin excitation, here we describe three different normalization. The first is to sum each excitation over all atoms in a each slice Δz as done in [Geremia06]. The second normalization, is to divide each spin excitation by the total number of atoms in the slice, as done in [Gorshkov07b], and the third normalization is to use the density of the spin excitation, i.e. each spin excitation is divided by the slice length as done in [Kupriyanov05, Mishina07]. The last two definitions are formally written as:

$$|\mu\rangle \langle v|^{(n=2)} (z,t) = \frac{1}{n(z)\Delta z} \sum_{z<z'<z+\Delta z} |\mu\rangle \langle v|^a (z',t) \tag{F.1}$$

$$|\mu\rangle \langle v|^{(n=3)} (z,t) = \frac{1}{\Delta z} \sum_{z<z'<z+\Delta z} |\mu\rangle \langle v|^a (z',t) \tag{F.2}$$

Here the superscript ($n = 2/3$) is to distinguish between the two different normalization, the superscript a is to identify the operator of a single atom, and $n(z)$ is the atomic line density. These two definitions have different advantages: the second normalization (Eq. F.1) describes the fraction of atoms in such a state (dimensionless), therefore its easier to see the atom number (or optical depth) dependence in the propagation equation. The third normalization (Eq. F.2) describes directly the density. The two normalization gives two different commutation relations:

$$\left[|\mu_1\rangle \langle v| (z), |v\rangle \langle \mu_2| (z')\right]^{(n=2)} = \frac{1}{n(z)} |\mu_1\rangle \langle \mu_2|^{(n=2)} (z)\delta(z-z') \tag{F.3}$$

$$\left[|\mu_1\rangle \langle v| (z), |v\rangle \langle \mu_2| (z')\right]^{(n=3)} = |\mu_1\rangle \langle \mu_2|^{(n=3)} (z)\delta(z-z') \tag{F.4}$$

with $\delta(z-z')$ the Dirac delta function[1]. Note that in this thesis we use the third normalization, given by Eq. F.4.

---

[1]The units of Dirac delta function is one over length.

Realization of 3-axis magnetic servo-loop

Here we describe a magnetic servo-loop [Bechhoefer05] used to effectively cancel the gravitational sag. In chapter 9 we have showed the usage of the servo-loop, and in this appendix we describe the actual realization of it. In Fig. G.1 we describe the different elements of our implementation. Even though this schematic is very detailed it contains three basic ingredients: 1) producing the magnetic field (current controller, coils, and change the B-filed), 2) measuring the magnetic field (B-field sensor, sensor controller, and matrix invertor), and 3) PID controller (feedback and feed forward).

Step 1, produces the magnetic field by controlling the current passing through three different set of Helmholtz coils and is described in section G.1. In the second step, section G.2, we measure the magnetic field at a resolution of 50μGauss and 150μGauss at a bandwidth of @100kHz using two similar detectors. The last step, section G.3, we describe the feedback circuit.
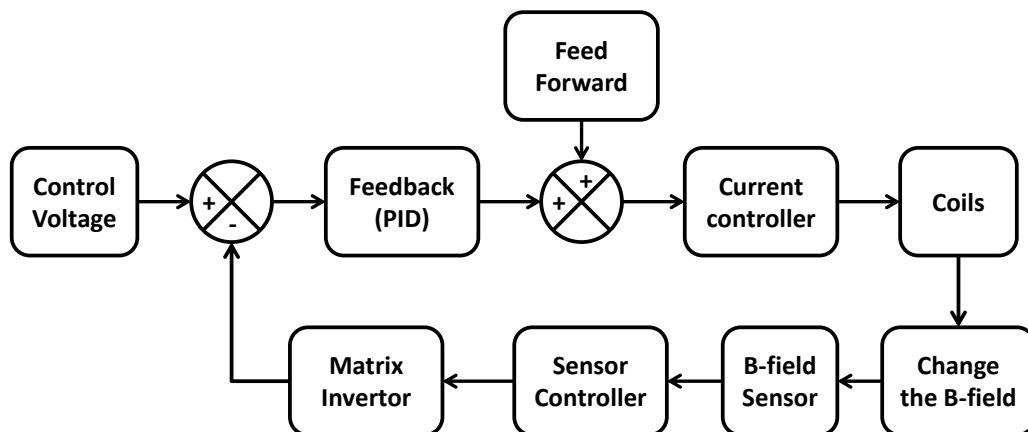

Figure G.1: The feed back logic schematic

G.1 The current controller

A current control for driving the coils requires sufficient voltage to overcome the coils inductance, since the coil resistivity and the maximum voltage sets the maximum current. To regulate the current we use the linear region of a power transistor. Here we are interested in having the freedom to drive both
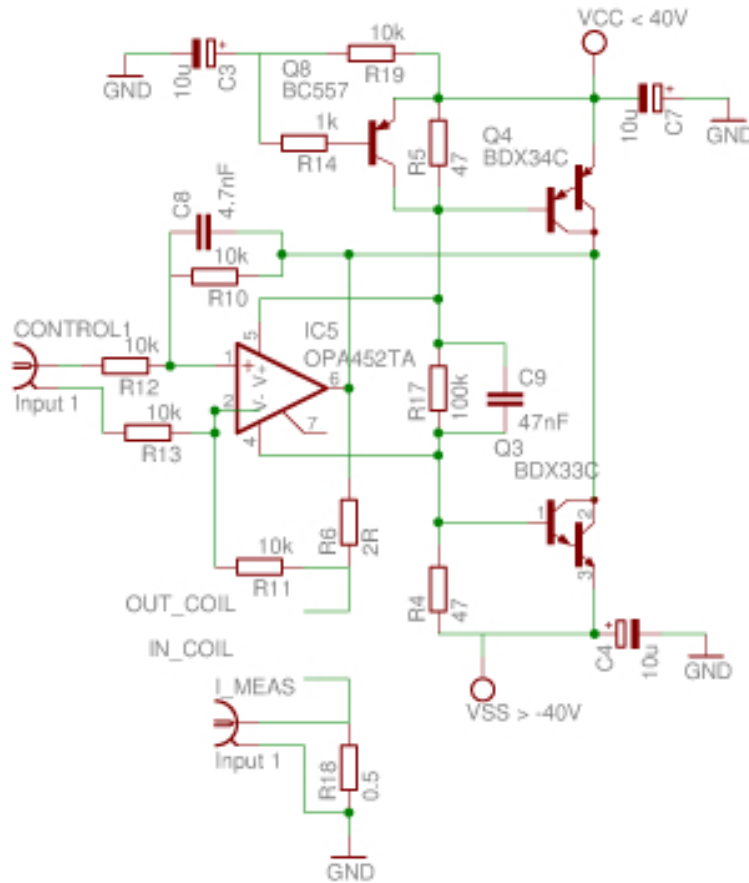
Figure G.2: The current controller electric circuite.

positive and negative voltages therefore we use two transistors. For stabilizing the current we use an operational amplifier as a feedback sensing the current.

We have chosen to implement a variation of a class AB push-pull current driver, and in Fig. G.2 we show the electronic circuite schematic. The control voltage is the input into the operational amplifier. The current is initially drown from the operational amplifier, which is drown from the supply line that drops as the current increases. This voltage drop on resistors R5 or R4 opens the corresponding transistor such that it will supply the current. The operational amplifier regulates the current through the sense resistor ($R6 = 2\Omega$).
 The purpose of resistor R17 is to connect the gates of the two transistors and ensures that only one of them will work at a given time. To prevent oscillations we have added a capacitor (C9) parallel to the resistor that slows down the changes, thus prevents oscillations. Note that for coils with lower resistivity and lower DC inductive there is no need for this capacitor. Our DC resistivity and inductive are: $R \simeq 12 - 16\Omega$ & $L \simeq 16 - 25$mH (which gives a DC cutoff frequency $f_c = \frac{R}{2\pi L} \approx 125$Hz). With a resonance frequency of about 325Hz, and the 3dB is found at $500 - 600$Hz, as shown in Fig. G.6.

G.2 Measuring the magnetic field

There are several different types of sensors that can be used to measure the magnetic field, that differ in the range and accuracy [Caruso98]. We have chosen to work with a commercial sensor, based on a metallic strip that changes its resistivity due to an external magnetic field. This magnetoresistive sensor is made from a nickel-iron (Permalloy) thin film deposited on a silicon wafer. The

variation in the resistance is measured using a Wheatstone bridge, i.e. $\Delta R/R$.

The sensor output is taken to a differential operational amplifier with gain of 470 and a 135kHz bandwidth. To remove high frequencies noise source we have added an additional low pass filter with a corner frequency of $f \approx 360$kHz. We used a load resistor with similar values to the Wheatstone bridge resistors, which reduced the signal but increased the overall sensitivity. This configuration gives noise levels for two similar sensors of 50μV and 150μV that corresponds to 50μGauss and 150μGauss.

The sensor [Hon] output is given by Eq. G.1, with $g = 470$ is the operational amplifier gain, S is the sensor sensitivity, V_{offset} is an additional offset that is due to the resistor mismatch during the manufacture process [Hon]. For this type of sensor there is no preferred magnetization axis thus we need to magnetize the sensor to a given direction. Setting the direction is refer to as set/reset operation which defines the sign in Eq. G.1.

$$V_{sen} = g \left(\pm S \cdot B + V_{offset} \right) \tag{G.1}$$

The sensor board was designed to be small (4×5cm^2) and we send the signal over a long cable to the sensor controller (see Fig. G.1), which enables putting the sensor close to the actual system. We translate the signal to the magnetic field, by measuring V_{offset} and subtracting it from the actual signal.

The measurement is done using two Digital to Analog Converter[1] (DAC) and two Analog to Digital Converter[2] (ADC). The second measurement is needed to cancel out the additional offset values from the DAC. Since the DAC and ADC are limited to $0-4V$ and the sensor signal is in the range ± 10V, we need to rescale the signal. The transformed signal is:

$$V_c(t) = \frac{2}{11} V_{sen}(t) + 2\frac{V_{ref}}{4.2} - DAC_1 - \frac{DAC_2}{128} \tag{G.2}$$

Here DAC_1 and DAC_2 are the DAC's output voltage, V_{ref} is a voltage reference with value of 4.096V. For setting the DACs values first we measure the input signal during the set operation and during the reset operation. Then we set them to be:

$$DAC_1 = 2 + \frac{2}{11} g V_{offset} + \frac{1}{11} g S \Delta B + V_1 \tag{G.3}$$

$$DAC_2 = \frac{128}{2} \left(\Delta V_c(t_1) + \Delta V_c(t_2) + 2V_1 \right) \tag{G.4}$$

Here V_1 is the DAC_1 offset voltages, ΔB is the magnetic field difference between the two measurements at the set and reset operations[3]. $\Delta V_c(t_1)$ is the difference between measuring V_c when both $DAC_1 = DAC_2 = 0$V and measuring V_c after setting DAC_1 to that first measured value ($\Delta V_c(t_1)$), i.e. we measure the remainder from the first measurement. $\Delta V_c(t_1)$ is measured while the sensor is magnetized with a set operation, and $\Delta V_c(t_2)$ is similarly measured only while the sensor is magnetized with a reset operation. Both $\Delta V_c(t_1)$ and $\Delta V_c(t_2)$ contribution is to removing the internal DAC's offset V_1 usually a few millivolts, and to improving by several bits the resolution limited by the DAC noise levels. The total time for this operation is 380μs.

---

[1]type TLV5618
[2]type MCP3302
[3]The time difference is about $\sim 150\mu s$

After the set/reset operation we get:

$$V_c(t) = \frac{2}{11}gSB(t) - \frac{1}{11}gS\Delta B \cong S_t B(t) \tag{G.5}$$

With $S_t \approx 1\frac{\text{mGauss}}{\text{mV}}$ the total conversion factor and the signal range is $V_c = \pm 2\text{V}$. In addition we assume that the difference in magnetic field at the different times is small. We estimate ΔB by measuring the signal and find about 20mGauss noise at frequencies of $50 - 100\text{Hz}$ that can cause fluctuations of $220 - 440\mu\text{Gauss}$. A way to overcome this noise fluctuation is to first start the feedback then after removing this noise then doing the set/reset operation on a second sensor. Thus ΔB will be reduced to below the noise level. We note that we do not use this method.
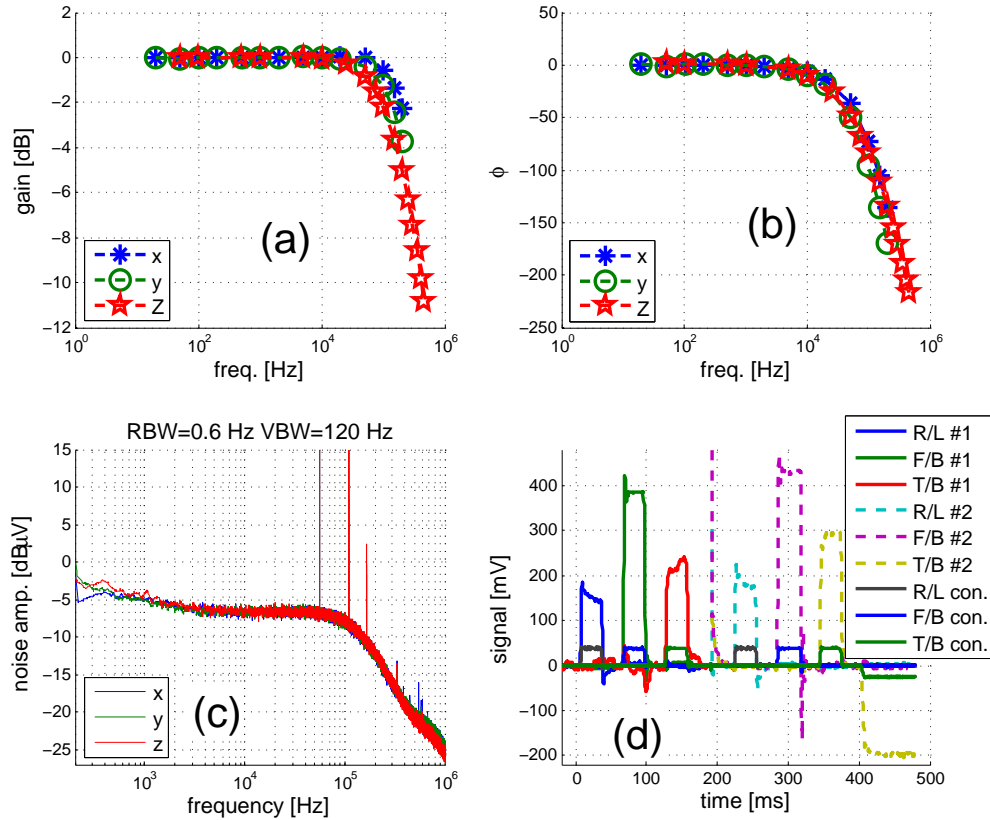

Figure G.3: (a) and (b): The magnetic sensor transfer function amplitude and phase respectively; (c): the noise power spectrum with respect to $1\mu\text{V}$, this spectrum is also valid for $1\mu\text{Gauss}$ since the transformation is about $1\text{V}/\text{Gauss}$; (d): the performance of the voltage mixture which ensures that the sensor and coils axis are aligned.

In Fig. G.3 (a) & (b) we show the sensor measured transfer function. The 3dB drop is at about 150kHz, and the phase starts to change from zero at 10kHz and reaches 90 degrees at 100kHz. This is well inside our specification for the servo-loop at bandwidth of 1kHz.

The noise equivalent power (NEP) is measured after amplifying the signal by $3 - 4$ order of magnitude, and fourier transform the signal. The NEP is given in Fig. G.3 (c) as a function of frequency. The reference is given with respect to $1\mu\text{V}$, we see that the noise is flat and drops by 3dB at around 150kHz. We also measured the mean noise level using a 100kHz low pass filter to be $50\mu\text{Gauss}$ for one detector and $150\mu\text{Gauss}$ for a second identical one.

For the servo-loop we would like to decouple the three axis, i.e. that each axis on the sensor will measure the change in the magnetic field due to only one

coil. This we achieve by multiplying the sensor output with an appropriate matrix. This matrix rotates and stretches the magnetic signal such that its output is aligned (digitalized) along the coils axis.

$$\mathbf{V}_{mix} = M_{mix}\mathbf{V}_c = M_{mix}M_{sys}\mathbf{B} \tag{G.6}$$

Where M_{mix} is the mixture matrix, $\mathbf{V}_c$ is the signal output from the sensor Eq. G.2 and Eq. G.5, $\mathbf{B}$ is the magnetic field at the sensor, and M_{sys} is the system matrix that transforms the magnetic field to all three axis on the sensor board. To decouple the axis we need $M_{mix}M_{sys} = D$, where D is a diagonal matrix.

We have build a circuit that realizes the mixture matrix (M_{mix}), and is described as the matrix inverter box in Fig. G.1. Each input signal is splitted to a positive and negative values then sent to three different digital potentiometers. The signals are summed using an operational amplifiers thus realizing the matrix multiplication. This combination allows us to do both rotations (with nine different potentiometers) and stretch (by using the appropriate resistors at the summing operational amplifier). For convenience we use digital potentiometers ("AD5292") with 10 bit resolution.

In our system we need to use two different sensors one that will work during the operation of the QUICK trap and the second sensor will work after the trap magnetic field was turned off. Since during the operation of the QUICK trap the sensor and its environment are magnetized, we have minimized the number of ferromagnetic components near the sensors. This is done to reduce sensitivity to the magnetic history before operating the sensor. To emphasize the problem, initially we had a small inductive high pass filter (π-filter) that was magnetized by the external magnetic fields and was removed due to its influence on the measured magnetic field. In the final version there is still an additional small effect due to the capacitors and resistors, since they have a protective Nickel layer, but its below our sensitivity.

For the reasons stated above, i.e. the influence of the magnetic field environment history, the alignment procedure was done under working conditions. To measure the sensors response to each of the coils we gave a long ($\geq$ 30ms) rectangle pulse in each of the coils with a time delay between the three pulses, see control signals in Fig. G.3 (d). We started by aligning the sensor to the best of our ability along the coils axis (without using the mixture matrix circuit). Then we connected the mixture matrix and changed the different elements until we got a diagonal matrix. The end result is given in Fig. G.3 (d).

Note that we cannot remove the eddy currents. Thats why we needed to give long enough pulses that we could see the eddy currents. In Fig. G.3-(d), the influence of the eddy currents are visible in the R/L #1 and T/B #1 signals.

G.3 The magnetic feedback

We have designed the feedback circuit such that we can operate it either with external control or with internal control. The internal control gives us the ability to first measure the magnetic field signal and then to set the internal control to that value. Thus minimize the initial difference between the two control voltages to a few millivolt[4]. We have implemented these options by inserting several analog switches, thus enable us to change from different configurations without adding a kick to the servo-loop.

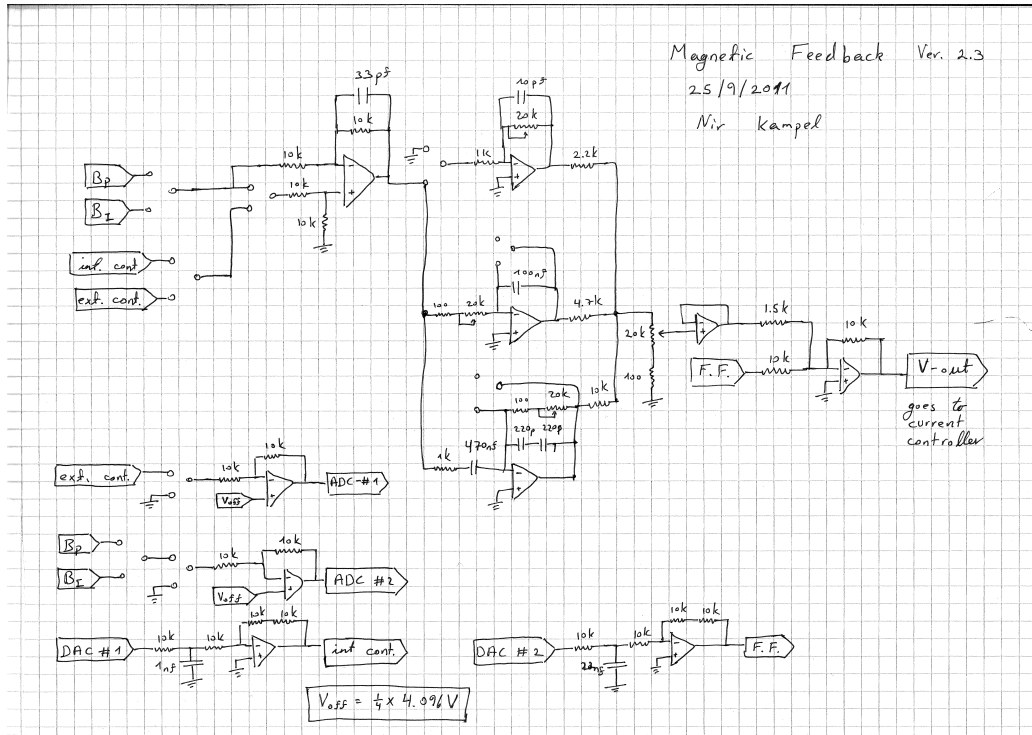[4]Note that this corresponds to a few milli-Gauss.

Figure G.4: The schematic of the PID feedback circuite.

In our design we also allow working with two different magnetic signals that come from two different sensors. This can be used either to switching between the sensors to eliminate the extra noise source ΔB in Eq. G.1 or to allow the feedback to operate at two different times with each sensor is aligned to a different magnetic environment e.g. during the time the QUICK trap is on and off (for the absorbtion imaging) as shown in Fig. G.3 (d). Here we use the latter option.

In Fig. G.4 we show the schematic of the electronic circuit for the magnetic feedback. On the bottom left of the figure the different measurements scheme of both the control and the magnetic field are shown, in addition how we create the internal control voltage and the feed forward using DACs is shown. Note that since the ADC's range is $0 \rightarrow 4.1$V we nominally set the switch to be connected to the ground. This ensures that the ADC's do not saturate and will not be overdriven. The switches, ADCs, and DACs are controlled using a micro-controller.

In the top left part of Fig. G.4 we show the two different magnetic sensors input and the internal and external control voltage. Which are sent to a differential operational amplifier that implements the error signal. We have also added an additional switch that shorts the error signal, which enables us to open/close the servo-loop at will.

The usage of the internal control is shown in Fig. G.5-(a), and the servo-loop is closed within 60μs. There is a small cross talk spike in the signal (at high frequencies ~ 1MHz), due to closing the switch. As the external trigger is given we measure the magnetic field value ($\sim 30\mu$s), then we set the internal control to that value, see green line, which also takes about $\sim 30\mu$s. Thus it takes about 60μs to close the servo-loop.

There is an additional problem that needs overcoming. Ideally the initial magnetic field signal and the control voltage will be same. But since the 50Hz noise
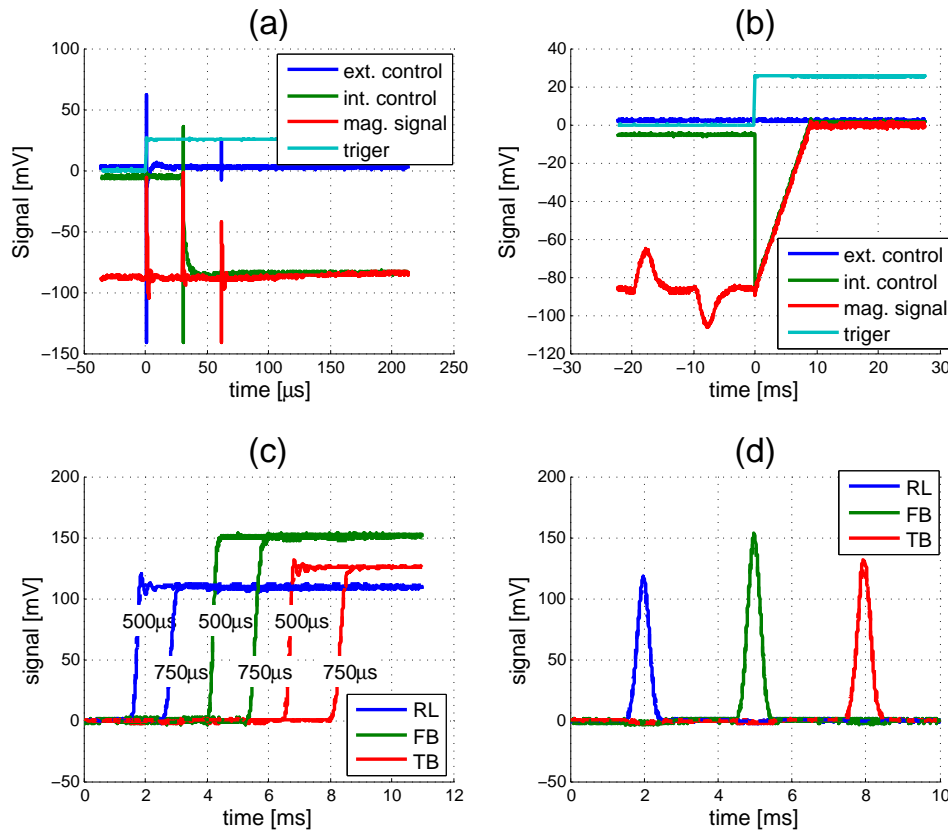
Figure G.5: Operation of the magnetic feedback; (a): initial steps of the feedback operation 1) measuring the magnetic signal and the external control ($\sim 30\mu s$), 2) setting the internal control to the magnetic signal measured value, and 3) closing the servo-loop using the internal control; (b): A close loop operation, measuring and setting the initial value and slowly changing the magnetic field to the external control value. (c): An error function step response with a $500\mu s$ and $750\mu s$ rise time for all three axis; (d): a $1ms$ wide gaussian ($\sigma = 170\mu s$ pulse;

is about 40mV we have designed the internal control signal to slowly shift the magnetic field value from the initial value to the wanted control voltage. This operation is shown in Fig. G.5-(b). For illustration purposes we set the external control value to differ from the magnetic field. Here we chose a slope of 1mV every $100\mu s$ (10mV/ms), and once the two have the same value we switch from the internal control to the external control.

We have implemented an analog proportional integrate differential (PID) feedback circuit, and each of the PID implementation is shown in Fig. G.4. Since there are long times where the servo-loop is open we have added the option of resetting each of the PID components. Our operation logic is to reset the PID components before closing the servo-loop. To have a control on the strength of each of the PID we also used here digital potentiometers with a 10-bit resolution.

The output of the different PID are summed and passed through a follower operational amplifier. This gives us the possibility of reducing the gain, and sum with different weight the different PID components. The output of the follower operational amplifier is summed with an internal feed forward, then send to the current controller described in section G.1.

We have tested the operation of the servo-loop in several different ways. A fast step pules with a rise/fall time which are determined by an error function ($-2\sigma \rightarrow 2\sigma$) with different total duration, and a 1ms gaussian pulse ($\sigma = 170\mu s$).
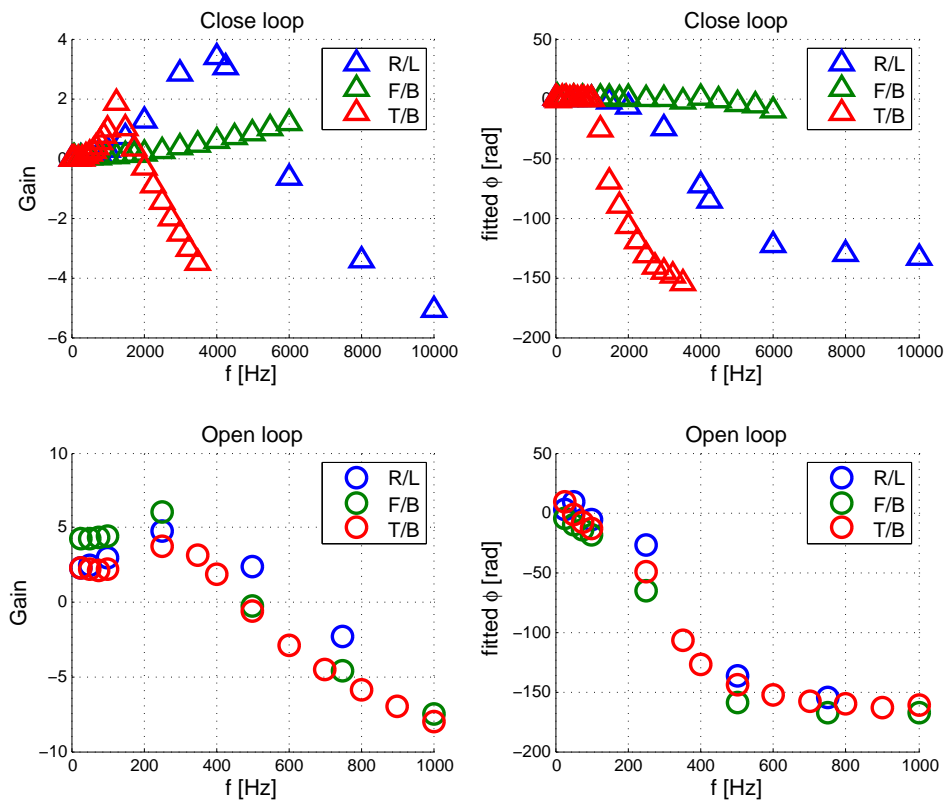
Figure G.6: The close/open transfer function of the magnetic field; Top: close loop servo-loop, left - gain and right - phase; Bottom: open loop, left - gain and right - phase;

The results of these pulses are given in Fig. G.5-(c) and Fig. G.5-(d). When the pulse rise time is faster than 750μs the magnetic field has oscillations that decay within a few hundred of microsecond.

We measured the Bode plot to characterizing the open/close loop response function [Bechhoefer05], see Fig. G.6. From the open loop measurements we can see that the coil resonance is found at about 250Hz and that the phase is gradually falling. While in the close loop configuration we find a flat phase response up to 1kHz, with a gain that peaks at a certain frequency depending on the coil.

While the servo-loop described above works, it is still misses one last component. We need to measure the magnetic field at the atoms and translate the measured signal from the sensor to the actual magnetic field at the atoms. So far we have not measured this, which means that we do not necessarily reduce the noise at the atoms but reduce the noise at the sensor. This can of course add extra noise if the magnetic field at the sensor is bigger than the one at the atoms.

Bibliography

[Appel09]   Jürgen Appel, Andrew MacRae, and A I Lvovsky, *A versatile digital GHz phase lock for external cavity diode lasers*, Measurement Science and Technology, **20**(5), 055302 (2009), doi:10.1088/0957-0233/20/5/055302

[Bar-Gill07]   Nir Bar-Gill, Eitan E. Rowen, and Nir Davidson, *Spectroscopy of strong-pulse superradiance in a Bose-Einstein condensate*, Phys. Rev. A, **76**, 043603 (2007), doi:10.1103/PhysRevA.76.043603

[Bechhoefer05]   John Bechhoefer, *Feedback for physicists: A tutorial essay on control*, Rev. Mod. Phys., **77**, 783 (2005), doi:10.1103/RevModPhys.77.783

[Bennett84]   C. H. Bennett and G. Brassard, *Quantum Cryptography: Public key distribution and coin tossing*, in *in Proceedings of the IEEE International Conference on Computers, Systems and Signal Processing, Bangalore, India (IEEE, New York)* (1984), 175–179

[Bergmann98]   K. Bergmann, H. Theuer, and B. W. Shore, *Coherent population transfer among quantum states of atoms and molecules*, Rev. Mod. Phys., **70**, 1003 (1998), doi:10.1103/RevModPhys.70.1003

[Berlok12]   Thomas Berlok, *Interaction of hot Bose-Einstein condensates with resonant light An experimental study* (2012)

[Burnett96]   K. Burnett, P. S. Julienne, and K.-A. Suominen, *Laser-Driven Collisions between Atoms in a Bose-Einstein Condensed Gas*, Phys. Rev. Lett., **77**, 1416 (1996), doi:10.1103/PhysRevLett.77.1416

[Caruso98]   Michael J. Caruso, Tamara Bratland, Carl H. Smith, and Robert Schneider, *A New Perspective on Magnetic Field Sensing* (1998)

[Castin96]   Y. Castin and R. Dum, *Bose-Einstein Condensates in Time Dependent Traps*, Phys. Rev. Lett., **77**, 5315 (1996), doi:10.1103/PhysRevLett.77.5315

[Dawkins11]   S. T. Dawkins, R. Mitsch, D. Reitz, E. Vetsch, and A. Rauschenbeutel, *Dispersive Optical Interface Based on Nanofiber-Trapped Atoms*, Phys. Rev. Lett., **107**, 243601 (2011), doi:10.1103/PhysRevLett.107.243601

[Deng10a]   L. Deng, E. W. Hagley, Qiang Cao, Xiaorui Wang, Xinyu Luo, Ruquan Wang, M. G. Payne, Fan Yang, Xiaoji Zhou, Xuzong Chen, and Mingsheng Zhan, *Observation of a Red-Blue Detuning Asymmetry in Matter-Wave Superradiance*, Phys. Rev. Lett., **105**, 220404 (2010), doi:10.1103/PhysRevLett.105.220404

[Deng10b]   L. Deng, M. G. Payne, and E. W. Hagley, *Electromagnetic Wave Dynamics in Matter-Wave Superradiant Scattering*, Phys. Rev. Lett., **104**, 050402 (2010), doi:10.1103/PhysRevLett.104.050402

[Deng11]   —, *Deng, Payne, and Hagley Reply:*, Phys. Rev. Lett., **106**, 118902 (2011), doi:10.1103/PhysRevLett.106.118902

[Dicke54]   R. H. Dicke, *Coherence in Spontaneous Radiation Processes*, Phys. Rev., **93**, 99 (1954), doi:10.1103/PhysRev.93.99

[Duan01]   L.-M. Duan, M. D. Lukin, J. I. Cirac, and P. Zoller, *Long-distance quantum communication with atomic ensembles and linear optics*, Nature, **414**, 413 (2001), doi:10.1038/35106500

[Dudin10]   Y. O. Dudin, R. Zhao, T. A. B. Kennedy, and A. Kuzmich, *Light storage in a magnetically dressed optical lattice*, Phys. Rev. A, **81**, 041805 (2010), doi:10.1103/PhysRevA.81.041805

[Fioretti98]   A Fioretti, A.F Molisch, J.H Müller, P Verkerk, and M Allegrini, *Observation of radiation trapping in a dense Cs magneto-optical trap*, Optics Communications, **149**(4-6), 415 (1998), doi:10.1016/S0030-4018(97)00704-9

[Firstenberg09] Ofer Firstenberg, Paz London, Moshe Shuker, Amiram Ron, and Nir Davidson, *Elimination, reversal and directional bias of optical diffraction*, Nature Phys., **5**, 665 (2009), doi:10.1038/nphys1358

[Gallagher89]   Alan Gallagher and David E. Pritchard, *Exoergic collisions of cold* Na$^{/emph>}$*-Na*, Phys. Rev. Lett., **63**, 957 (1989), doi:10.1103/PhysRevLett.63.957

[Garrison08]   J. C. Garrison and R. Y. Chiao, *Quantum Optics*, Oxford University Press Inc., New York (2008)

[Geremia06]   J. M. Geremia, John K. Stockton, and Hideo Mabuchi, *Tensor polarizability and dispersive quantum measurement of multilevel atoms*, Phys. Rev. A, **73**, 042112 (2006), doi:10.1103/PhysRevA.73.042112

[Gisin02]   Nicolas Gisin, Grégoire Ribordy, Wolfgang Tittel, and Hugo Zbinden, *Quantum cryptography*, Rev. Mod. Phys., **74**, 145 (2002), doi:10.1103/RevModPhys.74.145

[Gorshkov07a]   Alexey V. Gorshkov, Axel André, Mikhail D. Lukin, and Anders S. Sørensen, *Photon storage in Λ-type optically dense atomic media. I. Cavity model*, Phys. Rev. A, **76**, 033804 (2007), doi:10.1103/PhysRevA.76.033804

[Gorshkov07b]   —, *Photon storage in Λ-type optically dense atomic media. II. Free-space model*, Phys. Rev. A, **76**, 033805 (2007), doi:10.1103/PhysRevA.76.033805

[Gross82]   M. Gross and S. Haroche, *Superradiance: An essay on the theory of collective spontaneous emission*, Physics Reports, **93**(5), 301 (1982), doi:10.1016/0370-1573(82)90102-8

[Hammerer10]   Klemens Hammerer, Anders S. Sørensen, and Eugene S. Polzik, *Quantum interface between light and atomic ensembles*, Rev. Mod. Phys., **82**, 1041 (2010), doi:10.1103/RevModPhys.82.1041

[HAPPER72]   WILLIAM HAPPER, *Optical Pumping*, Rev. Mod. Phys., **44**, 169 (1972), doi:10.1103/RevModPhys.44.169

[Heinze10]   G. Heinze, A. Rudolf, F. Beil, and T. Halfmann, *Storage of images in atomic coherences in a rare-earth-ion-doped solid*, Phys. Rev. A, **81**, 011401 (2010), doi:10.1103/PhysRevA.81.011401

[Hilliard08a] A. Hilliard, F. Kaminski, R. le Targat, C. Olausson, E. S. Polzik, and J. H. Müller, *Rayleigh superradiance and dynamic Bragg gratings in an end-pumped Bose-Einstein condensate*, Phys. Rev. A, **78**, 051403 (2008), doi:10.1103/PhysRevA.78.051403

[Hilliard08b] Andrew Hilliard, *Collective Rayleigh scattering in a Bose Einstein condensate* (2008), ph.D. thesis, University of Copenhagen, Denmark

[Hobbs09]   Philip C. Hobbs, *Building electro-optical systems Making it all work*, John Wiley and Sons, Inc., second edn. (2009)

[Hon]   Honeywell SSEC, *1- and 2-Axis Magnetic Sensors, Datasheet*, rev. b edn.

[Horowitz01]   Paul Horowitz and Hill Winfield, *The art of electronics*, Cambridge University Press, second edn. (2001)

[Hosseini11a] M. Hosseini, G. Campbell, B. M. Sparkes, P. K. Lam, and B. C. Buchler, *Unconditional room-temperature quantum memory*, Nature Phys., **7**, 794 (2011), doi:10.1038/nphys2021

[Hosseini11b] M. Hosseini, B. M. Sparkes, G. Campbell, P. K. Lam, and B. C. Buchler, *High efficiency coherent optical memory with warm rubidium vapour*, Nature Commun., **2**, 174 (2011), doi:10.1038/ncomms1175

[Inouye99]   S. Inouye, A. P. Chikkatur, D. M. Stamper-Kurn, J. Stenger, D. E. Pritchard, and W. Ketterle, *Superradiant Rayleigh Scattering from a Bose-Einstein Condensate*, Science, **285**(5427), 571 (1999), doi:10.1126/science.285.5427.571

[Jack09]   B. Jack, J. Leach, J. Romero, S. Franke-Arnold, M. Ritsch-Marte, S. M. Barnett, and M. J. Padgett, *Holographic Ghost Imaging and the Violation of a Bell Inequality*, Phys. Rev. Lett., **103**, 083602 (2009), doi:10.1103/PhysRevLett.103.083602

[Jensen10]   K. Jensen, W. Wasilewski, H. Krauter, T. Fernholz, B. M. Nielsen, M. Owari, M. B. Plenio, A. Serafini, M. M. Wolf, and E. S. Polzik, *Quantum memory for entangled continuous-variable states*, Nature Phys., **7**, 13 (2010), doi:10.1038/nphys1819

[Jones06]   Kevin M. Jones, Eite Tiesinga, Paul D. Lett, and Paul S. Julienne, *Ultracold photoassociation spectroscopy: Long-range molecules and atomic scattering*, Rev. Mod. Phys., **78**, 483 (2006), doi:10.1103/RevModPhys.78.483

[Julienne96]   P. S. Julienne, *Cold Binary Atomic Collisions in a Light Field*, J. Res. Natl. Inst. Stand. Technol., **101**, 487 (1996)

[Julsgaard04]   Brian Julsgaard, Jacob Sherson, J. Ignacio Cirac, Jaromír Fiurášek, and Eugene S. Polzik, *Experimental demonstration of quantum memory for light*, Nature, **432**, 482 (2004), doi:10.1038/nature03064

[Kaminski12a]   F. Kaminski, N. Kampel, M. Steenstrup, A. Griesmaier, E. Polzik, and J. Müller, *In-situ dual-port polarization contrast imaging of Faraday rotation in a high optical depth ultracold ^{87}Rb atomic ensemble*, Eur. Phys. J. D, **66**, 1 (2012), doi:10.1140/epjd/e2012-30038-0

[Kaminski12b]   Franziska Kaminski, *Coherent Atom-Light Interaction in an Ultracold Atomic Gas*, Ph.d., University of Copenhagen, Denmark, Copenhagen, Denmark (2012), ph.D. thesis, University of Copenhagen, Denmark

[Kampel12]   N. S. Kampel, A. Griesmaier, M. P. Hornbak Steenstrup, F. Kaminski, E. S. Polzik, and J. H. Müller, *Effect of Light Assisted Collisions on Matter Wave Coherence in Superradiant Bose-Einstein Condensates*, Phys. Rev. Lett., **108**, 090401 (2012), doi:10.1103/PhysRevLett.108.090401

[Ketterle01]   W. Ketterle and S. Inouye, *Collective enhancement and suppression in dilute Bose-Einstein condensates*, in *Compte rendus de l'académie des sciences* (2001), vol. 2, 339–380, `arXiv: cond-mat/0101424`

[Ketterle11]   Wolfgang Ketterle, *Comment on "Electromagnetic Wave Dynamics in Matter-Wave Superradiant Scattering"*, Phys. Rev. Lett., **106**, 118901 (2011), doi:10.1103/PhysRevLett.106.118901

[Koschorreck09] M. Koschorreck and M. W. Mitchell, *Unified description of inhomogeneities, dissipation and transport in quantum light-atom interfaces*, Journal of Physics B: Atomic, Molecular and Optical Physics, **42**(19), 195502 (2009)

[Kupriyanov05]   D. V. Kupriyanov, O. S. Mishina, I. M. Sokolov, B. Julsgaard, and E. S. Polzik, *Multimode entanglement of light and atomic ensembles via off-resonant coherent forward scattering*, Phys. Rev. A, **71**, 032348 (2005), doi:10.1103/PhysRevA.71.032348

[Kurucz08]   Z. Kurucz and M. Fleischhauer, *Continuous-variable versus electromagnetically-induced-transparency-based quantum memories*, Phys. Rev. A, **78**, 023805 (2008), doi:10.1103/PhysRevA.78.023805

[Labeyrie03]   G. Labeyrie, E. Vaujour, C. A. Müller, D. Delande, C. Miniatura, D. Wilkowski, and R. Kaiser, *Slow Diffusion of Light in a Cold Atomic Cloud*, Phys. Rev. Lett., **91**, 223904 (2003), doi:10.1103/PhysRevLett.91.223904

[Lauritzen10]   Björn Lauritzen, Ji řiMinář, Hugues de Riedmatten, Mikael Afzelius, Nicolas Sangouard, Christoph Simon, and Nicolas Gisin, *Telecommunication-Wavelength Solid-State Memory at the Single Photon Level*, Phys. Rev. Lett., **104**, 080502 (2010), doi:10.1103/PhysRevLett.104.080502

[Lin09]   Y.-J. Lin, A. R. Perry, R. L. Compton, I. B. Spielman, and J. V. Porto, *Rapid production of ^{87}Rb Bose-Einstein condensates in a combined magnetic and optical potential*, Phys. Rev. A, **79**, 063631 (2009), doi:10.1103/PhysRevA.79.063631

[Lukin03]   M. D. Lukin, *Colloquium: Trapping and manipulating photon states in atomic ensembles*, Rev. Mod. Phys., **75**, 457 (2003), doi:10.1103/RevModPhys.75.457

[Lvovsky09]   Alexander I. Lvovsky, Barry C. Sanders, and Wolfgang Tittel, *Optical quantum memory*, Nature Photonics, **3**, 706 (2009), doi:10.1038/nphoton.2009.231

[Marte02]   A. Marte, T. Volz, J. Schuster, S. Dürr, G. Rempe, E. G. M. van Kempen, and B. J. Verhaar, *Feshbach Resonances in Rubidium 87: Precision Measurement and Analysis*, Phys. Rev. Lett., **89**, 283202 (2002), doi:10.1103/PhysRevLett.89.283202

[Mishina07]   O. S. Mishina, D. V. Kupriyanov, J. H. Müller, and E. S. Polzik, *Spectral theory of quantum memory and entanglement via Raman scattering of light by an atomic ensemble*, Phys. Rev. A, **75**, 042326 (2007), doi:10.1103/PhysRevA.75.042326

[Moore00]   M. G. Moore and P. Meystre, *Generating Entangled Atom-Photon Pairs from Bose-Einstein Condensates*, Phys. Rev. Lett., **85**, 5026 (2000), doi:10.1103/PhysRevLett.85.5026

[Movre77]   M Movre and G Pichler, *Resonance interaction and self-broadening of alkali resonance lines. I. Adiabatic potential curves*, Journal of Physics B: Atomic and Molecular Physics, **10**(13), 2631 (1977)

[Movre80]   —, *Resonance interaction and self-broadening of alkali resonance lines. II. Quasi-static wing profiles*, Journal of Physics B: Atomic and Molecular Physics, **13**(4), 697 (1980)

[Radnaev10]   A. G. Radnaev, Y. O. Dudin, R. Zhao, H. H. Jen, S. D. Jenkins, A. Kuzmich, and T. A. B. Kennedy, *A quantum memory with telecom-wavelength conversion*, Nature Phys., **6**, 894 (2010), doi:10.1038/nphys1773

[Raymer81]   M. G. Raymer and J. Mostowski, *Stimulated Raman scattering: Unified treatment of spontaneous initiation and spatial propagation*, Phys. Rev. A, **24**, 1980 (1981), doi:10.1103/PhysRevA.24.1980

[Reim11]   K. F. Reim, P. Michelberger, K. C. Lee, J. Nunn, N. K. Langford, and I. A. Walmsley, *Single-Photon-Level Quantum Memory at Room Temperature*, Phys. Rev. Lett., **107**, 053603 (2011), doi:10.1103/PhysRevLett.107.053603

[Riedl12]   Stefan Riedl, Matthias Lettner, Christoph Vo, Simon Baur, Gerhard Rempe, and Stephan Dürr, *Bose-Einstein condensate as a quantum memory for a photonic polarization qubit*, Phys. Rev. A, **85**, 022318 (2012), doi:10.1103/PhysRevA.85.022318

[Ritter12]   Stephan Ritter, Christian Nolleke, Carolin Hahn, Andreas Reiserer, Andreas Neuzner, Manuel Uphoff, Martin Mucke, Eden Figueroa, Joerg Bochmann, and Gerhard Rempe, *An elementary quantum network of single atoms in optical cavities*, Nature, **484**, 195 (2012), doi:10.1038/nature11023

[Sakurai94]   J. J. Sakurai, *Modern Quantum Mechanics*, Addison-Wesley Publishing Company, Inc., revised edn. (1994)

[Sangouard11]   Nicolas Sangouard, Christoph Simon, Hugues de Riedmatten, and Nicolas Gisin, *Quantum repeaters based on atomic ensembles and linear optics*, Rev. Mod. Phys., **83**, 33 (2011), doi:10.1103/RevModPhys.83.33

[Schneble03]   Dominik Schneble, Yoshio Torii, Micah Boyd, Erik W. Streed, David E. Pritchard, and Wolfgang Ketterle, *The Onset of Matter-Wave Amplification in a Superradiant Bose-Einstein Condensate*, Science, **300**(5618), 475 (2003), doi:10.1126/science.1083171

[Schneble04]   Dominik Schneble, Gretchen K. Campbell, Erik W. Streed, Micah Boyd, David E. Pritchard, and Wolfgang Ketterle, *Raman amplification of matter waves*, Phys. Rev. A, **69**, 041601 (2004), doi:10.1103/PhysRevA.69.041601

[Schnorrberger09] U. Schnorrberger, J. D. Thompson, S. Trotzky, R. Pugatch, N. Davidson, S. Kuhr, and I. Bloch, *Electromagnetically Induced Transparency and Light Storage in an Atomic Mott Insulator*, Phys. Rev. Lett., **103**, 033003 (2009), doi:10.1103/PhysRevLett.103.033003

[Shor94]   P. Shor, *Algorithms for quantum computation: Discrete logarithms and factoring*, in *in Proc. 35th Annu. Symp. on the Foundations of Computer Science,Santa Fe, NM, November, IEEE Computer Society Press* (1994), 124–134

[Shuker08]   M. Shuker, O. Firstenberg, R. Pugatch, A. Ron, and N. Davidson, *Storing Images in Warm Atomic Vapor*, Phys. Rev. Lett., **100**, 223601 (2008), doi:10.1103/PhysRevLett.100.223601

[Simon10]   C. Simon, M. Afzelius, J. Appel, A. Boyer de la Giroday, S. J. Dewhurst, N. Gisin, C. Y. Hu, F. Jelezko, S. Kröll, J. H. Müller, J. Nunn, E. S. Polzik, J. G. Rarity, H. De Riedmatten, W. Rosenfeld, A. J. Shields, N. Sköld, R. M. Stevenson, R. Thew, I. A. Walmsley, M. C. Weber, H. Weinfurter, J. Wrachtrup, and R. J. Young, *Quantum memories*, Eur. Phys. J. D, **58**(1), 1 (2010), doi:10.1140/epjd/e2010-00103-y

[Sokolov09]   I. M. Sokolov, M. D. Kupriyanova, D. V. Kupriyanov, and M. D. Havey, *Light scattering from a dense and ultracold atomic gas*, Phys. Rev. A, **79**, 053405 (2009), doi:10.1103/PhysRevA.79.053405

[Specht11]   Holger P. Specht, Christian Nolleke, Andreas Reiserer, Manuel Uphoff, Eden Figueroa, Stephan Ritter, and Gerhard Rempe, *A single-atom quantum memory*, Nature, **473**, 190 (2011), doi:10.1038/nature09997

[Stam07]   K. M. R. van der Stam, E. D. van Ooijen, R. Meppelink, J. M. Vogels, and P. van der Straten, *Large atom number Bose-Einstein condensate of sodium*, Review of Scientific Instruments, **78**(1), 013102 (2007), doi:10.1063/1.2424439

[Steck08]   Daniel Adam Steck, *Rubidium 87 D Line Data*, 2.0.1 edn. (2008), `http://steck.us/alkalidata`

[Steger12]   M. Steger, K. Saeedi, M. L. W. Thewalt, J. J. L. Morton, H. Riemann, N. V. Abrosimov, P. Becker, and H.-J. Pohl, *Quantum Information Storage for over 180 s Using Donor Spins in a 28Si "Semiconductor Vacuum"*, Science, **336**(6086), 1280 (2012), doi:10.1126/science.1217635, `http://www.sciencemag.org/content/336/6086/1280.full.pdf`

[Svistunov90]   B. V. Svistunov and G. V. Shlyapnikov, *Resonance optics of the low-temperature quantum gases H and D*, Sov. Phys. JETP, **70**, 460 (1990)

[Timoney12]   N. Timoney, B. Lauritzen, I. Usmani, M. Afzelius, and N. Gisin, *Atomic frequency comb memory with spin-wave storage in $^{153}Eu^{3+}$:Y_2SiO_5*, Journal of Physics B: Atomic, Molecular and Optical Physics, **45**(12), 124001 (2012), doi:10.1088/0953-4075/45/12/124001

[Tittel10]   W. Tittel, M. Afzelius, T. Chaneliére, R.L. Cone, S. Kröll, S.A. Moiseev, and M. Sellars, *Photon-echo quantum memory in solid state systems*, Laser and Photonics Reviews, **4**(2), 244 (2010), doi:10.1002/lpor.200810056

[Varshalovich88] D. A. Varshalovich, A. N. Moskalev, and V. K. Khersonskii, *Quantum Theory of Angular Momentum*, World Scientific Singapore (1988)

[Vuletić99]   Vladan Vuletić, Cheng Chin, Andrew J. Kerman, and Steven Chu, *Suppression of Atomic Radiative Collisions by Tuning the Ground State Scattering Length*, Phys. Rev. Lett., **83**, 943 (1999), doi:10.1103/PhysRevLett.83.943

[Weiner99]   John Weiner, Vanderlei S. Bagnato, Sergio Zilio, and Paul S. Julienne, *Experiments and theory in cold and ultracold collisions*, Rev. Mod. Phys., **71**, 1 (1999), doi:10.1103/RevModPhys.71.1

[Windpassinger09] Patrick J Windpassinger, Marcin Kubasik, Marco Koschorreck, Axel Boisen, Niels Kjærgaard, Eugene S Polzik, and Jörg Helge Müller, *Ultra low-noise differential ac-coupled photodetector for sensitive pulse detection applications*, Measurement Science and Technology, **20**(5), 055301 (2009)

[Wootters82]   W. K. Wootters and W. H. Zurek, *A single quantum cannot be cloned*, Nature, **299**, 802 (1982), doi:10.1038/299802a0

[Yoshikawa04]   Yutaka Yoshikawa, Toshiaki Sugiura, Yoshio Torii, and Takahiro Kuga, *Observation of superradiant Raman scattering in a Bose-Einstein condensate*, Phys. Rev. A, **69**, 041603 (2004), doi:10.1103/PhysRevA.69.041603

[You96]   L. You, Maciej Lewenstein, Roy J. Glauber, and J. Cooper, *Quantum field theory of atoms interacting with photons. III. Scattering of weak cw light from cold samples of bosonic atoms*, Phys. Rev. A, **53**, 329 (1996), doi:10.1103/PhysRevA.53.329

[Zeuthen11]   Emil Zeuthen, Anna Grodecka-Grad, and Anders S. Sørensen, *Three-dimensional theory of quantum memories based on Λ-type atomic ensembles*, Phys. Rev. A, **84**, 043838 (2011), doi:10.1103/PhysRevA.84.043838

[Zhang09]   Rui Zhang, Sean R. Garner, and Lene Vestergaard Hau, *Creation of Long-Term Coherent Optical Memory via Controlled Nonlinear Interactions in Bose-Einstein Condensates*, Phys. Rev. Lett., **103**, 233602 (2009), doi:10.1103/PhysRevLett.103.233602

[Zhao09]   R. Zhao, Y. O. Dudin, S. D. Jenkins, C. J. Campbell, D. N. Matsukevich, T. A. B. Kennedy, and A. Kuzmich, *Long-lived quantum memory*, Nature Phys., **5**, 100 (2009), doi:10.1038/nphys1152

[Zobay05]   O. Zobay and Georgios M. Nikolopoulos, *Dynamics of matter-wave and optical fields in superradiant scattering from Bose-Einstein condensates*, Phys. Rev. A, **72**, 041604 (2005), doi:10.1103/PhysRevA.72.041604

[Zobay06]   —, *Spatial effects in superradiant Rayleigh scattering from Bose-Einstein condensates*, Phys. Rev. A, **73**, 013620 (2006), doi:10.1103/PhysRevA.73.013620

Publications

Peer reviewed

1. N. S. Kampel, M.P. Hornbak Steenstrup, E. S. Polzik, and J. H. Müller,
   Homodyne imaging of a high optical depth Raman memory in the presence of losses
   In preparation, to be submitted to Phys. Rev. A

2. N. S. Kampel, A. Griesmaier, M. P. Hornbak Steenstrup, F. Kaminski, E. S. Polzik, and J. H. Müller,
   Effect of Light Assisted Collisions on Matter Wave Coherence in Superradiant Bose-Einstein Condensates
   Phys. Rev. Lett. **108**, 090401 (2012)

3. F. Kaminski, N. S. Kampel, M. P. Steenstrup, A. Griesmaier, E. S. Polzik and J. H. Müller,
   In-Situ Dual-Port Polarization Contrast Imaging of Faraday Rotation in a High Optical Depth Ultracold 87Rb Atomic Ensemble
   Eur. Phys. J. D, **66**, 227 (2012)

4. N. S. Kampel, A. Rikanati, I. Be'ery, U. Avni, A. Ben-Kish, A. Fisher, A. Ron,
   Feasibility of nitrogen-recombination soft X-ray laser using capillary discharge Z-pinch
   Phys. Rev. E, **78**, 056404 (2008)

Meeting and Conference Contributions

Talks

1. Seminar, "High optical depth off-resonance Raman memory in presence of losses", September 2012, Basel, Switzerland

2. Seminar, "Light assisted collisions in BEC (superradiAnce asymmetry) and first steps towards Raman memory in a dense sample", October 2011, Stuttgart, Germany

3. QUANTOP Meeting, "BEC lab: Next steps and status", September 2009, Copenhagen, Denmark

Posters

1. Conference - The 23rd International Conference on Atomic Physics ICAP 2012, July 2012, Paris, France

2. Conference - High dimensional entanglement, June 2011, Como, Italy

3. Conference - Frontiers of matter wave optics, March 2011, Obergurgl, Austria

4. Conference - Mixed states of light and matter, February 2009, Bonn, Germany

Version long - Changes